

Fabrication of Two-dimensional MoS₂ based Heterostructures for Photodetector and Gas-sensing Applications

Doctoral Thesis

by

Riya Wadhwa

(2017PHZ0006)



DEPARTMENT OF PHYSICS

INDIAN INSTITUTE OF TECHNOLOGY ROPAR

July 2023

Fabrication of Two-dimensional MoS₂ based Heterostructures for Photodetector and Gas-sensing Applications

A Thesis Submitted

In Partial Fulfillment of the Requirements for the Degree of

DOCTOR OF PHILOSOPHY

by

Riya Wadhwa

(2017PHZ0006)



DEPARTMENT OF PHYSICS

INDIAN INSTITUTE OF TECHNOLOGY ROPAR

July 2023

Riya Wadhwa: *Fabrication of Two-dimensional MoS₂ based Heterostructures for Photodetector and Gas-sensing Applications*

Copyright © 2023, Indian Institute of Technology Ropar

All Rights Reserved

DEDICATED
TO
MY PARENTS

Declaration of Originality

I hereby declare that the work which is being presented in the thesis entitled “**Fabrication of Two-dimensional MoS₂ based Heterostructures for Photodetector and Gas-sensing Applications**” has been solely authored by me. It presents the result of my own independent investigation/research conducted during the time period from January 2018 to April 2023 under the supervision of Dr. Mukesh Kumar, Associate Professor, and Indian Institute of Technology Ropar. To the best of my knowledge, it is an original work, both in terms of research content and narrative, and has not been submitted or accepted elsewhere, in part or in full, for the award of any degree, diploma, fellowship, associateship, or similar title of any university or institution. Further, due credit has been attributed to the relevant state-of-the-art and collaborations (if any) with appropriate citations and acknowledgments, in line with established ethical norms and practices. I also declare that any idea/data/fact/source stated in my thesis has not been fabricated/ falsified/ misrepresented. All the principles of academic honesty and integrity have been followed. I fully understand that if the thesis is found to be unoriginal, fabricated, or plagiarized, the Institute reserves the right to withdraw the thesis from its archive and revoke the associated Degree conferred. Additionally, the Institute also reserves the right to appraise all concerned sections of society of the matter for their information and necessary action (if any). If accepted, I hereby consent for my thesis to be available online in the Institute’s Open Access repository, inter-library loan, and the title & abstract to be made available to outside organizations.



Signature:

Name: Riya Wadhwa

Entry Number: 2017PHZ0006

Department: Physics

Indian Institute of Technology Ropar

Rupnagar, Punjab 140001

Date: July 14, 2023

Certificate

This is to certify that the thesis entitled “**Fabrication of Two-Dimensional MoS₂ based Heterostructures for Photodetector and Gas Sensing Applications**” submitted by Riya Wadhwa (2017PHZ0006) for the award of the degree of Doctor of Philosophy of Indian Institute of Technology Ropar, is a record of bonafide research work carried out under my (our) guidance and supervision. To the best of my knowledge and belief, the work presented in this thesis is original and has not been submitted, either in part or full, for the award of any other degree, diploma, fellowship, associateship or similar title of any university or institution.

In my (our) opinion, the thesis has reached the standard of fulfilling the requirements of the regulations relating to the Degree.



Signature:

Name: Dr. Mukesh Kumar

Department: Physics

Indian Institute of Technology Ropar

Rupnagar, Punjab 140001

Date: July 14, 2023

Acknowledgments

First, I would like to express my sincere gratitude to my supervisor, Dr. Mukesh Kumar, Principal Investigator, Functional and Renewable Energy Materials (FREM) Laboratory at IIT Ropar, for his consistent guidance and motivation. He has been a constant support of encouragement, and his exceptional research aptitude plays a crucial role in the success of this thesis work. Without his support, this work would not have been possible. He is always open to discussion and tried his best to provide a good research environment and facilities to work in the lab. I acquired valuable insights from him about investigating and interpreting experimental data, and his confidence in my work inspired me to strive for better outcomes. He always pushes to think high and achieve goals in life. It was an incredibly fortunate and unforgettable experience to have the opportunity to work under his reflective and revered guidance. His optimistic nature and boundless kindness cannot be fully expressed in words, but I am immensely grateful for his unwavering support throughout this journey.

I also would like to thank my Doctoral Committee (DC) members, Dr. Rajesh V. Nair, Dr. Sandeep Gautam, Dr. Rajendra Srivastava, and DC chairperson Dr. Shubhrangshu Dasgupta for keep evaluating my performance and for their thoughtful discussions and suggestions. I am also thankful to all faculty and staff members of the Physics department for their constant support during my tenure.

I sincerely acknowledge our collaborators, Dr. Suman Kalyan Pal and his group at IIT Mandi, Dr. Pradeep Kumar and his group at IIT Mandi, Dr. Mahesh Kumar and his group at IIT Jodhpur, Prof. Manoj A G Namboothiry and his group at IISER Thiruvananthapuram, Dr. Sudip Chakraborty at HRI Allahabad and Prof. Rajeev Ahuja at IIT Ropar and their group, Prof. Quinn Qiao and his group from Syracuse University (USA) for their contribution in carrying out present thesis work.

I am thankful to the Ministry of Human Resource & Development (MHRD) for providing fellowship throughout my Ph.D. tenure. I am highly grateful to the central research facility (CRF) at IIT Ropar for providing characterization facilities. Additionally, I appreciate the support provided by the technical staff/ operators, Mr. Amit Kaushal (SEM and XRD), Mr. Damninder Singh (Raman), and Mr. Harsimranjit Singh (AFM). I gratefully acknowledge Mr. Anshu Vaid, Sr. Assistant, Department of Physics, for smoothly carrying up all the documentation work. Also, I would like to thank the Library, IIT Ropar, for granting me access to research papers and books essential to my work.

Additionally, my heartfelt gratitude goes out to my colleagues and alumni of the FREM lab. I am highly grateful to the Doctoral group (Dr. Naveen Kumar, Dr. Kanika Arora, Dr. Abhay.V Agrawal, Dr. Kulwinder Kaur, and Dr. Nisika) for their discussions and suggestions. It was wonderful to work with you all and I really appreciate the time when we worked together in the lab. Everyone owes a special place in my heart that I cannot express in a few words. I have learned a lot from you all. Apart from that, I really cherished those parties that we were having outside the lab. I want to thank Mr. Vishal Kumar for his assistance in many lab activities. He was the happiest person in the lab and exceptionally hardworking. I am grateful to Dr. Anupam Ghosh for his contribution to my research article. He has a caring gesture and always offers help to others. Also, I am highly thankful to Damanpreet Kaur for always being supportive. She is more like a friend or sister to me, and I really enjoyed her company in the lab. I want to thank other FREM lab members: Gaurav Bassi, Shivani, Puja, and Rohit for their assistance in the lab activities. I also want to thank Vinit and Dr. Rajeev Ray as warm-hearted members of our lab.

I would like to especially thank Mr. Piyush Pratap Singh for his constant support during this journey. I am grateful to Ms. Arzoo Sharma for always keeping me motivated. I will always cherish the time spent with Ankita, Nazim, Rakhi, Dr. Taranjot, Chetan, Swati, Pratibha, and Paramjeet during campus life.

Above all, I owe my heartfelt gratitude to my parents: my mother and father, and my brother (Vipul Wadhwa) for their unconditional love and support. I am also thankful to all the other members who have directly and indirectly supported me in this journey.

At last, I am thankful to the almighty God for his blessings and making me capable of completing this task successfully.

Abstract

In the past decade, two-dimensional (2D) layered materials have emerged as a promising area of research, with significant efforts devoted to their fundamental studies and practical device applications. Due to their unique layered structure and atomic-scale thickness, these materials possess exclusive electrical and optical properties, which make them attractive for various applications. Among these materials, molybdenum disulfide (MoS_2) is the most widely studied transition metal dichalcogenide. Its direct and tunable bandgap, high carrier mobility, large current on/off ratio, thermal and chemical stability, and other unique characteristics make it an ideal choice for applications such as photodetectors, solar cells, sensors, transistors, etc.

Recent research has shown that vertically aligned MoS_2 (VA- MoS_2) flakes exhibit enhanced electrical, optical, and catalytic activities, compared to in-plane MoS_2 , due to their high aspect ratio, large surface area, and more exposed edges. As a result, these materials have become an attractive choice for photodetection and gas-sensing applications. However, large-area controlled growth of VA- MoS_2 flakes is necessary to realize their potential in commercial 2D technology. The fabrication of photodetectors using in-plane MoS_2 has revealed limited optical absorbance, which significantly hinders its photodetection capability. Furthermore, pristine MoS_2 photodetectors exhibit slow response times due to the high carrier recombination rate in bare MoS_2 and the absence of a high-quality junction. In addition, the active wavelength detection range of pristine MoS_2 -based devices is confined to its bandgap, which severely restricts their potential for broadband photodetection.

To overcome these limitations, integrating MoS_2 with other potential semiconductor materials has proven to be a viable option for high-performance photodetector fabrication. Despite considerable research in this field, the carrier dynamic at the interface remains a critical factor affecting device performance. Therefore, details studies are required to fully harness the potential of heterostructures for practical applications by optimizing their interface properties. Additionally, the choice of materials is also important to ensure that they complement each other and contribute to the overall performance of the device.

In the present thesis work, we addressed the challenges related to the controlled growth of large-area VA- MoS_2 flakes, as well as the fabrication of high-performance broadband photodetectors and gas sensors using MoS_2 heterostructures. To overcome these challenges, we employed a facile and efficient magnetron sputtering technique, which enabled the growth of large-area MoS_2 flakes with a controlled morphology ranging from in-plane to VA- MoS_2 ,

through precise control of the growth parameters. We carried out a comprehensive analysis of the morphology, structure, and spectroscopic properties of the MoS₂ film, which revealed the transition from in-plane to VA-MoS₂ flakes. Furthermore, we fabricated multiple heterostructures of MoS₂, including MoS₂/ReS₂, MoS₂/Ga₂O₃, and Pt@MoS₂, for broadband photodetection, and performed a detailed investigation of their photodetector performance. The results demonstrate that the fabricated heterostructures exhibited high responsivity, high detectivity, and fast optical switching when compared to pristine MoS₂. In order to gain a deeper understanding of the device mechanism, we utilized advanced techniques such as photoelectron spectroscopy and kelvin probe force microscopy to investigate the energy band alignment and charge carrier dynamics at the heterointerface.

Finally, we explored the interaction of gas molecules and VA-MoS₂. We fabricated Pt nanoparticles decorated VA-MoS₂ (Pt@MoS₂) sensor that showed selective hydrogen sensing at room temperature. We systematically investigated the sensing performance of the Pt@MoS₂ sensor and discuss the possible sensing mechanism. Our fabricated sensor demonstrates excellent sensitivity and low detection ability (>1 ppm), highlighting, its potential for use in hydrogen vehicles and other related technologies in near future.

Table of Contents

Acknowledgments.....	vii
Abstract	ix
List of symbols, and abbreviations	xiv
List of Figures	xvii
List of Tables.....	xxv
Chapter 1: Introduction.....	1
1.1 Background	1
1.2 Transition metal dichalcogenides	1
1.3 Molybdenum disulfide (MoS ₂).....	3
1.3.1 Properties of MoS ₂	3
1.3.1.1 Crystal structure	3
1.3.1.2 Band structure	5
1.3.1.3 Photoluminescence.....	6
1.3.1.4 Absorbance.....	8
1.3.1.5 Vibrational modes (Raman)	9
1.4 Synthesis of MoS ₂	10
1.4.1 Mechanical exfoliation	10
1.4.2 Chemical exfoliation.....	11
1.4.3 Chemical vapor deposition	12
1.4.4 Sputtering.....	13
1.5 Vertically aligned MoS ₂	14
1.6 Applications of MoS ₂	14
1.7 Photodetectors	14
1.7.1 General characteristics of the photodetector.....	15
1.7.2 Photodetection mechanism	16
1.8 A brief historical overview of photodetectors based on 2D materials: MoS ₂ and its heterostructures	19
1.9 Gas sensors	24
1.9.1 General characteristics of the gas sensor	24
1.9.2 Gas sensing mechanism in MoS ₂ and its heterostructure	25
1.10 Challenges and Motivation.....	28
1.11 Objective of the present thesis work	30
1.12 Outline of the thesis.....	30
References	32

Chapter 2: Fabrication and characterization techniques.....	39
2.1 Deposition techniques	39
2.1.1 Magnetron sputtering.....	39
2.1.2 Chemical vapor deposition	41
2.2 Characterization techniques	42
2.2.1 X-ray diffraction	42
2.2.2 Scanning electron microscope and Energy Dispersive X-ray	43
2.2.3 Raman spectroscopy	44
2.2.4 Photoluminescence spectroscopy	45
2.2.5 Ultraviolet-Visible (UV-Vis) spectroscopy	45
2.2.6 X-ray photoelectron spectroscopy and Ultra-violet photoelectron spectroscopy	46
2.2.7 Kelvin probe force microscopy (KPFM)	47
2.3 Device fabrication and characterization	48
2.3.1 Metal electrode deposition through the thermal evaporator	48
2.3.1 Photodetector measurement.....	49
2.3.2 Gas sensing measurement.....	50
References	52
Chapter 3: Large area growth of MoS₂ from in-plane to vertically oriented flakes.....	53
3.1 Requirement of large area growth of vertically aligned MoS ₂ flakes	53
3.2 Experimental section	54
3.2.1 Synthesis of MoS ₂	54
3.2.2 Characterizations of MoS ₂	55
3.2.3 Photodetector fabrication and measurements	55
3.3 Results and Discussion.....	55
3.4 Proposed growth mechanism.....	63
3.5 Photodetector performance.....	64
3.6 Conclusions	66
References	67
Chapter 4: 2D MoS₂ heterostructures for broadband photodetection.....	69
4.1 Requirement of highly sensitive, fast, and broadband photodetectors	69
4.2 MoS ₂ based heterostructures for broadband photodetection	69
4.2.1 MoS ₂ -ReS ₂ heterostructure	69
4.2.1.1 Experimental Section	70
4.2.1.2 Results and discussion	72
4.2.1.3 Conclusions	87

4.2.2 MoS ₂ /Ga ₂ O ₃ heterostructure	87
4.2.2.1 Experimental Section	88
4.2.2.2 Results and discussion	89
4.2.2.3 Conclusions	102
4.2.3 Plasmonic Pt NPs decorated MoS ₂ (Pt@MoS ₂)	102
4.2.3.1 Experimental Section	103
4.2.3.2 Results and discussion	104
4.2.3.3 Conclusions	119
References	120
Chapter 5: 2D MoS₂ heterostructures for hydrogen sensing	127
5.1 Requirement of highly sensitive room temperature hydrogen sensor	127
5.2 Experimental section	128
5.2.1 Synthesis of MoS ₂ and Pt NPs decorated MoS ₂ (Pt@MoS ₂)	128
5.2.2 Characterizations	129
5.2.3 Device fabrication and gas sensing measurements.....	130
5.3 Results and Discussions	130
5.3.1 Structural, optical, and chemical properties	130
5.3.2 Gas sensing performance	132
5.3.3 Proposed sensing mechanism	140
5.4 conclusions	144
References	145
Chapter 6: Summary and Scope for Future Studies.....	149
6.1 Summary	149
6.1.1 Large area growth of MoS ₂ from in-plane to vertically oriented flakes.....	149
6.1.2 2D MoS ₂ heterostructures for broadband photodetection	150
6.1.2.1 MoS ₂ /ReS ₂ heterostructure	150
6.1.2.2 MoS ₂ /Ga ₂ O ₃ heterostructure	151
6.1.2.2 Platinum nanoparticles decorated MoS ₂ heterostructure	151
6.1.3 2D MoS ₂ heterostructures for hydrogen sensing	152
6.2 Scope for future studies	153
Appendix I.....	155
Appendix II	157
List of Publications.....	161
Conferences/Workshops Attended	162
Curriculum Vitae	163

List of symbols, and abbreviations

Symbol/ abbreviations	Description
2D	Two-dimensional
2DSCs	Two-dimensional semiconductors
TMDs	Transition metal dichalcogenides
MoS ₂	Molybdenum disulfide
Mo	Molybdenum
MoO ₃	Molybdenum trioxide
S	Sulfur
VA	Vertically aligned
ReS ₂	Rhenium disulfide
Ga ₂ O ₃	Gallium oxide
Pt	Platinum
Pd	Palladium
Au	Gold
Ag	Silver
In	Indium
NPs	Nanoparticles
NSs	Nanosheets
CQDs	Colloidal quantum dots
JCPDS	Joint Committee of Power Diffraction Standards
VBM	Valence band maximum
CBM	Conduction band minimum
SEM	Scanning electron microscope
EDX	Energy dispersive X-ray spectroscopy
XPS	X-ray photoelectron spectroscopy
UPS	Ultraviolet photoelectron spectroscopy
AFM	Atomic force microscopy
KPFM	Kelvin probe force microscopy
PL	Photoluminescence
GIXRD	Grazing incidence X-ray diffraction
PVD	Physical vapor deposition
CVD	Chemical vapor deposition
APCVD	Atmospheric vapor deposition
SP	Surface potential
V _{CPD}	Contact potential difference

ϕ_B	Schottky barrier height
ϕ	Work function
χ	Electron affinity
W	Emission width
CBO	Conduction band offset
VBO	Valence band offset
E_g	Bandgap
E_F	Fermi Energy
FWHM	Full width half maxima
DFT	Density functional theory
CCD	Charge density difference
Ar	Argon
O ₂	Oxygen
CO ₂	Carbon dioxide
NO ₂	Nitrogen dioxide
NH ₃	Ammonia
H ₂	Hydrogen
H ₂ O	Dihydrogen monoxide
CO	Carbon monoxide
H ₂ S	Molybdenum
SO ₂	Sulfur dioxide
ppm	Parts per million
E_a (meV)	Adsorption energy
q	Electronic charge
ΔQ (e)	Charge transfer
RT	Room temperature
LSPR	Localized surface plasmon resonance
UV	Ultraviolet
Vis	Visible
NIR	Near-infrared
nm	Nanometer
τ	Carrier lifetime
τ_{tr}	Carrier transit time
n	Ideality factor
k	Boltzmann constant
T	Temperature
T	Transmission

I_{photo}	Photocurrent
I_{dark}	Dark current
I_{light}	Illumination current (Current under light conditions)
PDCR	Photo-to-dark current ratio
P	Incident power
A	Active area
A*	Richardson constant
R	Responsivity
D*	Specific detectivity
EQE	External quantum efficiency
G	Photogain
SNR	Signal to noise ratio
NEP	Noise equivalent power
h	Planck constant
T_r	Rise time
T_f	Fall time
μ	Mobility
L	Channel length
DC	Direct current
RF	Radio frequency
A	Absorbance
α	Absorption coefficient
M-S-M	Metal-semiconductor-metal

List of Figures

Figure 1.1 (a) Highlighted transition metals (group 4-10) and chalcogenides in the periodic table that form layered structures, partially highlighted transition metals indicate only some of the dichalcogenides form layered structures. (b) Stacking of hexagonally packed planes bounded by the van der Waals force. Possible coordination unit of layered TMDs (c) Trigonal prismatic (AbA) (d) Octahedron (AbC) [5].	2
Figure 1.2 Crystal structure of MoS ₂ (a) 2H phase (b) 1T phase, with a schematic representation of the gradual filling of d orbitals that are situated in the bandgap between bonding (σ) and anti-bonding states (σ^*) [5, 14].	4
Figure 1.3 (a) Brillouin zone of 2H-MoS ₂ , Calculated band structures of MoS ₂ from bulk to monolayer (a) Bulk (b) Quadrilayer (c) Bilayer and (d) Monolayer [16, 17].	6
Figure 1.4 (a) Band structure of the bulk and monolayer MoS ₂ , where A and B indicate the direct-gap transitions, and I represent the indirect-gap transition. The indirect gap for the bulk is denoted by Eg' and direct gap for the monolayer is indicated as Eg . (b) PL spectra for mono and bilayer MoS ₂ , inset displaying the relative quantum yield of MoS ₂ as a function of layer number, (c) The normalized PL spectra with respect to layer number [18].	6
Figure 1.5 Schematic illustration of the optical transition occurring at the K-point of the Brillouin zone in different regions of MoS ₂ , including monolayer, bilayer, and bulk. The A-exciton peak experiences a red shift due to the reduction of the first exciton level. The B-exciton peak position remains relatively the same because the decrease in the exciton level is balanced by an increase in the valence band splitting energy [21].	7
Figure 1.6 (a) Optical absorbance spectra of MoS ₂ with layer number, (b) The calculated absorption coefficient for monolayer MoS ₂ [22, 24].	8
Figure 1.7 (a) All possible vibrational modes ($E2g2$, $E1g$, $E2g1$, $A1g$ and $E1u1$, $A2u1$) in bulk MoS ₂ (b) Two Raman active modes ($A1g$ and $E2g1$) in mono and few-layers MoS ₂ (c) Raman spectra of MoS ₂ with layer number, (d) Variation in frequency and peak position of $E2g1$ and $A1g$ modes as a function of layer number [25, 27].	9
Figure 1.8 Different synthesis techniques to grow 2D MoS ₂ . The top-down approach includes (a) Mechanical exfoliation, (b,c) Chemical exfoliation; the Bottom-up approach includes (d) Chemical vapor deposition, (e,f) Sputtering [30, 32, 34-38].	12
Figure 1.9 Mobility versus on/off ratio values for 2D semiconductors [80].	19

Figure 1.10 Optical image of monolayer MoS ₂ . (b) Photoresponsivity as a function of wavelength, indicating the cut-off wavelength of 680 nm. Schematic of the monolayer MoS ₂ photodetector shown in the inset. (c) Photoresponsivity as a function of incident power of the same device [84, 85].....	20
Figure 1.11 (a) 3D schematic of MoS ₂ /MoTe ₂ heterojunction device under illumination, (b) MoS ₂ /PbS QD hybrid under light illumination with device performance, (c) 2D/3D vertical heterostructure of MoS ₂ /Si under illumination and photocurrent map at junction, (d) Schematic of a plasmon-enhanced MoS ₂ photodetector and power-dependent photocurrent of pristine MoS ₂ and MoS ₂ with incorporated Au–NPs [106-109].	23
Figure 1.12 Schematic of charge transfer between MoS ₂ and (a) NO ₂ (electron acceptor), and (b) NH ₃ (electron donor) gas. In situ PL spectra recorded from MoS ₂ in presence of (c) NO ₂ and (d) NH ₃ gas molecules [117].	26
Figure 2.1 Schematic illustration of the sputtering system.	40
Figure 2.2 Schematic representation of common elementary steps of the CVD process.....	42
Figure 2.3 Schematic representation of the interaction volume resulting from the interaction between the primary electron beam and sample	43
Figure 2.4 Schematic illustration of the light interaction with the molecule depicting Rayleigh and Raman scattering.	44
Figure 2.5 Schematic representation of band alignment between the sample and the tip in a typical KPFM set-up under different conditions. (a) Non-contact (b) External electrical contact (c) Applied DC voltage.	48
Figure 2.6 Physical shadow mask used for electrode deposition. (a) Interdigitated mask (b) Striped mask.....	49
Figure 2.7 Schematic illustration of the experimental setup used to measure spectral response of MoS ₂ based photodetectors.	50
Figure 2.8 Schematic of gas sensing setup.....	51
Figure 3.1 FESEM images of MoS ₂ films grown at different pressure (a) 3 mTorr (b) 5 mTorr (c) 10 mTorr (d) 15 mTorr.	56
Figure 3.2 (a) Raman spectra and (b) XRD pattern of MoS ₂ films grown on Si/SiO ₂ substrate at variable pressure varied from 3 mTorr to 15 mTorr and (c) Absorbance spectra of the MoS ₂ film grown on quartz at different growth pressure.....	57
Figure 3.3 FESEM images of MoS ₂ films deposited at (a) 5-10 min, (b) 11 min, (c) 12 min, (d) 13 min, (e) 16 min and (f) 30 min. (g) Cross-sectional FESEM image of vertical flakes of	

MoS ₂ deposited for 30 min (h) Surface roughness of MoS ₂ films as a function of growth time.	
(i) Raman measurements plots of MoS ₂ films grown at different times.....	58
Figure 3.4 (a) XRD spectra and (b) XPS survey scan of sputtered MoS ₂ , acquired from the sample deposited at 5 min (in-plane MoS ₂) and 30 min (vertically aligned MoS ₂), respectively.	
.....	59
Figure 3.5 High resolution XPS spectra of (a) Mo 3d, (b) S 2p core and (c) O 1s levels, acquired from the sample deposited at 5 min (in-plane MoS ₂) and 30 min (vertically aligned MoS ₂), respectively.....	60
Figure 3.6 (a) As synthesized vertically aligned MoS ₂ flakes on 2-inch Si/SiO ₂ wafer. (b) Synthesized MoS ₂ on 2-inch wafer are divide into 76 units (area-5×5 mm ²) for spectral analysis. (c-e) Raman spectra of vertically aligned MoS ₂ and its spatial mapping on 76 locations corresponding to <i>E2g</i> 1 and <i>A1g</i> peak position.	61
Figure 3.7 (a) Raman spectra of vertically aligned MoS ₂ deposited at various substrates, including Si, Si/SiO ₂ , Sapphire, Quartz, and carbon fiber. FESEM images of MoS ₂ flakes deposited on (b) Silicon, (c) Sapphire, (d) Quartz, and (e) Carbon fiber substrate, inset shows the high magnification image of MoS ₂ flakes.	62
Figure 3.8 Growth model for the formation of vertically aligned MoS ₂ flakes. (a-c) Initially, layer-by-layer growth occurs by mass transport arriving at the substrate. (d) Vertically aligned growth of MoS ₂ starts due to island formation, where strain and defects are present. (e) Vertically aligned growth continues and branches parallel to the substrate. (f-h) Cross-sectional image of MoS ₂ grown film at different growth stage.....	63
Figure 3.9 Photoresponse behaviour of vertically aligned MoS ₂ (a) I-V characteristics in dark and light (532 nm laser) condition, inset shows the fabricated device image. (b) Temporal response under 532 nm illumination at 5V bias. (c) Responsivity and (d) Detectivity of MoS ₂ photodetector as a function of incident power at an applied bias of 5V.	64
Figure 4.1 Schematic of fabrication of MoS ₂ -ReS ₂ photodetector. (a) Synthesis of VA-MoS ₂ flakes by APCVD. (b) VA-MoS ₂ flakes deposited on Si/SiO ₂ substrate. (c) Patterned interdigitated Au electrode on top of MoS ₂ (pristine MoS ₂ photodetector). (d) ReS ₂ NSs drop casting on MoS ₂ -Au contact photodetector. (e) Schematic of MoS ₂ -ReS ₂ heterostructure.....	71
Figure 4.2 SEM image of (a) VA-MoS ₂ (b) MoS ₂ -ReS ₂ heterostructure, ReS ₂ drop casted onto VA-MoS ₂ flakes grown over Si/SiO ₂ substrate. The average size of ReS ₂ NSs is less than ~ 100 nm. It can be seen as clusters deposited over VA-MoS ₂ . (c) Enlarge view of MoS ₂ -ReS ₂ heterostructure. (d) Rectangular box is the area selected for the EDX elemental mapping of	

MoS ₂ -ReS ₂ heterostructure. (e) Cumulative EDX elemental mapping. (f) Rhenium. (g) Molybdenum. (h) Sulfur. (i) Silicon.....	73
Figure 4.3 (a) Raman spectrum of MoS ₂ -ReS ₂ heterostructure (Red), pristine MoS ₂ (blue) and pristine ReS ₂ (black). (b) Raman spectrum of MoS ₂ and MoS ₂ -ReS ₂ (zoomed spectrum, in the range 350-450 cm^{-1}). (c) Raman spectrum of ReS ₂ and MoS ₂ -ReS ₂ (zoomed spectrum, in the range 110-290 cm^{-1}). (d) Comparative PL spectrum of MoS ₂ and MoS ₂ -ReS ₂ heterostructure, each PL peak is deconvoluted into three peaks corresponding to A – negative trion (cyan), A0 neutral exciton (orange) and B exciton (magenta).....	74
Figure 4.4 (a) Core-level spectra of Mo 3d. (b) Valence band spectra of pristine MoS ₂ . (c) Core-level spectra of Re 4f. (d) Valence band spectra of ReS ₂ . (e) The Mo 3d and Re 4f core-level at heterointerface of MoS ₂ -ReS ₂ . (f) Energy band alignment at MoS ₂ -ReS ₂ heterojunction. Core-level binding energy peak positions given in the parenthesis.	75
Figure 4.5 Bandgap of (a) MoS ₂ and (b) ReS ₂ obtained from Tauc plot.	76
Figure 4.6 Ultraviolet photoelectron spectroscopy (UPS) spectra of (a) pristine MoS ₂ , (b) pristine ReS ₂ , (c) Energy band-alignment by Anderson’s affinity rule.	77
Figure 4.7 Schematic energy band diagram of MoS ₂ and ReS ₂ . (a) Before contact. (b) After contact under illumination, illustrating the transport of photo-excited charge carriers (CBM, VBM and CL represent the conduction band minima, valence band maxima and position of core-level relative to Fermi-level).	78
Figure 4.8 Comparative photoresponse of pristine MoS ₂ with different ReS ₂ solution based MoS ₂ -ReS ₂ heterostructure.....	79
Figure 4.9 SEM images of different volume drop-casted ReS ₂ solution based MoS ₂ -ReS ₂ heterostructure (a) MoS ₂ -ReS ₂ 25 (b) MoS ₂ -ReS ₂ 35 (c) MoS ₂ -ReS ₂ 50 (d) MoS ₂ -ReS ₂ 70 (e) Absorbance of MoS ₂ -ReS ₂ heterostructure, absorption first increases with increasing ReS ₂ and then decreases, indicating significant ReS ₂ -ReS ₂ homo nanophase formed with MoS ₂ -ReS ₂ hetero phase. Numbering in MoS ₂ -ReS ₂ denotes the solution in μ L dropcasted on MoS ₂ flakes.	80
Figure 4.10 I-V characteristics of (a) Pristine MoS ₂ , (b) MoS ₂ -ReS ₂ heterostructure, respectively. (c) Comparative photocurrent of MoS ₂ and MoS ₂ -ReS ₂ under incident radiation of 800 nm. (d) Responsivity, (e) Detectivity of bare MoS ₂ and MoS ₂ -ReS ₂ at 1 V under illumination of Visible-NIR radiation, respectively. (f) Comparative transient photoresponse. (g)-(h) Rise time and decay time of MoS ₂ and MoS ₂ -ReS ₂ , respectively at 800 nm. (i) Comparison of pristine MoS ₂ and MoS ₂ -ReS ₂ heterojunction device performance, parameter:	

responsivity and response time. Inset of Figures 7 (a) and (b) shows the cross-sectional view of the device under illumination.....	82
Figure 4.11 (a) Self-bias transient photoresponse of MoS ₂ -ReS ₂ heterostructure at spectral range covering from 400-1100 nm. (b) Response time at 800 nm. (c) Responsivity and Detectivity of MoS ₂ -ReS ₂ at self-driven mode under visible-NIR radiation	86
Figure 4.12 (a) Raman spectra (b) PL spectra (c) Absorbance spectra of pristine MoS ₂ , bare Ga ₂ O ₃ and MoS ₂ /Ga ₂ O ₃ on quartz substrate.....	89
Figure 4.13 Binding energy measurements (XPS-UPS) and band-alignment of MoS ₂ /Ga ₂ O ₃ heterojunction. (a), (b) High-resolution core-level XPS spectra of Ga 2p and Mo 3d for Ga ₂ O ₃ , MoS ₂ and MoS ₂ /Ga ₂ O ₃ interface. (c) Valence band spectra of pristine MoS ₂ and Ga ₂ O ₃ . (d) Energy band-diagram of MoS ₂ /Ga ₂ O ₃ heterostructure, exhibiting type-I alignment.....	90
Figure 4.14 Bandgap of (a) MoS ₂ and (b) Ga ₂ O ₃ obtained from Tauc plot	91
Figure 4.15 Ultraviolet photoelectron spectroscopy (UPS) spectra of (a) pristine MoS ₂ , (b) amorphous Ga ₂ O ₃ , and (c) Energy band-alignment by Anderson's affinity rule.....	92
Figure 4.16 (a) Schematic illustration of surface and junction mode used for KPFM measurement. (b) Schematic representation of energy level-alignment between MoS ₂ and Ga ₂ O ₃ under illumination.	93
Figure 4.17 (a) and (b) Surface potential images of pristine MoS ₂ in dark and light, (c) Distribution of the surface potential of MoS ₂ under dark and white light conditions.....	94
Figure 4.18 Surface potential images of MoS ₂ /Ga ₂ O ₃ heterojunction in (a) Surface mode and (b) Junction mode under dark (c) Distribution of the surface potential of MoS ₂ /Ga ₂ O ₃ in two different modes under dark conditions.	95
Figure 4.19 (a) Surface topography of MoS ₂ /Ga ₂ O ₃ (Ga ₂ O ₃ film on top of MoS ₂), (b) and (c) are surface potential images of MoS ₂ /Ga ₂ O ₃ heterojunction in surface and junction mode under white light illumination, (d) Photovoltage map, (e) Surface potential profiles for MoS ₂ /Ga ₂ O ₃ sample in two different modes under illumination.....	95
Figure 4.20 (a,b) I-V Characteristics of MoS ₂ and MoS ₂ /Ga ₂ O ₃ heterojunction under dark and light condition. (c) Comparative photocurrent of MoS ₂ and heterojunction under incident light of 600 nm. (d-f) Temporal response of MoS ₂ and MoS ₂ /Ga ₂ O ₃ heterojunction devices under incident radiation of 600 nm, 365 nm and 254 nm, respectively. Comparative response plot between pristine MoS ₂ and MoS ₂ /Ga ₂ O ₃ heterojunction for (g) Responsivity, (h) EQE, and (i) Detectivity at 5V biasing as a function of wavelength.....	97
Figure 4.21 Transient photoresponse of MoS ₂ /Ga ₂ O ₃ heterojunction from deep UV to NIR at low bias (1V).....	98

Figure 4.22 Transient photoresponse of MoS₂/Ga₂O₃ heterostructure in broad spectrum range from UV-C to NIR light irradiation at 1V bias over time in ambient conditions. The fabricated device shows negligible performance degradation after leaving in the ambient for 1500 hours.

..... 100

Figure 4.23 Energy band diagram of MoS₂/Ga₂O₃ heterojunction. (a) At equilibrium (V=0) under dark, (b) and (c) Reverse bias (V<0) and forward bias (V>0) conditions under illumination. 101

Figure 4.24 (a) Schematic of Au/Pt@MoS₂/Au M-S-M photodetector. (b) FESEM image of Pt@MoS₂. (c) Magnified FESEM image of (b), inset shows particle size histogram. (d) Area selected for elemental mapping. Elemental mapping of (e) Cumulative, (f) Molybdenum, (g) Sulfur, (h) Platinum. 104

Figure 4.25 (a) Raman spectra, (b) Photoluminescence spectra, (c) Optical absorbance spectra of MoS₂ and Pt@MoS₂ samples, inset consist of absorbance of Pt NPs on quartz. (d) Tauc plot and Urbach energy calculation (inset) for both samples. 106

Figure 4.26 The I-V characteristics under dark and illumination of (a) MoS₂ and (b) Pt@MoS₂. (c) The dark I-V characteristics (semi-logarithmic) of pristine MoS₂ and Pt@MoS₂ is presented for comparison, Pt@MoS₂ exhibits less dark current. (d) Photo-to-dark current ratio (PDCR) of MoS₂ and Pt@MoS₂, Pt@MoS₂ device shows superior photoresponse as compared to pristine MoS₂. 108

Figure 4.27 (a) Experimental and theoretical calculated responsivity of MoS₂ and Pt@MoS₂ photodetector at 1V. (b) Responsivity as a function of wavelength for different bias voltage. (c) External quantum efficiency. (d) Detectivity and NEP of the fabricated photodetector of MoS₂ and Pt@MoS₂ photodetector in broad visible-NIR regime at an applied bias of 1 V. 110

Figure 4.28 Detectivity versus responsivity plot for plasmon enhanced MoS₂ based photodetector. 114

Figure 4.29 (a) Transient photoresponse of Au/Pt@MoS₂/Au for broad spectral range (400 nm - 1100 nm) at 5 V. (b) Temporal response of Au/MoS₂/Au and Au/Pt@MoS₂/Au device under 600 nm illumination at 1 V. (c) and (d) Corresponding response time (rise and fall time) of MoS₂ and Pt@MoS₂ photodetector, respectively. 115

Figure 4.30 Transient photoresponse of Pt@MoS₂ in visible (600 nm) and NIR (800 nm) illumination measured at 5 V, showing initially measured response and response after 30 days of the same sample stored at normal ambient conditions. The data reveals high repeatability of the photoresponse with time. 116

Figure 4.31 Device schematics and photodetection mechanisms. (a) Schematic illustration of plasmonic Pt NPs induced MoS ₂ device under illumination. (b) Photoconduction mechanism at Pt-MoS ₂ junction, hot electron of Pt transfers into the conduction band of MoS ₂	118
Figure 5.1 Structural composition and synthesis process of Pt@MoS ₂	129
Figure 5.2 The particle size distribution of Pt nanoparticles sputtered for (a) 5s and (b) 10s. The bar graph shows that particles have an average size of 4 nm ± 2 nm for 5s Pt sample and 10 nm ± 5 nm for 10s Pt sample.....	129
Figure 5.3 (a) FESEM image of Pt NPs decorated vertically aligned MoS ₂ flakes, inset shows high magnification image. (b) Raman and (c) PL spectrum of MoS ₂ (open-blue) and Pt@MoS ₂ (solid-green).	130
Figure 5.4 (a) Core level spectrum of Mo 3d (b) S 2p of MoS ₂ and Pt@MoS ₂ , lower binding energy shift of Mo 3d and S 2p in Pt@MoS ₂ indicate further p-doping in MoS ₂ after incorporation of Pt NPs (c) Pt 4f spectrum of Pt@MoS ₂ (d), (e) UPS spectrum of MoS ₂ and Pt@MoS ₂ respectively (f) Band alignment of pristine MoS ₂ and Pt@MoS ₂ determined from UPS data.	131
Figure 5.5 (a) Real time change in resistance of MoS ₂ as function of NO ₂ concentration at room temperature. (b) Corresponding response plot of MoS ₂ . (c) Resistance versus time profile of MoS ₂ as a function under different H ₂ concentration at room temperature. (d) Corresponding response plot of MoS ₂ . (e) Selectivity response against six different gases of MoS ₂ sensor at room temperature.	133
Figure 5.6 (a) Response versus time profile of MoS ₂ and Pt@MoS ₂ sensors for 50 ppm (H ₂ gas); Here, 5 and 10 in Pt@MoS ₂ represent the sputter time in seconds of Pt NPs deposited over pristine MoS ₂ (b) Comparative response of the fabricated sensors (MoS ₂ and Pt@MoS ₂) as a function of H ₂ concentration.	134
Figure 5.7 (a) Schematic of Pt NPs decorated VA-MoS ₂ sensor. (b) Dynamic resistance change of Pt@MoS ₂ sensor upon exposure to H ₂ gas ranging from 50 to 0.5 ppm at room temperature (c) Corresponding response plot of Pt@MoS ₂ sensor (d) Response of the fabricated Pt@MoS ₂ sensor as a function of hydrogen concentration (e) Response and recovery time of the sensor for hydrogen concentration vary from 0.5 ppm to 50 ppm.	135
Figure 5.8 (a) Repeatability and (b) Stability of the fabricated Pt@MoS ₂ gas sensor at room temperature when exposed to 50 ppm H ₂ , (c) Selectivity test histogram for Pt@MoS ₂ against H ₂ , NO ₂ , NH ₃ , H ₂ S, SO ₂ , CO ₂ gas at room temperature.	136
Figure 5.9 Base resistance of Pt@MoS ₂ as a function of temperature.....	137

Figure 5.10 (a)Temperature dependent response curve of Pt@MoS ₂ for H ₂ sensing, at 100 °C sensor shows maximum response (b) Repetitive cycles of response variation of Pt@MoS ₂ gas sensor at 100 °C towards 50 ppm H ₂ concentration, (c) Response of the Pt@MoS ₂ sensor towards 50 ppm to 0.5 ppm of H ₂ at 100 °C (d) Response time plot of single cycle at 100 °C to calculate response and recovery time (e) Response and (f) Recovery speed of our fabricated Pt@MoS ₂ sensor as a function of H ₂ concentration at 100 °C.	138
Figure 5.11 (a) Variation in baseline resistance with relative humidity from 20% to 80% for Pt@MoS ₂ at 100 °C, (b) Corresponding response of Pt@MoS ₂ at 50 ppm H ₂ exposure under different relative humidity conditions.	139
Figure 5.12 Proposed sensing mechanism of Pt@MoS ₂ by Hydrogen spillover effect.	141
Figure 5.13 Charge density difference (CDD) plots of (a) NO ₂ adsorbed on MoS ₂ at the Mo-edge (T _M site) and S-edge (T _S site) (b) NO ₂ adsorbed on Pt@MoS ₂ at T _M and T _S site. Considering isosurface value of 0.001 e/Å ³ and 0.0005 e/Å ³ corresponds to T _M and T _S site, respectively. The yellow and cyan regions indicate the increase and decrease in the charge density values after gas adsorption.....	142
Figure 5.14 Charge density difference (CDD) plots of (a) H ₂ adsorbed on MoS ₂ at the Mo-edge (T _M site) and S-edge (T _S site) (b) H ₂ adsorbed on Pt@MoS ₂ at T _M and T _S site. Considering isosurface value of 0.0005 e/Å ³ and 0.0001 e/Å ³ corresponds to T _M and T _S site, respectively. The yellow and cyan regions indicate the increase and decrease in the charge density values after gas adsorption.	143

List of Tables

Table 1.1 The calculated adsorption energy (E_a in meV), charge transfer value (ΔQ in e) between the MoS_2 and gas molecules and distance (d in \AA) between the adsorbed gas molecule and MoS_2 for different gaseous molecules using DFT by Yue et al. [116].	27
Table 3.1 Comparative performance of MoS_2 photodetector	65
Table 4.1 Parameters calculated for MoS_2 and ReS_2 from UPS spectrum.	78
Table 4.2 Comparison of MoS_2 - ReS_2 heterostructure photodetector with recently developed other 2D/2D heterostructure devices at moderate bias.	83
Table 4.3 Comparison of self-powered photoresponse	86
Table 4.4 Comparison of MoS_2/Ga_2O_3 photodetector performance with reported literature.	99
Table 4.5 Device performance of different Pt @ MoS_2 devices under illumination of 800 nm at 5 V bias.	116
Table 4.6 Comparative performance of plasmon enabled MoS_2 photodetector. FL = few layer	117
Table 5.1 Comparative response between the reported 2D materials based H_2 gas sensor and the present work	140
Table 5.2 Calculated gas adsorption energy, bond length and Bader charge difference (charge in the isolated state subtracted from the charge in the gas adsorbed state) of the gas adsorbed on MoS_2 and Pt@ MoS_2 .	144

Chapter 1: Introduction

Starting with a brief background of two-dimensional (2D) materials this chapter presents a comprehensive overview of transition metal dichalcogenides (TMDs), with a particular focus on MoS₂. The fundamental structural, optical, and electrical properties of MoS₂ are discussed in detail, emphasizing its potential for a wide range of applications. Different synthesis methods used to grow MoS₂, including top-down and bottom-up approaches, are briefly discussed. The chapter also highlights the advantages of vertically aligned MoS₂ flakes over in-plane MoS₂ in terms of their electrical, optical, and catalytic properties. Moreover, MoS₂ is recognized as a promising candidate for photodetector and gas-sensing applications. The subsequent section provides an overview of the current state-of-the-art 2D material-based photodetectors and gas sensors, discussing the key challenges faced in their development. Finally, the chapter outlines the scope and objective of the current doctoral thesis.

1.1 Background

Over the last five decades, microelectronic devices have evolved according to Moore's law, reaching the 10 nm domain. However, further miniaturization encounters limitations dictated by quantum physics. In this regard, nanomaterials and nanotechnology have provided avenues for ultimate miniaturization, with 2D materials playing a significant role due to their extraordinary physical properties. 2D materials are the simplest nanoscale materials, having an atomically thin planar structure that is fully governed by quantum mechanics. Charge carriers in 2D materials are subject to strong quantum confinement, leading to many extraordinary properties that cannot be observed in other materials. Graphene was the first 2D material discovered, and recently other 2D materials, such as TMDs, hexagonal boron nitride, and perovskite-based 2D materials have also been investigated [1]. Various techniques have emerged for the preparation, characterization, and fabrication of devices, including multi-layer heterostructures, using 2D materials. The ease of preparation, integration with silicon technology, planar device architecture, and other advantageous properties make 2D materials a promising candidate for device fabrication [2].

1.2 Transition metal dichalcogenides

After the groundbreaking discovery of graphene, the immense potential of 2D materials has been demonstrated for a wide range of electronic and physical applications [3]. Unlike their bulk counterparts, 2D materials possess unique properties due to their atomically thin nature.

For instance, graphene exhibits remarkable electronic, mechanical, and thermal properties however, its lack of a band gap restricts its use in switching devices [4]. To overcome this issue, scientists have explored other novel two-dimensional semiconductors (2DSCs) with sizable band gaps and are naturally abundant [5-7].

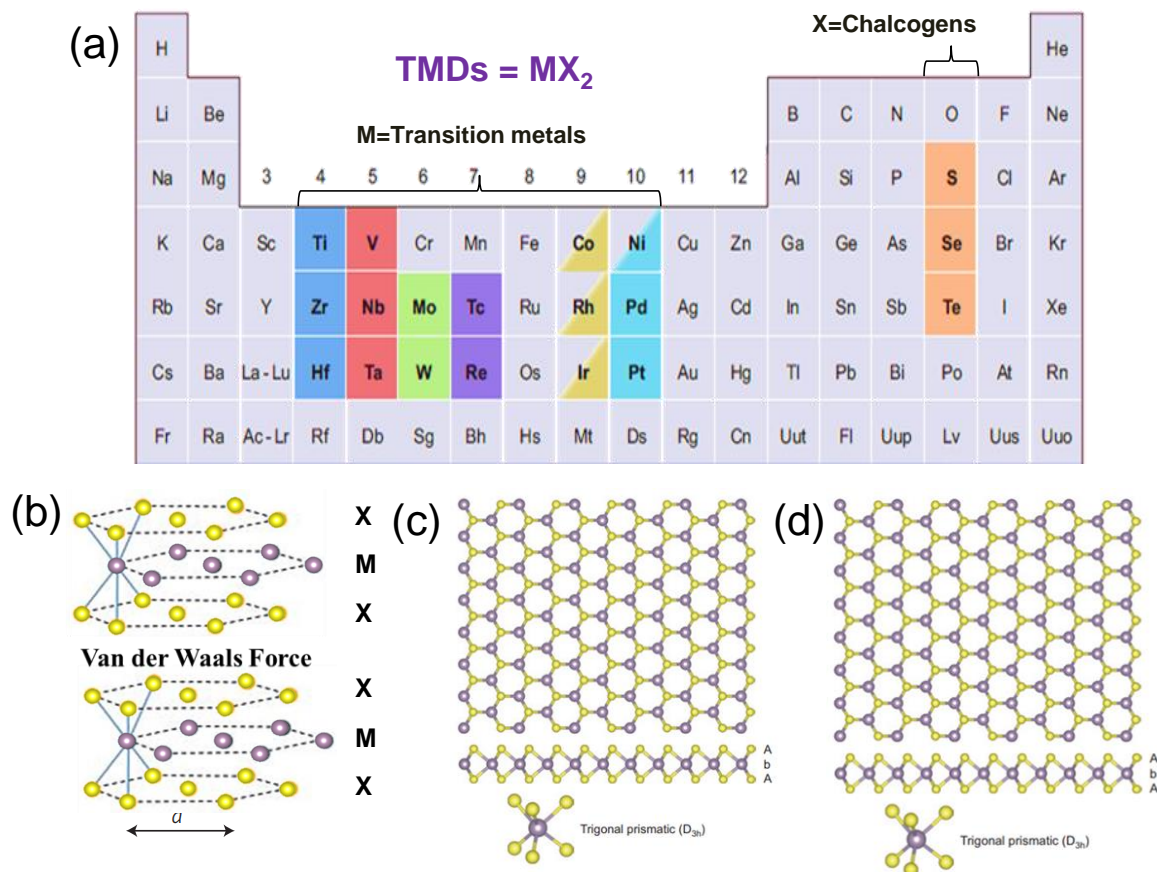


Figure 1.1 (a) Highlighted transition metals (group 4-10) and chalcogenides in the periodic table that form layered structures, partially highlighted transition metals indicate only some of the dichalcogenides form layered structures. (b) Stacking of hexagonally packed planes bounded by the van der Waals force. Possible coordination unit of layered TMDs (c) Trigonal prismatic (AbA) (d) Octahedron (AbC) [5].

Among the explored 2DSCs, the transition metal dichalcogenides (TMDs) have gained special attention due to their excellent stability, electronic performance, and strong spin-orbit interaction. These properties offer numerous opportunities for fundamental and applied research in various fields, including electronics (e.g., transistors and logic circuits), sensing, energy storage, and catalysis [8, 9].

TMDs feature a layered MX_2 structure, where the hexagonal lattice of transition metal ($M=Mo, W$, etc.) is sandwiched between two hexagonal lattices of chalcogen atoms ($X=S, Se, Te$). Despite having the same empirical formula, TMDs display a wide range of physical properties.

Some TMDs, such as HfS_2 , are insulators, while others, like MoS_2 and WSe_2 , are semiconductors. Still others, like WTe_2 and TiSe_2 , are semimetals, and a few, including NbS_2 and VSe_2 , are metals. These diverse electronic properties of TMDs are due to the electron configuration of the non-bonding d-orbitals of transition metals. To date, more than 40 different 2D layered compounds have been reported in the literature. Figure 1.1 (a) highlights the transition metal and chalcogenides in the periodic table, with Co, Rh, Ir, and Ni partially highlighted to indicate that only some of the dichalcogenides form layered structures. For example, NiS_2 has an apyrite structure while NiTe_2 forms a layered compound [5, 7].

In layered materials, thickness of each layer is $\sim 6\text{-}7$ Å. The M-X bonds within each layer are mainly covalent in nature, whereas weak van der Waals forces maintain the interlayer attraction between each monolayer, as depicted in Figure 1.1 (b). This weak interlayer interaction enables these materials to be cleaved into 2D layered structures from their 3D counterparts. The oxidation state of the metal (M) and chalcogen (X) atoms is +4 and -2, respectively. The lone-pair electrons of the chalcogen atoms terminate the surface of the layers, creating a chemically stable surface without dangling bonds on the basal planes of TMDs, similar to that of graphene. The M-M bond length in TMDs depends on the size of metal and chalcogen ions, ranging from 3.15 Å to 4.03 Å, which is 15-25% larger than the bond length in their elemental transition metal solid, indicating the limited spatial overlap of d orbitals in TMDs [5]. The metal coordination of layered TMDs can be either trigonal prismatic (D_{3h}) or octahedral (O_h or D_{3d}), based on the thermodynamically preferred configuration, as shown in Figures 1.1 (c) and 1.1 (d), respectively.

MoS_2 is a prominent member of TMDs family, which has garnered significant attention owing to its exceptional semiconductor properties [10-12]. MoS_2 possess a direct bandgap, high absorption coefficient, high carrier mobility, and large current on/off ratio. These features make it highly suitable candidate for a wide range of applications such as photodetectors, solar cells, sensors, transistors, etc. These characteristics of MoS_2 have led to its widespread study and continued exploration for novel device applications.

1.3 Molybdenum disulfide (MoS_2)

1.3.1 Properties of MoS_2

1.3.1.1 Crystal structure

MoS_2 has a crystal structure composed of hexagonal layers of S-Mo-S that are weakly bonded by van der Waals forces. Each layer is around 0.65 nm thick and consists of two sulfur (S) atom

layers with a single molybdenum (Mo) atom layer in between. There are two types of MoS₂ polymorphs: 2H-MoS₂ and 1T-MoS₂. 2H-MoS₂ is the more common form and belongs to the hexagonal symmetry with a lattice constant of $a=b=3.16 \text{ \AA}$, $c=12.29 \text{ \AA}$, and space group P63/mmc [13]. In 2H-MoS₂, the coordination of Mo with S is trigonal prismatic, with each molybdenum atom surrounded by six sulfur atoms to form a trigonal prism. The sulfur atoms in the upper layer directly align above those in the lower layer. Conversely, 1T-MoS₂ shares a similar hexagonal structure to 2H-MoS₂. Still, the molybdenum atoms occupy the center positions of the octahedral interstices of the S layers, and the sulfur atoms in the upper and lower planes are displaced from each other [14].

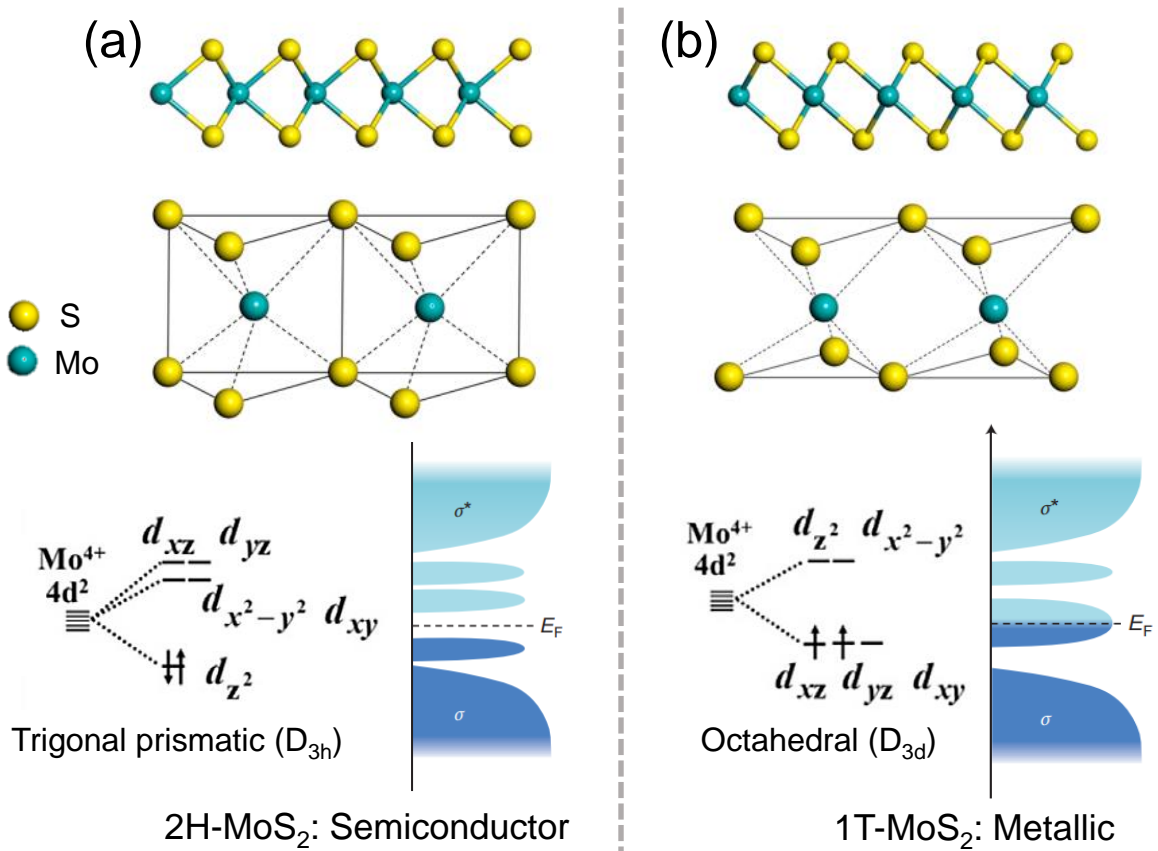


Figure 1.2 Crystal structure of MoS₂ (a) 2H phase (b) 1T phase, with a schematic representation of the gradual filling of d orbitals that are situated in the bandgap between bonding (σ) and anti-bonding states (σ^*) [5, 14].

The 2H-MoS₂ and 1T MoS₂ phases belong to D_{3h} and D_{3d} point groups, respectively. These two phases have different electrical properties, with 2H-MoS₂ exhibiting semiconductor behavior and 1T-MoS₂ showing metallic conductivity [15]. The diverse electrical nature of MoS₂ in these phases can be explained by Crystal field theory. The d-orbitals of transition metal Mo consist of five degenerate orbitals: $d_{x^2-y^2}$, d_{z^2} , d_{xy} , d_{yz} , and d_{zx} , located between

the bonding (σ) and antibonding (σ^*) states. In trigonal prismatic (D_{3h}) symmetry, the orbitals split into three non-degenerate levels: d_{z^2} (a_1), $d_{x^2-y^2} + d_{xy}$ (e), and $d_{yz} + d_{zx}$ (e'). Similarly, octahedral (D_{3d}) symmetry splits in two non-degenerate levels: $d_{z^2} + d_{x^2-y^2}$ (e_g) orbitals and d_{xy} , d_{yz} , and d_{zx} (t_{2g}) orbitals. MoS₂ has a d electron count of d^2 , with fully occupied lowest level d_{z^2} in 2H-MoS₂. Partially filled highest orbitals give rise to metal-like conductivity in 1T-MoS₂, whereas complete filling of orbitals results in semiconducting behavior in 2H-MoS₂. These characteristics are illustrated in Figures 1.2 (a) and 1.2 (b), which depict the gradual filling of d-orbitals in both phases.

1.3.1.2 Band structure

MoS₂ is a semiconductor material with a unique band structure that is strongly influenced by the number of layers present in the crystal. Each layer of MoS₂ is coupled by weak van der Waals forces, resulting in a layered structure. When the bulk MoS₂ is thinned down to a monolayer, the bandgap changes from indirect to direct and the bandgap energy increases from 1.2 eV to 1.8 eV. This change in band structure is due to the different electronic states involved in the formation of the conduction and valence bands, which are mainly composed of a linear combination of S and Mo orbitals [16].

The Brillouin zone of MoS₂ has three symmetry points: Γ , M, and K as shown in Figure 1.3. As the layer number decreases, the theoretically calculated electronic band structure of MoS₂ shifts from indirect to direct semiconducting behavior. In bulk MoS₂, the conduction band minimum (CBM) is situated between the Γ and K points, whereas the valence band maximum (VBM) is located at the Γ point. The VBM at the Γ point and CBM between the K and Γ points change significantly as the layer number decreases to quadrilayer and bilayer. This is due to the electronic states near the Γ and K points are being composed of out-of-plane orbitals, which are strongly affected by interlayer coupling. Conversely, electronic states at the K point experience barely any change with thickness, as both the CBM and VBM at this point mainly comprise by the localized in-plane orbitals of Mo (3d) and S (2p) atom. Thus, the shift observed from indirect to direct bandgap in monolayer MoS₂ is the result of quantum confinement effect.

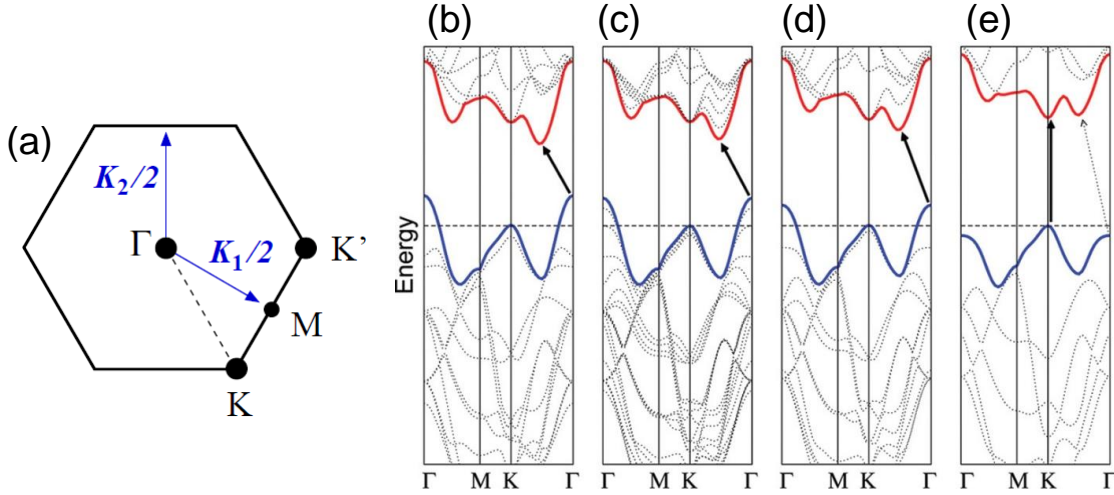


Figure 1.3 (a) Brillouin zone of 2H-MoS₂, Calculated band structures of MoS₂ from bulk to monolayer (a) Bulk (b) Quadrilayer (c) Bilayer and (d) Monolayer [16, 17].

1.3.1.3 Photoluminescence

MoS₂ exhibits thickness-dependent tunable photoluminescence (PL). The PL spectra of MoS₂ shows two peaks labeled ‘A’ and ‘B’, which arise due to the splitting of the valence band into two energy levels (v_1 and v_2) [18]. In monolayer MoS₂, spin-orbit coupling and broken inversion symmetry cause the valence band splitting, while in the bilayer and few-layer MoS₂, the splitting in the valence band arises due to spin-orbit coupling and interlayer interaction [19, 20]. The ‘A’ and ‘B’ peaks are associated with direct exciton transitions at the K symmetry point of the Brillouin zone (Figure 1.4 (a)).

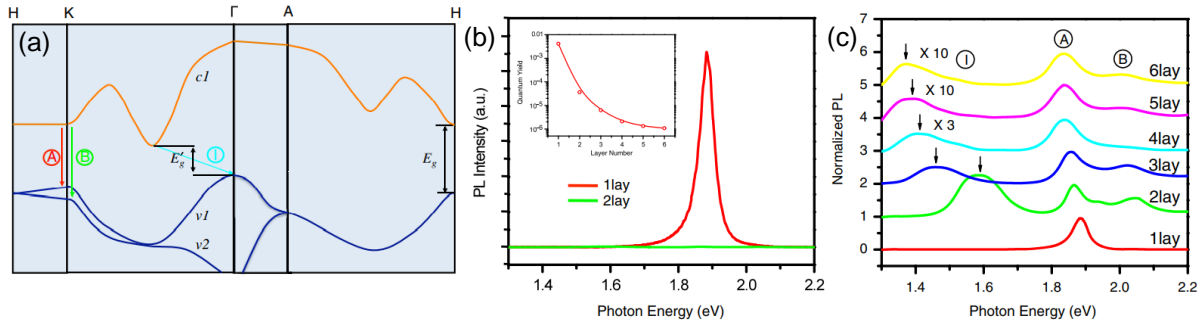


Figure 1.4 (a) Band structure of the bulk and monolayer MoS₂, where A and B indicate the direct-gap transitions, and I represent the indirect-gap transition. The indirect gap for the bulk is denoted by E'_g and direct gap for the monolayer is indicated as E_g . (b) PL spectra for mono and bilayer MoS₂, inset displaying the relative quantum yield of MoS₂ as a function of layer number, (c) The normalized PL spectra with respect to layer number [18].

The PL emission peak of monolayer MoS₂ is highly intense at 1.9 eV (peak A) due to direct gap luminescence, as shown in Figure 1.4 (b). However, as the number of layer increases, the PL intensity decreases, with bulk MoS₂ exhibiting the lowest intensity (Figure 1.4 (c)). This is

because bulk MoS₂ has an indirect bandgap, which suppresses the PL quantum yield with increasing layer numbers. The luminescence quantum efficiency can be determined by the given equation [16]:

$$\eta = K_{rad} / (K_{rad} + K_{defect} + K_{relax}) \quad (1.1)$$

Where, K_{rad} , K_{defect} , and K_{relax} represent the radiative recombination rates, defect trapping rates, and electron relaxation rates within the valence band and conduction band, respectively. The direct exciton transitions at the K-point in monolayer and bulk MoS₂ remain at the same energy level; therefore, K_{rad} does not change appreciably with thickness. However, in bulk MoS₂, the intraband relaxation rate (K_{relax}) is high, resulting in low intensity of PL emission. As the thickness of MoS₂ decreases, the indirect bandgap increases, leading to a crossover to a direct bandgap. This results in a higher PL intensity in monolayer MoS₂, as the K_{relax} monotonically decreases with decreasing thickness [16]. The A-exciton peak shows a redshift behavior with an increase in the number of layers due to the lowering of the 1st exciton level or energy gap between the band edge, or a combined effect of both. In contrast, the B-exciton peak position remains almost unchanged with layer numbers as the decrement in exciton energy level is balanced by additional splitting in the valence band edge, as shown in Figure 1.5.

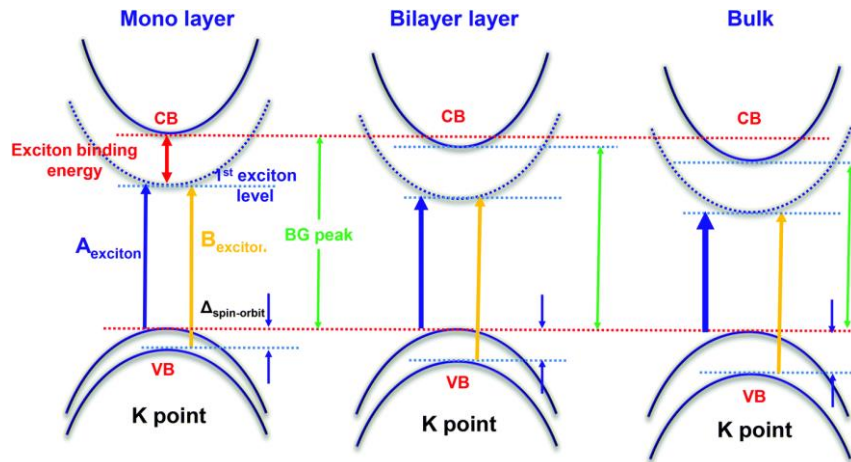


Figure 1.5 Schematic illustration of the optical transition occurring at the K-point of the Brillouin zone in different regions of MoS₂, including monolayer, bilayer, and bulk. The A-exciton peak experiences a red shift due to the reduction of the first exciton level. The B-exciton peak position remains relatively the same because the decrease in the exciton level is balanced by an increase in the valence band splitting energy [21].

1.3.1.4 Absorbance

MoS₂ is optically transparent up to 85%, with an absorption efficiency is around 10% in the visible-NIR regime for a few nanometers thick layers. The absorbance spectra of MoS₂ consists of two prominent peaks at ~660 nm (A-exciton) and ~605 nm (B-exciton) and one broad peak at position ~440 nm (C-exciton). The A and B peaks are associated with optical absorption by the band edge excitons, originating from direct gap transitions at the K point of the Brillouin zone [22]. The broad peak C is attributed to the absorption by excitons associated with the van Hove singularity of MoS₂ [23]. The broad C peak is not realized experimentally in PL spectra, which often used with an excitation wavelength of ~500 nm. However, this feature is present in a recent study of reflectance and photocurrent spectroscopy [23]. The absorbance spectra of MoS₂ increase gradually with film thickness and become opaque above six to eight layers. Figure 1.6 (a) illustrates the thickness-dependent absorbance spectra of MoS₂ (one to six layers) as a function of excitation wavelength. MoS₂ also displays a high absorption coefficient across a broad spectral range, as depicted in Figure 1.6 (b). The absorbance spectra further reveal a redshift in the A-exciton peak position with increasing layer number, while the B-exciton peak remains relatively constant, consistent with PL spectra.

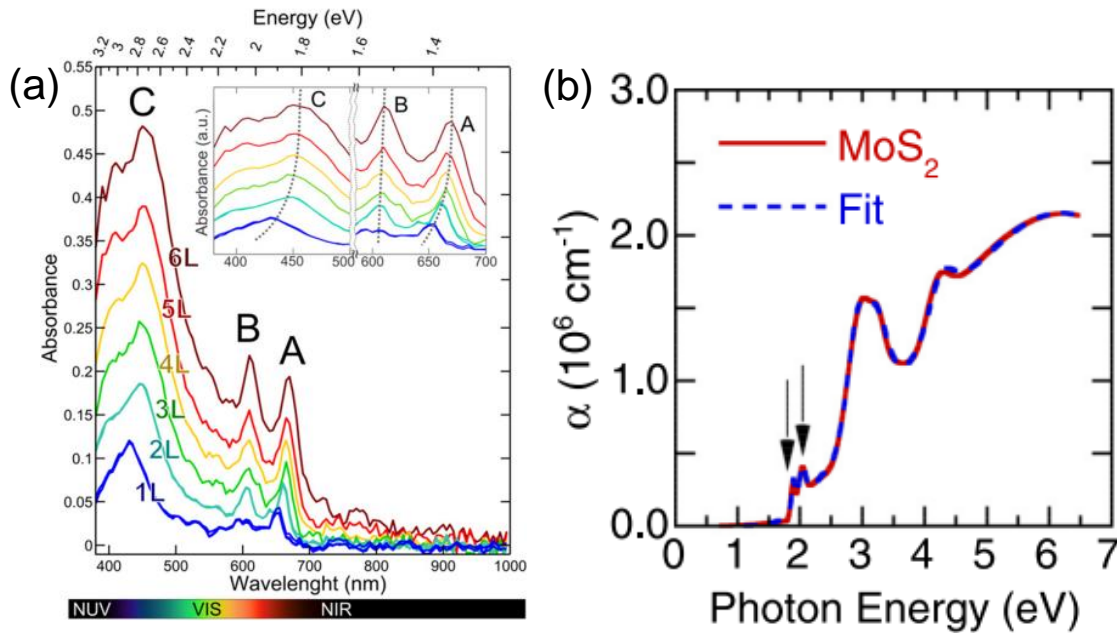


Figure 1.6 (a) Optical absorbance spectra of MoS₂ with layer number, (b) The calculated absorption coefficient for monolayer MoS₂ [22, 24].

1.3.1.5 Vibrational modes (Raman)

Raman spectroscopy is a non-destructive and effective technique that provides information about the lattice vibration, doping, number of layers, and strain present in MoS₂ films. Bulk MoS₂ has four Raman active modes (E_{2g}^2 , E_{1g} , E_{2g}^1 , A_{1g}) and two IR active modes (E_{1u}^1 and A_{2u}^1) as shown in Figure 1.7(a). On the other hand, monolayer and few-layer MoS₂ exhibit only two Raman active modes, A_{1g} and E_{2g}^1 . Here, the E_{2g}^1 peak arises due to in-plane vibration of Mo and S atoms in the opposite direction, while the A_{1g} peak is attributed to the out-of-plane vibration of S atom in the opposite direction along the c-axis, where the Mo atom is held stationary (Figure 1.7(b)). The other two Raman modes, E_{1g} and E_{2g}^2 cannot be observed due to the selection rules of scattering geometry [25]. The low-frequency phonon mode (E_{2g}^2) around 30 cm⁻¹ to 40 cm⁻¹ is difficult to distinguish from the Rayleigh background scattering. To detect such low-frequency phonon modes, a specialized triple-grating Raman spectrometer and dedicated filters are required [26].

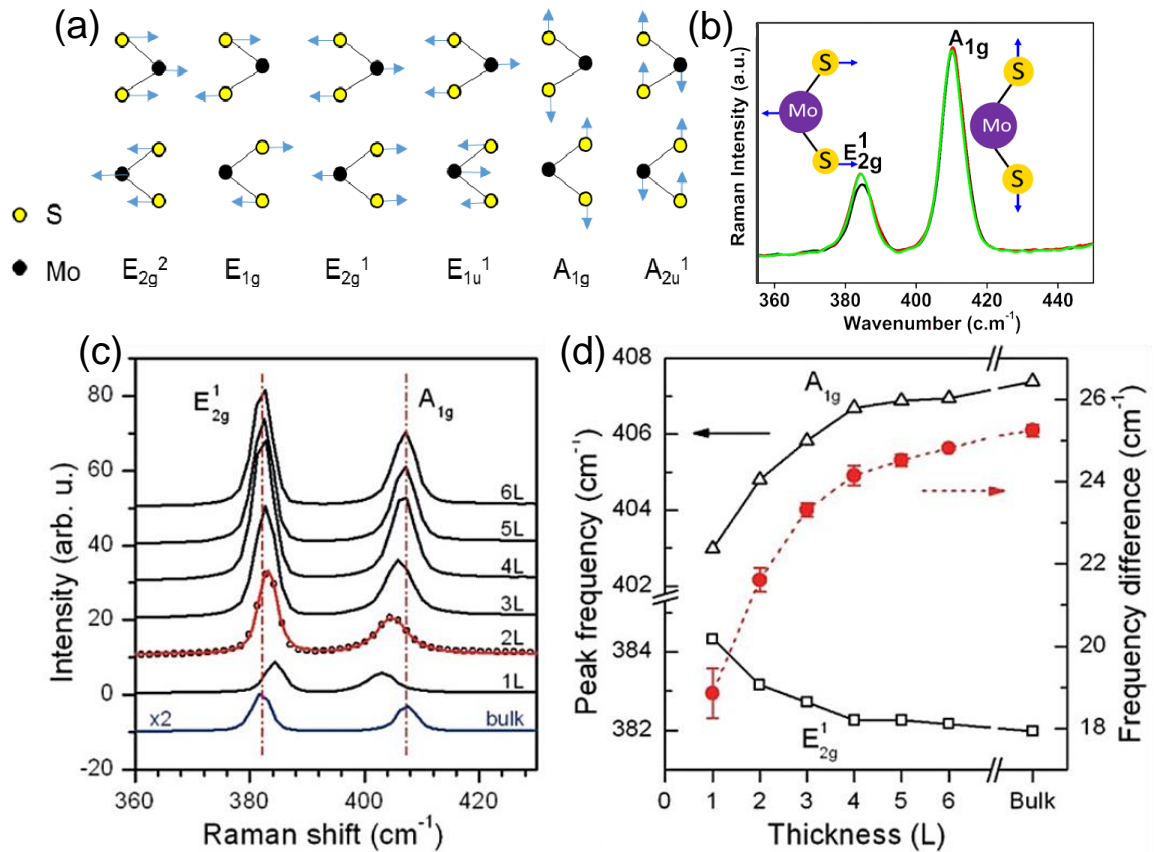


Figure 1.7 (a) All possible vibrational modes (E_{2g}^2 , E_{1g} , E_{2g}^1 , A_{1g} and E_{1u}^1 , A_{2u}^1) in bulk MoS₂ (b) Two Raman active modes (A_{1g} and E_{2g}^1) in mono and few-layers MoS₂ (c) Raman spectra of MoS₂ with layer number, (d) Variation in frequency and peak position of E_{2g}^1 and A_{1g} modes as a function of layer number [25, 27].

In monolayer MoS₂, the Raman spectrum displays two characteristic peaks at approximately 384 cm⁻¹ and 402 cm⁻¹, which correspond to the E_{2g}^1 and A_{1g} modes, respectively. With an increase in the number of layers, the E_{2g}^1 mode experiences a red shift, while the A_{1g} mode undergoes a blue shift. The magnitude of the Raman shift, which represents the difference between these two modes, increases as the number of layers increases, making it a reliable indicator of MoS₂ thickness [28]. While van der Waals interactions are responsible for the bonding between consecutive layers, resulting in an increase in the restoring force on each atom with each additional layer, experimental results show a discrepancy with this prediction. This suggests that the frequency shift is not solely influenced by van der Waals interlayer coupling. Instead, factors such as surface reconstruction and long-range Coulomb interaction play an essential role in reducing the overall restoring force on the atoms [25].

The E_{2g}^1 mode is the in-plane vibrational mode, and the A_{1g} mode is the out-of-plane vibrational mode. Thus, the intensity ratio of E_{2g}^1/A_{1g} can be used to define the growth structure and orientation of MoS₂ flakes. This ratio is highly sensitive to the presence of strain and doping in MoS₂ films [29].

1.4 Synthesis of MoS₂

MoS₂ is a versatile material with distinct properties and diverse film structures, making it an ideal choice for a wide range of applications. However, the suitability of MoS₂ for specific applications critically depends on the synthesis method used. Therefore, it is crucial to explore and discuss various synthesis methods to optimize the properties of MoS₂.

Two main approaches: Top-down and bottom-up have been developed to grow large-area and uniform atomic layers of 2D-MoS₂. Top-down methods involve the controlled removal of material from a bulk MoS₂ crystal, while bottom-up methods involve the growth of MoS₂ layers from atoms or molecules. The following sub-sections briefly discuss the most commonly employed synthesis technique to grow 2D MoS₂ and their respective advantages and limitations.

1.4.1 Mechanical exfoliation

Mechanical exfoliation is a top-down technique used to obtain thin layers of MoS₂ from a bulk crystal. This method involves peeling off the layers of the crystal using adhesive tape or other mechanical means, as shown in Figure 1.8(a). The process entails repeatedly exfoliating MoS₂ layers from the bulk crystal using scotch tape, followed by gently rubbing the tape with the

newly cleaved MoS₂ flakes onto the desired substrate [30]. As the tape is removed, mono-, bi-, and few-layered MoS₂ films are left on the substrate. This technique is convenient for producing high-quality, crystalline mono- to few-layered MoS₂ with a lateral size of several nanometers to tens of micrometers [31]. However, this approach lacks consistent control in producing 2D monolayers and does not ensure the size or thickness uniformity of the exfoliated MoS₂ flakes. Therefore, the mechanical exfoliation technique is not suitable for large area and high throughput applications.

1.4.2 Chemical exfoliation

Chemical exfoliation is a promising approach for producing large quantities of mono and few-layer MoS₂ nanosheets. The technique involves the insertion of ions between the MoS₂ layers in a liquid environment, leading to the swelling of the crystal and weakening of the interlayer attraction [32]. Chemical force or sonication is then employed to separate the layers as shown in Figure 1.8 (b). Generally, Li-ions are inserted between the MoS₂ layers that form LiMoS₂, which disperses quickly in water compared to pristine MoS₂. The intercalated Li-ions react with water and produce hydrogen gas and LiOH, which separates the layers from the bulk crystal. Then dispersed MoS₂ flakes can be recovered through precipitation or filtration. However, Li intercalation can alter the quality of the produced MoS₂ due to structural change from 2H to 1T phase [33, 34], leading to a loss of semiconducting properties in the exfoliated layers.

Alternatively, 2D MoS₂ nanosheets can be produced via electrochemical lithiation, which utilizes an external electric field to drive the insertion of lithium ions into MoS₂ [34]. This process is conducted in a battery cell, where an electrode made of MoS₂ is immersed in an electrolyte solution containing lithium ions, as shown in Figure 1.8 (c). When a voltage is applied across the electrodes, lithium ions migrate from the electrolyte solution into the MoS₂ electrode, leading to the electrochemical lithiation of the material. Electrochemical lithiation occurs much more rapidly than Li intercalation due to the external electric field forcing lithium ions to migrate into the MoS₂ electrode at a much faster rate. This method preserves the semiconducting properties of the resulting 2D-MoS₂ nanosheets. However, scalability, contamination, non-uniformity, and reproducibility of MoS₂ growth remain limitations of this method. Hence, further research is needed to optimize the synthesis process for industrial-scale production.

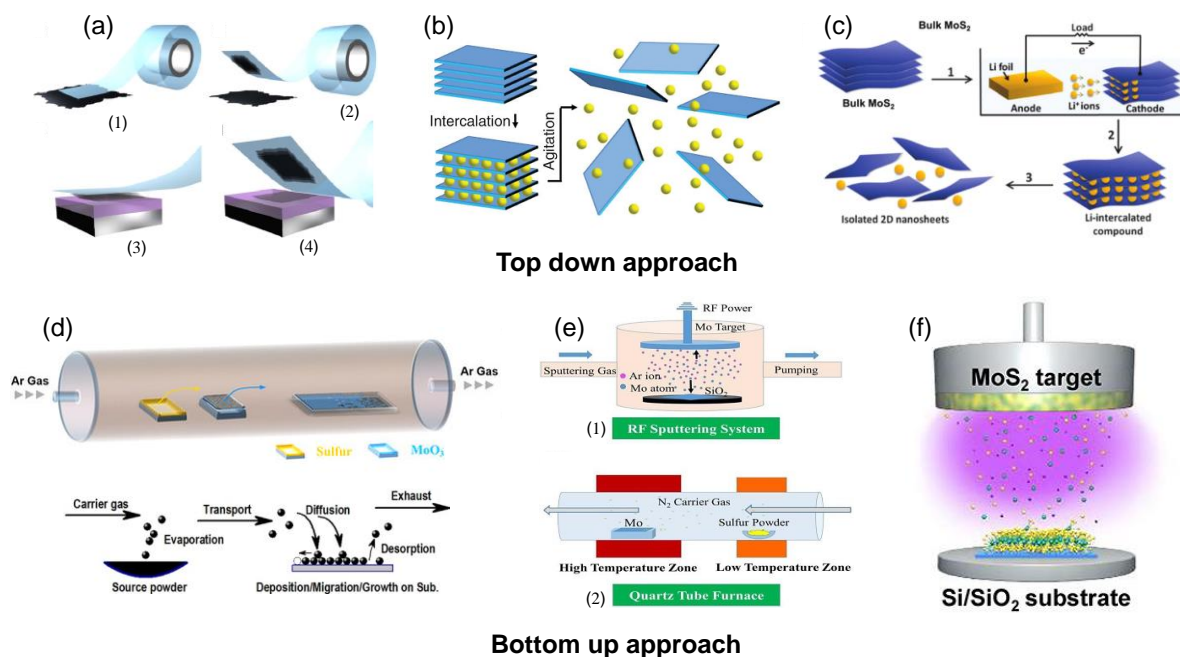


Figure 1.8 Different synthesis techniques to grow 2D MoS₂. The top-down approach includes (a) Mechanical exfoliation, (b,c) Chemical exfoliation; the Bottom-up approach includes (d) Chemical vapor deposition, (e,f) Sputtering [30, 32, 34-38].

1.4.3 Chemical vapor deposition

Chemical vapor deposition (CVD) is a popular bottom-up technique used to synthesize large-area 2D materials, such as MoS₂, with high crystalline quality. CVD processes can be categorized into several types, such as atmospheric pressure CVD, low-pressure CVD, plasma-enhanced CVD, and metal-organic CVD, all of which involve the same growth procedure to form MoS₂. In a typical CVD process, Mo source precursors such as molybdenum trioxide (MoO₃) [39, 40] and molybdenum pentachloride (MoCl₅) [41] as well as a sulfur source such as sulfur powder or reactive hydrogen sulphide (H₂S) gas are injected inside the reaction chamber (tube). As the temperature rises, the precursors evaporate and are transferred along the tube through the gas flow stream. These precursors react and deposited on the substrate via some means of chemical reaction [38], as depicted in Figure 1.8 (d). Some volatile by-products are often produced in this reaction, which are removed by the gas flow stream through the tube.

The growth behavior of 2D MoS₂ is affected by several key parameters, including carrier gas flow rate, growth temperature, precursor amount, substrate positions, and promoters, which influence the nucleation and growth modes of MoS₂. However, the CVD technique has limited control over deposition properties, such as vapor rates of the constituent precursors which can result in gradient properties even on the same wafer [42]. Additionally, CVD technique requires

high precision and monitoring operates at high temperatures, and some by-products are toxic, which limits the ability to grow large-area materials in a single domain.

To overcome these limitations, there are various modifications that can be made to the process, such as optimizing growth parameters [43], using catalysts [44] or promoters [45], or exploring alternative synthesis methods. One such method is the use of a two-step process, for instance, sputtering followed by sulfurization [36], which can enhance the uniformity of the deposited material. In this process, a thin layer of MoO_3 or Mo metal is deposited onto the substrate using techniques such as sputtering or thermal evaporation. The pre-deposited substrate is then annealed at a high temperature in an inert gas environment, which helps to convert the MoO_3 or Mo metal layer into a uniform layer of MoO_x . This MoO_x layer acts as a precursor material for subsequent sulfurization. In the last step, the MoO_x layer is exposed to a sulfur-containing gas or material, such as hydrogen sulfide (H_2S) gas or sulfur powder [36, 46]. The sulfur reacts with the MoO_x to form MoS_2 (Figure 1.8 (e)). This method offers better reproducibility and uniformity of the MoS_2 grown film.

1.4.4 Sputtering

Sputtering is a physical vapor deposition technique used to fabricate thin films. It involves the formation of a gaseous plasma from inert gas ions, electrons, and target material using an electric field applied to the material to be deposited, illustrated in Figure 1.8 (f). This technique allows precise control over the thickness and uniformity of the deposited film [47]. Recently, there has been a growing interest in using sputtering to grow high-quality MoS_2 films. The growth parameters such as growth pressure, base pressure, power, and substrate temperature affect the growth of MoS_2 , leading to the optimization of growth parameters to obtain thin films with desired characteristics. To obtain high-quality films, controlling the substrate temperature is a commonly used parameter during sputtering growth. However, a more effective growth strategy for MoS_2 layers involves room temperature or low-temperature growth, followed by post-annealing at high temperature [48, 49]. This approach has been shown to produce MoS_2 films with conductivity comparable to those produced by other attractive methods, such as CVD and mechanical exfoliation.

Direct sputtering from MoS_2 targets is a simple and commonly employed single-step growth method. However, this approach has been observed to produce MoS_2 layers that are not stoichiometric [42]. To improve the stoichiometry of the films, reactive sputtering with H_2S gas from MoS_2 targets can be utilized [50]. This process involves introducing of H_2S gas into

the sputtering chamber during deposition, which reacts with the MoS_x target to produce stoichiometric MoS_2 films. Additionally, sputtering a Mo metal target in a vaporized sulfur ambient has been shown to produce wafer-scale high-quality MoS_2 films [51, 52]. This approach produces large-area, uniform, continuous layers and is comparable in quality to other commonly preferred methods. Therefore, sputtering is more suitable for large-scale industrial applications, and further optimization of sputtering parameters is expected to enhance the quality of the produced MoS_2 films.

1.5 Vertically aligned MoS_2

Compared to in-plane MoS_2 , vertically aligned MoS_2 (VA- MoS_2) offers several advantages, including a high aspect ratio, large surface area, and more exposed edges [53]. These edges provide a greater number of active sites, which results in enhanced electrical and catalytic properties. Additionally, the edges act as one-dimensional metallic wires, increasing conductivity and catalytic reactivity [54, 55]. The vertical orientation of MoS_2 also leads to improved optical absorption and gas adsorption due to the larger height of the vertical flakes and the presence of more exposed edges [56, 57]. Moreover, longitudinal intra-layer charge transport is faster in VA- MoS_2 [58].

1.6 Applications of MoS_2

MoS_2 exhibits a range of intriguing properties including a direct and tunable bandgap, high absorption coefficient, large on/off ratio, and availability in the form of mineral molybdenite. Additionally, it possesses a high Young's modulus, good mechanical flexibility, and thermal and chemical stability, making it highly versatile [12, 59, 60]. As a result, it has gained significant attention and is utilized in a wide range of applications, such as transistors, solar cells, light-emitting diodes, hydrogen evolution reactions, sensing devices, and energy storage devices [10, 11, 61-65]. Herein, we focused on MoS_2 -based sensing devices, which are divided into two categories: (1) light sensing or photodetectors and (2) gas sensing.

1.7 Photodetectors

Photodetectors are electronic devices designed to detect and measure light signals by converting them into electrical signals. Photodetector operates by absorbing photons and generating free electron-hole pairs in the semiconductor material. The resulting charge carriers are then induced by an electric field or biasing voltage to create a photocurrent that can be amplified, processed, and analyzed. Photodetectors can operate across a wide range of the

electromagnetic spectrum, including X-ray, ultraviolet (UV), visible, infrared (IR), and terahertz (THz) ranges, depending on the bandgap of the material used to fabricate the photodetector. Photodetectors have numerous applications, including biomedical imaging, remote sensing, communication systems, and astronomy [66]. Photodetectors are the critical components in many modern technologies, and ongoing research and development continue to improve their sensitivity, efficiency, and performance.

1.7.1 General characteristics of the photodetector

To evaluate photodetector performance under different operating conditions and sizes, specific figures of merit are defined. Here, we briefly discussed the significance of each figure of merit.

Responsivity: Responsivity is a key parameter that characterizes the performance of a photodetector, which is defined as the ratio of the photo-generated current to the total incident optical power on the detector. In other words, it reflects the detector's ability to convert incident photons into electric current. The responsivity is expressed by the relation (1.2).

$$R = \frac{I_{photo}}{P} \quad (1.2)$$

Here, I_{photo} represents the photocurrent and P is the input optical power. A higher responsivity indicates a more efficient conversion of optical power into an electrical signal.

External quantum efficiency (EQE): It quantifies the probability that a single incident photon generates an electron-hole pair that contributes to the photocurrent of the device. The EQE is typically expressed as the ratio of the number of electron-hole pairs collected by the device to the number of incident photons and is given by:

$$\eta = \frac{I/e}{P/h\nu} = \frac{Rhc}{\lambda} \quad (1.3)$$

A high EQE indicates that a device is capable of efficiently converting incident photons into electrical current, collecting a high fraction of the generated electron-hole pairs.

Photo-gain: Photo-gain refers to the number of photo-excited carriers generated per incident photon. This parameter can also be expressed as the ratio of the photo-generated carrier lifetime to the transient carrier lifetime.

$$G = \frac{\tau}{\tau_{tr}} = \frac{\tau \mu V}{L^2} \quad (1.4)$$

Where, τ and τ_{tr} are the photogenerated carrier lifetime and carrier transit time, μ is the mobility, V is the applied bias voltage, and L is the channel length.

Noise equivalent power (NEP): It is a measure of the sensitivity of a device that detects light signals. It refers to the minimum optical power required to generate a signal that is comparable in size to the noise of the device, which can be considered as the threshold level of the device's detection capability. The lower the NEP value, the more sensitive the device is to detect low-level optical signals.

Detectivity: Detectivity is a fundamental measure of the sensitivity of an optical detector that quantifies its ability to detect weak optical signals in the presence of noise. It is inversely proportional to the noise equivalent power and is defined by equation (1.5). A higher detectivity value indicates a more efficient detector that can detect weaker signals.

$$D^* = \frac{\sqrt{AB}}{\text{NEP}} = \frac{R\sqrt{A}}{(2eI_{\text{dark}})^{1/2}} \quad (1.5)$$

Here, A and B are the active area & bandwidth of the detector, respectively. I_{dark} is the current flow in a detector in the absence of light radiation, also known as dark current.

Response time: Response time is a critical parameter that measures how quickly a detector can detect the photo-generated signal. The rise time is the time taken for the signal to rise from 10% to 90% of its maximum value, while the decay time is the time taken for the signal to fall from 90% to 10% of its maximum value. In order to ensure efficient and fast processing of the device, a low response time is essential. The faster the detector can respond to the photo-generated signal, the more accurate and reliable the device will be in its detection capabilities.

Spectral range: The spectral range of a photodetector describes the wavelengths of electromagnetic radiation that it can detect and convert into an electrical signal. This range is typically determined by the material properties of the detector, such as its bandgap, as well as the design of the detector. A wider spectral range in a photodetector enables it to detect light across a broader range of wavelengths. This capability is particularly useful in applications such as remote sensing or spectroscopy, where the detection of a wide range of wavelengths is essential.

1.7.2 Photodetection mechanism

The conversion of light signals into electrical signals typically involves two primary mechanisms: one is related to the electric field induced by optical radiation, including Photovoltaic, Photoconductive, and photo-gating effect, and the other is related to a thermal process involving the photo-thermoelectric effect and photo-bolometric effect. Here, all the photo-conversion mechanisms are briefly discussed.

Photovoltaic effect: The photovoltaic effect occurs when a material is exposed to light with sufficient energy ($h\nu \geq E_g$), resulting in the creation of electron-hole pairs through photon absorption. These generated electron-hole pairs are separated by an internal built-in electric field, which can be created by forming a p-n or Schottky junction at the interface between a semiconductor and a metal contact. Devices that exhibit the photovoltaic effect show non-Ohmic I-V characteristics [67]. In the case of a p-n junction, the forward current is exponentially proportional to the applied bias voltage ($I \propto e^V - 1$), while the reverse current is negligible until the breakdown voltage is reached. When illuminated without any applied bias voltage ($V = 0$), the internal electric field separates the free excited charge carriers, resulting in a short circuit current (I_{sc}). If the circuit is open, the electron-hole pairs accumulate at the opposite terminal, leading to the open-circuit voltage (V_{oc}).

This type of detector typically operates in self-bias or reverse bias mode. In photovoltaic mode of operation, the dark current is lowest, leading to higher detectivity. Phototransistors and various types of photodiodes, including PN, PIN, and Schottky photodiodes, have been developed based on the working principle of the Photovoltaic effect.

Photoconducting effect: In the photoconductive effect, excess free charge carriers are generated by photon absorption, modulating the electrical resistance of the semiconductor. Without illumination, a small source-drain current can flow (I_d) across the semiconductor device by an applied bias (V_{ds}). Under illumination, electron-hole pairs are created by photons with an energy level greater than the bandgap of the semiconductor. The applied bias voltage then separates the pairs, causing the free electrons and holes to drift in opposite directions towards the metal electrodes. This results in a net increase in the current (I_{ph}), which combines with the dark current to reduce the resistance of the device. To observe the photoconducting effect, an applied bias voltage (V_{ds}) is required [68]. For efficient devices, an Ohmic contact is preferred to separate the excess photo-generated free charge carriers.

Photogating effect: The photogating effect is a special case of the photoconducting effect observed in defected or hybrid structures. In this effect, one type of photogenerated charge carriers are trapped in a localized state that cannot participate in forming the photocurrent, while the other types of carriers can flow within the channel material, modulating the conductance of the material and thus forming the photocurrent [69]. Since the trapped charge carriers have a longer lifetime, this effect leads to a large photoconductive gain. The trapped charge carriers can generate an additional local gate voltage that shifts the transfer

characteristics horizontally from the dark state (ΔV_g). The photocurrent can be increased or decreased depending on the shift in V_g [70].

Photo-thermoelectric effect: The photo-thermoelectric effect refers to the generation of a photovoltage in a semiconductor device due to a local temperature gradient induced by non-uniform heating. Specifically, when a small laser spot is applied to a semiconductor channel, it results in a temperature difference (ΔT) across the channel at the two ends of the device. This temperature difference then produces a photovoltage via the Seebeck effect, which drives a current through the device without the need for any external biasing [70].

The magnitude of the induced photo-thermoelectric voltage is proportional to the temperature difference and the difference in Seebeck coefficients across the device, represented as $V_{PTE} = (S_2 - S_1)\Delta T$ [71]. The Seebeck coefficients themselves are generally expressed in terms of the conductivity of the material through the Mott formula [72],

$$S = \frac{\pi^2 k^2 T}{3e} \frac{d\sigma(E)}{dE} \quad (1.6)$$

Where k is the Boltzmann constant, $\sigma(E)$ represents conductivity as a function of energy (E), and the derivative of conductivity with respect to energy is evaluated at the Fermi energy E_F . The sign of the Seebeck coefficient is determined by the polarity of the majority charge carriers in the semiconductor. In addition to local illumination, a temperature gradient can also be induced by global illumination through strongly different absorption in various parts of the channel device [73]. However, the magnitude of the photo-thermoelectric voltage is often small, ranging from $1\mu V$ to $10mV$.

Photo-bolometric effect: The photo-bolometric effect is based on the modulation of the resistivity of a temperature-sensitive material induced by uniform light heating. Under homogeneous thermal illumination, the size of this effect is relative to the conductance change of a material with temperature (dG/dT) and the homogeneous temperature increment (ΔT) prompted by laser heating. However, the resistance of the temperature-sensitive material could be increased or decreased, and the photocurrent could be increased or decreased accordingly at fixed applied bias voltage [74]. The photo-bolometric effect could not be observed without applying any external bias voltage, unlike the photo-thermoelectric effect.

1.8 A brief historical overview of photodetectors based on 2D materials: MoS₂ and its heterostructures

Traditionally, photodetectors made from Si, InSb, and InGaAs have dominated the market for decades due to their abundance, high performance, ease of integration, and large-scale production [75-77]. However, Si has an indirect bandgap of 1.1 eV, which limits its light absorption to the visible to near-infrared range, greatly reducing its efficiency. Additionally, silicon's brittleness, rigidity, and opacity make it unsuitable for wearable, flexible, and bendable device applications. While HgCdTe, GaSb, and InSb have shown promising photodetector performance in the mid-wave and long-wave IR wavelength range, they require cryogenic temperatures to function, making them impractical for many applications [78, 79]. Therefore, a new generation of optoelectronic materials is needed to overcome the limitations of traditional photodetectors. These new materials must have broadband UV-Visible-NIR light absorption capabilities, fast on/off switching ratios, strong light-matter interaction properties, and easy integration with currently available complementary metal oxide semiconductor technology. Fortunately, 2D materials possess all of these properties and could be the ideal solution to overcome the limitations of traditional photodetectors. Additionally, 2D materials are flexible, transparent, and lightweight, making them ideal for wearable and flexible devices [1]. They can also be easily integrated with existing technologies, allowing for seamless incorporation into current systems.

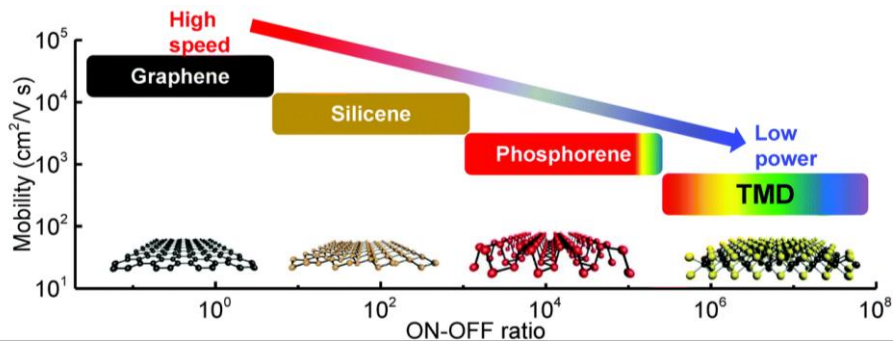


Figure 1.9 Mobility versus on/off ratio values for 2D semiconductors [80].

In 2004, the discovery of single-layer graphene sheet from graphite caused a worldwide sensation in the research community. This incredible material has outstanding properties such as ultra-high mobility ($2 \times 10^5 \text{ cm}^2 \text{ V}^{-1} \text{ s}^{-1}$), superior mechanical strength (130 GPa), and broadband optical absorption coefficient ($7 \times 10^5 \text{ cm}^{-1}$) [11, 81]. Despite its unique properties, graphene lacks bandgap and limits its potential for switching devices. Silicene is a 2D allotrope

of silicon, similar to graphene, having a narrow but finite bandgap. However, its potential applications are still limited due to the complexity of material synthesis and device fabrication [80]. Phosphorene or Black Phosphorus (BP), has gained attention in the research community due to its remarkable properties, including a large and tunable bandgap (0.3 to 2 eV), high mobility, and moderate on-off ratio [82]. It bridges the gap between the mobility and current on-off ratio of TMDs and 2D allotropes of group 4 semiconductors, depicted in Figure 1.9. Despite its excellent properties, phosphorene's instability in the ambient environment is a major challenge for the development of semiconductor devices [83].

TMDs material with wide range of bandgaps are widely used in low-power electronics due to their excellent physical and chemical properties. Although TMDs have the lowest mobility compared to graphene and phosphorene, they have the highest current on-off ratio, making them a promising candidate for photodetector applications [80]. MoS₂ is the primary option for researchers when developing 2D TMDs photodetectors, and recent advancements in this field have poised it for early stages of commercialization in the near future [11]. This section comprises a brief overview of the recent developments in MoS₂-based photodetectors.

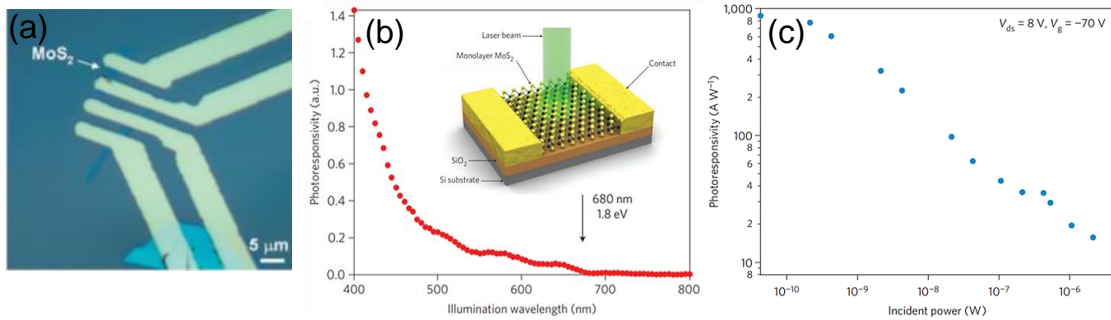


Figure 1.10 Optical image of monolayer MoS₂. (b) Photoresponsivity as a function of wavelength, indicating the cut-off wavelength of 680 nm. Schematic of the monolayer MoS₂ photodetector shown in the inset. (c) Photoresponsivity as a function of incident power of the same device [84, 85].

MoS₂ photodetectors are commonly implemented as field-effect transistors (FETs). The first MoS₂ photodetector was fabricated by Radisavljevic et al. using mechanically exfoliated monolayer MoS₂ [84]. This FET device achieved a responsivity of 7.5 mA/W and a response time of 50 ms under an optical power illumination of 80 μW and a gate voltage of 50 V. Lopez et al. reported an ultrasensitive monolayer MoS₂ photodetector with an improved responsivity of 880 A/W under an illumination power of 150 pW [85]. The responsivity was highly sensitive to illumination power and decreased sub-linearly due to existing trap states in MoS₂ or at the interface between MoS₂ and SiO₂ under high-intensity illumination (Figure 1.10 (c)).

Moreover, the photodetector showed longer response time ($\sim 4/9$ s), which is attributed to the large photo gain induced by the presence of trap states. The photodetector also demonstrated a low NEP of 1.8×10^{-15} W/Hz, which is comparable to commercially available Si photodiodes. This extremely low NEP was due to low shot noise limited to dark current. The photodetection cut-off wavelength was 680 nm, corresponding to the MoS₂ bandgap, which limits the detection ability beyond the bandgap (Figure 1.10 (b)).

Zhang et al. achieved even higher responsivity of 2200 A/W under vacuum and 780 A/W in air for CVD grown monolayer MoS₂ film [86]. The electronic and optoelectronic properties of MoS₂ are greatly affected by moisture and absorbates present in air due to large surface to volume ratio [87, 88]. Thus, mobility, photogain and photoresponse are reduced, as they are assisted by the recombination centres, reducing the carrier lifetime in trap states. Similarly, López et al. observed low responsivity of 1.1 mA/W at 1.5 V biasing under illumination of 514.5 nm laser for monolayer MoS₂ grown by CVD [89].

The large variation in responsivity for monolayer MoS₂ is attributed to many factors such as difference in device resistance, device geometry or interdigitated electrode geometry, applied external biased voltage and gate voltage, difference in light detection tool, for instance, area of laser spot, incident power of light source, limit of measurement set-up (RC constant). Hence, all the above-mentioned factors contribute to the performance of the device.

Monolayer MoS₂ photodetectors were extensively studied, which showed better performance than the graphene photodetectors, but suffered from low absorption [84]. Afterward, multiple approaches were adopted to design high performance multilayer MoS₂ (ML MoS₂) devices [90, 91]. Yu et al reported a first vertical MoS₂ heterostructure for efficient photon harvesting in 2013 [92]. After that several groups have studied 2D heterostructures for photodetector applications. Lee et al. fabricated a vertical p-n junction by using p-type WSe₂ and n-type MoS₂ [93]. The difference between bandgap and work function of monolayer MoS₂ and WSe₂ makes an atomically sharp interface with type II band-alignment. The type II (staggered gap) alignment favours separation and transportation of charge carriers and allows interlayer excitation, that effectively broadens the photodetection range. Sinha et al. proposed a van der Waals heterostructure between the bilayer MoS₂ and bilayer WS₂ with excellent responsivity 2.51×10^5 A/W and detectivity 4.2×10^{14} jones [94]. The ultrahigh responsivity is attributed to favourable type-II alignment and efficient absorption of incident wavelength. Similarly, Zhang et al. demonstrated a type II MoS₂/MoTe₂ van der Waals heterostructure [95]. The formation

of type II band alignment reduced the energy gap between VBM of MoTe₂ and CBM of MoS₂ up to 0.657 eV (equivalent to 1.8 μm), which is less than the bandgap of their individual constituent. Thus, hybrid device structure exhibited photoresponse for illumination wavelength of 1.5 μm (Figure 1.11(a)). Therefore, 2D heterostructures are capable to effectively broaden the photodetection range.

Colloidal quantum dots (CQD) are highly photosensitive materials with excellent bandgap tunability via size quantization. They allow spectral tuning of absorption profile of semiconductor, covering broad spectral range from UV-visible up to mid-IR, which makes it attractive for light detection applications [96-98]. Indeed, an immense improvement of photoresponsivity has been achieved after the formation of hybrid photodetector by combining semiconducting CQD with MoS₂ [99-102]. Kufer et al. reported highly sensitive MoS₂/PbS QD hybrid photodetector extended spectral response up to 1.5 μm with large photoresponsivity [99]. MoS₂/PbS hybrid structure synthesized by spin-coating of p-type PbS QDs on top of mechanically exfoliated n-type MoS₂. Under illumination, PbS QDs absorbed the light and separated the photo-excited charge carriers at the interface between p-type PbS and n-type MoS₂ due to built-in electric field at junction (Figure 1.11 (b)). The generated electrons transferred to MoS₂ channel, while holes remain trapped in QDs. The electrons circulated multiple times within the MoS₂ channel due to applied field (V_{ds}) until the holes are de-trapped and collected by electrode, thus leads to high optical gain 10^6 and responsivity of 5×10^5 A/W. The photoresponse of hybrid device was much better than individual pristine MoS₂ and pristine PbS QD photodetector. The reported device was suffered from slow response of 0.3 s due to large trapping lifetime of holes in QDs.

The progress in synthesis and film transfer techniques of MoS₂ are now becoming more abundant, which makes integration of MoS₂ with 3D traditional bulk materials to form heterostructures. Si, GaAs, GaN are primary 3D bulk materials to formed heterostructure with MoS₂ [57, 103-105]. Either a p-n or n-n junction is formed between a 3D bulk semiconductor and MoS₂, which enables rapid separation of photo-generated electron-hole pairs due to strong built-in electric field at depletion region. As a result, such MoS₂/3D hybrid detector exhibits high detectivity and fast response. The spatial map of the photocurrent generated at the vertical p-n junction of MoS₂/Si (Figure 1.11 (c)) highlights the significance of the junction. The map clearly illustrates that the photocurrent is predominantly concentrated at the junction area, rather than near the contact. This observation emphasizes the importance of the junction in facilitating efficient charge separation and collection in the device.

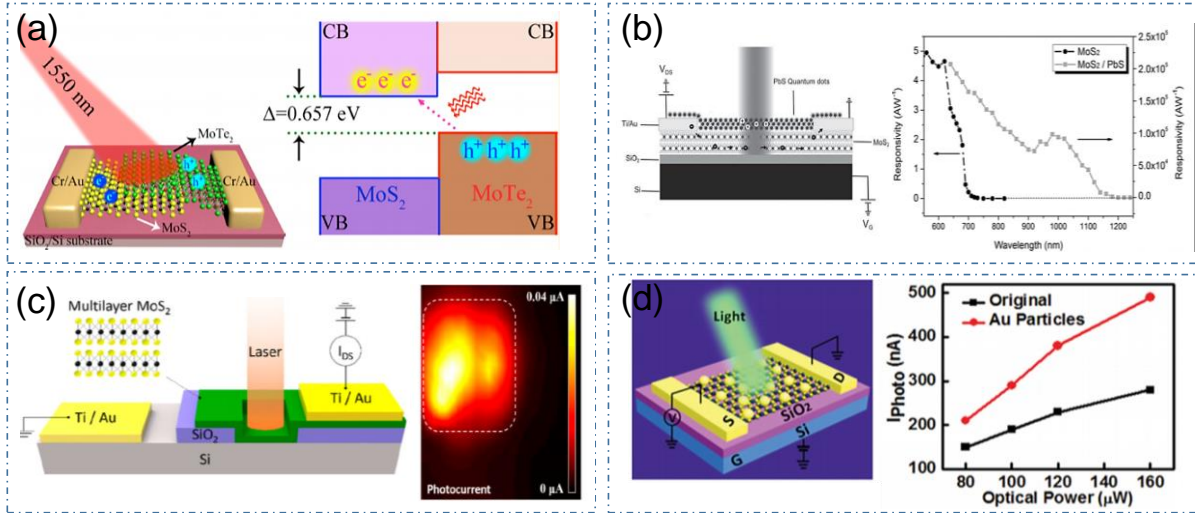


Figure 1.11 (a) 3D schematic of MoS₂/MoTe₂ heterojunction device under illumination, (b) MoS₂/PbS QD hybrid under light illumination with device performance, (c) 2D/3D vertical heterostructure of MoS₂/Si under illumination and photocurrent map at junction, (d) Schematic of a plasmon-enhanced MoS₂ photodetector and power-dependent photocurrent of pristine MoS₂ and MoS₂ with incorporated Au-NPs [106-109].

Plasmonic nanostructures such as metal-NPs, nanoantenna's, nanodiscs have been incorporated with 2D MoS₂ to further enhance light-matter interaction. Surface plasmons (SPs) are the coherent delocalized electrons oscillations, propagating at the interface between two mediums (commonly metal and dielectric), which differ from the dielectric constant's real part (opposite sign). They generate an electromagnetic field near the metal surface. The associated charge motion on a metal surface coupled with the electromagnetic field produces surface plasmon polaritons (SPPs). SPPs are always higher in frequency than incident photons. Therefore, they may have stronger spatial confinement and localized field intensity. By this approach, the plasmon-enhanced optical field significantly assists the interaction between light and matter.

Miao et al. incorporated 4 nm thick Au NPs onto the MoS₂ layer (Figure 1.11 (d)) [109]. They observed two-fold enhancement in the photocurrent due to enhanced absorption in MoS₂, which was attributed to the light trapping and enhanced optical field near Au NPs. Using the same approach, Rahmati et al. decorated Au NPs on CVD grown vertical MoS₂ and observed 20-fold enhancement in photocurrent due to plasmonic effect and increasing light scattering [110]. The ability to generate hot electrons in plasmonic nanostructures through surface plasmon decay enables the photodetection of 2D material beyond the bandgap limit. Hot electrons can be injected directly into the MoS₂ across the Schottky barrier at the metal-semiconductor interface, capable to generate photocurrent beyond the bandgap limitation. Wang et al. adopted the same approach and reported the hot electron-based NIR bi-layer MoS₂ photodetector, with

asymmetric Au plasmonic nanoantenna array [111]. The device exhibits strong photoresponse beyond the bandgap originating from energetic hot carriers injection in MoS₂ via surface plasmon-induced non-radiative decay process, under illumination. In addition, a high photo gain of 10⁵ obtained in the infrared regime (at 1070 nm) is the result of a high photo-responsivity of 5.2 A/W. Thus, enhanced absorption in 2D film via plasmonic nanostructures resulted in a significant enhancement of the photoresponse of the device.

1.9 Gas sensors

Gas sensors are crucial devices used to detect specific gases present in the environment. It comprises two essential components: a receptor unit and a transducer unit. The receptor unit interacts with gas molecules and produces chemical information, which is then transmitted to the transducer unit as an electrical signal. The gas detection device reads this electrical signal and processes it further [112].

Among the various types of gas sensors, chemiresistive gas sensors have emerged as the most promising due to their easy integration, manufacturing, real-time monitoring, and stability in harsh environments. These sensors work by measuring the change in the resistance of a sensing film when exposed to gas molecules. Chemiresistive gas sensors have a wide range of applications, including industrial process control, air quality monitoring, and gas leak detection in hazardous environments [113]. They are critical in preventing accidents and ensuring the safety of people and the environment.

1.9.1 General characteristics of the gas sensor

Gas sensors are typically assessed based on a set of performance parameters. The following key figures of merit are commonly used to evaluate their performance:

Sensor response: Sensor response is the measure of its ability to detect changes in the presence of gas. It is defined as the ratio of change in the resistance of a sensor when exposed to gas molecules, relative to its resistance in the presence of air, and can be expressed as [114]:

$$\Delta R = \frac{(R_a - R_g)}{R_a} \times 100\% \quad (1.7)$$

$$\Delta R = \frac{R_g}{R_a} \quad (1.8)$$

$$\Delta R = \frac{R_a}{R_g} \quad (1.9)$$

Selectivity: It is the ability of the sensor to detect a specific gas in the presence of other interfering gases. Selectivity is important in ensuring that the gas sensor responds only to the gas of interest, reducing false readings.

Response and recovery time: The response time of the sensor is the time required to reach 90% of the maximum response upon gas exposure. The recovery time is time taken to return 10% of the base value of response after removal of target gas. A gas sensor with fast response and recovery times can provide accurate and early detection of gases, making it a critical tool for ensuring safety in various applications.

Limit of detection: This is the lowest concentration of the target gas that the sensor can reliably detect. A low detection limit is desirable for applications that require the detection of low concentrations of gas.

Stability: It is the ability of the sensor to maintain its performance over time and under different environmental conditions. A stable gas sensor can provide accurate and reliable measurements over a long period of time.

1.9.2 Gas sensing mechanism in MoS₂ and its heterostructure

The gas sensing mechanism involves the interaction between gas molecules and the surface of a material, leading to changes in its electronic properties that can be detected as a change in electrical resistance [115]. In the case of MoS₂, gas molecules adsorb on the surface, resulting in changes in the local charge distribution and electronic band structure. This can lead to an increase or decrease in the electrical resistance of the material, depending on the type and concentration of the gas.

Yue et al. used first-principles density functional theory (DFT) to investigate the gas adsorption of several molecules, including NO₂, H₂, O₂, NH₃, NO, CO and H₂O on monolayer MoS₂ [116]. The calculation results reveal that the gas molecules were primarily physisorbed on the surface of MoS₂, with a small charge transfer occurring. MoS₂ can act as either a charge acceptor or a charge donor, depending on the gas type and the adsorption site [116]. The adsorption energy and charge transfer depend on the adsorption site of the gas molecule, which can occur at four possible sites of MoS₂: H sites (top of the hexagon), T_S (top of S atom), T_M (top of Mo atom), and B (top of Mo and S bond). The minimum distance between the adsorbed gas molecule and the relaxed MoS₂ surface known as equilibrium height, is used to determine the adsorption of gas molecules. The gas adsorption in MoS₂ surface is highly position dependent due to the large variation in adsorption energy and charge transfer at different adsorption sites of MoS₂.

Cho et al. conducted an experiment to demonstrate charge transfer between gas molecules (NO_2 and NH_3) and MoS_2 sensing layers. The in-situ PL measurements were conducted before and after gas exposure. The results showed that the resistance of the MoS_2 layer increased and decreased upon exposure of NO_2 and NH_3 gas, respectively. The PL of MoS_2 has two emission peaks, at 1.8413 and 1.8424 eV, which correspond to $A^{+/-}$ trions and A^0 neutral excitons, respectively [117]. When NO_2 gas molecules were adsorbed on the surface of MoS_2 , excess holes were generated, leading to the conversion of a neutral exciton (A^0) to a positive trions (A^+) from p-type MoS_2 . This caused an increase in the PL intensity of the A^+ peak and a decrease in the intensity of the A^0 peak. Conversely, PL intensity of A^+ peak is reduced in presence of NH_3 gas molecules, leading to an enhanced intensity of A^0 peak, which is ascribed to the dissociation of A^+ trions from A^0 exciton, as illustrated in Figure 1.12.

From DFT calculations (Table 1.1), it has been observed that MoS_2 has highly favorable adsorption sites (H, Ts, and B-sites) for NO_2 gas, exhibiting larger adsorption energy and charge transfer compared to other gas molecules. On the other hand, MoS_2 shows only one favorable site, namely the T_M site, for H_2 gas adsorption. Experimental results confirm that MoS_2 sensors can selectively detect NO_2 gas in the environment while exhibiting little sensitivity towards H_2 gas [10, 118]. However, vertically aligned MoS_2 has shown promising results in detecting hydrogen gas at room temperature due to the presence of favorable adsorption sites along the edges of MoS_2 [40]. Nevertheless, the selective detection of hydrogen is hindered by other active sites present on the surface of MoS_2 .

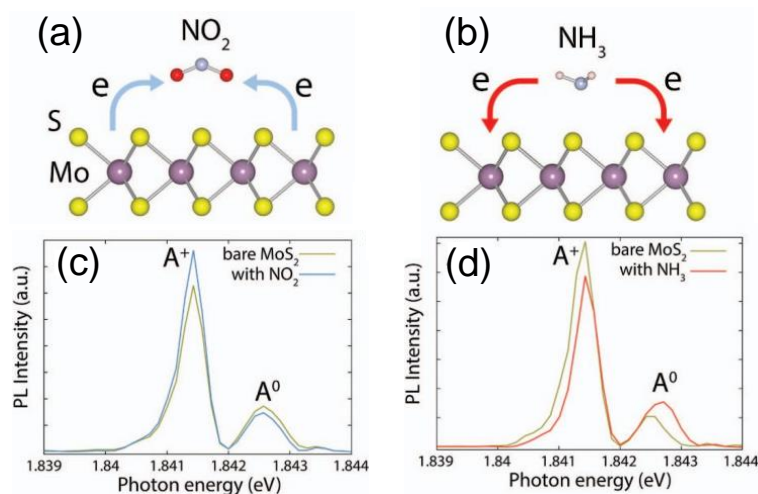


Figure 1.12 Schematic of charge transfer between MoS_2 and (a) NO_2 (electron acceptor), and (b) NH_3 (electron donor) gas. In situ PL spectra recorded from MoS_2 in presence of (c) NO_2 and (d) NH_3 gas molecules [117].

Table 1.1 The calculated adsorption energy (E_a in meV), charge transfer value (ΔQ in e) between the MoS₂ and gas molecules and distance (d in Å) between the adsorbed gas molecule and MoS₂ for different gaseous molecules using DFT by Yue et al. [116].

Gas	H-Site			T _M -Site			T _S -Site			B-Site		
	d	E_a	ΔQ	d	E_a	ΔQ	d	E_a	ΔQ	d	E_a	ΔQ
NO ₂	2.65	-276	0.1	-	-	-	2.71	-249	0.119	2.62	-249	0.114
H ₂	2.62	-70	0.004	2.61	-82	0.004	3.02	-49	0.008	-	-	-
O ₂	2.79	-106	0.034	2.71	-116	0.041	3.19	-64	0.020	-	-	-
NH ₃	2.46	-250	-0.07	2.61	-222	-0.05	3.21	-100	-0.024	-	-	-
NO	2.68	-195	0.011	2.90	-185	0.011	2.88	-152	0.039	2.83	-211	0.002
CO	2.95	-198	0.020	3.22	-124	0.006	3.28	-86	0.016	3.15	-128	0.013
H ₂ O	2.59	-234	0.012	2.67	-222	0.016	3.13	-110	0.009	-	-	-

To improve the selectivity and sensitivity towards hydrogen gas, MoS₂ nanocomposites or heterostructures are widely employed. However, the use of heterostructures can complicate the sensing mechanism, making it crucial to understand the involved mechanisms. In 2D/0D heterostructure, noble metal nanoparticles, and metal oxide QDs are often used to improve the sensing properties of 2D materials. Noble metal nanoparticles, including Pt and Pd, can facilitate gas-sensing reactions with the active sites of 2D materials by aiding in the dissociation of gas molecules [114, 119]. 0D QDs such as MoO₃, TiO₂, with appropriate energy band structures, can create diverse types of heterostructures with 2D materials, leading to improved sensing properties due to the modulation of the barrier height and interfacial charge transfer after gas exposure [120, 121].

1D nanowires or nanorods, have also been utilized to enhance the sensing properties of 2D materials by forming 2D/1D heterostructures. The improved sensing properties are attributed to the synergistic effect, where 2D materials act as conducting channels and 1D nanomaterials act as active sites for gas adsorption [115]. This facilitates the orientation of charge transfer at the 2D/1D interface and further modulation of the barrier height between these two materials.

In 2D/2D heterostructures, the atomic thickness of the 2D materials allows gas molecules to interact with the two different 2D materials independently. This results in larger modulation of the barrier height at the heterointerface and band alignments caused by gas adsorption due to the variation in charge transfer between the adsorbed gas and different 2D materials [115, 122]. Thus, the use of heterostructures can significantly improve the sensitivity and selectivity of hydrogen gas, but understanding the underlying mechanisms is crucial to optimize the design and performance of the sensor.

1.10 Challenges and Motivation

CVD has emerged as a promising technique for growing high-quality MoS₂ flakes. However, the large-scale growth of MoS₂ via CVD remains a challenge due to issues related to precise control over growth parameters, morphology, uniformity, and reproducibility. Despite significant progress, synthesizing large-scale, uniform, and highly reproducible MoS₂ flakes using CVD is still an open challenge. Thus, an alternative approach that is highly reproducible, uniform, and scalable is required to overcome the limitations of the CVD technique.

Sputtering is one such approach that offers highly uniform and large-area growth of MoS₂ with high reproducibility. However, it requires proper optimization of growth parameters to achieve high-quality MoS₂. Additionally, the growth parameters can be tuned to control the morphology of the resulting film. Therefore, sputtering can be a potential alternative technique to overcome the challenges associated with CVD-based MoS₂ growth in the present work.

Despite the remarkable progress in the performance of MoS₂ photodetectors, the use of a single material inherently constrains their photodetection capability. MoS₂ suffers from low optical absorbance due to its atomically thin nature, restricts its ability to detect light efficiently. Moreover, the response times of pristine MoS₂ photodetectors are often slow due to the lack of a high-quality junction, limiting their performance. Additionally, the active wavelength detection range of pristine MoS₂-based devices is limited to its bandgap, which restricts their potential in broadband photodetection.

One promising solution to overcome these limitations is the integration of two or more high-absorbing materials with complementary bandgaps. This approach enables superior light absorption across a wide spectral range, resulting in significant enhancement in device performance. By forming heterostructures with other high-optical-absorbing materials, the optical absorption of MoS₂ can be improved, leading to a more efficient light detection capability. Heterostructure photodetector devices exhibit superior photoresponse compared to

individual materials, allowing them to access more functionality. Moreover, the surface of 2D materials is free from dangling bonds, which makes them easily to integrate without any restriction of lattice misfit. As a result, a large number of heterostructure combinations with different dimensionality are possible due to the existence of interlayer coupling in 2D materials. Ultimately, heterostructures offer a viable choice for high-performance photodetector fabrication, offering advantages such as increased responsivity, lower response time, and broadband response.

In addition to the development of heterostructure, it is very critical to understand the charge carrier dynamics at heterostructure interface. The device performance is strongly affected by the band alignment and charge extraction at the interface. The junction characteristics and charge transport are directly correlated, and charge transport can be effectively influenced by modulating the interface. Therefore, it is imperative to study the interface in order to gain a deeper understanding of the underlying mechanisms that affect the performance of the device.

Hydrogen is emerging as a promising energy source for the future due to its renewable and clean production [123, 124]. With a high combustion energy of 142 kJ/g, hydrogen is an attractive option for various sectors, including aerospace, transportation, chemical industry and petroleum extraction [114]. However, the high flammability and explosiveness of hydrogen gas, especially at concentration greater than 4%, possess a significant safety risk to human life [125]. Moreover, hydrogen flame is completely invisible to the naked eyes, further exacerbates this danger. To minimize the risk, it is crucial to have early and accurate detection of H₂ gas with high selectivity and sensitivity.

Currently, pristine MoS₂ gas sensors are less sensitive or insensitive to hydrogen gas. However, MoS₂ heterostructures or their nanocomposites exhibit a high response to hydrogen gas. Nevertheless, these heterostructure-based gas sensors suffer from slow response time and incomplete recovery at room temperature. On the other hand, vertically aligned MoS₂ (VA-MoS₂) has more reactive edge sites, which can enhance gas adsorption. However, designing room-temperature and hydrogen-selective sensors using VA-MoS₂ remains challenging due to the high adsorption energy of other gases at different active sites on MoS₂ flakes. Therefore, developing VA-MoS₂-based hydrogen gas sensors with high sensitivity and selectivity at room temperature is an active area of research.

1.11 Objective of the present thesis work

The aim of this research thesis is to employ a facile and efficient technique to synthesize uniform, reproducible, and large-area MoS₂ flakes for photodetector and gas sensing applications. The main objectives of the present thesis are as follows:

1. Controlled growth of high-quality and large-area MoS₂
2. To study the charge carrier dynamics of MoS₂ based heterostructures for efficient carrier transport
3. Fabrication of highly sensitive and broadband photodetector of MoS₂-based heterostructures
4. Fabrication of highly selective hydrogen gas sensor working at room temperature

1.12 Outline of the thesis

The thesis is organized into the following six chapters to accomplish predefined objectives.

Chapter 1: Introduction

This chapter provides a brief overview of the physical properties of TMDs, with a special focus on MoS₂, and their relevance to device applications. A systematic review of recently published works in this area is included to provide context for the research carried out in this thesis. The chapter also addresses outstanding issues in large area growth of MoS₂ and the challenges in developing high-performance broadband photodetectors and selective hydrogen sensing, particularly at room temperature. Finally, the chapter concludes by presenting the objectives and aims of the present thesis work.

Chapter 2: Fabrication and characterization techniques

This chapter discusses the synthesis and characterization techniques employed in the present study. The mechanisms behind various deposition and characterization methods are explained. It provides a brief description of each technique and its role in understanding the structural and optical properties of MoS₂ and its interface.

Chapter 3: Large area growth of MoS₂ from in-plane to vertically oriented flakes

This chapter systematically investigates the large area growth of highly uniform MoS₂ using a facile and scalable sputtering technique. It provides a detailed understanding of the growth mechanism and the role of various parameters in optimizing the growth of MoS₂.

Chapter 4: 2D MoS₂ heterostructures for broadband photodetection

In this chapter, various heterostructures of 2D/2D (MoS₂-ReS₂), 2D/3D (MoS₂/Ga₂O₃) and 2D/Plasmonic metal NPs (Pt@MoS₂) are studied for broadband photodetection. The chapter emphasizes the importance of interface and energy level alignment in determining device performance. It provides a detailed understanding of charge carrier dynamics at the interfaces, using photoelectron spectroscopy and Kelvin Probe Force Microscopy (KPFM). Finally, the photodetector performance of pristine MoS₂ is compared with heterostructures and examined in detail.

Chapter 5: 2D MoS₂ heterostructures for hydrogen sensing

This chapter presents Pt NPs decorated vertically aligned MoS₂ flakes (Pt@MoS₂) for selective hydrogen sensing at room temperature. The effect of Pt NPs size and operating temperature on the sensing performance are also investigated in detail.

Chapter 6: Summary and Scope for Future Studies

This chapter summarises the entire thesis work and presents future directions for the further development of 2D materials growth and devices.

References

1. Mas-Ballesté, R., et al., *2D materials: to graphene and beyond*. Nanoscale, 2011. **3**(1): p. 20-30.
2. Zhao, P., et al. *2D layered materials: From materials properties to device applications*. in *2015 IEEE International Electron Devices Meeting (IEDM)*. 2015.
3. Geim, A.K. and K.S. Novoselov, *The rise of graphene*. Nature Materials, 2007. **6**(3): p. 183-191.
4. Geim, A.K., *Graphene: Status and Prospects*. Science, 2009. **324**(5934): p. 1530-1534.
5. Chhowalla, M., et al., *The chemistry of two-dimensional layered transition metal dichalcogenide nanosheets*. Nature Chemistry, 2013. **5**(4): p. 263-275.
6. Mattheiss, L.F., *Band structures of transition-metal-dichalcogenide layer compounds*. Physical Review B, 1973. **8**(8): p. 3719.
7. Kolobov, A.V. and J. Tominaga, *Chemistry of Chalcogenides and Transition Metals*, in *Two-Dimensional Transition-Metal Dichalcogenides*, A.V. Kolobov and J. Tominaga, Editors. 2016, Springer International Publishing: Cham. p. 7-27.
8. Jariwala, D., et al., *Emerging Device Applications for Semiconducting Two-Dimensional Transition Metal Dichalcogenides*. ACS Nano, 2014. **8**(2): p. 1102-1120.
9. Wang, Q.H., et al., *Electronics and optoelectronics of two-dimensional transition metal dichalcogenides*. Nature Nanotechnology, 2012. **7**(11): p. 699-712.
10. Agrawal, A.V., N. Kumar, and M. Kumar, *Strategy and Future Prospects to Develop Room-Temperature-Recoverable NO₂ Gas Sensor Based on Two-Dimensional Molybdenum Disulfide*. Nano-Micro Letters, 2021. **13**(1): p. 38.
11. Wadhwa, R., A.V. Agrawal, and M. Kumar, *A strategic review of recent progress, prospects and challenges of MoS₂-based photodetectors*. Journal of Physics D: Applied Physics, 2022. **55**(6): p. 063002.
12. Li, X. and H. Zhu, *Two-dimensional MoS₂: Properties, preparation, and applications*. Journal of Materiomics, 2015. **1**(1): p. 33-44.
13. He, Z. and W. Que, *Molybdenum disulfide nanomaterials: Structures, properties, synthesis and recent progress on hydrogen evolution reaction*. Applied Materials Today, 2016. **3**: p. 23-56.
14. Jin, Q., et al., *Mechanisms of Semiconducting 2H to Metallic 1T Phase Transition in Two-dimensional MoS₂ Nanosheets*. The Journal of Physical Chemistry C, 2018. **122**(49): p. 28215-28224.
15. Sun, X., et al., *Origin of Structural Transformation in Mono- and Bi-Layered Molybdenum Disulfide*. Scientific Reports, 2016. **6**(1): p. 26666.
16. Splendiani, A., et al., *Emerging Photoluminescence in Monolayer MoS₂*. Nano Letters, 2010. **10**(4): p. 1271-1275.
17. Ridolfi, E., et al., *A tight-binding model for MoS₂ monolayers*. Journal of Physics: Condensed Matter, 2015. **27**(36): p. 365501.
18. Mak, K.F., et al., *Atomically Thin MoS₂: A New Direct-Gap Semiconductor*. Physical Review Letters, 2010. **105**(13): p. 136805.
19. Alidoust, N., et al., *Observation of monolayer valence band spin-orbit effect and induced quantum well states in MoX₂*. Nature Communications, 2014. **5**(1): p. 4673.
20. Zhu, Z.Y., Y.C. Cheng, and U. Schwingenschlogl, *Giant spin-orbit-induced spin splitting in two-dimensional transition-metal dichalcogenide semiconductors*. Physical Review B, 2011. **84**(15): p. 153402.
21. Dhakal, K.P., et al., *Confocal absorption spectral imaging of MoS₂: optical transitions depending on the atomic thickness of intrinsic and chemically doped MoS₂*. Nanoscale, 2014. **6**(21): p. 13028-13035.

22. Castellanos-Gomez, A., et al., *Spatially resolved optical absorption spectroscopy of single- and few-layer MoS₂ by hyperspectral imaging*. Nanotechnology, 2016. **27**(11): p. 115705.
23. Klots, A.R., et al., *Probing excitonic states in suspended two-dimensional semiconductors by photocurrent spectroscopy*. Scientific Reports, 2014. **4**(1): p. 6608.
24. Liu, H.-L., et al., *Optical properties of monolayer transition metal dichalcogenides probed by spectroscopic ellipsometry*. Applied Physics Letters, 2014. **105**(20): p. 201905.
25. Lee, C., et al., *Anomalous Lattice Vibrations of Single- and Few-Layer MoS₂*. ACS Nano, 2010. **4**(5): p. 2695-2700.
26. Zhao, Y., et al., *Interlayer Breathing and Shear Modes in Few-Trilayer MoS₂ and WSe₂*. Nano Letters, 2013. **13**(3): p. 1007-1015.
27. Ye, M., et al. *Recent Advancement on the Optical Properties of Two-Dimensional Molybdenum Disulfide (MoS₂) Thin Films*. Photonics, 2015. **2**, 288-307 DOI: 10.3390/photonics2010288.
28. Li, H., et al., *From Bulk to Monolayer MoS₂: Evolution of Raman Scattering*. Advanced Functional Materials, 2012. **22**(7): p. 1385-1390.
29. Kukucska, G. and J. Koltai, *Theoretical Investigation of Strain and Doping on the Raman Spectra of Monolayer MoS₂*. physica status solidi (b), 2017. **254**(11): p. 1700184.
30. Hu, Z., Z.-B. Liu, and J.-G. Tian, *Stacking of Exfoliated Two-Dimensional Materials: A Review*. Chinese Journal of Chemistry, 2020. **38**(9): p. 981-995.
31. Magda, G.Z., et al., *Exfoliation of large-area transition metal chalcogenide single layers*. Scientific Reports, 2015. **5**(1): p. 14714.
32. Nicolosi, V., et al., *Liquid Exfoliation of Layered Materials*. Science, 2013. **340**(6139): p. 1420-+.
33. Zeng, Z., et al., *Single-Layer Semiconducting Nanosheets: High-Yield Preparation and Device Fabrication*. Angewandte Chemie International Edition, 2011. **50**(47): p. 11093-11097.
34. Zhang, W., et al., *Synthesis and sensor applications of MoS₂-based nanocomposites*. Nanoscale, 2015. **7**(44): p. 18364-18378.
35. Park, H., et al., *Exceptionally Uniform and Scalable Multilayer MoS₂ Phototransistor Array Based on Large-Scale MoS₂ Grown by RF Sputtering, Electron Beam Irradiation, and Sulfurization*. ACS Applied Materials & Interfaces, 2020. **12**(18): p. 20645-20652.
36. Shahzad, R., T. Kim, and S.-W. Kang, *Effects of temperature and pressure on sulfurization of molybdenum nano-sheets for MoS₂ synthesis*. Thin Solid Films, 2017. **641**: p. 79-86.
37. Liu, H.F., S.L. Wong, and D.Z. Chi, *CVD Growth of MoS₂-based Two-dimensional Materials*. Chemical Vapor Deposition, 2015. **21**(10-11-12): p. 241-259.
38. Shi, Y., et al., *MoS₂ Surface Structure Tailoring via Carbonaceous Promoter*. Scientific Reports, 2015. **5**(1): p. 10378.
39. Arafat, A., et al., *Atomistic reaction mechanism of CVD grown MoS₂ through MoO₃ and H₂S precursors*. Scientific Reports, 2022. **12**(1): p. 16085.
40. Agrawal, A.V., et al., *Controlled Growth of MoS₂ Flakes from in-Plane to Edge-Enriched 3D Network and Their Surface-Energy Studies*. ACS Applied Nano Materials, 2018. **1**(5): p. 2356-2367.
41. Yu, Y., et al., *Controlled Scalable Synthesis of Uniform, High-Quality Monolayer and Few-layer MoS₂ Films*. Scientific Reports, 2013. **3**(1): p. 1866.

42. Acar, M. and E. Gür, *Sputtered 2D transition metal dichalcogenides: from growth to device applications*. Turkish Journal of Physics, 2021. **45**(3): p. 131-147.
43. Zhao, Z., et al., *Highly sensitive all-polymer photodetectors with ultraviolet-visible to near-infrared photo-detection and their application as an optical switch*. Journal of Materials Chemistry C 2021. **9**(16): p. 5349-5355.
44. Chen, L., et al., *Study on the catalyst effect of NaCl on MoS₂ growth in a chemical vapor deposition process*. CrystEngComm, 2021. **23**(31): p. 5337-5344.
45. Ling, X., et al., *Role of the Seeding Promoter in MoS₂ Growth by Chemical Vapor Deposition*. Nano Letters, 2014. **14**(2): p. 464-472.
46. Campbell, P.M., et al., *Plasma-assisted synthesis of MoS₂*. 2D Materials, 2018. **5**(1): p. 015005.
47. Mouloua, D., et al. *Recent Progress in the Synthesis of MoS₂ Thin Films for Sensing, Photovoltaic and Plasmonic Applications: A Review*. Materials, 2021. **14**, DOI: 10.3390/ma14123283.
48. Samassekou, H., et al., *Viable route towards large-area 2D MoS₂ using magnetron sputtering*. 2D Materials, 2017. **4**(2): p. 021002.
49. Hussain, S., et al. *Large-area, continuous and high electrical performances of bilayer to few layers MoS₂ fabricated by RF sputtering via post-deposition annealing method*. Scientific reports, 2016. **6**, 30791 DOI: 10.1038/srep30791.
50. Jang, H.Y., et al., *One-step H₂S reactive sputtering for 2D MoS₂/Si heterojunction photodetector*. Nanotechnology, 2020. **31**(22): p. 225205.
51. Rigi, V.J.C., M.K. Jayaraj, and K.J. Saji, *Envisaging radio frequency magnetron sputtering as an efficient method for large scale deposition of homogeneous two dimensional MoS₂*. Applied Surface Science, 2020. **529**: p. 147158.
52. Ling, Z.P., et al., *Large-scale two-dimensional MoS₂ photodetectors by magnetron sputtering*. Optics Express, 2015. **23**(10): p. 13580-13586.
53. Stern, C., et al., *Growth Mechanisms and Electronic Properties of Vertically Aligned MoS₂*. Scientific Reports, 2018. **8**(1): p. 16480.
54. Bollinger, M., et al., *One-dimensional metallic edge states in MoS₂*. Physical review letters, 2001. **87**(19): p. 196803.
55. Hernandez Ruiz, K., et al., *Effect of microstructure on HER catalytic properties of MoS₂ vertically standing nanosheets*. Journal of Alloys and Compounds, 2018. **747**: p. 100-108.
56. Cho, S.-Y., et al., *Highly Enhanced Gas Adsorption Properties in Vertically Aligned MoS₂ Layers*. ACS Nano, 2015. **9**(9): p. 9314-9321.
57. Wang, L., et al., *MoS₂/Si Heterojunction with Vertically Standing Layered Structure for Ultrafast, High-Detectivity, Self-Driven Visible–Near Infrared Photodetectors*. Advanced Functional Materials, 2015. **25**(19): p. 2910-2919.
58. Qiao, S., et al., *A vertically layered MoS₂/Si heterojunction for an ultrahigh and ultrafast photoresponse photodetector*. Journal of Materials Chemistry C, 2018. **6**(13): p. 3233-3239.
59. Li, R., et al., *Thermal stability and high-temperature photoluminescence of chemical vapor deposited MoS₂ in different atmosphere*. Journal of Vacuum Science & Technology A, 2022. **40**(5): p. 052201.
60. Castellanos-Gomez, A., et al., *Elastic Properties of Freely Suspended MoS₂ Nanosheets*. Advanced Materials, 2012. **24**(6): p. 772-775.

61. Singh, E., et al., *Atomically Thin-Layered Molybdenum Disulfide (MoS₂) for Bulk-Heterojunction Solar Cells*. ACS Applied Materials & Interfaces, 2017. **9**(4): p. 3223-3245.
62. Voiry, D., et al., *Conducting MoS₂ Nanosheets as Catalysts for Hydrogen Evolution Reaction*. Nano Letters, 2013. **13**(12): p. 6222-6227.
63. Choi, M., et al., *Flexible active-matrix organic light-emitting diode display enabled by MoS₂ thin-film transistor*. Science Advances. **4**(4): p. eaas8721.
64. Wang, T., et al., *MoS₂-Based Nanocomposites for Electrochemical Energy Storage*. Advanced Science, 2017. **4**(2): p. 1600289.
65. Radisavljevic, B., et al., *Single-layer MoS₂ transistors*. Nature Nanotechnology, 2011. **6**(3): p. 147-150.
66. Nabet, B., *Photodetectors: Materials, Devices and Applications*. 2023: Woodhead Publishing.
67. Rehman, A.u., et al., *n-MoS₂/p-Si Solar Cells with Al₂O₃ Passivation for Enhanced Photogeneration*. ACS Applied Materials & Interfaces, 2016. **8**(43): p. 29383-29390.
68. Furchi, M.M., et al., *Mechanisms of Photoconductivity in Atomically Thin MoS₂*. Nano Letters, 2014. **14**(11): p. 6165-6170.
69. Fang, H. and W. Hu, *Photogating in Low Dimensional Photodetectors*. Advanced Science, 2017. **4**(12): p. 1700323.
70. Buscema, M., et al., *Photocurrent generation with two-dimensional van der Waals semiconductors*. Chemical Society Reviews, 2015. **44**(11): p. 3691-3718.
71. Ashcroft, N.W. and N.D.J.A.N. Mermin, *Solid state physics (saunders college, philadelphia, 1976)*. 2010. **166**: p. 87.
72. Nolas, G.S., J. Sharp, and J. Goldsmid, *Thermoelectrics: basic principles and new materials developments*. Vol. 45. 2001: Springer Science & Business Media.
73. Buscema, M., et al., *Large and Tunable Photothermoelectric Effect in Single-Layer MoS₂*. Nano Letters, 2013. **13**(2): p. 358-363.
74. Richards, P.L., *Bolometers for infrared and millimeter waves*. Journal of Applied Physics, 1994. **76**(1): p. 1-24.
75. Casalino, M., et al. *Near-Infrared Sub-Bandgap All-Silicon Photodetectors: State of the Art and Perspectives*. Sensors, 2010. **10**, 10571-10600 DOI: 10.3390/s101210571.
76. Fang, Z. and C.Z.J.I.S.R.N. Zhao, *Recent progress in silicon photonics: a review*. 2012. **2012**.
77. Soref, R.A.J.P.o.t.I., *Silicon-based optoelectronics*. 1993. **81**(12): p. 1687-1706.
78. Rogalski, A., *HgCdTe infrared detector material: history, status and outlook*. Reports on Progress in Physics, 2005. **68**(10): p. 2267.
79. Rogalski, A., *New material systems for third generation infrared photodetectors*. 2008. **16**(4): p. 458-482.
80. Liu, Y., et al., *Two-dimensional transistors beyond graphene and TMDCs*. Chemical Society Reviews, 2018. **47**(16): p. 6388-6409.
81. Xia, F., et al., *Ultrafast graphene photodetector*. Nature Nanotechnology, 2009. **4**(12): p. 839-843.
82. Liu, H., et al., *Phosphorene: An Unexplored 2D Semiconductor with a High Hole Mobility*. ACS Nano, 2014. **8**(4): p. 4033-4041.
83. Island, J.O., et al., *Environmental instability of few-layer black phosphorus*. 2D Materials, 2015. **2**(1): p. 011002.
84. Yin, Z., et al., *Single-layer MoS₂ phototransistors*. ACS nano, 2011. **6**(1): p. 74-80.
85. Lopez-Sanchez, O., et al., *Ultrasensitive photodetectors based on monolayer MoS₂*. Nature Nanotechnology, 2013. **8**(7): p. 497-501.

86. Zhang, W., et al., *High-gain phototransistors based on a CVD MoS₂ monolayer*. *Advanced materials*, 2013. **25**(25): p. 3456-3461.
87. Tongay, S., et al., *Broad-range modulation of light emission in two-dimensional semiconductors by molecular physisorption gating*. *Nano Lett*, 2013. **13**(6): p. 2831-6.
88. Late, D.J., et al., *Hysteresis in single-layer MoS₂ field effect transistors*. *ACS Nano*, 2012. **6**(6): p. 5635-41.
89. Perea-Lopez, N., et al., *CVD-grown monolayered MoS₂ as an effective photosensor operating at low-voltage*. *2D Materials*, 2014. **1**(1): p. 011004.
90. Lee, H.S., et al., *MoS₂ Nanosheet Phototransistors with Thickness-Modulated Optical Energy Gap*. *Nano Letters*, 2012. **12**(7): p. 3695-3700.
91. Choi, W., et al., *High-detectivity multilayer MoS₂ phototransistors with spectral response from ultraviolet to infrared*. *Advanced materials*, 2012. **24**(43): p. 5832-5836.
92. Yu, W.J., et al., *Highly efficient gate-tunable photocurrent generation in vertical heterostructures of layered materials*. *Nature nanotechnology*, 2013. **8**(12): p. 952.
93. Lee, C.-H., et al., *Atomically thin p–n junctions with van der Waals heterointerfaces*. *Nature nanotechnology*, 2014. **9**(9): p. 676.
94. Sinha, S., et al., *Enhanced interlayer coupling and efficient photodetection response of in-situ grown MoS₂–WS₂ van der Waals heterostructures*. *Journal of Applied Physics* 2021. **129**(15): p. 155304.
95. Zhang, K., et al., *Interlayer Transition and Infrared Photodetection in Atomically Thin Type-II MoTe₂/MoS₂ van der Waals Heterostructures*. *ACS Nano*, 2016. **10**(3): p. 3852-8.
96. Sukhovatkin, V., et al., *Colloidal quantum-dot photodetectors exploiting multiexciton generation*. *Science*, 2009. **324**(5934): p. 1542-4.
97. Keuleyan, S., et al., *Mid-infrared HgTe colloidal quantum dot photodetectors*. *Nature Photonics*, 2011. **5**(8): p. 489-493.
98. Konstantatos, G., et al., *Ultrasensitive solution-cast quantum dot photodetectors*. *Nature*, 2006. **442**(7099): p. 180-3.
99. Kufer, D., et al., *Hybrid 2D–0D MoS₂–PbS quantum dot photodetectors*. *Advanced materials*, 2015. **27**(1): p. 176-180.
100. Ra, H.-S., D.-H. Kwak, and J.-S. Lee, *A hybrid MoS₂ nanosheet–CdSe nanocrystal phototransistor with a fast photoresponse*. *Nanoscale*, 2016. **8**(39): p. 17223-17230.
101. Zhang, S., et al., *Ultrasensitive Hybrid MoS₂–ZnCdSe Quantum Dot Photodetectors with High Gain*. *ACS applied materials & interfaces*, 2019. **11**(26): p. 23667-23672.
102. Huo, N., S. Gupta, and G.J.N.I. Konstantatos, *MoS₂–HgTe quantum dot hybrid photodetectors beyond 2 μ m*. *Nano letters*, 2017. **29**(17): p. 1606576.
103. Zhang, X., et al., *Design and Integration of a Layered MoS₂/GaN van der Waals Heterostructure for Wide Spectral Detection and Enhanced Photoresponse*. *ACS Applied Materials & Interfaces*, 2020. **12**(42): p. 47721-47728.
104. Xu, Z., et al., *Monolayer MoS₂/GaAs heterostructure self-driven photodetector with extremely high detectivity*. *Nano Energy*, 2016. **23**: p. 89-96.
105. Guo, J., et al., *Broadband photodetector based on vertically stage-liked MoS₂/Si heterostructure with ultra-high sensitivity and fast response speed*. *Scripta Materialia*, 2020. **176**: p. 1-6.
106. Zhang, K., et al., *Interlayer Transition and Infrared Photodetection in Atomically Thin Type-II MoTe₂/MoS₂ van der Waals Heterostructures*. *ACS Nano*, 2016. **10**(3): p. 3852-3858.
107. Kufer, D., et al., *Hybrid 2D–0D MoS₂–PbS Quantum Dot Photodetectors*. *Advanced Materials*, 2015. **27**(1): p. 176-180.

108. Shin, G.H., et al., *Si–MoS₂ Vertical Heterojunction for a Photodetector with High Responsivity and Low Noise Equivalent Power*. ACS Applied Materials & Interfaces, 2019. **11**(7): p. 7626-7634.
109. Miao, J., et al., *Surface Plasmon-Enhanced Photodetection in Few Layer MoS₂ Phototransistors with Au Nanostructure Arrays*. Small, 2015. **11**(20): p. 2392-2398.
110. Rahmati, B., et al., *Plasmonic improvement photoresponse of vertical-MoS₂ nanostructure photodetector by Au nanoparticles*. Applied Surface Science, 2019. **490**: p. 165-171.
111. Wang, W.Y., et al., *Hot Electron-Based Near-Infrared Photodetection Using Bilayer MoS₂*. Nano Letters, 2015. **15**(11): p. 7440-7444.
112. Awang, Z., *Gas sensors: A review*. Sens. Transducers, 2014. **168**(4): p. 61-75.
113. Chen, X., et al. *Nanostructured Gas Sensors: From Air Quality and Environmental Monitoring to Healthcare and Medical Applications*. Nanomaterials, 2021. **11**, DOI: 10.3390/nano11081927.
114. Tian, X., et al., *Recent advances in MoS₂-based nanomaterial sensors for room-temperature gas detection: a review*. Sensors & Diagnostics, 2023.
115. Zhang, J., et al., *A review on two-dimensional materials for chemiresistive- and FET-type gas sensors*. Physical Chemistry Chemical Physics, 2021. **23**(29): p. 15420-15439.
116. Yue, Q., et al., *Adsorption of gas molecules on monolayer MoS₂ and effect of applied electric field*. Nanoscale Research Letters, 2013. **8**(1): p. 425.
117. Cho, B., et al., *Charge-transfer-based Gas Sensing Using Atomic-layer MoS₂*. Scientific Reports, 2015. **5**(1): p. 8052.
118. Kumar, R., et al., *Highly selective and reversible NO₂ gas sensor using vertically aligned MoS₂ flake networks*. Nanotechnology, 2018. **29**(46): p. 464001.
119. Barbosa, M.S., et al., *Investigation of electronic and chemical sensitization effects promoted by Pt and Pd nanoparticles on single-crystalline SnO nanobelt-based gas sensors*. Sensors and Actuators B: Chemical, 2019. **301**: p. 127055.
120. Li, W., et al. *Highly Sensitive NO₂ Gas Sensors Based on MoS₂@MoO₃ Magnetic Heterostructure*. Nanomaterials, 2022. **12**, DOI: 10.3390/nano12081303.
121. Singh, S., S. Raj, and S. Sharma, *Ethanol sensing using MoS₂/TiO₂ composite prepared via hydrothermal method*. Materials Today: Proceedings, 2021. **46**: p. 6083-6086.
122. Liu, Z., et al., *A 2D/2D/2D Ti₃C₂Tx@TiO₂@MoS₂ heterostructure as an ultrafast and high-sensitivity NO₂ gas sensor at room-temperature*. Journal of Materials Chemistry A, 2022. **10**(22): p. 11980-11989.
123. Dutta, S., *A review on production, storage of hydrogen and its utilization as an energy resource*. Journal of Industrial and Engineering Chemistry, 2014. **20**(4): p. 1148-1156.
124. Singh, P.P., N. Nirmalkar, and T. Mondal, *Catalytic steam reforming of simulated bio-oil for green hydrogen production using highly active LaNixCo_{1-x}O₃ perovskite catalysts*. Sustainable Energy & Fuels, 2022. **6**(4): p. 1063-1074.
125. Cracknell, R.F., et al., *Safety Considerations in Retailing Hydrogen*. SAE Transactions, 2002. **111**: p. 922-926.

Chapter 2: Fabrication and characterization techniques

This chapter briefly reviews the fabrication and characterization techniques used to deposit and characterize 2D MoS₂. Several characterization tools are employed to analyze the structural, morphological, and optical properties of MoS₂. RF magnetron sputtering and chemical vapor deposition (CVD) are used to synthesize MoS₂ flakes in the present work. The structural, morphological, and compositional properties of MoS₂ are investigated by XRD, SEM, and EDS. The optical properties are studied using Raman, PL, and UV-Vis-NIR spectroscopy. The chemical, elemental, and electronic properties of MoS₂ are explored using X-ray photoelectron spectroscopy (XPS) and ultraviolet photoelectron spectroscopy (UPS). Finally, the device fabrication and measurement techniques used to investigate the performance of photodetector and gas sensors are discussed.

2.1 Deposition techniques

2.1.1 Magnetron sputtering

Sputtering is a physical vapor deposition technique that involves the ejection of atoms from the target material through the bombardment of energetic ions. It is a widely used technique for depositing thin films on various substrates in a scalable manner. Figure 2.1 provides a schematic representation of the sputtering system, which includes a deposition chamber that is evacuated to low-pressure or high vacuum using a turbo molecular pump system backed by a roughing rotary pump. Once a high vacuum (10⁻⁶ torr) is achieved, a controlled amount of inert Ar gas is introduced into the sputtering chamber, and a high negative potential is applied to the target. The stray electrons in the chamber are accelerated and collide with the Ar gas, leading to ionization of the gas atoms and plasma formation. Positively charged Ar ions accelerate towards the cathode (target) and collide with the target atoms, causing ejection or sputtering of atoms through momentum transfer. These ejected atoms have enough kinetic energy to travel through the chamber and reach the substrate, forming a thin film [1].

Magnetron sputtering enables plasma confinement due to the strong magnetic and electric fields. Electrons in the magnetic field follow a helical path around the magnetic field lines, increasing the ionization of gas neutrals near the target surface. This increased plasma density leads to a higher deposition rate [1]. There are two kinds of sputtering: direct current (DC) sputtering and radio frequency (RF) sputtering. In DC sputtering, the target is connected to a direct DC power supply to produce plasma. It creates a static electric field and accelerates the electrons away from the target (cathode). The accelerated electrons by this static electric field

ionize the inert gas atoms. The positive ions striking the target surface erode the target material and the sputtered atoms get deposited on the substrate. DC sputtering cannot deposit insulating and ceramic materials due to the formation of space charge regions that repels incoming Ar ions and cause loss of plasma [2].

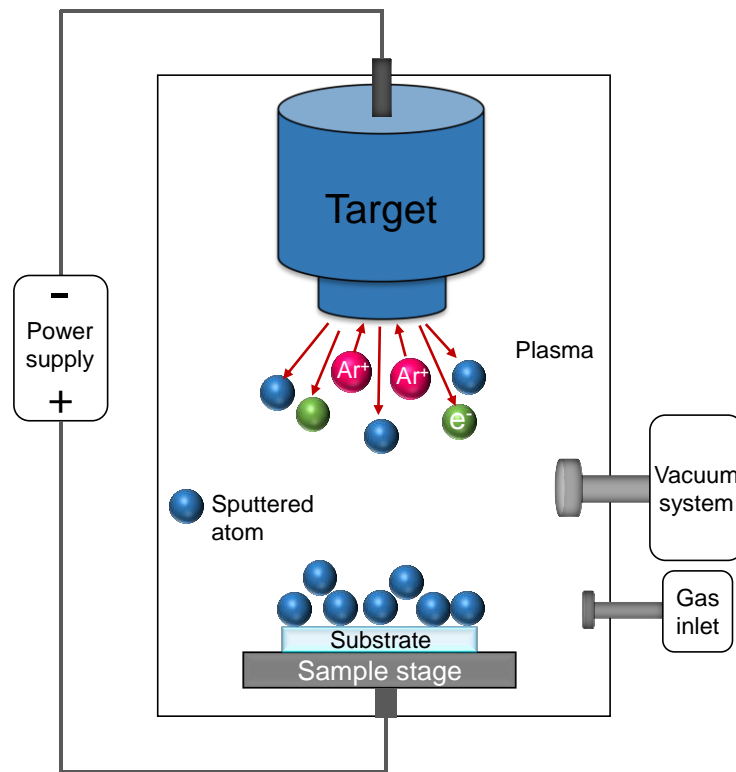


Figure 2.1 Schematic illustration of the sputtering system.

Instead of a DC power source, RF sputtering operates using an alternative voltage of radio frequency (RF, 13.56 MHz). This is not limited to depositing metals, as insulating and semi-insulating materials can also be deposited using RF sputtering [2]. During the first half of the negative RF cycle, positive Ar ions are accelerated towards the cathode (or target), while during the next positive half cycle, electrons are accelerated towards the target. As a result, the target acts as a cathode during the negative half cycle and as an anode during the positive half cycle, neutralizing the charged surface. The cathode and anode change their polarity on each cycle. The electrons have higher mobility than the ions and reach the target faster. Thus, the target acts as an anode for a shorter duration than a cathode. The ions ejected from the target settle on the substrate surface, forming a thin film. These ions then ejected atoms from the target, which settle on the substrate surface, forming a thin film.

In this study, MoS₂ is deposited via RF magnetron sputtering (Excel instruments). The system is attached to a rotary pump (FD20) manufactured by Hind High Vacuum Technologies, India, and a Pfeiffer Turbo Molecular Pump (HiPace 700) to evacuate the pressure of 10⁻⁷ Torr. To monitor the vacuum status of the chamber, a low vacuum Pirani gauge and a high vacuum penning gauge were attached to the chamber. To achieve high temperatures (up to 700 °C), the sputtering chambers were equipped with a heater arrangement connected to a proportional integral derivative (PID) controller. To deposit uniform and high-quality films, a heater assembly was connected to a DC motor, which rotated the sample stage. The sample stage was capable of comfortably holding a 2-inch wafer substrate. The sputtering system used in the present thesis work and the real-time image of MoS₂ plasma are provided in Appendix I (Figure AI.1).

2.1.2 Chemical vapor deposition

Chemical vapor deposition (CVD) is a widely used technique for synthesizing 2D materials or thin films. It involves the chemical reaction of gas-phase precursors that leads to the formation of thin films on a heated substrate [3]. Despite different types of CVD, the fundamental process remains the same and involves a series of common elementary steps. Figure 2.2 presents a schematic representation of the working principle of CVD. Initially, the reactant gases (represented as blue balls) are transported into the reaction chamber (step 1). Then, reactant gases can follow two possible routes. The first one involves direct diffusion of the reactant gases through the boundary layer (step 2) where they can then adsorb to the substrate (step 3). The second one involves homogeneous gas-phase reactions, resulting in the formation of intermediate reactants (green balls) and gaseous by-products (pink balls) (step 4). These intermediate reactants and reactant gases can then be deposited onto the substrate via diffusion (step 2) and adsorption (step 3). In both cases, the reactant gases and intermediate reactants attach to the heated substrate surface and diffuse along its surface. The subsequent gas-solid heterogeneous reactions (step 5) give rise to the formation of a continuous thin film through nucleation, growth, and coalescence, as well as the production of reaction by-products. Finally, any remaining unreacted species and gaseous products are removed from the reaction zone via desorption (step 6). Gas-phase reactions occur when the temperature is high enough, while heterogeneous reactions rely on the surface catalysis of the underlying substrate during the deposition reaction.

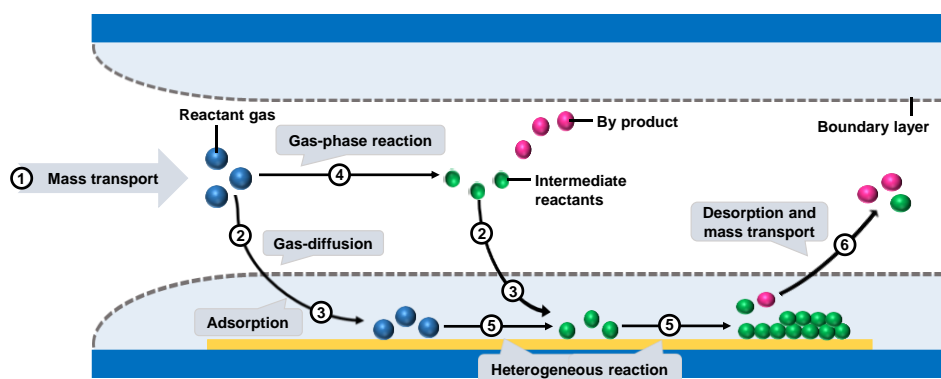


Figure 2.2 Schematic representation of common elementary steps of the CVD process

In this study, we utilized atmospheric pressure chemical vapor deposition (APCVD), which operates at atmospheric pressure and does not require any vacuum environment. The APCVD system is equipped with three independent heating zones, each with its own temperature profile controlled by a PID controller, capable of reaching temperatures up to 1100 °C. A large quartz tube with a diameter of 55 mm and a length of 900 mm is employed as the reaction chamber for depositing MoS₂ during this thesis work. The APCVD setup utilized in this study is provided in Appendix I (Figure AI.2).

2.2 Characterization techniques

During this study, various characterization tools were utilized to investigate the structural, physical, chemical, optical, and electrical properties of MoS₂. This section presents a concise overview of these tools and their associated mathematical models.

2.2.1 X-ray diffraction

X-ray diffraction (XRD) is a widely used technique for determining the crystal structure and lattice parameter of crystalline solids and thin films. XRD also provides valuable information about the stress/strain, phase, and crystallite size of the materials being analyzed. The XRD system typically includes three main components: an X-ray source, a sample stage, and a detector [4]. When a crystalline material is irradiated with X-rays, the electrons of the atoms in the crystal lattice interact with the light waves and undergo constructive interference at a specific angle, known as the Bragg condition. This can be expressed as $2d \sin \theta = n\lambda$, where d is the interplanar spacing, n is the order of reflection, λ is the wavelength of the X-ray source, and θ is the angle of incidence with respect to the crystal planes. In this study, the grown MoS₂ films were characterized using a multipurpose diffractometer (PANalytical X-pert pro) equipped with high-intensity CuK α (0.1504 nm) radiation. A Cu X-ray source was used with

an operating voltage of 45 kV and a current of 40 mA in the Bragg-Brentano high-resolution configuration. The resulting XRD spectrum of MoS₂ was compared to a standard dataset provided by the Joint Committee of Power Diffraction Standards (JCPDS) for MoS₂ (card number- 371492).

2.2.2 Scanning electron microscope and Energy Dispersive X-ray

The Scanning Electron Microscope (SEM) is an extensively used tool for analyzing the morphological structure of materials and conducting in-depth inspections of micro-scale objects. SEM is typically equipped with Energy Dispersive X-ray (EDX) detectors, which allow for the examination of the local elemental composition of thin films. When a sample is subjected to a high-energy electron beam in the SEM, various signals are collected from the sample as a result of the interaction [5]. Figure 2.3 illustrates the interaction volume generated within the sample due to the incident electron beam. This volume can range from 100 nm to 5 μm , depending on the energy of the incident electrons and the sample material. The interaction leads to the production of X-rays, Auger electrons, secondary electrons, and backscattered electrons, which can be detected by various components of the SEM. The secondary electron detector collects surface topography information, while the backscattered electron detector provides elemental composition information [6]. For the present thesis work, a NOVA NANOSEM integrated with an EDX system is utilized to image MoS₂ flakes.

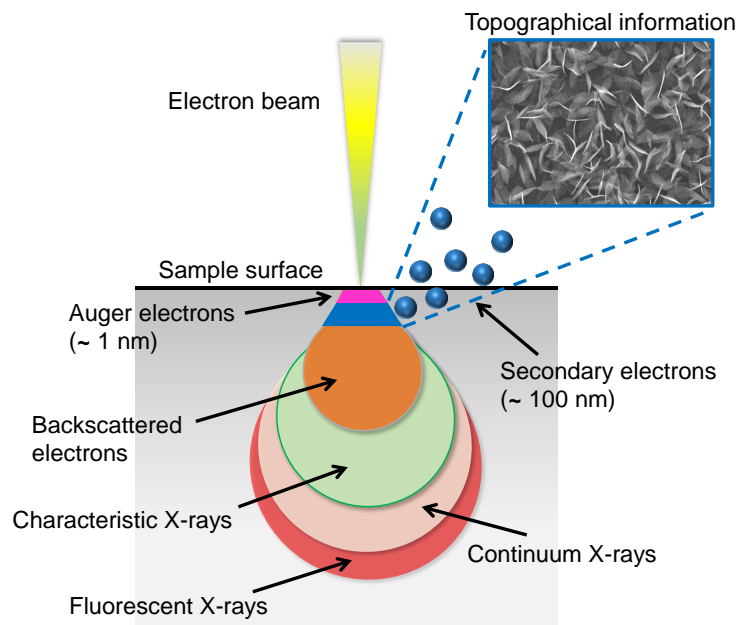


Figure 2.3 Schematic representation of the interaction volume resulting from the interaction between the primary electron beam and sample.

2.2.3 Raman spectroscopy

Raman spectroscopy is a powerful and non-destructive analytical technique used to obtain detailed information about the chemical composition, structure, phase, and polymorphs of the investigated material. It allows the interaction between incident light and the chemical structure of the material. When the light interacts with the material, the majority of the photons get scattered with the same wavelength as the incident light, which is referred to as Rayleigh (elastic) scattering. However, a small number of photons scatter at different wavelengths, which is known as Raman (inelastic) scattering [7]. The energy difference between the incident and scattered photons is referred to as the Raman shift and provides valuable insight into the vibrational modes and energies of the atoms and molecules in the sample. Stoke's scattering occurs when the scattered photons have less energy than the incident photons, while anti-Stoke scattering occurs when the scattered photons have higher energy than the incident photon as shown in Figure 2.4.

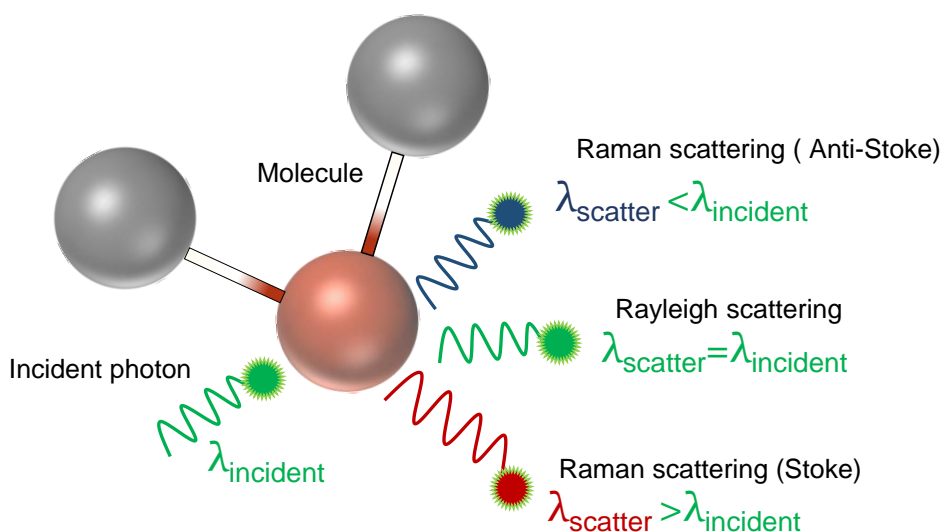


Figure 2.4 Schematic illustration of the light interaction with the molecule depicting Rayleigh and Raman scattering.

XRD solely is not sufficient to accurately identify the phase of MoS_2 , as different crystal structures of MoS_2 (such as the 2H and 1T phases) have similar XRD patterns [8]. However, the MoS_2 phase can be precisely determined using Raman spectroscopy, which is sensitive to rotational and vibrational modes. In this study, Raman scattering measurements were conducted using a LabRAM Horiba scientific instrument, with an excitation laser of 532 nm.

2.2.4 Photoluminescence spectroscopy

PL spectroscopy is a non-destructive technique that is widely used to investigate the optical properties of materials. When light is directed onto a material, photoexcitation occurs, causing electrons to become excited and subsequently de-excite to the ground state. This process leads to the emission of photons (radiative transition) and phonons (non-radiative transitions), resulting in the emission of light or luminescence energy known as PL [7]. The energy released during band-to-band transitions corresponds to the bandgap of the material.

In this study, we recorded PL spectra at room temperature using a micro-PL/Raman system (LabRAM Horiba scientific). The samples were excited with a laser source of wavelength 532 nm, and signals were collected in reflection mode by a 100× objective lens. This approach allowed us to obtain valuable information on the electronic and luminescence properties of the materials with minimal damage to the samples.

2.2.5 Ultraviolet-Visible (UV-Vis) spectroscopy

UV-Vis spectroscopy is an optical analytic technique that measures the optical properties of thin films, such as reflectance, transmittance, and absorbance. It determines the intensity of light passing through a sample with respect to the substrate. The intensity of light transmitted through the reference sample is denoted as I_0 while the intensity passing through the target sample is defined as I [9]. If the sample does not absorb light at a particular wavelength, the intensity of the sample beam is the same as the intensity of the reference beam i.e. $I = I_0$. If the sample absorbs light, then $I < I_0$. Transmittance (T) and absorbance (A) can be calculated using the Beer-Lambert law, which is represented by equation (2.1)

$$T = \frac{I}{I_0} \quad \text{and} \quad A = \log \left(\frac{I_0}{I} \right) \quad (2.1)$$

The absorption coefficient (α) for a thin film having a thickness (t) is given by equation (2.2).

$$\alpha = \frac{1}{t} \ln \left[\frac{1}{T} \right] \quad (2.2)$$

The bandgap (E_g) can be calculated by equation (2.3),

$$(\alpha h\nu)^2 = A (h\nu - E_g) \quad (2.3)$$

Here h is Planck's constant and $h\nu$ is the photon energy. The graph between $(\alpha h\nu)^2$ vs. $h\nu$ is known as Tauc plot. The bandgap of the material is evaluated by linear extrapolation of $(\alpha h\nu)^2$ vs. $h\nu$ curve on the energy ($h\nu$) axis. However, several sources of error can affect the accuracy of this method. One critical consideration is selecting an appropriate energy range for the intercept. In Tauc's plot, the linear portion corresponds to the absorption edge, and the intercept represents the bandgap energy. It is essential to choose an energy range where the data points exhibit linearity and avoid regions with non-linear behavior. Including non-linear data can introduce errors and inaccuracies in determining the bandgap. Deviation from linearity in the linear portion of Tauc's plot can introduce errors, even with a slight deviation. Various factors, such as impurities, defects, or scattering effects in the material can cause these deviations. It is necessary to carefully assess the linearity of the plot and exclude data points that significantly deviate from the linear trend. Additionally, other systematic errors in the experimental data can affect the accuracy of determining the bandgap using Tauc's plot. These errors may arise from instrumental limitations, sample preparation techniques, or uncertainties in measuring the absorption coefficient.

In this study, the Shimadzu UV-2450 spectrometer (Agilent Technologies, US) and Perkin Elmer Lambda 950 UV-Vis-NIR spectrophotometer were used to measure the optical absorbance of MoS₂ and other materials such as ReS₂ and Ga₂O₃.

2.2.6 X-ray photoelectron spectroscopy and Ultra-violet photoelectron spectroscopy

XPS is a surface-sensitive technique based on the photoelectric effect used to study the chemical composition of a material. In XPS, a sample is irradiated with soft X-rays, which causes the emission of electrons from the surface of the material. These emitted electrons are then collected and measured using an electron energy analyzer to determine their kinetic energy and intensity. The emitted photoelectron is the result of the complete transfer of the X-ray energy to a core-level electron. The kinetic energy of the emitted electrons is related to the chemical state of the elements present in the sample, which allows the identification and quantification of elements present in the sample. The binding energy of these ejected photoelectrons is determined by equation (2.4).

$$BE = h\nu - K.E - \phi \quad (2.4)$$

Here, ϕ , $K.E$, $h\nu$, and BE represents the work function of the spectrophotometer, kinetic energy, photon energy, and binding energy, respectively [10, 11].

The average penetration depth for XPS is around 5-10 nm. Therefore, Ar ion etching is performed to clean the sample surface and remove any surface contamination. The ion gun is used to etch the sample surface and obtain XPS spectra. To probe the interface, XPS depth profile is performed by combining a series of etching cycles, providing the chemical information from top to bottom layer. In contrast to XPS, UPS uses lower-energy photons that are restricted to the valence band region. UPS employs a gas discharge lamp filled with helium to generate ultraviolet photons. UPS explicitly measures the density of states in the valence band, Fermi-level edge, and electronic work function of the material [11]. In this study, XPS measurements were performed using ThermoFisher Scientific: Nexsa base employing Al K α X-rays ($h\nu = 1486.86$ eV), under an ultrahigh vacuum chamber. UPS measurements were performed using a He (I) discharge lamp ($h\nu = 21.2$ eV).

2.2.7 Kelvin probe force microscopy (KPFM)

KPFM is an advanced scanning probe microscopy technique that offers high-precision measurement of local variations in the work function of a material with nanometer resolution. The technique operates in non-contact mode and can quantify the contact potential difference (CPD) between the tip and the sample. The local contact potential difference (LCPD) between the tip and the sample is affected by short-range forces between them [12]. KPFM can detect and map these variations in LCPD, providing valuable information about the material's electrical properties. KPFM works by aligning the Fermi levels of the sample and the tip as they approach each other, resulting in electron flow from one material to the other. This causes an offset in the vacuum levels and induces a CPD between the sample and the tip. Fig. 2.6 (a) shows the energy level alignment between the tip and sample when there is no electrical contact. Fig. 2.6 (b) illustrates the Fermi level alignment and offset in the vacuum levels after an electrical contact. The contact potential difference (VCPD) is calculated by equation (2.5),

$$V_{CPD} = \frac{\phi_t - \phi_s}{q} \quad (2.5)$$

Here, q is the elementary charge, ϕ_t and ϕ_s are the tip and sample work function. The induced V_{CPD} generates an electrical force that can be nullified by applying a DC voltage of opposite polarity between the tip and sample, as depicted in Figure 2.5 (c). This nullified voltage equals the difference in the work function of the tip and sample, allowing for evaluation of the sample's work function if the tip's work function is known [12].

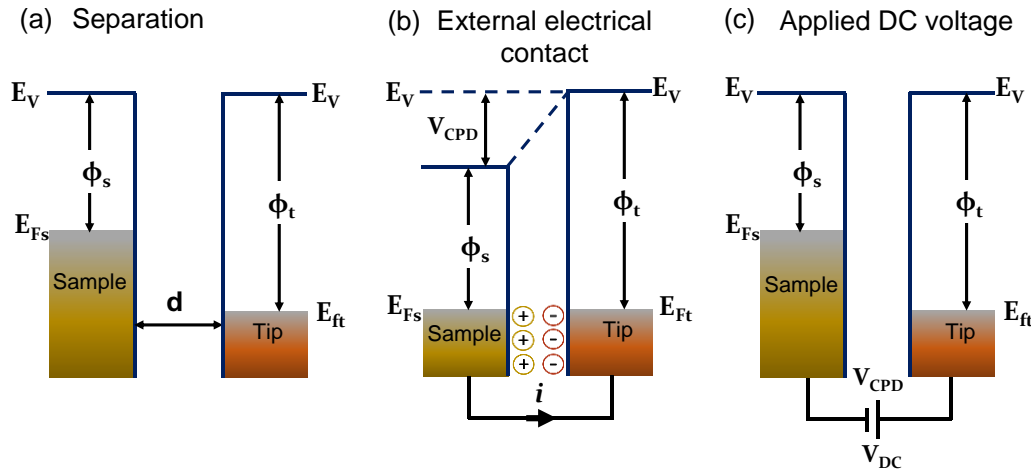


Figure 2.5 Schematic representation of band alignment between the sample and the tip in a typical KPFM set-up under different conditions. (a) Non-contact (b) External electrical contact (c) Applied DC voltage.

In the present work, an Agilent 5500 scanning probe microscopy was used to take the atomic force microscopy (AFM) images. KPFM measurements were performed by amplitude modulation using a Budget Sensors Cr/Pt coated Multi 75-EG tip. The Force constant was 3 Nm^{-1} and the tip resonance frequency was 75 kHz, respectively. The electrostatic force between the tip and sample was induced by the electrical oscillation of the tip, which was nullified by a DC offset to the scanning tip. A Dolan-Jenner MI-150 Fiber Optic Illuminator was used for KPFM measurement under illumination.

2.3 Device fabrication and characterization

2.3.1 Metal electrode deposition through the thermal evaporator

Thermal evaporation is a physical vapor deposition technique that is commonly used for depositing metal contacts. During the process, the substrate is placed upside down in the sample holder within the chamber and alumina-coated Mo boats are used to evaporate the metal. The boats are heated by passing high-current through them via a step-down transformer, causing the metal to evaporate and deposit onto the substrate, forming electrodes. To ensure high-quality electrode deposition, it is important to achieve a high vacuum ($\sim 10^{-6}$ - 10^{-7} hPa) environment in the chamber. This helps to prevent contamination from background gases and moisture and offers a large mean-free path, thereby preventing collisions between molecules and enabling direct collisions of metal atoms with the substrate. The high vacuum in the evaporation chamber is attained using a Pfeiffer rotary pump and Turbo Molecular Pump (HiPace 80) of an excel instrument. The thickness of the deposited metal can be controlled

precisely, typically ranging from a few nanometers to microns. The geometry and dimensions of the deposited electrodes are determined by the shadow mask used during deposition. In the present thesis work, two different physical shadow masks were used, as shown in Figure 2.6.

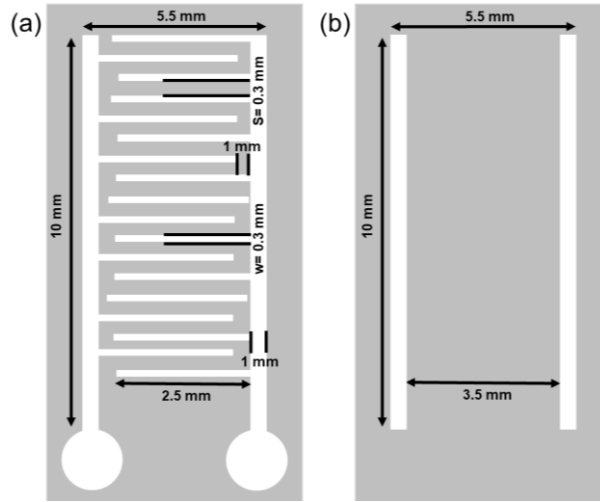


Figure 2.6 Physical shadow mask used for electrode deposition. (a) Interdigitated mask (b) Striped mask.

2.3.1 Photodetector measurement

The performance of the MoS₂-based photodetectors that were fabricated was evaluated through photoresponse testing, which was conducted using the Bentham (PVE 300) equipped with a monochromator (TMC 300), 75 W xenon and 100 W quartz halogen lamps, a lock-in amplifier, and a chopper that was connected to a sub-femtoamp sensitive Keithley-6430 SMU. The schematic representation of the monochromator setup is depicted in Figure 2.7, whereas the actual experimental setup is displayed in Appendix I (Figure AI.3). The monochromator was utilized to measure the photodetector responses in the wavelength range of 400-1200 nm. The optical power of different incident wavelengths was calibrated using a standard Si (model: DH_Si_29987)/Ge (model: DH_Ge_5) photodiode. The UV wavelength regime measurements were performed using a handheld UV lamp with dual wavelengths of 254 nm and 365 nm, and an intensity of 17 $\mu\text{W}/\text{cm}^2$. Additionally, red/green lasers (HOLMARC, intensity: 5 mW/cm^2) and a pen-ray UV lamp (intensity: 4 mW/cm^2) were utilized to evaluate photodetector measurements in the present study. All the device measurements were carried out under ambient conditions in an optically enclosed chamber to avoid any hindrance from the outside source.

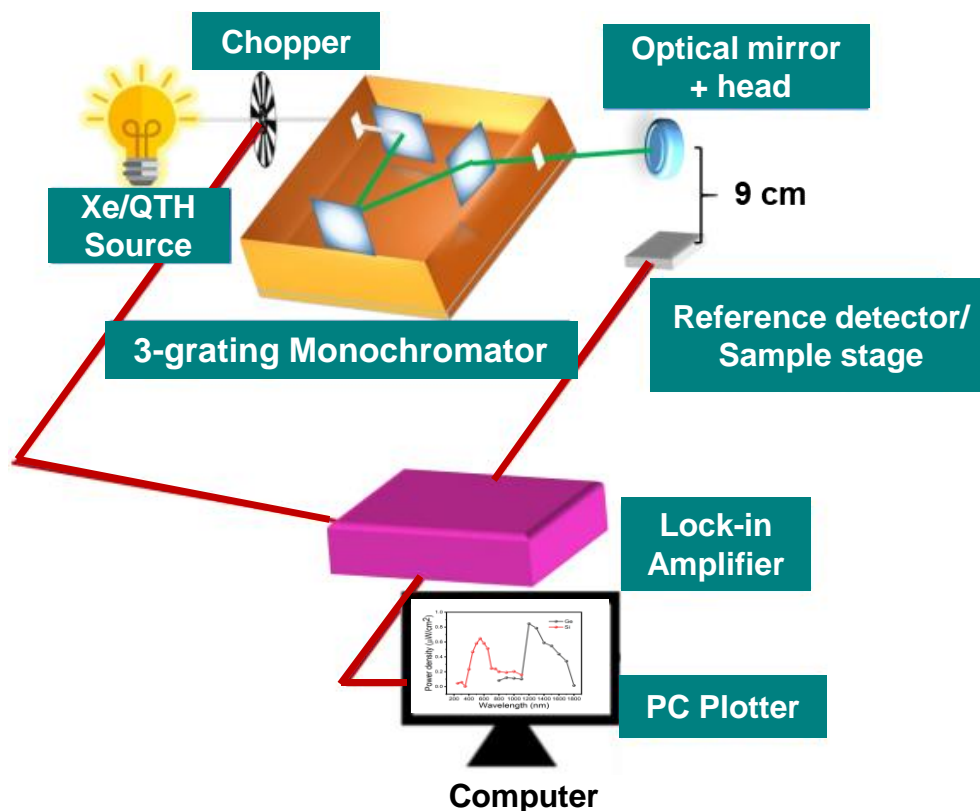


Figure 2.7 Schematic illustration of the experimental setup used to measure spectral response of MoS₂ based photodetectors.

2.3.2 Gas sensing measurement

Gas-sensing measurements were performed in a vacuum-sealed chamber to eliminate any interference from external gases. The fabricated sensing device was placed on a sample stage within the chamber and two probes were connected to the sample stage to enable electrical measurements. The temperature of the sample stage was controlled using a PID controller to maintain a constant temperature throughout the experiment. Sensor performance was evaluated using a computer-controlled Keithley-4200 SCS. To introduce the target gas into the sensing chamber, a micro-syringe was used. The volume of the sensing chamber was 3.5 liters, and a known amount of the target gas (in milliliters) was injected into the chamber using the syringe. The gas concentration was calculated using equation (2.6)

$$\text{Gas concentration (ppm)} = \frac{\text{Gas taken in syringe (ml)}}{\text{Volume of sensing chamber (ml)}} \times \text{Gas in cylinder (ppm)} \quad (2.6)$$

Gas sensing measurements were conducted over a broad temperature range from room temperature to 150 °C while maintaining a constant relative humidity. The relative humidity was monitored throughout the experiment using a high-precision humidity sensor (SHT31-

APR, Sensirion AG, Switzerland). The schematic for the gas sensing setup is depicted in Figure 2.8, while the actual experimental setup for sensing measurement is presented in Appendix I (Figure AI.4). This experimental setup allowed for precise control of temperature and humidity conditions during the sensing measurements, enabling accurate evaluation of the sensor's performance.

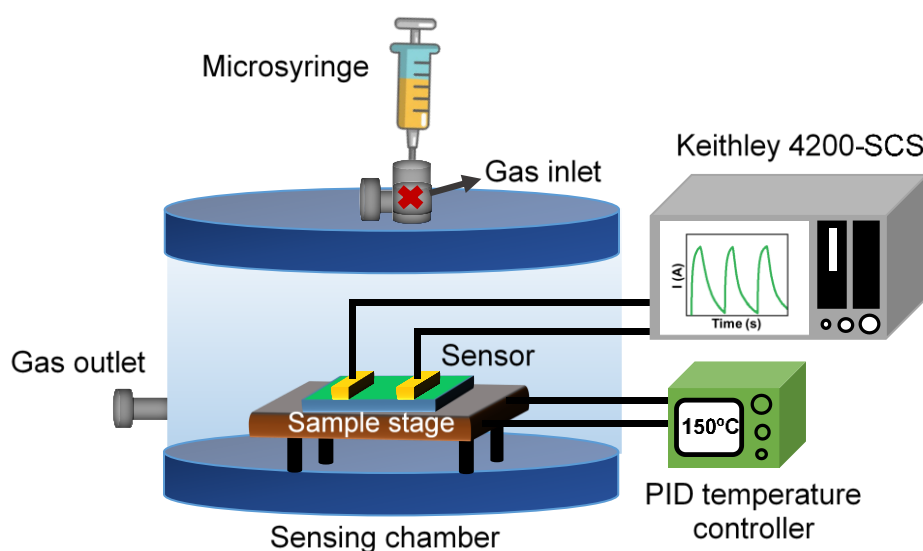


Figure 2.8 Schematic of gas sensing setup.

References

1. Mattox, D.M., *Handbook of physical vapor deposition (PVD) processing*. 2010: William Andrew.
2. Ohring, M., *The materials science of thin films*. Appl. Opt, 1992. **31**(34): p. 7162.
3. Sun, L., et al., *Chemical vapour deposition*. Nature Reviews Methods Primers, 2021. **1**(1): p. 5.
4. Cullity, B. and S. Stock, *Elements of x-ray diffraction*, Prentice Hall. Upper Saddle River, NJ, 2001: p. 388.
5. Dehm, G., J.M. Howe, and J. Zweck, *In-situ electron microscopy: Applications in physics, chemistry and materials science*. 2012: John Wiley & Sons.
6. Akhtar, K., et al., *Scanning electron microscopy: Principle and applications in nanomaterials characterization*. Handbook of materials characterization, 2018: p. 113-145.
7. Perkowitz, S., *Optical characterization of semiconductors: infrared, Raman, and photoluminescence spectroscopy*. 2012: Elsevier.
8. Yao, Y., et al. *MoS₂ Coexisting in 1T and 2H Phases Synthesized by Common Hydrothermal Method for Hydrogen Evolution Reaction*. Nanomaterials, 2019. **9**, DOI: 10.3390/nano9060844.
9. Perkampus, H.-H., *UV-VIS Spectroscopy and its Applications*. 2013: Springer Science & Business Media.
10. Chastain, J. and R.C. King Jr, *Handbook of X-ray photoelectron spectroscopy*. Perkin-Elmer Corporation, 1992. **40**: p. 221.
11. Stevie, F.A. and C.L. Donley, *Introduction to x-ray photoelectron spectroscopy*. Journal of Vacuum Science & Technology A, 2020. **38**(6): p. 063204.
12. Melitz, W., et al., *Kelvin probe force microscopy and its application*. Surface Science Reports, 2011. **66**(1): p. 1-27.

Chapter 3: Large area growth of MoS₂ from in-plane to vertically oriented flakes

In this chapter, the controlled growth of MoS₂ from in-plane to vertically aligned MoS₂ flakes by scalable sputtering technique is discussed in detail. This method offers large-scale production, low cost, and easy controllability, making it suitable for current industrial processes. The MoS₂ films were grown at different growth pressure and time to control the surface morphology from in-plane to highly dense interconnected vertical-oriented flakes. The vertically aligned MoS₂ was also achieved on different substrates such as p and n-doped Si, c-plane sapphire, quartz, and carbon fibre, implying a substrate-independent growth. Moreover, the growth of vertically aligned MoS₂ shows high uniformity and reproducibility and is fabricated on a wafer scale. The detailed morphological, structural, and spectroscopic analysis is carried out to characterize MoS₂ films, reveals the transition from in-plane MoS₂ to vertically aligned MoS₂ flakes. This work paves the way for designing mass production of high-quality 2D materials, which will advance their practical applications by integration into device architectures in various fields.

3.1 Requirement of large area growth of vertically aligned MoS₂ flakes

With the rapid advancement of 2D materials-based technology, a large-scale growth process compatible with industrial requirements is a prerequisite to facilitate the integration of MoS₂ into real-world electronics and catalytic applications. On the laboratory scale, monolayer or few-layer MoS₂ is widely obtained through the mechanical exfoliation method. This exfoliation method produces very good structural quality flakes, as observed from the performance of different kinds of devices [1-4]. However, it is not suitable for large-scale practical applications. The possibility of growing good quality MoS₂ using the chemical vapor deposition (CVD) method can be obtained extensively in large areas to some extent, but this method is not capable to produce continuous films [5, 6]. An effort towards large-area growth of continuous 2D MoS₂ film using CVD creates defective and misaligned arrays at the grain boundaries with colliding triangular flakes, which lowers the quality of the film. [7]. Other growth techniques, such as pulse laser deposition [8], molecular beam epitaxy [9], hydrothermal [10], and atomic layer deposition [11], have been extensively used to grow high-quality layered material. Although, there have been some reports about synthesis of large-area film using these techniques at centimeter-scale [8, 9] or wafer scale [11], the present growth techniques suffer from several issues, such as requirement of ultrahigh vacuum, use of harmful

toxic precursor, high cost, and relatively low quality of the grown film in comparison to other methods mentioned. Alternatively, radio frequency magnetron sputtering is a simple and reliable technique to grow high-quality, large-area MoS₂ film with high repeatability and controllability. The current research is more focused towards synthesizing monolayer and few-layered MoS₂ [5, 12], however, contrary to mono/few layers in-plane MoS₂, vertically aligned MoS₂ offers greater advantages. It has the advantage of a high aspect ratio, more reactive edge-sites, and quick longitudinal intra-layer charge transport, which enhances the electrical and catalytic activity [13, 14]. Hence, more efforts are needed for large-scale growth of vertically aligned edge-enriched MoS₂.

Recently, there have been a few attempts to grow vertically aligned MoS₂ with a large no. of active edges via sputtering [15, 16]. Reported studies suggest that the growth of MoS₂ is greatly influenced by substrate temperature and produces good-quality MoS₂ film at elevated temperatures [17]. Moreover, the vertical growth of MoS₂ is achieved because of the difference in growth rate due to its anisotropy, faster and stepped deposition on the edge directions than in the basal plane [18]. Nevertheless, the reported literature is not focused on growth; rather they showed interest in either improving film crystallinity or utilizing the vertical MoS₂ for the device fabrication with enhanced performance [15-17]. However, proper optimization of the growth parameters is required to achieve various morphological structures of MoS₂ with good crystallinity even at lower temperatures.

3.2 Experimental section

3.2.1 Synthesis of MoS₂

MoS₂ thin films were synthesized by radio frequency magnetron sputtering using a 99.99% pure 2H-MoS₂ target (Kurt J. Lesker). Substrates (Si/SiO₂, Si, *c*-plane sapphire, quartz, carbon fiber) were chemically cleaned prior to deposition by ultrasonication in DI water, acetone, and propanol for 30 minutes each. A base pressure of 2.5×10^{-6} Torr was achieved in a sputtering chamber before the deposition. In this work, two sets of samples have been prepared. The first set of samples was grown under different growth pressure ranging from 3 mTorr to 15 mTorr. The second set of samples was prepared independently at 10 mTorr growth pressure with different growth times (5 min- 30 min) to observe the thickness-dependent characteristics of the grown samples. The substrate temperature and power were kept constant during the deposition at 400 °C and 50 W, respectively.

3.2.2 Characterizations of MoS₂

The surface morphology and cross-sectional view of the grown MoS₂ samples were characterized by FESEM at a working potential of 10 kV. The crystallographic orientation of the films was studied using grazing incident X-ray diffraction (GIXRD) at a fixed incident angle of 1° using PANalytical X-pert pro multipurpose diffractometer with Cu K α ($\lambda = 1.54 \text{ \AA}$) radiation. The Raman measurements of the samples were recorded at room temperature using Horiba LabRAM HR Evolution with an excitation wavelength of 532 nm. Raman mapping was performed to show the uniformity in the deposited MoS₂ film. JMP software was used to map the wafer. The MoS₂ samples were deposited on quartz substrate to measure optical absorbance. The absorption spectra of the films were performed using Perkin Elmer Lambda 950, UV-Vis-NIR spectrophotometer within the wavelength range of 400 nm-1100 nm. The X-ray photoelectron spectroscopy (XPS) measurements were carried out using a Nexa, Thermofisher Scientific system under an ultrahigh vacuum chamber. The system employed monochromatic Al K α X-ray source ($h\nu = 1486.68 \text{ eV}$) with binding energy calibrated with gold (Au), silver (Ag) and copper (Cu) references.

3.2.3 Photodetector fabrication and measurements

For device fabrication, an interdigitated Ag metal contacts (250 nm) were patterned on vertically aligned MoS₂ flakes using shadow mask by thermal evaporator. Photoresponse of the device was evaluated by 532 nm laser (5mW) in optically enclosed chamber to prevent outer light interference, Neutral density filters were used to modulate the intensity of incident laser source. A Keithley 4200 was used to measure the change in current of the device.

3.3 Results and Discussion

To understand the growth dynamics of the MoS₂ films deposited under different growth pressures, thin films were subjected to morphological, chemical, structural, and optical characterizations. Figure 3.1 depicts the FESEM images of MoS₂ films grown at 3 mTorr, 5 mTorr, 10 mTorr and 15 mTorr pressure via magnetron sputtering. It is clearly demonstrated that the morphology is significantly affected by the growth pressure. MoS₂ film deposited at low pressure (3 mTorr) shows a continuous layered structure, whereas nano-worms (5mTorr) and nanowalls (10 mTorr and 15 mTorr) like vertically aligned structures formed at higher growth pressure. [19]. It is observed from the FESEM images that the flake size of MoS₂ grown at a pressure of 10 mTorr is larger than the MoS₂ flakes grown at 15 mTorr. Due to the larger flake size of the 10 mTorr sample, the density of MoS₂ flakes is less as compared to the 15

mTorr sample. The growth of MoS₂ is highly uniform over a large area, which makes it possible to synthesize at the wafer scale.

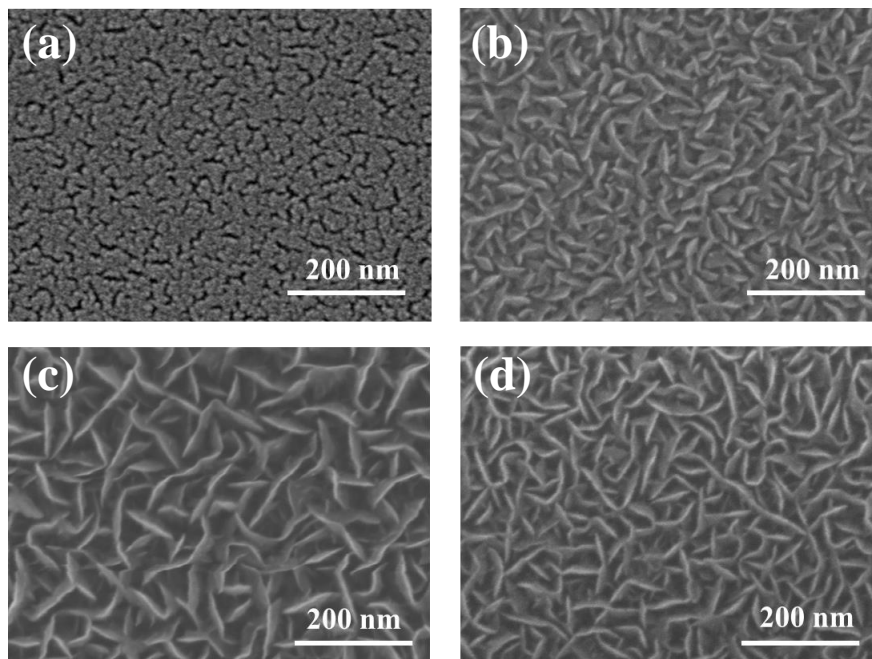


Figure 3.1 FESEM images of MoS₂ films grown at different pressure (a) 3 mTorr (b) 5 mTorr (c) 10 mTorr (d) 15 mTorr.

The Raman spectra of MoS₂ films synthesized at variable pressure are presented in Figure 3.2 (a). The two prominent Raman peaks of MoS₂ appeared at nearly 380 cm⁻¹ and 410 cm⁻¹ corresponding to in-plane (E_{2g}^1) and out of plane (A_{1g}) vibrational modes, respectively [20]. No significant shift in the peak positions of these two modes was observed in the samples grown at different pressure. Notably, no vibrational modes corresponding to MoO₃ or MoO₂ were observed in the Raman spectra, signifying a single 2H MoS₂ phase. The XRD of the films grown under different pressure is also carried out (Figure 3.2 (b)) to study the crystallinity and crystallographic orientation of the prepared sample. The broad hump in the diffraction pattern with no visible sharp peak evidently confirms the amorphous or less crystalline nature of MoS₂ film deposited at 3mTorr growth pressure. Whereas MoS₂ films deposited at 5 mTorr, 10 mTorr and 15 mTorr (Figure 3.2 (b)) exhibit two distinctive peaks at (2θ) around 34° and 59.54° corresponding to the (10 l) ($l=0,1$) and (110) of the 2H MoS₂ phase (JCPDS-37-1492). The turbostratic peak (10 l) that appears in the XRD spectra is attributed to either random S–Mo–S stacking of MoS₂ molecule due to weak bonding between the layers or a shift in the basal planes between layers [21, 22]. The high intensity of the (100) crystal plane indicates better crystallinity and vertical orientation of the flakes to the substrate for the sample deposited at

10 mTorr. Furthermore, the optical absorbance of all the films is also investigated, as displayed in Figure 3.2 (c). The synthesized MoS₂ films exhibit strong absorbance in the visible-NIR regime. The vertical flakes of MoS₂ deposited under 10 mTorr pressure showed larger absorbance than other deposited MoS₂ films due to the large surface area and more exposed edges.

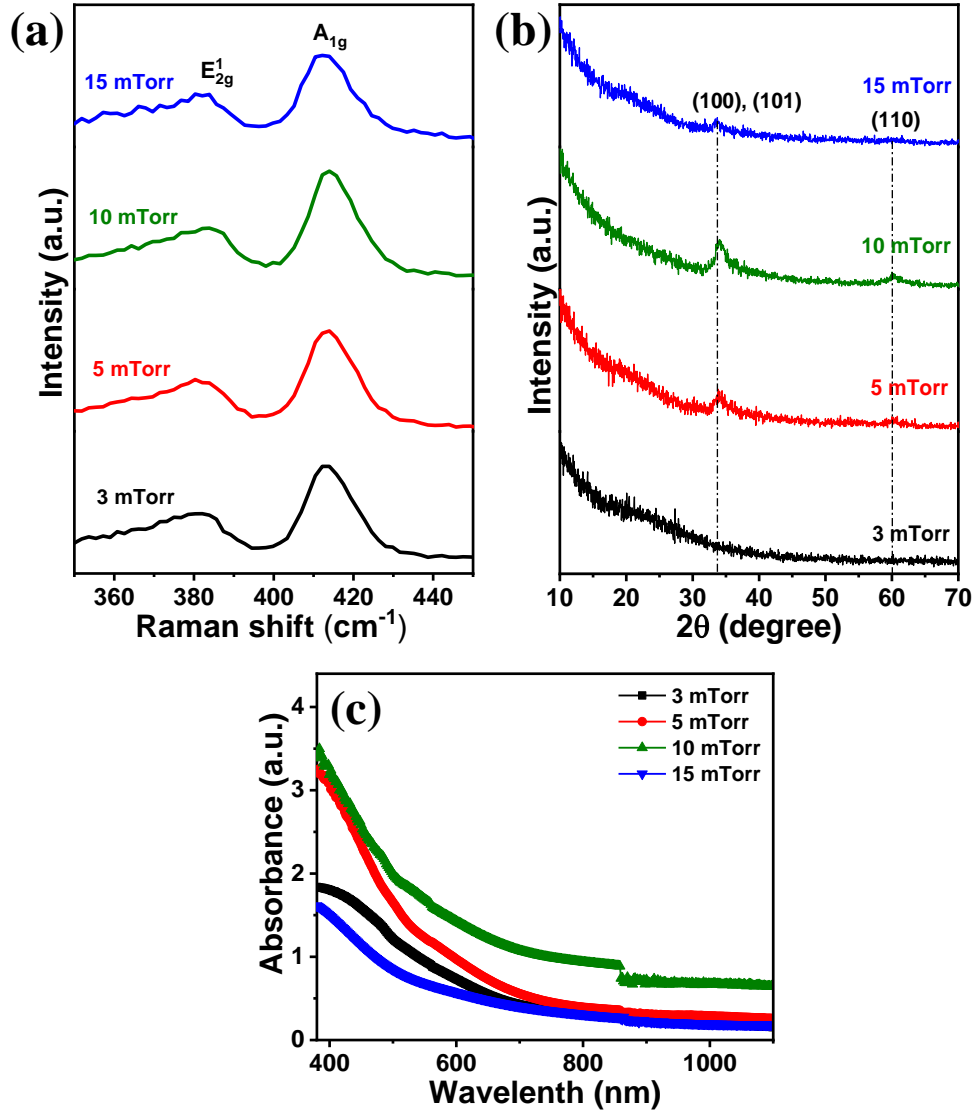


Figure 3.2 (a) Raman spectra and (b) XRD pattern of MoS₂ films grown on Si/SiO₂ substrate at variable pressure varied from 3 mTorr to 15 mTorr and (c) Absorbance spectra of the MoS₂ film grown on quartz at different growth pressure.

The next set of samples is prepared at high growth pressure to investigate the effect of thickness on growth dynamic. During sample depositions, the deposition pressure was kept constant at 10 mTorr and the thickness of the film is varied by varying the deposition time (5 min-30 min). The surface topography and Raman spectra of these time-dependent MoS₂ films are presented in Figure 3.3. The FESEM images of MoS₂ clearly shows that a smooth layered film is formed

initially for the less deposition time (5 and 10 min). As the deposition time increases, the transformation of growth from 2D in-plane to 3D vertical structures starts emerging in the MoS₂ films as bright spots (Figure 3.3 (b)), which provide nucleation for the vertical standing growth. This vertical growth of MoS₂ is further increased with increasing growth time. However, in the beginning, the low curling force at the boundary leads to the formation of highly dense maze-like structure (Figure 3.3 (c)), which eventually grows into large petal-like structures (Figure 3.3 (d)-(f)) over time due to the expansion of the film. Figure 3g shows the cross-sectional view of the vertically aligned MoS₂ flakes (30 min). The height of the exposed edges of the MoS₂ flakes is about 380-420 nm across all regions of the deposited substrate, which can further increase with increasing deposition time.

The surface roughness of the thickness-dependent MoS₂ films is evaluated from atomic force microscopy micrographs. The thin MoS₂ film (5 min) has a low surface roughness of 2.5 nm, confirming the smooth layer-by-layer growth as observed in FESEM. While the surface roughness of the film increases with increasing growth time, as illustrated in Figure 3.3 (h). The transition in MoS₂ growth from in-plane to complete vertical occurs between 10 to 16 min. The samples deposited for a time less than 10 min or at 10 min showed complete planar structure, corroborated by FESEM. The high surface roughness value of the 16 min sample reflects the highly exposed edge-sites of MoS₂.

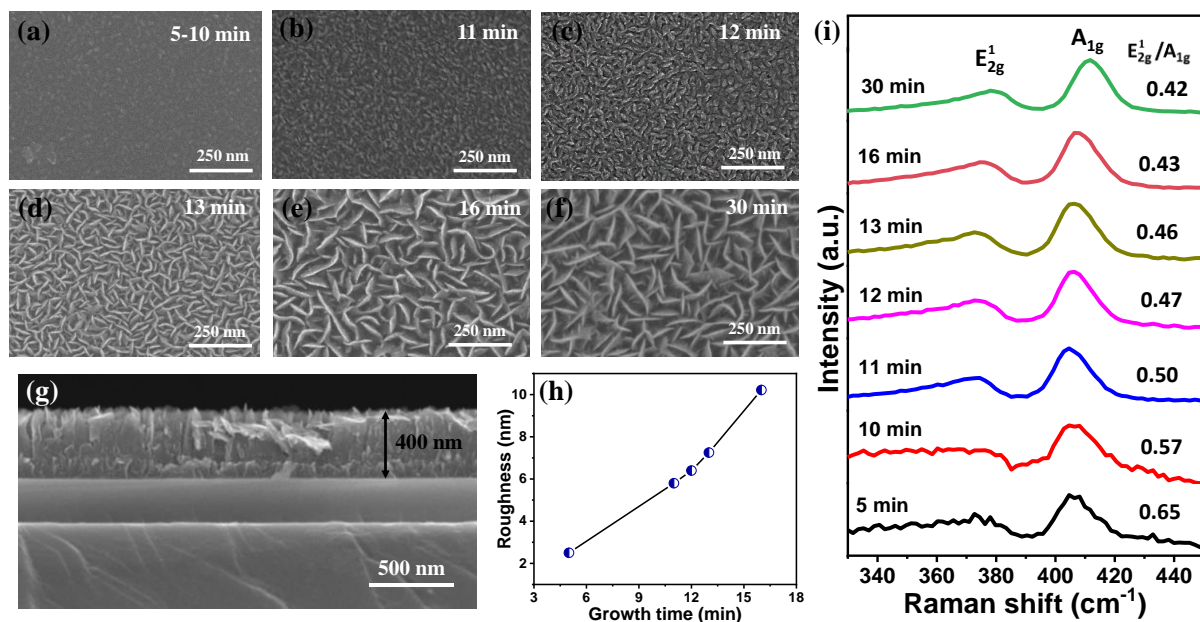


Figure 3.3 FESEM images of MoS₂ films deposited at (a) 5-10 min, (b) 11 min, (c) 12 min, (d) 13 min, (e) 16 min and (f) 30 min. (g) Cross-sectional FESEM image of vertical flakes of MoS₂ deposited for 30 min (h) Surface roughness of MoS₂ films as a function of growth time. (i) Raman measurements plots of MoS₂ films grown at different times.

The Raman measurements of MoS₂ thin films grown on Si/SiO₂ is displayed in Figure 3.3 (i). The MoS₂ films exhibits two characteristics peak at $\sim 376\text{ cm}^{-1}$ and 404 cm^{-1} associated with E_{2g}^1 and A_{1g} vibrational modes, respectively. The characteristics peak of E_{2g}^1 vibrational mode is red-shifted, while the A_{1g} vibrational mode is blue-shifted with increasing deposition time due to the increased number of layers. The intensity ratio of E_{2g}^1/A_{1g} plays an important role in defining the orientation of the exposed MoS₂ sites. Here, the E_{2g}^1 peak arises due to in-plane vibration of Mo and S atoms in opposite direction while A_{1g} peak is attributed to the out of plane vibration of S atom in the opposite direction along c -axis, where Mo atom is held stationary [23]. The vibration of E_{2g}^1 and A_{1g} is preferentially excited by the terrace-site (basal plane) and edge-sites of MoS₂, respectively. Thereby, the intensity arising due to E_{2g}^1 mode represents the in-plane MoS₂, while the intensity corresponding to the A_{1g} mode represents the existence of vertical MoS₂ [24-26]. The intensity ratio of E_{2g}^1/A_{1g} varied from 0.65 to 0.42, which increasing growth time, indicating the dominantly exposed MoS₂ edge-sites for thicker samples.

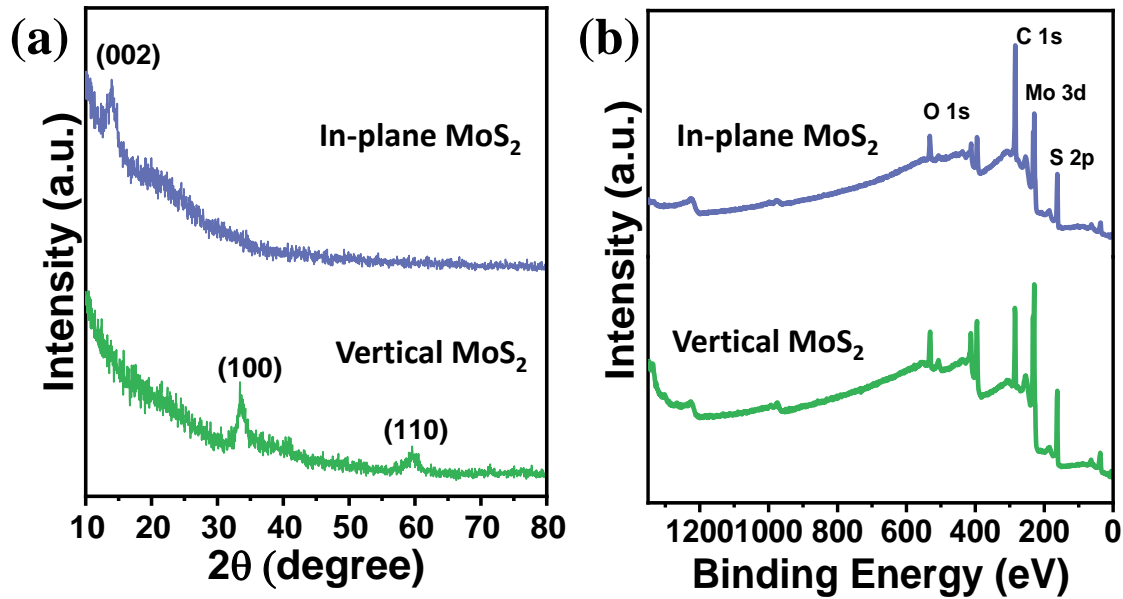


Figure 3.4 (a) XRD spectra and (b) XPS survey scan of sputtered MoS₂, acquired from the sample deposited at 5 min (in-plane MoS₂) and 30 min (vertically aligned MoS₂), respectively.

To gain more insight into the transition from in-plane to vertically oriented MoS₂ structure, we have performed XRD and XPS for the two extreme samples, namely 5 min (in-plane MoS₂) and 30 min (vertically aligned MoS₂). The thin MoS₂ sample (5 min) shows a diffraction peak at 14° corresponding to the (002) plane of 2H-MoS₂, JCPDS-37-1492 (Figure 3.4 (a)). The (002) plane represents the basal plane of MoS₂, suggesting horizontally-aligned exposed edges

of MoS₂ (parallel to the substrate) [27]. In contrast, the thick MoS₂ sample (30 min) exhibits two diffraction peaks at 33.36° and 59.5° corresponding to (100) and (110) planes of MoS₂. The (100) plane is assigned to the edge plane of MoS₂ (crystal structure perpendicular to the basal plane), indicating vertically aligned edges are exposed [13]. This implies that vertical growth of MoS₂ only occurs when the sample is few-layer thick or more. Thus, the XRD analysis is consistent with the results obtained from FESEM and Raman spectroscopy.

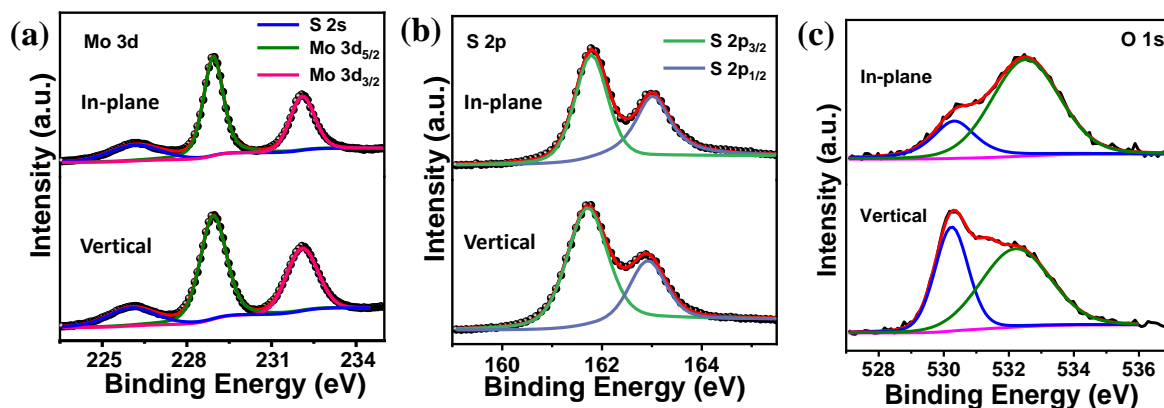


Figure 3.5 High resolution XPS spectra of (a) Mo 3d, (b) S 2p core and (c) O 1s levels, acquired from the sample deposited at 5 min (in-plane MoS₂) and 30 min (vertically aligned MoS₂), respectively.

Further, XPS was performed to investigate the elemental and chemical composition of the MoS₂ surface and to understand the orientation of the deposited MoS₂ films. The full XPS survey spectrum of MoS₂ (Figure 3.4 (b)) has Mo, S, C, and O elements. C and O elements are observed due to surface contamination. The carbon correction was done using an adventitious C1s peak at 284.8 eV. Figure 3.5 (a) and (b) displays high-resolution XPS spectra of Mo 3dS 2p core levels of both in-plane MoS₂ and vertically aligned MoS₂. The Mo 3d core level of MoS₂ splits into two peaks Mo 3d_{5/2} and Mo 3d_{3/2} centred at 228.9 eV and 232.1 eV, respectively, associated with to Mo⁺⁴ oxidation state. The core level of S 2p is de-convoluted into two peaks S 2p_{3/2} and S 2p_{1/2} located at 161.7 eV and 163 eV, respectively, corresponds to S⁻². These binding energy peak positions of Mo 3d and S 2p core levels are the same for both in-plane and vertically aligned MoS₂, confirming the presence of 2H-MoS₂ [28]. However, the full width at half maximum (FWHM) of in-plane MoS₂ and vertically aligned MoS₂ for Mo 3d (0.83 and 1.1, respectively) and S 2p (0.78 and 0.96, respectively) are slightly different. The higher FWHM of vertically aligned MoS₂ compared to in-plane MoS₂ is attributed to more oxygen adsorption at the exposed edge sites of vertically aligned MoS₂ due to its higher surface energy than the exposed basal plane. Furthermore, the adsorption of oxygen in MoS₂ is verified by the O1s peak located at ~ 530.2 eV (Figure 3.5 (c)), corresponding to the binding energy of

oxygen in Mo⁺⁴ O₂, reflecting the existence of Mo-O bond [29]. While the peak located at ~532 eV is attributed to the adsorbed water. The more pronounced peak of O1s near 530 eV in vertically aligned MoS₂ infers more oxygen adsorbed at the edge sites of MoS₂ than the basal plane of MoS₂. The elemental composition of the MoS₂ films is also evaluated. The S: Mo ratio is 1.85 for in-plane MoS₂, while it is 1.54 for vertical MoS₂, corroborating the higher S-vacancy and more adsorption of oxygen at the edges of MoS₂ flakes.

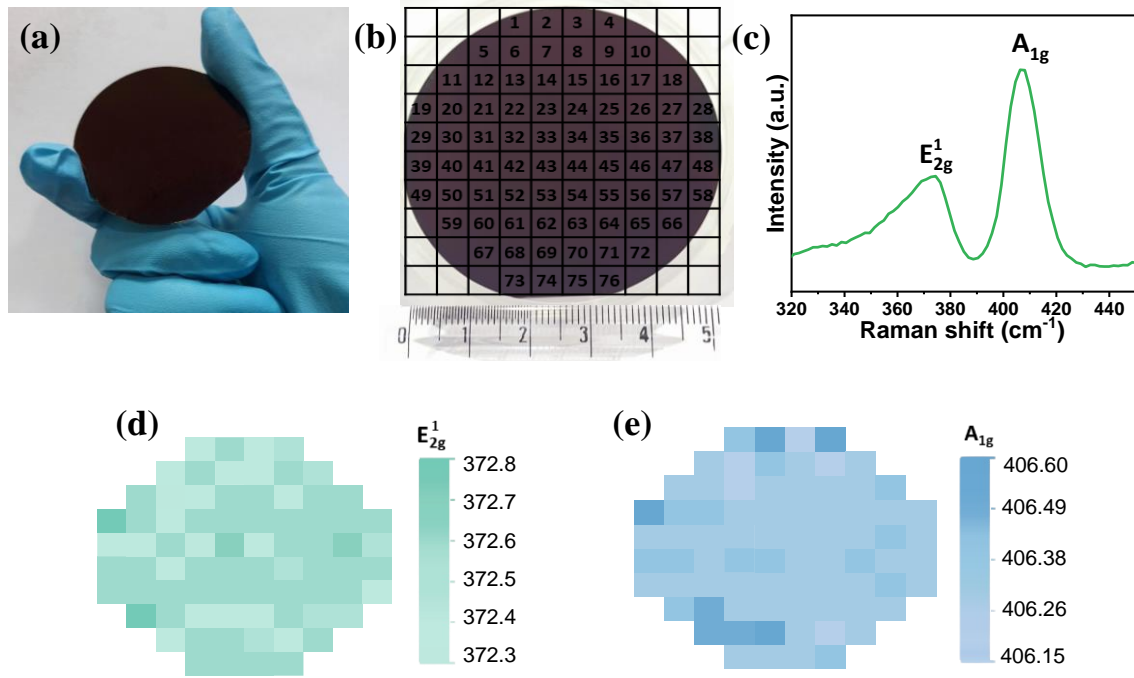


Figure 3.6 (a) As synthesized vertically aligned MoS₂ flakes on 2-inch Si/SiO₂ wafer. (b) Synthesized MoS₂ on 2-inch wafer are divide into 76 units (area-5×5 mm²) for spectral analysis. (c-e) Raman spectra of vertically aligned MoS₂ and its spatial mapping on 76 locations corresponding to E_{2g}^1 and A_{1g} peak position.

The vertically aligned MoS₂ flakes were synthesized on 2-inch Si/SiO₂ wafer substrate under optimized condition (10 mTorr, 16min) in order to show large area growth. A wafer scale spectroscopic analysis was carried out using Raman to demonstrate the uniform growth of MoS₂ over the entire wafer (Figure 3.6). The 5 × 5 mm² unit pixel size was selected for the spatial Raman mapping. A random point within one-pixel area was characterized for mapping. Thus, a total of 76 Raman spectra corresponding to each pixel unit were examined. Figure 5c displays a typical Raman spectrum of vertically aligned MoS₂ representing E_{2g}^1 and A_{1g} characteristics peaks of MoS₂. The Raman data acquired from the 76 different locations on 2-

inch wafer-scale grown MoS₂ depicts the spatial distribution corresponding to E_{2g}^1 and A_{1g} peak (Figure 3.6 (d) and (e)). The peak position of E_{2g}^1 varies from 372.3 to 372.8 cm⁻¹ and the value of A_{1g} peak position ranged from 406.15 to 406.6 cm⁻¹. The low deviation value of the characteristic peak positions confirms the uniform Raman signal. Hence, the synthesized vertically aligned MoS₂ flakes are highly uniform over the entire wafer.

Furthermore, the growth of highly uniform inter-connected vertically aligned MoS₂ flakes under same optimum condition (10 mTorr, 16 min) was repeated on various substrates such as Si, *c*-plane sapphire, quartz and carbon fiber. The prepared MoS₂ films on different substrates were characterized by Raman spectroscopy (Figure 3.7 (a)), which confirms the formation of 2H-MoS₂. The surface morphology of the grown film on different substrate was also investigated using FESEM as displayed in Figure 3.7 (b)-(e). Both Raman and FESEM of MoS₂ flakes clearly demonstrates that the present work is highly reproducible to synthesize large-area vertical MoS₂ flakes even on variable substrate.

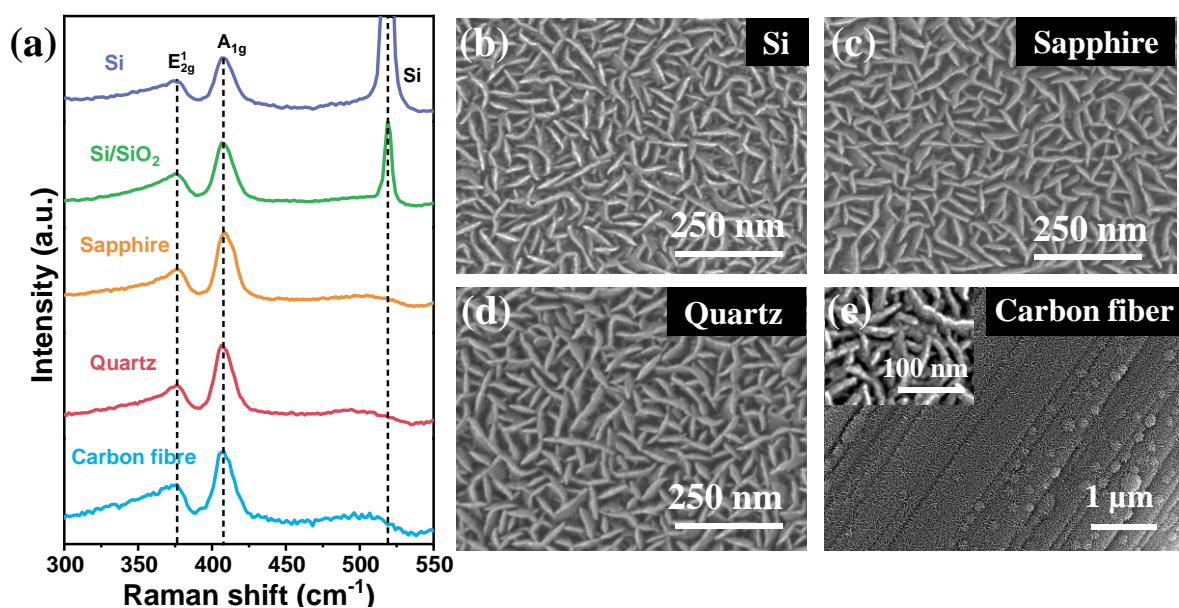


Figure 3.7 (a) Raman spectra of vertically aligned MoS₂ deposited at various substrates, including Si, Si/SiO₂, Sapphire, Quartz, and carbon fiber. FESEM images of MoS₂ flakes deposited on (b) Silicon, (c) Sapphire, (d) Quartz, and (e) Carbon fiber substrate, inset shows the high magnification image of MoS₂ flakes.

3.4 Proposed growth mechanism

Figure 3.8 illustrates the schematic diagram of growth dynamics of MoS₂ by RF sputtering. The growth of MoS₂ by sputtering can be divided into three stages: Initial, Intermediate (nucleation stage) and final (growth stage). These stages are schematically represented by Figures 3.8 (a)-(e), respectively. First, layer-by-layer 2D MoS₂ growth starts parallel to the substrate. This can be inferred from the direct evidence in cross-sectional FESEM image (Figure 3.8 (f)) along with less surface roughness (Figure 3.3 (h)), suggest smooth surface. Even the XRD pattern of this smooth surface, which corresponds to the 2D layer-by-layer growth exhibits the diffraction from (002) plane due to its 2D confined nature (Figure 3.4 (a)). In the second stage, as the growth time increases, layers of the MoS₂ film increase and at certain thickness (so-called critical thickness) nucleation starts on the MoS₂ surface at some point to grow vertical structure as well as 2D growth between them. FESEM image of 11 min sample (Figure 3.3 (b)) shows that some of vertical flakes of MoS₂ begin to emerge on the surface, which have not yet coalesced exhibiting evolution of vertical growth. The corresponding cross-sectional image of MoS₂ grown on Si/SiO₂ substrate displays bright spots at the interface between film and substrate (Figure 3.8 (g)). This cross-sectional region shows layer-by-layer growth of MoS₂ upto few-layers and after that MoS₂ island formation has been started. The corresponding Raman spectra demonstrate the decrease in intensity (E_{2g}^1/A_{1g}) ratio to ~ 0.5 , reflecting the suppression of exposed basal plane.

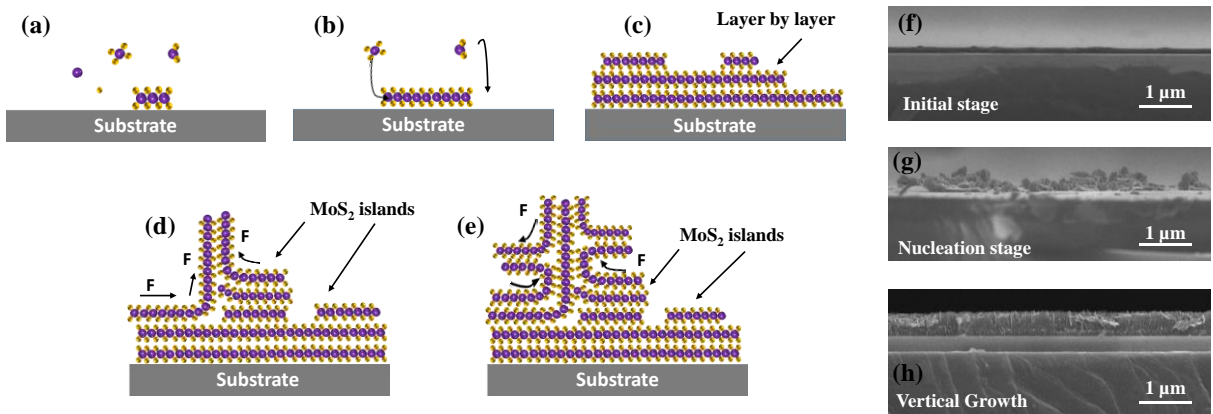


Figure 3.8 Growth model for the formation of vertically aligned MoS₂ flakes. (a-c) Initially, layer-by-layer growth occurs by mass transport arriving at the substrate. (d) Vertically aligned growth of MoS₂ starts due to island formation, where strain and defects are present. (e) Vertically aligned growth continues and branches parallel to the substrate. (f-h) Cross-sectional image of MoS₂ grown film at different growth stage.

At this point, it is critical to understand growth dynamic and how these vertical flakes are formed. Our proposed growth mode (Figure 3.8) suggests that MoS₂ island form on the surface after layer-by layer growth (of a few-layers) due to defect and strain to acquire an energetic favorable morphology as per the Stranski-Krastanov growth model [19, 30]. After that the growth continues and MoS₂ islands merge together and extend to form 3D vertical-standing flakes (Figure 3.8 (h)). Furthermore, as growth time becomes longer, the whole surface is covered by petal-like vertical MoS₂ flakes. The obtained cross-sectional images of MoS₂ at different growth stage evidently confirms the evolution of vertical growth starts from in-plane MoS₂.

3.5 Photodetector performance

Finally, to evaluate opto-electronic behaviour of vertically aligned MoS₂, we have fabricated metal-semiconductor-metal (MSM) photodetector on optimized sample (10 mtorr, 16 min). The vertically aligned MoS₂ flakes are well-suited for the photodetector applications, exhibiting high optical absorbance due to more exposed edges. Figure 3.9 (a) displays the I-V characteristics of representative device under different light intensity of 532 nm. A sharp increment in photocurrent is observed under illumination, which increases with increasing optical power depicting the high photo-response in vertically aligned MoS₂.

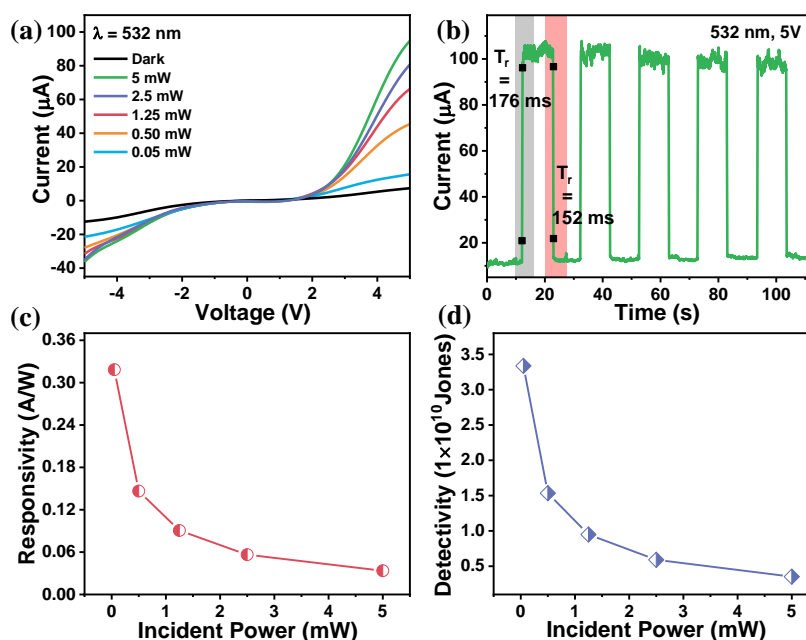


Figure 3.9 Photoresponse behaviour of vertically aligned MoS₂ (a) I-V characteristics in dark and light (532 nm laser) condition, inset shows the fabricated device image. (b) Temporal response under 532 nm illumination at 5V bias. (c) Responsivity and (d) Detectivity of MoS₂ photodetector as a function of incident power at an applied bias of 5V.

The temporal photoresponse of the device was also performed to investigate the practical applicability and feasibility of the fabricated MoS₂ photodetector. The periodic on-off switching of incident light shows high repeatability of the photodiode with fast response time (176 ms/150 ms). The photoresponsivity (R) and specific detectivity (D*) of the device was calculated by the given formula [31, 32]:

$$R = \frac{(I_{light} - I_{dark}) * S_{beam}}{P * A} \quad (3.1)$$

$$D^* = \frac{R \sqrt{A}}{\sqrt{2eI_{dark}}} \quad (3.2)$$

Here, I_{dark} and I_{light} is the current under dark and illumination, P is the optical power of incident laser, S_{beam} represents the spot size of laser beam and A is the active are of the device. The estimated R and D* value of the photodetector as a function of incident power is presented in Figure 3.9 (c-d). At low illumination power (0.05 mW), the device reaches a photoresponsivity of 0.32 A/W and detectivity of 3.3×10^{10} Jones, which is much higher than the previously reported monolayer or multilayer MoS₂ photodetector [33, 34]. A comparison between our fabricated vertically aligned MoS₂ photodetector with other reported monolayer/multilayer MoS₂ photodetectors is shown in Table 3.1, which signifies the advantage of vertically aligned MoS₂ over mono/multilayer MoS₂. Thereby, vertically aligned MoS₂ has a great choice for the development of next generation optoelectronics.

Table 3.1 Comparative performance of MoS₂ photodetector

S. No	Material	Synthesis Method	Wavelength	Responsivity (mA/W)	Detectivity (Jones)	Ref.
1.	Monolayer MoS ₂	Exfoliation	532 nm	7.5	-	[33]
2.	Monolayer MoS ₂	CVD	514 nm	1.1	-	[34]
3.	Multi-layer MoS ₂	Exfoliation	633 nm	120	10^{11}	[35]
4.	Multi-layer MoS ₂	Pulse laser deposition	589 nm	34.6	1.06×10^9	[36]
5.	Vertically aligned MoS ₂	RF Sputtering	532 nm	320	3.3×10^{10}	This work

3.6 Conclusions

We have successfully demonstrated wafer scale growth of vertically aligned MoS₂ with an industrially compatible scalable sputtering process. This method produces large-area good quality film with high uniformity and reproducibility. It has been observed that MoS₂ growth is strongly dependent upon the growth pressure. The XRD and FESEM results revealed that the sample grown under 10 mTorr pressure have better quality and larger flake size as compared to the other samples. To study the evolution of MoS₂ structures, time-dependent samples were also grown at 10 mTorr pressure. The detailed morphological, structural and spectroscopic analysis revealed that the transition of 2D layered MoS₂ structure turns into 3D vertical standing MoS₂ flakes after a critical thickness. Hence, Stranski–Krastanov growth model is dominant. In addition, the large area vertical flakes of MoS₂ grown directly on several substrates (Si, quartz, sapphire, carbon fibre) suggest substrate independent growth. This work serves as a proof-of-concept for an alternative and facile route that is complementary to CVD grown MoS₂ and other TMDs film.

References

1. Lopez-Sanchez, O., et al., *Ultrasensitive photodetectors based on monolayer MoS₂*. Nature Nanotechnology, 2013. **8**(7): p. 497-501.
2. Radisavljevic, B., et al., *Single-layer MoS₂ transistors*. Nature Nanotechnology, 2011. **6**(3): p. 147-150.
3. Bao, W., et al., *High mobility ambipolar MoS₂ field-effect transistors: Substrate and dielectric effects*. Applied Physics Letters, 2013. **102**(4): p. 042104.
4. Zhang, K., et al., *Interlayer Transition and Infrared Photodetection in Atomically Thin Type-II MoTe₂/MoS₂ van der Waals Heterostructures*. ACS Nano, 2016. **10**(3): p. 3852-3858.
5. Chang, M.-C., et al., *Fast growth of large-grain and continuous MoS₂ films through a self-capping vapor-liquid-solid method*. Nature Communications, 2020. **11**(1): p. 3682.
6. Zhan, Y., et al., *Large-Area Vapor-Phase Growth and Characterization of MoS₂ Atomic Layers on a SiO₂ Substrate*. Small, 2012. **8**(7): p. 966-971.
7. van der Zande, A.M., et al., *Grains and grain boundaries in highly crystalline monolayer molybdenum disulphide*. Nature Materials, 2013. **12**(6): p. 554-561.
8. Serna, M.I., et al., *Large-Area Deposition of MoS₂ by Pulsed Laser Deposition with In Situ Thickness Control*. ACS Nano, 2016. **10**(6): p. 6054-6061.
9. Fu, D., et al., *Molecular Beam Epitaxy of Highly Crystalline Monolayer Molybdenum Disulfide on Hexagonal Boron Nitride*. Journal of the American Chemical Society, 2017. **139**(27): p. 9392-9400.
10. Chaudhary, N., et al., *Hydrothermal synthesis of MoS₂ nanosheets for multiple wavelength optical sensing applications*. Sensors and Actuators A: Physical, 2018. **277**: p. 190-198.
11. Kim, D.H., et al., *Wafer-Scale Growth of a MoS₂ Monolayer via One Cycle of Atomic Layer Deposition: An Adsorbate Control Method*. Chemistry of Materials, 2021. **33**(11): p. 4099-4105.
12. Yan, A., et al., *Direct Growth of Single- and Few-Layer MoS₂ on h-BN with Preferred Relative Rotation Angles*. Nano Letters, 2015. **15**(10): p. 6324-6331.
13. Cho, S.-Y., et al., *Highly Enhanced Gas Adsorption Properties in Vertically Aligned MoS₂ Layers*. ACS Nano, 2015. **9**(9): p. 9314-9321.
14. Qiao, S., et al., *A vertically layered MoS₂/Si heterojunction for an ultrahigh and ultrafast photoresponse photodetector*. Journal of Materials Chemistry C, 2018. **6**(13): p. 3233-3239.
15. Chen, X., et al., *Vertically aligned MoS₂ films prepared by RF-magnetron sputtering method as electrocatalysts for hydrogen evolution reactions*. Composite Interfaces, 2021. **28**(7): p. 707-716.
16. Wang, L., et al., *MoS₂/Si Heterojunction with Vertically Standing Layered Structure for Ultrafast, High-Detectivity, Self-Driven Visible–Near Infrared Photodetectors*. Advanced Functional Materials, 2015. **25**(19): p. 2910-2919.
17. Kim, H.-S., et al., *Vertical growth of MoS₂ layers by sputtering method for efficient photoelectric application*. Sensors and Actuators A: Physical, 2018. **269**: p. 355-362.
18. Chen, G., et al. *Effects of Deposition and Annealing Temperature on the Structure and Optical Band Gap of MoS₂ Films*. Materials, 2020. **13**, DOI: 10.3390/ma13235515.
19. Li, H., et al., *Synthesis and characterization of vertically standing MoS₂ nanosheets*. Scientific Reports, 2016. **6**(1): p. 21171.
20. Wadhwa, R., et al., *Investigation of charge transport and band alignment of MoS₂-ReS₂ heterointerface for high performance and self-driven broadband photodetection*. Applied Surface Science, 2021. **569**: p. 150949.

21. Moser, J. and F. Lévy, *Random stacking in MoS₂-x sputtered thin films*. Thin Solid Films, 1994. **240**(1): p. 56-59.
22. Koçak, Y. and E. Gür, *Growth Control of WS₂: From 2D Layer by Layer to 3D Vertical Standing Nanowalls*. ACS Applied Materials & Interfaces, 2020. **12**(13): p. 15785-15792.
23. Lee, C., et al., *Anomalous Lattice Vibrations of Single- and Few-Layer MoS₂*. ACS Nano, 2010. **4**(5): p. 2695-2700.
24. Agrawal, A.V., et al., *Controlled Growth of MoS₂ Flakes from in-Plane to Edge-Enriched 3D Network and Their Surface-Energy Studies*. ACS Applied Nano Materials, 2018. **1**(5): p. 2356-2367.
25. Kong, D., et al., *Synthesis of MoS₂ and MoSe₂ Films with Vertically Aligned Layers*. Nano Letters, 2013. **13**(3): p. 1341-1347.
26. Li, S., et al., *Edge-Enriched 2D MoS₂ Thin Films Grown by Chemical Vapor Deposition for Enhanced Catalytic Performance*. ACS Catalysis, 2017. **7**(1): p. 877-886.
27. Kumar, R., et al., *Highly selective and reversible NO₂ gas sensor using vertically aligned MoS₂ flake networks*. Nanotechnology, 2018. **29**(46): p. 464001.
28. Eda, G., et al., *Photoluminescence from Chemically Exfoliated MoS₂*. Nano Letters, 2011. **11**(12): p. 5111-5116.
29. Xie, J., et al., *Controllable Disorder Engineering in Oxygen-Incorporated MoS₂ Ultrathin Nanosheets for Efficient Hydrogen Evolution*. Journal of the American Chemical Society, 2013. **135**(47): p. 17881-17888.
30. Zhu, M., et al., *A mechanism for carbon nanosheet formation*. Carbon, 2007. **45**(11): p. 2229-2234.
31. Nie, C., et al., *Ultrafast growth of large-area monolayer MoS₂ film via gold foil assistant CVD for a highly sensitive photodetector*. Nanotechnology, 2017. **28**(27): p. 275203.
32. Li, J., et al., *Enhancement of the Photoresponse of Monolayer MoS₂ Photodetectors Induced by a Nanoparticle Grating*. ACS Applied Materials & Interfaces, 2020. **12**(7): p. 8429-8436.
33. Yin, Z., et al., *Single-Layer MoS₂ Phototransistors*. ACS Nano, 2012. **6**(1): p. 74-80.
34. Perea-López, N., et al., *CVD-grown monolayered MoS₂ as an effective photosensor operating at low-voltage*. 2D Materials, 2014. **1**(1): p. 011004.
35. Choi, W., et al., *High-Detectivity Multilayer MoS₂ Phototransistors with Spectral Response from Ultraviolet to Infrared*. Advanced Materials, 2012. **24**(43): p. 5832-5836.
36. Xie, Y., et al., *Ultrabroadband MoS₂ Photodetector with Spectral Response from 445 to 2717 nm*. Advanced Materials, 2017. **29**(17): p. 1605972.

Chapter 4: 2D MoS₂ heterostructures for broadband photodetection

In this chapter, we investigate the potential of 2D MoS₂ for photodetector application. To achieve enhanced photoresponse, we introduce various heterostructures of MoS₂, such as MoS₂-ReS₂, MoS₂/Ga₂O₃, and Pt@MoS₂, for broadband (UV-NIR/Vis-NIR) photodetection. We performed a detailed investigation of the photodetector performance for all the fabricated heterostructures, which demonstrate high responsivity, high detectivity, and fast optical switching when compared to pristine MoS₂. The energy band alignment at the heterojunction's interface critically affects photodetector performance, and an understanding of photo-generated carrier dynamics at the interface is crucial for high-performance devices. To gain intrinsic physical insights into device behavior, we analyze energy band diagrams and charge carrier dynamics using photoelectron spectroscopy (XPS and UPS) and kelvin probe force microscopy (KPFM). The demonstration of MoS₂ heterostructures as high-performance broadband photodetectors offer exciting opportunities for efficient optoelectronics and imaging applications.

4.1 Requirement of highly sensitive, fast, and broadband photodetectors

Broadband photodetectors are currently a highly sought-after technology in nano-optoelectronics due to their crucial role in various applications, including medical imaging, environmental monitoring, and optical communication [1-3]. To effectively serve these purposes, it is essential for photodetectors to possess high sensitivity to light in a broad-spectrum range and have fast response speeds. Pristine MoS₂ photodetectors have demonstrated excellent responsivity, however, their performance is often limited by slow response times and low detectivity due to the high carrier recombination rate in bare MoS₂ and the lack of a high-quality junction. In addition, bare MoS₂-based devices limit the active wavelength detection range corresponding to its bandgap, thus restricting its potential in broadband photodetection.

4.2 MoS₂ based heterostructures for broadband photodetection

4.2.1 MoS₂-ReS₂ heterostructure

Rhenium disulfide (ReS₂) is a member of the TMDs family, which has attracted a lot of attention in the scientific community due to its unique electronic and optical properties. ReS₂ exhibits intriguing properties such as semiconducting behavior, layer-independent direct

bandgap, in-plane anisotropy, and weak interlayer coupling [4-6]. The crystal structure of ReS₂ is anisotropic, with a distorted 1T phase, which induces weak interlayer coupling, causing bulk ReS₂ to behave like vibrationally and electronically decoupled monolayers [7]. This property allows ReS₂ to maintain its unique electronic and optical properties even in bulk form. ReS₂ has a desirable direct bandgap, regardless of the number of layers. Few-layer ReS₂ with a large thickness exhibits high density of states and enhanced optical absorption in the visible-NIR region [8]. Therefore, ReS₂ has an excellent candidate for developing heterostructures with MoS₂ for photodetector application. The potential for developing heterostructures is exciting because of the synergistic effects that may arise from the combination of both the properties MoS₂ as well as ReS₂.

4.2.1.1 Experimental Section

4.2.1.1.1 Material synthesis

Synthesis of MoS₂: Vertically aligned MoS₂ (VA-MoS₂) flakes have been synthesized by the atmospheric pressure chemical vapor deposition (APCVD) technique on Si/SiO₂ substrate. Initially, we ultrasonicated the Si/SiO₂ substrate for 20 minutes in acetone, followed by nitrogen jet drying. High-quality precursors MoO₃ (0.058 g, 99.99%) and S powder (0.45 g, 99.99%) were purchased from Sigma-Aldrich to synthesize VA-MoS₂ flakes. To grow VA-MoS₂ flakes, MoO₃ and S powder precursors were placed in two zirconia boats in a small quartz tube, as shown in Figure 1a. This arrangement of small quartz tube with zirconia boats was inserted in the bigger quartz tube furnace equipped with three individual heating zones. The gas flow rate, temperature of each precursor, the position of boats and substrate have been properly optimized. The growth temperature profile of MoO₃ (zone 1) and S (zone 2) has been pre-set to the temperature values 800 °C and 350 °C, respectively. The gas flow rate throughout the deposition and growth time were 175 sccm and 30 minutes, respectively. Afterwards, APCVD system naturally cooled down to room temperature.

Synthesis of ReS₂: ReS₂ powder (99%) purchased from Alfa Aesar was used as received without further purification. ReS₂ nanosheets (NSs) were prepared by adopting liquid phase exfoliation technique. 100 mg ReS₂ powder was added in 20 ml of ethanol in 50 ml vial and sonicated for 7 hours in ultrasonication bath (Fisher brand, 280 W, 50/60 Hz) at room temperature. The resultant dispersion was first centrifuged at 1000 rpm to remove most of the unexfoliated material for 2 minutes. The upper suspension was re-centrifuged at 3000 rpm for 10 minutes to remove the heavier nanoflakes that were precipitated on the bottom of the centrifuge tube. Finally, the supernatant was gently transferred from the top of the dispersion

for further analysis. After that, MoS₂-ReS₂ heterostructure was fabricated by direct dispersion of ReS₂ NSs on top of VA-MoS₂.

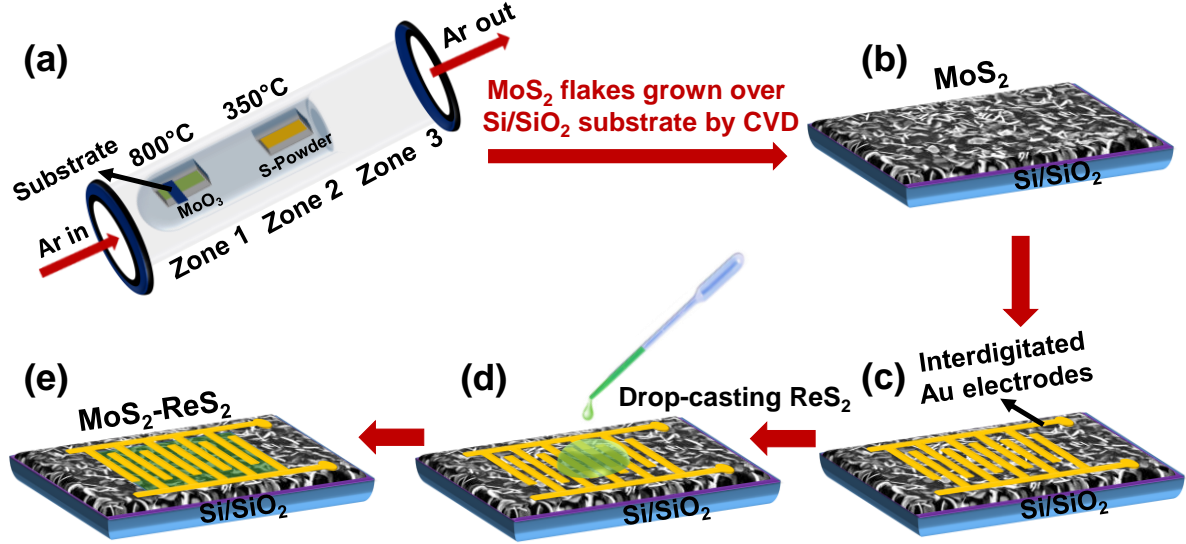


Figure 4.1 Schematic of fabrication of MoS₂-ReS₂ photodetector. (a) Synthesis of VA-MoS₂ flakes by APCVD. (b) VA-MoS₂ flakes deposited on Si/SiO₂ substrate. (c) Patterned interdigitated Au electrode on top of MoS₂ (pristine MoS₂ photodetector). (d) ReS₂ NSs drop casting on MoS₂-Au contact photodetector. (e) Schematic of MoS₂-ReS₂ heterostructure.

4.2.1.1.2 Material characterizations

Raman spectra were recorded by a confocal micro-Raman spectrometer (Witec Alpha 300 R), and PL spectra were acquired by LAB RAM HR800 spectrometer. A laser source of wavelength 532 nm was used to excite the samples. Surface morphology and elemental distribution map of MoS₂ and MoS₂-ReS₂ heterostructure were analyzed by Nova NanoSEM-450 coupled with an EDX system. A UV-Vis-NIR spectrophotometer (Perkin-Elmer Lambda 950) was employed to measure the optical absorbance of MoS₂, ReS₂, and MoS₂-ReS₂ heterostructure. In order to probe chemical ambient and energy level alignment at the MoS₂-ReS₂ heterointerface, X-ray photoelectron spectroscopy (XPS) and ultraviolet photoelectron spectroscopy (UPS) were performed as described in section 2.2.6 of chapter 2.

4.2.1.1.3 Device fabrication and measurement

The interdigitated gold (Au) electrodes having a thickness of 250 nm were patterned on VA-MoS₂ (sample size = 1.5 × 1 cm²) via shadow mask by the thermal evaporator. Initially, photodetector measurements were performed on the pristine MoS₂-Au contact device. Thereafter, ReS₂ NSs were dropped cast onto the VA-MoS₂ device as shown in Figure 4.1. The photodetector measurements were conducted using a PVE 300 Bentham (TMC 300)

monochromator comprising of 75 W Xenon and 100 W Quartz halogen (QTH) lamp that connected to Keithley (6430 SMU) as described in chapter 2. The photoresponse of photodetectors (MoS₂ and MoS₂-ReS₂) was recorded in the wavelength range of 400-1100 nm. The optical power of different incident wavelengths was calibrated by a standard Si photodiode. All the photodetector measurements were performed under ambient conditions in an optically closed box to block interference from the outer light source.

4.2.1.2 Results and discussion

Figure 4.2 illustrates the surface morphology of VA-MoS₂ and MoS₂-ReS₂ heterostructure. Energy dispersive spectroscopy (EDS) elemental mapping has been performed to affirm the presence of different elemental constituents in MoS₂-ReS₂ heterostructure. Figure 4. 2 (a) shows the scanning electron microscopy (SEM) image of uniformly grown VA-MoS₂ flakes on Si/SiO₂ substrate, and the average height of these flakes is ~ 500 nm. ReS₂ NSs can be seen as small clusters deposited over interconnected VA-MoS₂ flakes at different sites of the sample (Figure 4.2 (b)). Figure 4.2 (c) is the enlarged view of the MoS₂-ReS₂ heterostructure where ReS₂ is segregated over MoS₂ flakes. The average size of ReS₂ NSs is less than ~ 100 nm. It can be observed that most of the ReS₂ NSs are coated over the edges of VA-MoS₂ flakes, and some of the ReS₂ NSs can also diffuse into the MoS₂ flakes and reside over the Si/SiO₂ substrate. Since VA-MoS₂ flakes have a very large surface area [9], the drop cast ReS₂ will form a large area of contact, which is highly recommended for adequate carrier transportation at the interface [10]. Elemental mapping carried out for a selected area of MoS₂-ReS₂ heterojunction (Figure 4.2 (d)) confirms the presence of Re, Molybdenum (Mo), and Sulfur (S), and Silicon (Si) (present in the substrate) depicted in Figures 4.2 (e)-(i). Thereby, the presence of respective constituent elements in EDS mapping reveals the existence of both MoS₂ and ReS₂ at the heterojunction.

Raman measurements were performed for pristine MoS₂, ReS₂ and their heterostructure as illustrated in Figures 4.3 (a)-(c). The characteristic Raman peaks of pristine MoS₂ are identified at 383.49 cm^{-1} and 408.73 cm^{-1} corresponding to in-plane (E_{2g}^1) and out of plane (A_{1g}) vibrational modes, respectively [11]. The Raman shift between these two vibrational modes is observed to be 25.24 cm^{-1} , which indicates the existence of few-layer MoS₂ [12]. The intensity ratio of $I_{E_{2g}^1}/I_{A_{1g}}$ is 0.42, which also confirms the formation of vertically oriented MoS₂ flakes [13]. The characteristic peaks of ReS₂ are recognized at 150.43 cm^{-1} , 159.46 cm^{-1} and 211.54 cm^{-1} reciprocal to in plane (E_g) and out of plane (A_g –like) vibrational

modes [4]. The signature of characteristic peaks corresponding to both materials confirms the co-existence of both the materials and formation of heterointerface, as shown in Figure 4.3 (a).

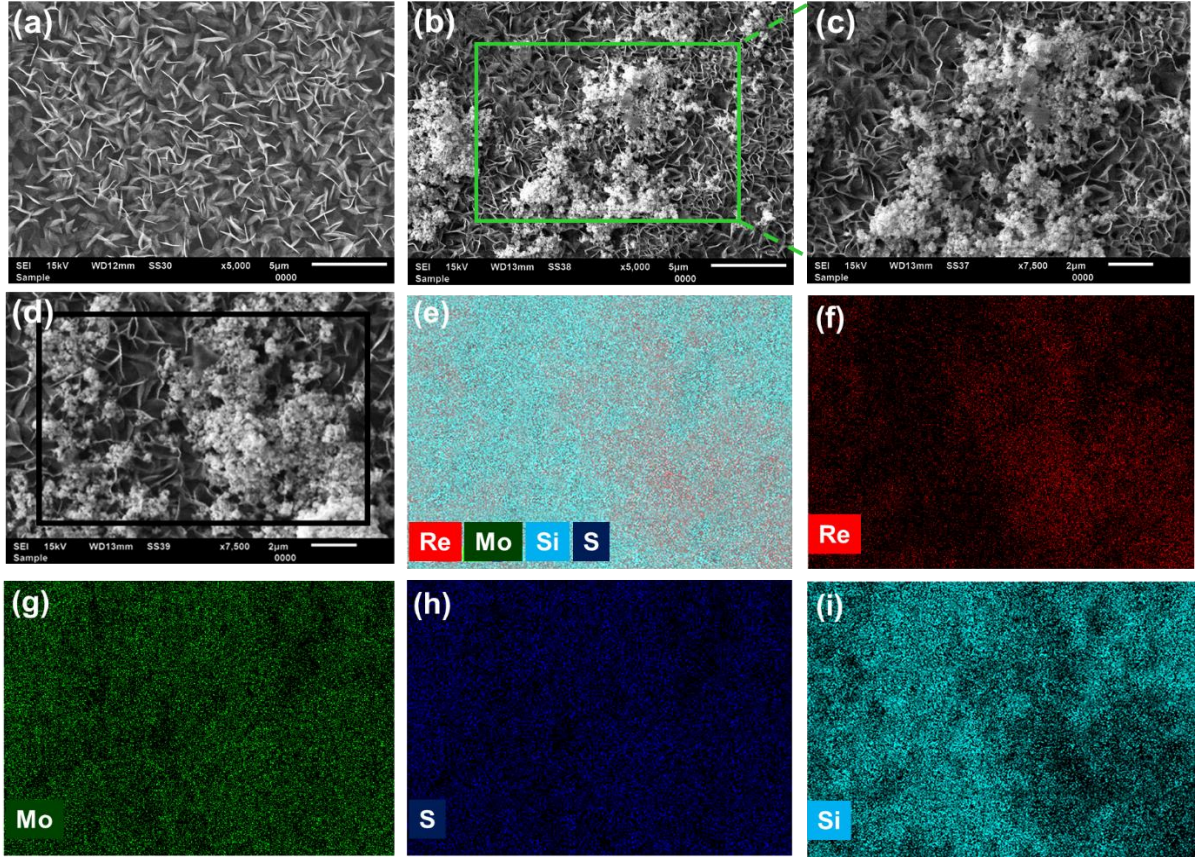


Figure 4.2 SEM image of (a) VA-MoS₂ (b) MoS₂-ReS₂ heterostructure, ReS₂ drop casted onto VA-MoS₂ flakes grown over Si/SiO₂ substrate. The average size of ReS₂ NSs is less than ~ 100 nm. It can be seen as clusters deposited over VA-MoS₂. (c) Enlarge view of MoS₂-ReS₂ heterostructure. (d) Rectangular box is the area selected for the EDX elemental mapping of MoS₂-ReS₂ heterostructure. (e) Cumulative EDX elemental mapping. (f) Rhenium. (g) Molybdenum. (h) Sulfur. (i) Silicon.

Interestingly, we have observed redshift in both vibrational modes (E_{2g}^1 and A_{1g}) of MoS₂ in MoS₂-ReS₂ heterostructure (Figure 4.3 (b)). It is evident from previous reports that both in plane and out of plane vibrational modes are sensitive to the induced stress or strain while variation in electron density only influences the out of plane mode [14, 15]. Thus, redshift (1.25 cm⁻¹) realized in E_{2g}^1 mode of MoS₂ is attributed to the produced tensile strain, while the redshift (1 cm⁻¹) in A_{1g} mode is combined effect of tensile strain and lower electron density in MoS₂. Nevertheless, ReS₂ does not experience any strain after coupling with MoS₂, as there is no significant change found in E_g modes of ReS₂. However, A_g -like vibration mode of ReS₂ displays slight redshift of 0.36 cm⁻¹ (Figure 4.3 (c)) which is ascribed to the higher electron

density in ReS₂ [16]. The redshift arises in respective vibrational modes of MoS₂ and ReS₂ in the heterojunction elucidates the origin of strong interlayer coupling between MoS₂ and ReS₂.

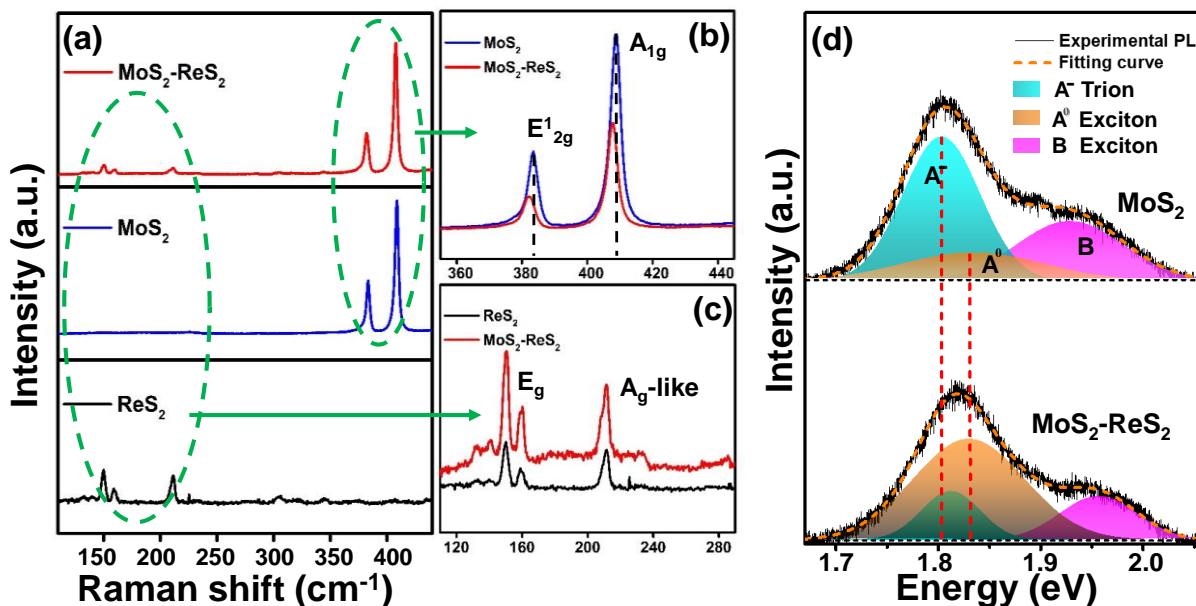


Figure 4.3 (a) Raman spectrum of MoS₂-ReS₂ heterostructure (Red), pristine MoS₂ (blue) and pristine ReS₂ (black). (b) Raman spectrum of MoS₂ and MoS₂-ReS₂ (zoomed spectrum, in the range 350-450 cm^{-1}). (c) Raman spectrum of ReS₂ and MoS₂-ReS₂ (zoomed spectrum, in the range 110-290 cm^{-1}). (d) Comparative PL spectrum of MoS₂ and MoS₂-ReS₂ heterostructure, each PL peak is deconvoluted into three peaks corresponding to A^- negative trion (cyan), A^0 neutral exciton (orange) and B exciton (magenta).

PL measurements were carried out to further investigate the interlayer coupling and charge transport behaviour at the heterointerface. Here, we have mainly focused on the PL behaviour of pristine MoS₂ and MoS₂-ReS₂ heterostructure, considering the goal of present work. The blueshift has been observed in the PL peak position of MoS₂-ReS₂ heterostructure compared to pristine MoS₂, with no significant change in PL intensity. To gain more insight into the role of ReS₂ onto the MoS₂, each PL peak is deconvoluted into three peaks correspond to A^- negative trion (cyan), A^0 neutral exciton (orange) and B exciton (magenta) as illustrated in Figure 4.3 (d). The A and B peak arises due to the direct bandgap and strong spin-orbit coupling in the valence band spectra of MoS₂ [17]. The integrated PL intensity ratio of A^- trion to A^0 exciton (I_{A^-}/I_{A^0}) peaks is associated with the relative population, depending upon the electron density doping in MoS₂ (higher intensity ratio leads to higher electron doping) [18, 19]. In pristine MoS₂, A^- trion peak (1.80 eV) is the most prominent and higher in intensity than the A^0 exciton peak (1.83 eV) due to its intrinsic n-doped nature [20]. However, in case of heterostructure, A^0 exciton is the primary contributor. The blueshift observed in heterostructure

is ascribed to the increased emission of A^0 exciton and decrease in emission of A^- trion (100 meV blueshift of A^- trion peak with no variation in A^0 exciton peak position). This clearly depicts that ReS₂ introduces p-doping in MoS₂, providing the carrier extraction effect into the MoS₂. Similar behaviour was also observed in MoS₂/hBN stacks, where bottom hBN flakes evade the effect of electron doping of Si/SiO₂ substrate on the MoS₂, resulting in a blueshift due to the reduced emission of A^- trion and enhanced emission of A^0 excitation [18]. Also, the calculated ratio of I_{A^-}/I_{A^0} is 12 times higher in pristine MoS₂ in contrast to MoS₂-ReS₂ heterostructure, which suggests higher electron concentration in pristine MoS₂. Hence, the findings of PL results are well consistent with the conclusions delivered by Raman spectroscopy.

The XPS and UPS measurements have been employed extensively to investigate the energy level alignment of MoS₂-ReS₂ heterojunction for in-depth understanding of the charge transfer mechanism. As per our knowledge, this is the first experimental report where band alignment and charge transport behaviour have been investigated across the interface of MoS₂-ReS₂ heterojunction. Bellus et al. have also calculated the energy band alignment; however, they performed first principle computational method to evaluate the alignment [21]. Thus, experimental investigations are remained to envisage the energy-level alignment of MoS₂-ReS₂ heterostructure.

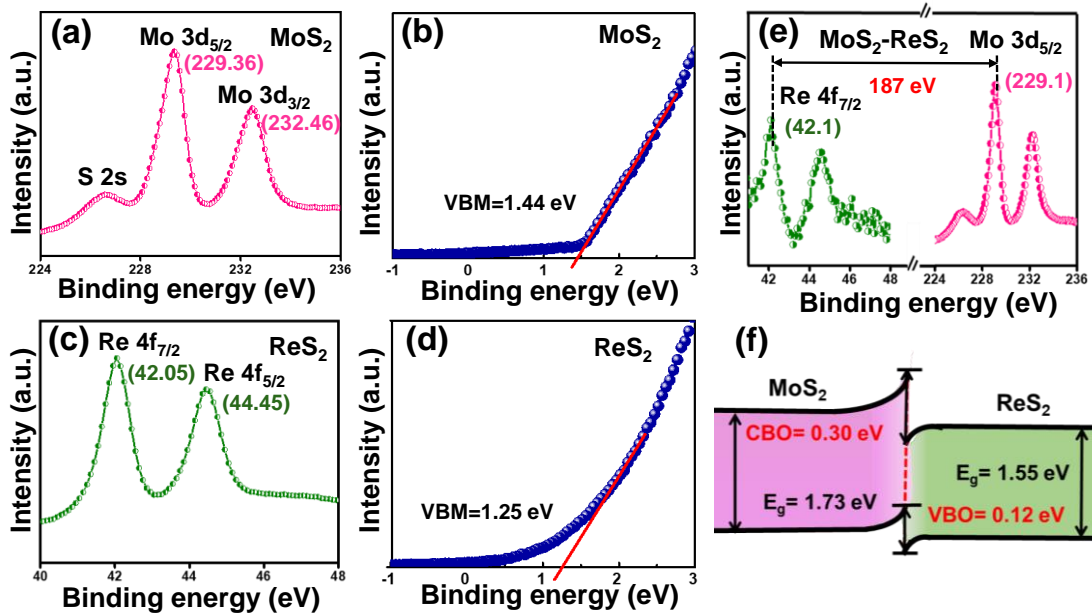


Figure 4.4 (a) Core-level spectra of Mo 3d. (b) Valence band spectra of pristine MoS₂. (c) Core-level spectra of Re 4f. (d) Valence band spectra of ReS₂. (e) The Mo 3d and Re 4f core-level at heterointerface of MoS₂-ReS₂. (f) Energy band alignment at MoS₂-ReS₂ heterojunction. Core-level binding energy peak positions given in the parenthesis.

Figures 4.4 (a) and (c) display the core-level spectra of Mo 3d and Re 4f for pristine MoS₂ and pristine ReS₂, respectively. The Mo 3d core-level splits into Mo 3d_{3/2} and Mo 3d_{5/2}, owing to spin-orbit coupling, centered at 232.46 eV and 229.36 eV, respectively. The Re 4f spectrum exhibits two core-level peaks at positions 42.05 eV and 44.45 eV, which correspond to Re 4f_{7/2} and Re 4f_{5/2}, respectively. All observed core-level binding energy peak positions of Re 4f and Mo 3d are well-consistent with the previously reported literature of pristine MoS₂ and ReS₂ [22, 23]. After careful analysis of XPS core-level energy spectrum at the heterointerface of MoS₂-ReS₂, the shift in core-level peaks of Re 4f and Mo 3d was recognized. There is a redshift of 0.26 eV in the peak position of Mo 3d_{5/2}, while Re 4f_{7/2} experienced blueshift of 0.05 eV at the MoS₂-ReS₂ heterojunction. The redshift in core-level spectra of Mo 3d reciprocates the p-doping in MoS₂ while blueshift appearance in Re 4f spectrum advocates the n-doping in ReS₂, which directly indicates the interlayer coupling between MoS₂ and ReS₂ [24]. Here, all the XPS core-level binding energy peak positions were calibrated using the carbon C (1s) spectrum, allocating the peak position at 284.4 eV.

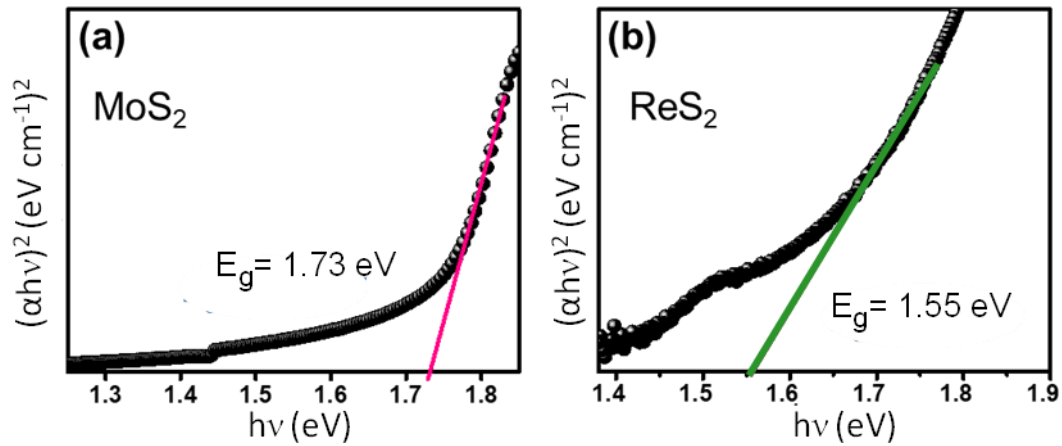


Figure 4.5 Bandgap of (a) MoS₂ and (b) ReS₂ obtained from Tauc plot.

The valence band maxima (VBM) positions were evaluated by extrapolating the linear fit of the leading edge of valence band spectra (relative to Fermi-level). The values of VBM corresponding to MoS₂ and ReS₂ come out to be 1.44 eV and 1.25 eV, respectively, illustrated in Figures 4.4 (b) and (d). The following Kraut's equation was used to evaluate the valence band offset (VBO) at the MoS₂-ReS₂ heterojunction [25].

$$VBO = (E_{Re\ 4f_{7/2}}^{MoS_2/ReS_2} - E_{Mo\ 3d_{5/2}}^{MoS_2/ReS_2}) - (E_{Re\ 4f_{7/2}}^{ReS_2} - E_{VBM}^{ReS_2}) + (E_{Mo\ 3d_{5/2}}^{MoS_2} - E_{VBM}^{MoS_2}) \quad (4.1)$$

where, first term is the separation between core-level energy of Re 4f and Mo 3d in the MoS₂-ReS₂ heterostructure, illustrated in Figure 4.4 (e). The second and third terms are the separation of metal core-level binding energy relative to the VBM of ReS₂ and MoS₂, respectively. The

calculated VBO for the MoS₂-ReS₂ heterojunction is 0.12 ± 0.1 eV. Here, the positive value of VBO represents that the valence band (VB) of MoS₂ lies above the VB of ReS₂. Subsequently, conduction band offset (CBO) can be assessed by taking account of the measured VBO and bandgap values of MoS₂ and ReS₂ using the following expression:

$$CBO = E_g^{MoS_2} - E_g^{ReS_2} + VBO \quad (4.2)$$

Where $E_g^{MoS_2}$ denotes the bandgap of MoS₂ (1.73 eV) and $E_g^{ReS_2}$ represents the bandgap of ReS₂ (1.55 eV), estimated from the Tauc plot, calculated by extrapolating the linear edge of the curve to meet the x-axis (energy-axis) as shown in Figure 4.5. Thus, the measured CBO is found to be 0.30 ± 0.1 eV at MoS₂-ReS₂ heterointerface. The band alignment calculated using kraut's rule is illustrated in Figure 4.4 (f) that represent type II heterostructure is formed between MoS₂-ReS₂.

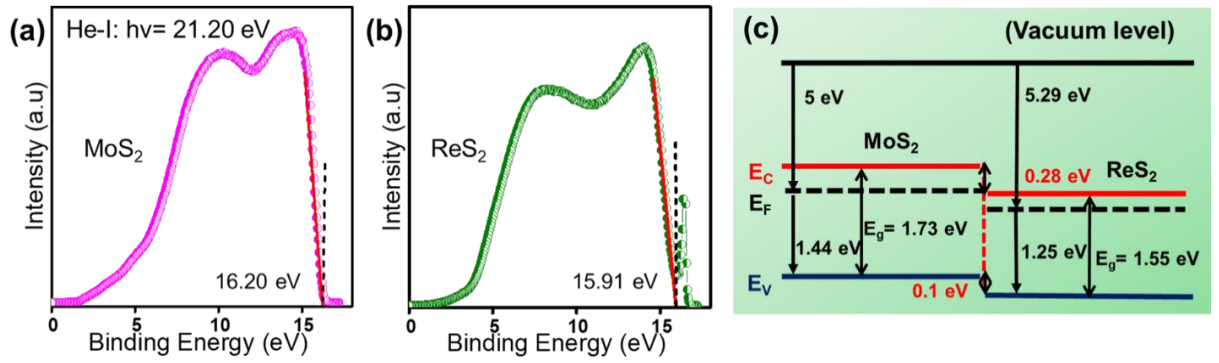


Figure 4.6 Ultraviolet photoelectron spectroscopy (UPS) spectra of (a) pristine MoS₂, (b) pristine ReS₂, (c) Energy band-alignment by Anderson's affinity rule.

Additionally, UPS spectra as demonstrated in Figures 4.6 (a) and (b) were used to evaluate work function (ϕ) and electron affinity (χ) of MoS₂ and ReS₂ using equations (4.3) and (4.4):

$$\phi = h\nu - \text{lower energy cut_off} \quad (4.3)$$

$$\chi = h\nu - W - E_g \quad (4.4)$$

where $h\nu$ is the photon energy (21.2 eV for He-1 source), and W is the emission width, which is the distance of the VBM from the lower energy electron cut-off position. Table 4.1 summarize the list of parameters obtained from the UPS analysis.

Table 4.1 Parameters calculated for MoS₂ and ReS₂ from UPS spectrum.

Parameters	MoS ₂	ReS ₂
Lower energy cut-off in B.E curve of UPS in eV	16.20	15.91
Work function (ϕ) in eV	5	5.29
Valance band maxima (VBM) in eV	1.44	1.25
Emission width (W) in eV	14.76	14.66
Electron affinity (χ) in eV	4.71	4.99

Then by using Anderson affinity rule, we have estimated the CBO is the difference between the electron affinities of the constituent material and VBO is the superposition of bandgap and CBO difference. Thus, CBO and VBO are determined by the following equations:

$$CBO = \chi_{ReS_2} - \chi_{MoS_2} \quad (4.5)$$

$$VBO = (\chi_{ReS_2} + E_g^{ReS_2}) - (\chi_{MoS_2} + E_g^{MoS_2}) \quad (4.6)$$

The calculated CBO (0.28 eV) and VBO (0.1 eV) values for MoS₂-ReS₂ interface using Anderson electron's affinity rule (Figure 4.6 (c)) is consistent with CBO and VBO values measured from the Kraut's rule (Figure 4.4 (f)). Therefore, experimentally evaluated CBO and VBO values confirm the type II band alignment at MoS₂-ReS₂ heterojunction, which is required for effective carrier transportation across the interface.

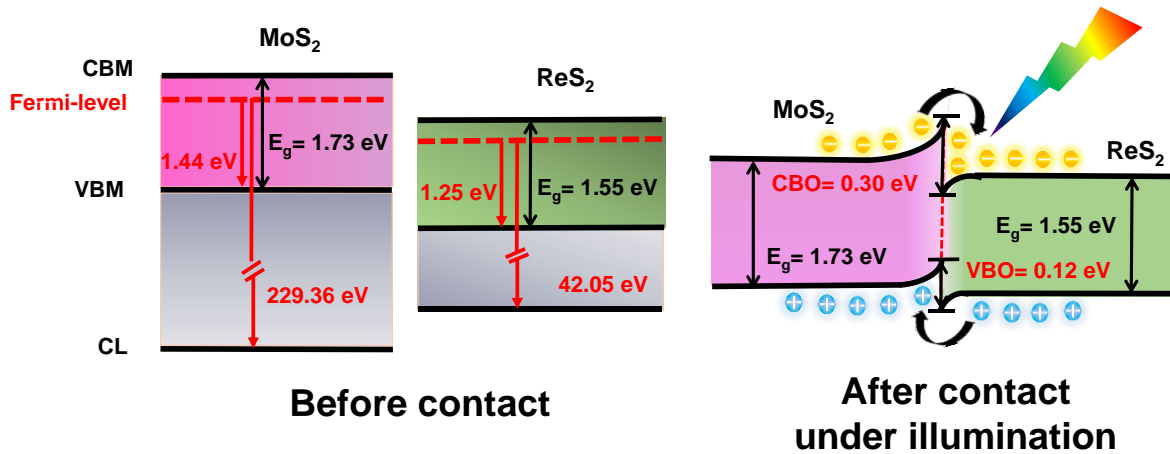


Figure 4.7 Schematic energy band diagram of MoS₂ and ReS₂. (a) Before contact. (b) After contact under illumination, illustrating the transport of photo-excited charge carriers (CBM, VBM and CL represent the conduction band minima, valence band maxima and position of core-level relative to Fermi-level).

Considering XPS and UPS evaluation, we proposed a charge transport mechanism across the MoS₂-ReS₂ interface. The individual band alignment of MoS₂ and ReS₂ is shown in Figure 4.7 (a). After contact, the energy band of MoS₂ and ReS₂ bends at the interface, and a built-in

electric field is generated due to driving of photo-generated carriers at the heterojunction to achieve equilibrium under dark condition. Under illumination, MoS₂ and ReS₂ both respond to the broad visible-NIR wavelength regime, thereby producing the photo-excited electron-hole pairs. The photo-generated electrons and holes get separated under the influence of an internal built-in electric field. The electrons migrate towards ReS₂ and accumulate in an energy valley form by n-n heterojunction, whereas holes migrate towards MoS₂ due to the favourable type II alignment (Figure 4.7 (b)). The type II alignment will also induce interlayer interaction corresponding to charge transfer states across the interface, which can significantly absorb the light equal to or greater than the energy of charge transfer states [26]. Moreover, strong interlayer coupling and large interface contact between MoS₂ and ReS₂ further improve the interface quality, thus evading the carrier recombination rate. Therefore, MoS₂-ReS₂ heterointerface manifest its potential for integrating into optoelectronic device applications.

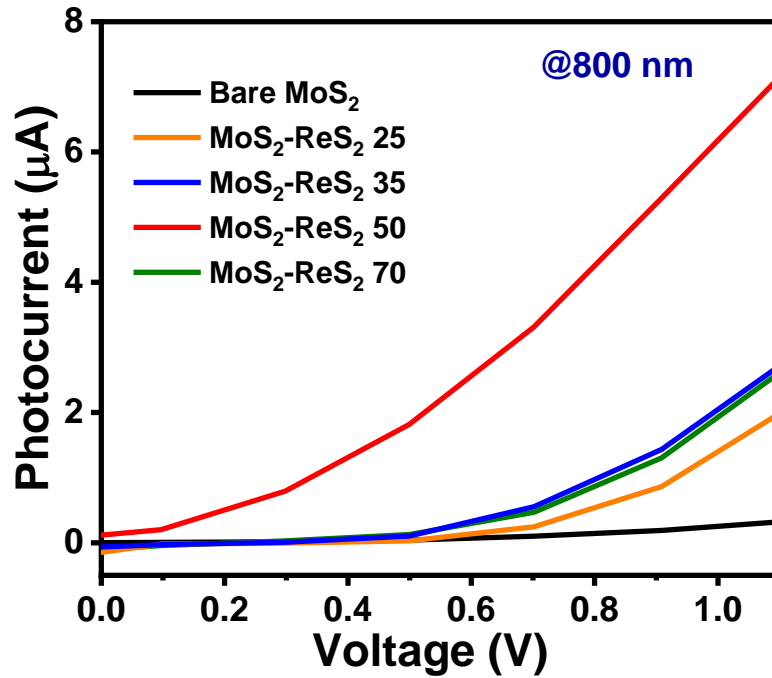


Figure 4.8 Comparative photoresponse of pristine MoS₂ with different ReS₂ solution based MoS₂-ReS₂ heterostructure.

As a proof of concept, photodetector measurements were conducted, which provide direct experimental evidence to our proposed charge transport mechanism at the MoS₂-ReS₂ heterointerface. Initially, photodetector measurements were performed for pristine MoS₂. Afterwards, ReS₂ NSs drop-casted over the same MoS₂ sample to compare the performances of pristine MoS₂ and heterostructure (MoS₂-ReS₂). We measured photoresponse of MoS₂-ReS₂ heterostructure with different amounts of drop-casted ReS₂ solution (25 μL – 70 μL) as

depicted in Figure 4.8. The photoresponse of heterostructure enhances as ReS₂ concentration increases, which gets saturated at 50 μL in our case. However, when amount of ReS₂ NSs exceeds 50 μL , the photocurrent starts decreasing. It suggests that 50 μL is the optimum amount of ReS₂ at the heterointerface to achieve the best device performance. This can also be understood by the two-fold effect. First, as the amount of ReS₂ NSs increases onto the MoS₂, it goes towards the newer sites and makes new heterojunctions. Thus, leading to enhanced photodetector performance. Second, it may also be possible that some amount of ReS₂ will reside over previously deposited ReS₂ NSs, which may hinder the absorption capacity of pre-existing heterojunction. When, second effect surpasses the first, device performance will start to decrease. Further, the type II band alignment offers interlayer interaction between VBM of MoS₂ to CBM of ReS₂, capable of generating photo-excited charge carrier's equivalent to transition gap. In addition, there is strong interlayer coupling between MoS₂ and ReS₂ owing to formation of heterojunction can introduce charge transfer states between the transition gap at the interface of two materials, which would absorb the light below (in energy) of both the constituents. The photo-induction of charge transfer states can be hindered by addition of ReS₂ because portion of light can be directly absorbed or scattered by ReS₂ and not letting the light reach the interfacial MoS₂-ReS₂.

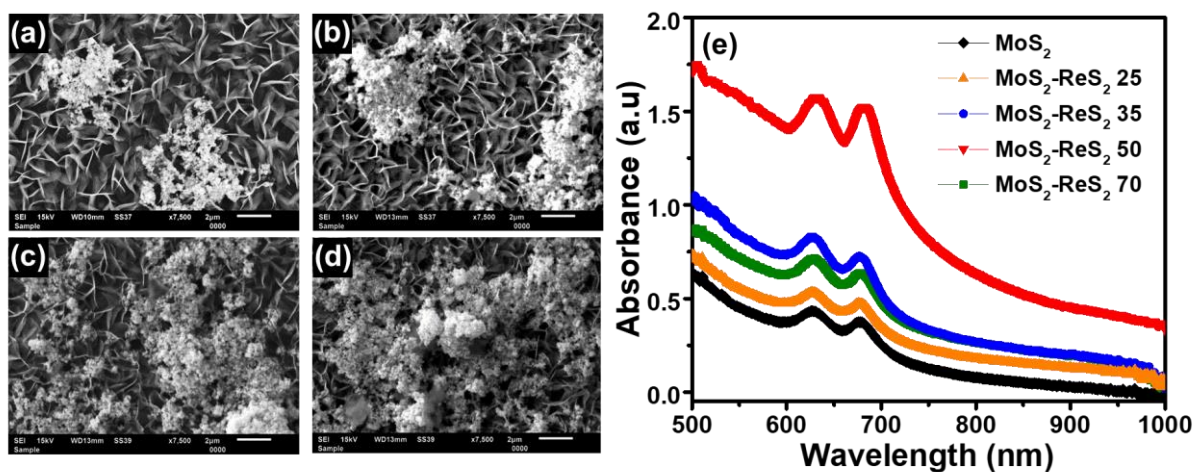


Figure 4.9 SEM images of different volume drop-casted ReS₂ solution based MoS₂-ReS₂ heterostructure (a) MoS₂-ReS₂ 25 (b) MoS₂-ReS₂ 35 (c) MoS₂-ReS₂ 50 (d) MoS₂-ReS₂ 70 (e) Absorbance of MoS₂-ReS₂ heterostructure, absorption first increases with increasing ReS₂ and then decreases, indicating significant ReS₂-ReS₂ homo nanophase formed with MoS₂-ReS₂ hetero phase. Numbering in MoS₂-ReS₂ denotes the solution in μL dropcasted on MoS₂ flakes.

To confirm this hypothesis, SEM and UV-Visible spectroscopy have been performed with different amounts of drop-casted ReS₂ solution (25 μL – 70 μL) onto the MoS₂ (Figure 6). The FESEM images shown in Figures 4.9 (a)-(d) clearly revealed that the density of ReS₂ NSs

increases with an increasing amount of drop-casted ReS₂ NSs onto the VA-MoS₂. Thus, newer sites of heterojunctions are formed between MoS₂ and ReS₂ with an increased amount of ReS₂ NSs. In addition, the thickness of pre-deposited ReS₂ NSs is also increased as some of the newly drop-casted ReS₂ NSs reside over the previously deposited ReS₂ NSs. The corresponding absorption profile for pristine MoS₂ and MoS₂ flakes drop-casted with different amounts of ReS₂ NSs are shown in Figure 4.9 (e). It is evident from the absorbance graph that after drop-casting ReS₂ NSs onto the vertical flakes of MoS₂, absorption increases significantly in the broad visible-NIR range owing to the formation of heterojunction. The maximum absorption is observed for the 50 μ L solution based heterojunction. However, the absorption decreased with further increase in the amount of ReS₂ solution (70 μ L). Initially, absorption of heterojunction increased due to the synergetic effect of MoS₂ and ReS₂. The maximum absorption at 50 μ L is attributed to the optimized density of ReS₂ NSs for the formation of the heterojunction, where most of the MoS₂ flakes were coated with ReS₂. The incident light passing through heterojunction and reached the MoS₂, resulting in enhanced absorption from MoS₂-ReS₂ junction. In contrast, a thick cluster of ReS₂ NSs deposited over MoS₂ at 70 μ L solution hinders the carrier transportation and potential role of heterostructure between the MoS₂ and ReS₂. The decrement in absorption intensity of 70 μ L ReS₂ solution based heterojunction indicates that major portion of the incident light directly absorbs and scatters through ReS₂ and does not let it reach the interface due to dominance of ReS₂-ReS₂ nanophase over MoS₂-ReS₂ junction, supports our hypothesis and photodetector results.

Henceforth, we have compared the performance of pristine MoS₂ photodetector with 50 μ L ReS₂ solution-based MoS₂-ReS₂ heterostructure. Figures 4.10 (a) and (b) illustrate the spectral photoresponse of pristine MoS₂ and MoS₂-ReS₂ heterojunction spanning wide spectrum from visible to NIR regime (400–1100 nm). The inset of Figures 4.10 (a) and (b) show the cross-sectional view of pristine MoS₂ and MoS₂-ReS₂ heterojunction photodetector under illumination. It is evident from the photoresponse that a very minimal increment in current was observed for pristine MoS₂ under irradiation compared to dark current, while substantial increment in photocurrent was obtained for MoS₂-ReS₂ heterojunction (Figure 4.10 (c)). The enhanced photoresponse behaviour observed in MoS₂-ReS₂ heterojunction is owing to increased absorption in Visible–NIR regime.

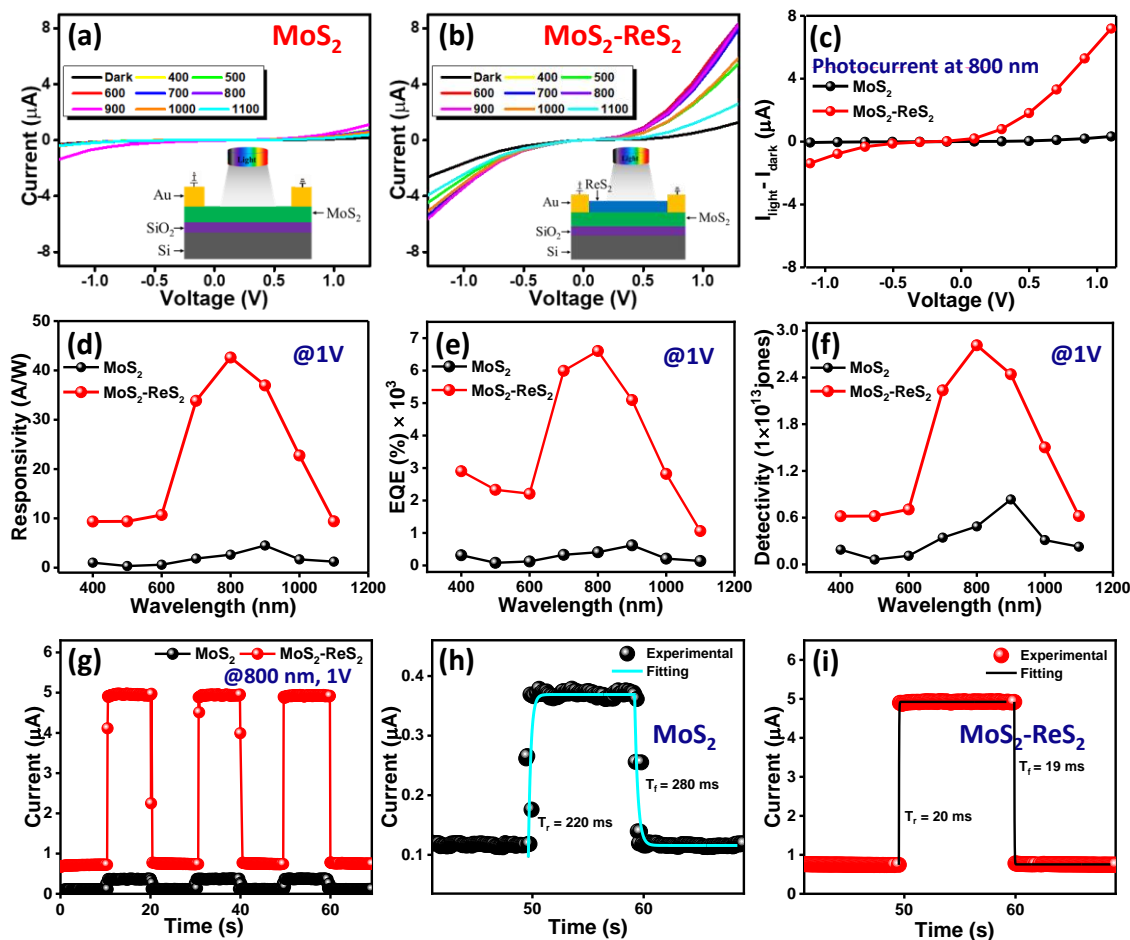


Figure 4.10 I-V characteristics of (a) Pristine MoS₂, (b) MoS₂-ReS₂ heterostructure, respectively. (c) Comparative photocurrent of MoS₂ and MoS₂-ReS₂ under incident radiation of 800 nm. (d) Responsivity, (e) Detectivity of bare MoS₂ and MoS₂-ReS₂ at 1 V under illumination of Visible-NIR radiation, respectively. (f) Comparative transient photoresponse. (g)-(h) Rise time and decay time of MoS₂ and MoS₂-ReS₂, respectively at 800 nm. (i) Comparison of pristine MoS₂ and MoS₂-ReS₂ heterojunction device performance, parameter: responsivity and response time. Inset of Figures 7 (a) and (b) shows the cross-sectional view of the device under illumination.

UV-Visible spectroscopy has been performed to verify the enhancement in the absorption of MoS₂-ReS₂ heterostructure compared to pristine MoS₂. The absorbance spectra of pristine MoS₂ and MoS₂-ReS₂ heterostructure are shown in Figure 4.9 (e). The absorbance spectra of MoS₂ exhibit two peaks A and B that corresponds to direct bandgap transition at the k-point of Brillion zone, and spin-orbit splitting in the valence band and interlayer coupling between multiple layers of MoS₂. It can be realized from the absorbance spectra that the MoS₂-ReS₂ heterostructure efficiently absorbed incident light in broad (Visible-NIR) wavelength range than the pristine MoS₂. This cannot be ascribed only to the cumulative response of absorption from MoS₂ and ReS₂ materials. However, absorption is prominently enhanced (especially in

NIR region) due to the formation of high-quality large-area heterointerface owing to interlayer interaction, which is attributed to the new charge transfer states due to the interface. The enhanced absorption in heterojunction produces more photo-excited charge carriers than the pristine MoS₂. The charge carriers rapidly separate due to the built-in electric field across the heterointerface and contribute to photocurrent after reaching the end electrodes under illumination. The poor photoresponse behaviour in pristine MoS₂ is attributed to the low absorption, high recombination rate and absence of a built-in electric field.

Table 4.2 Comparison of MoS₂-ReS₂ heterostructure photodetector with recently developed other 2D/2D heterostructure devices at moderate bias.

Device	Detection range	Responsivity (A/W)	Detectivity (Jones)	Self-powered	References
WS ₂ /ReS ₂	Visible (532 nm)	0.0018 @ V _d =1V	-	Yes	[27]
WSe ₂ /ReS ₂	Visible (532 nm)	3 @ V _g = -20V	8.39×10^{10}	Yes	[28]
MoS ₂ /NiTe ₂	Visible (405 nm)	0.392 @ V _d = 1V	1.2×10^9	No	[29]
MoS ₂ /MoSe ₂	UV-Visible (254-700 nm)	1.3 @ V _d = 5V	2.6×10^{11}	No	[30]
MoS ₂ /MoTe ₂	Visible-NIR (405-1310 nm)	0.86 @ V _d = -2V	2×10^{11}	Yes	[31]
MoS ₂ /WSe ₂	Visible-NIR (660-850 nm)	17.8 @ V _g =1V	-	No	[32]
MoS ₂ /BP	Visible-NIR (532-1550 nm)	22.3 @ V _d = 3V	3.18×10^{13}	Yes	[33]
MoS ₂ /ReS ₂	Visible (532 nm)	35.07 @ V _d = 2V,	-	No	[34]
MoS ₂ /ReSe ₂	Visible (633 nm)	6.75 @ V _d =1V	-	No	[35]
MoS ₂ -ReS ₂	Visible-NIR (400-1100 nm)	42.61 @ V _d =1V	2.81×10^{13}	Yes	This work

Responsivity is one of the important parameters of a photodetector, which evaluates the device performance. It quantifies the measured photocurrent per incident optical power, directly associated with efficiency of the device, expressed as follows:

$$R = \frac{I_{light} - I_{dark}}{P.A} = \frac{I_{photo}}{P.A} \quad (4.7)$$

Where I_{light} , I_{dark} , P and A are illumination current, dark current (absence of any light radiation), power density of incident light source, and photosensitive area of the device, respectively. Here, beam power of the incident wavelengths of monochromatic source used for

photodetector measurements were calibrated by standard Si photodetector and active area of the device is 0.125 cm². Figure 4.10 (d) depicts responsivity of MoS₂-ReS₂ heterojunction (red) and pristine MoS₂ (black), respectively at a low bias (1V) under Visible-NIR (400-1100 nm) illumination. The heterojunction possesses high responsivity of 42.46 A/W under illumination of 800 nm, which has largely surpassed the other reported 2D/2D heterojunction based photodetectors. Moreover, the responsivity of MoS₂-ReS₂ heterojunction is 16 times the pristine MoS₂ photodetector (2.63 A/W).

External quantum efficiency (EQE) is the photo-conversion efficiency of the device and is given by the following equation:

$$EQE = \frac{Rhc}{e\lambda} \times 100 \% \quad (4.8)$$

Here, h is Planck's constant, c is the speed of light and λ is the wavelength of incident light.

EQE for the heterostructure as well as for pristine MoS₂ is evaluated under a broad spectrum regime as demonstrated in Figure 4.11 (e). The calculated EQE for the MoS₂/Ga₂O₃ heterostructure and for pristine MoS₂ is $6.6 \times 10^3\%$ and $3.6 \times 10^2\%$, under 800 nm illumination. The heterostructure has 16 times higher EQE than the pristine MoS₂. An EQE greater than 100 % is evident of the fact that a higher number of electrons are extracted from a single incident photon, similar to typical photomultiplication photodetectors [36, 37]. This high EQE implies the highly sensitive nature of MoS₂-ReS₂ heterostructure even for the small optical signal. The high EQE can be attributed to the photoconductive gain of the device, which is defined by the following relation:

$$G = \frac{\tau}{\tau_{tr}} = \frac{\tau \mu V}{L^2} \quad (4.9)$$

where τ and τ_{tr} are the photogenerated carrier lifetime and carrier transit time, μ is the mobility, V is the applied bias voltage, and L is the channel length. The photoconductive gain is directly proportional to the photogenerated carrier lifetime and inversely proportional to carrier transit time. The high photo gain is attributed to the long carrier lifetime in trap states localized at the defects or surface of the semiconductor. Under light exposure, it traps one type of photo-excited charge carrier and allows others to circulate multiple times before recombination, resulting in more electrons being extracted from a single incident photon [58].

Another important characteristic that quantifies the photodetector performance is specific detectivity (D^*), which is evaluated by the given expression:

$$D^* = \frac{\sqrt{A} R}{(2eI_{\text{dark}})^{1/2}} \quad (4.10)$$

The estimated value of D^* evaluated using equation (4) is shown in Figure 4.11 (f) with different wavelength illumination at 1V for pristine MoS₂ and MoS₂-ReS₂ heterojunction photodetector. For heterojunction, a maximum D^* value of 2.81×10^{13} jones is achieved at 800 nm. To further explore the practical applicability and feasibility of MoS₂-ReS₂ photodetector, transient photoresponse measurements were carried out, which shows high reproducibility under periodical on-off switching of incident light. Under illumination, a sharp increment in photocurrent has been observed that rapidly decayed to the dark current after turning off the incident light as illustrated from I-T characteristics of pristine MoS₂ and MoS₂-ReS₂ heterojunction (Figure 4.14 (g)). It is evident from the temporal photoresponse that heterojunction leads to faster charge transport with a sharp rise in photocurrent. Using following exponential functions, the response time (rise/decay) is also evaluated:

$$I = I_{01} + A_1 e^{\frac{t}{\tau_r}} \quad (4.11)$$

$$I = I_{02} + A_2 e^{\frac{-t}{\tau_d}} \quad (4.12)$$

Where I_{01} , I_{02} are the steady state photocurrents, t is the time, A_1 and A_2 are the constants, and τ_r , τ_d are the rise time constant and decay time constant, respectively. For MoS₂-ReS₂ heterojunction, the rise/fall time is 20/19 ms, whereas, for pristine MoS₂, the response time is 220/280 ms at 1V under 800 nm, shown in Figures 4.41 (h) and (i). In addition to this, fast optical switching with low response time (order of millisecond) has been observed in heterojunction for all other incident Visible-NIR radiation as well. The substantial quenching of carrier recombination and efficient carrier transportation at the interface of the MoS₂-ReS₂ heterostructure leads to faster charge transport, thus, introduces significant improvement in photoresponse behavior of proposed heterostructure. Thereby, above analysis indicates that high absorption leads to high responsivity, while fast carrier transport at the MoS₂-ReS₂ heterointerface improves the response time. Table 4.2 illustrates the comparison of essential performance parameters of MoS₂-ReS₂ photodetector with recently developed 2D heterostructures at moderate bias. The superior performance of MoS₂-ReS₂ heterojunction results in a self-powered response of the device.

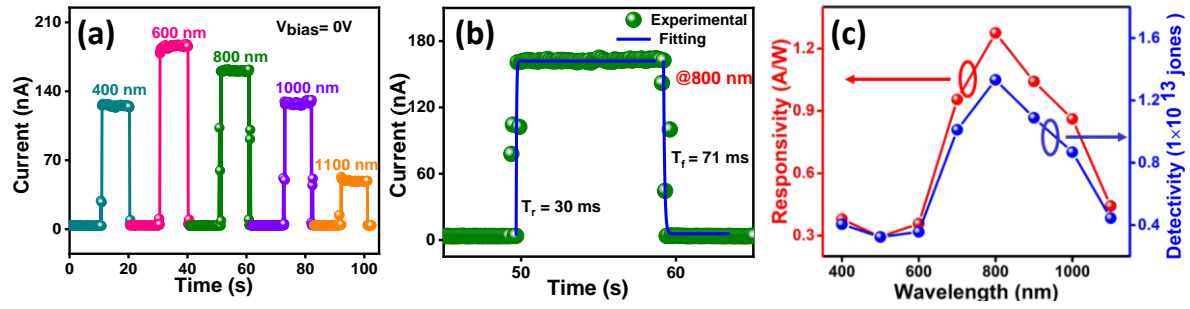


Figure 4.11 (a) Self-bias transient photoresponse of MoS₂-ReS₂ heterostructure at spectral range covering from 400-1100 nm. (b) Response time at 800 nm. (c) Responsivity and Detectivity of MoS₂-ReS₂ at self-driven mode under visible-NIR radiation.

Table 4.3 Comparison of self-powered photoresponse

Device	Detection range	Responsivity (A/W)	Detectivity (Jones)	References
MoS ₂ /GeSe	Visible-NIR (380-1064 nm)	0.10	1.03×10^{10}	[39]
MoS ₂ /MoTe ₂	Visible-NIR (405-1310 nm)	0.62	-	[31]
MoS ₂ /MoTe ₂	Visible-NIR (420-800 nm)	3.8×10^{-2}	-	[40]
MoS ₂ /WSe ₂	Visible (532 nm)	1×10^{-2}	-	[41]
MoS ₂ /WS ₂	Visible (532 nm)	4.36×10^{-3}	4.36×10^{13}	[42]
MoS ₂ -ReS ₂	Visible-NIR (400-1100 nm)	1.28	1.34×10^{13}	Present work

Furthermore, our fabricated MoS₂-ReS₂ heterostructure photodetector exhibits incredible self-driven features, which means that the device can generate the signal current under light irradiation without applying any external source of biasing ($V=0$). Figure 4.11 (a) illustrates that MoS₂-ReS₂ heterojunction works efficiently in self-driven mode under broad (400-1100 nm) illumination. The self-driven feature of device is ascribed to the built-in electric field owing to the high-quality interface of n-n heterojunction with a large active area that facilitates the spatial separation of charge carriers. Additionally, type II band alignment favours the charge transport in self-bias mode under illumination. Hence, photoresponse of MoS₂-ReS₂ validates the proposed charge carrier dynamics, thus, corroborating the evaluated type II band alignment. However, no self-driven response was observed for pristine MoS₂ photodetector. Figure 4.11 (c) shows the responsivity and detectivity of MoS₂-ReS₂ photodetector, calculated at different wavelength under self-driven mode. The device carries a high value of responsivity and detectivity of 1.28 A/W and 1.34×10^{13} Jones, respectively, at 800 nm under the self-bias condition, which is significantly higher than other reported self-powered heterojunction (Table

4.3). The device also exhibits a fast response with rise time and decay time of 31 ms and 70 ms, respectively, under optical switching (Figure 4.11 (b)). Such excellent performance of the device falls in the category of precious self-driven photodetectors, which can be further utilized in flexible and wearable future optoelectronics.

4.2.1.3 Conclusions

To summarize, we comprehensively investigated the band alignment and charge transfer mechanism at the MoS₂-ReS₂ heterointerface. Raman and PL spectroscopy demonstrated strong interlayer interaction between them. The red and blue shift observed in Raman and PL measurements, owing to the variation of electron density, suggests the extraction and injection of electrons in MoS₂ and ReS₂, respectively. Careful investigation of XPS and UPS measurement confirms the formation of type II band alignment, which is highly desirable for efficient charge transport and optoelectronic application. Evaluated band alignment proposed the charge transfer mechanism in which electrons transferred from MoS₂ to ReS₂ and holes move in the opposite direction, validating the results obtained from Raman, PL and XPS spectra. As a proof of concept, a highly sensitive broadband photodetector has been fabricated to demonstrate the practical applicability of this heterostructure. Our fabricated photodetector shows superior photoresponse than other reported 2D heterostructure based photodetectors. This work elevates the research in the area of 2D hetero-interface and paves the way for the development of novel devices.

4.2.2 MoS₂/Ga₂O₃ heterostructure

Gallium oxide (Ga₂O₃) is an ultra-wide bandgap semiconductor ($E_g \sim 4.5$ to 4.9 eV) with intrinsic solar-blindness, high absorption coefficient, and excellent electrical and optical properties [43, 44]. Its response spectrum encompasses the prominent UV-C region, making Ga₂O₃ an ideal material for solar-blind photodetection. The convergence of the ultra-wide bandgap of Ga₂O₃, which responds to the ultraviolet spectrum, and the narrow bandgap of MoS₂, which is active in the visible–NIR spectrum, provides the possibility for the development of a photodetector with broad-range of sensitivity. Studies on the integration of MoS₂ with Ga₂O₃ are limited, with a few reports on the utilization of MoS₂/Ga₂O₃ heterojunctions for solar-blind photodetectors [45, 46]. To the best of our knowledge, there have been no reports in the literature on utilizing this combination for the fabrication of a broadband photoresponse.

4.2.2.1 Experimental Section

4.2.2.1.1 Material synthesis

MoS₂ film of ~ 10 nm was deposited on Si/SiO₂ substrate by RF magnetron sputtering using a 99.99% pure 2H-MoS₂ target (Kurt J. Lesker). Prior to deposition, substrates were cleaned in ultra-sonication using DI water, acetone and propanol for 30 minutes, followed by blow-drying with a N₂ jet. A base vacuum of 2×10^{-6} Torr was attained inside sputtering chamber before deposition. The MoS₂ film was deposited at room temperature for 10 minutes. During sputtering, RF power and Ar gas pressure were set to 25 W and 10 mTorr, respectively. Then, as-deposited MoS₂ film was annealed under Ar ambient at 700 °C for 2 hours. To fabricate MoS₂/Ga₂O₃ heterojunction, Ga₂O₃ (~5 nm) was directly deposited over MoS₂ film via sputtering. The deposition was carried out at room temperature with Ar as the working gas (with 3% O₂), deposition pressure of 3 mTorr, and RF power of 100 W.

4.2.2.1.2 Material characterizations

For optical absorption measurements, samples were deposited on the quartz substrate. Perkin Elmer Lambda 950 UV-VIS-NIR spectrometer was used to record the absorbance spectra of MoS₂, Ga₂O₃, and MoS₂/Ga₂O₃. Raman and PL spectroscopy (Horiba LabRAM HR Evolution) measurements were carried out at room temperature with an excitation wavelength of 532 nm. XPS and UPS were performed under an ultrahigh vacuum chamber using a monochromatic Al K α X-ray source ($h\nu = 1486.68$ eV) and He (I) discharge lamp ($h\nu = 21.2$ eV), respectively. An Agilent 5500 scanning probe microscopy was used to take the atomic force microscopy (AFM) images. KPFM measurements were done by amplitude modulation using a Budget Sensors Cr/Pt coated Multi 75-EG tip as described in chapter 2.

4.2.2.1.3 Device fabrication and photoresponse measurements

For photodetector fabrication, Au (In) strip electrodes were deposited on top of MoS₂ (Ga₂O₃) with an interspacing of 3.5 mm via a physical shadow mask using a thermal evaporator. The photoresponse behavior of the heterojunction was evaluated by two light sources: Bentham PVE 300 which consists of a monochromator (TMC 300) was used to produce monochromatic light from visible to NIR region (400-1200 nm) and a hand-held UV lamp (dual wavelength: 254 nm and 365 nm, intensity: $17 \mu\text{W cm}^{-2}$) that offers illumination in UV region. Electrical measurements were performed using Keithley 6430-SMU. The response time of the fabricated photodetector was evaluated using red laser (HOLMARC)/ pen-ray UV lamp combined with an optical chopper and a digital oscilloscope (Tektronix MDO32). The active area of the photodetector was 0.175 cm^2 . All the device measurements were carried out under ambient

conditions in an optically enclosed chamber to avoid any hindrance from the surrounding. To check the stability of the fabricated photodetector, the device was stored in the laboratory (ambient condition) for months and re-examined the device in a similar manner.

4.2.2.2 Results and discussion

Figure 4.12 (a) illustrates Raman spectra of pristine MoS₂ and MoS₂/Ga₂O₃ heterojunction. The Raman spectrum of MoS₂ displays two intense peaks at 381.6 cm⁻¹ and 406.4 cm⁻¹ corresponding to in-plane (E_{2g}^1) and out-of-plane (A_{1g}) vibrational modes, respectively [47]. The separation between A_{1g} and E_{2g}^1 modes defines the number of layers present in the system, which is found to be 24.8, implying presence of few layers of MoS₂ [48]. No distinct change in the position or intensity of MoS₂ Raman peaks is observed, signifying the absence of stress or strain upon adding of the overlaying Ga₂O₃ layer [49]. Also, the top ultrathin Ga₂O₃ film is amorphous in nature, hence no peaks corresponding to any phase of Ga₂O₃ were observed in the Raman spectra [50]. To probe the interfacial charge transfer kinetics, PL was performed for pristine and heterojunction as depicted in Figure 4.12 (b). MoS₂ typically exhibits two characteristic peaks of PL emission at 1.81 eV and 1.97 eV corresponding to A and B excitons, respectively. The A and B excitons arise from direct bandgap transition at the K-point of the Brillion zone and the spin-orbit coupling in the valence band [51]. The PL intensity of MoS₂ is significantly decreased in heterojunction, suggesting PL quenching which is ascribed to the efficient charge transfer between MoS₂ and Ga₂O₃ [52].

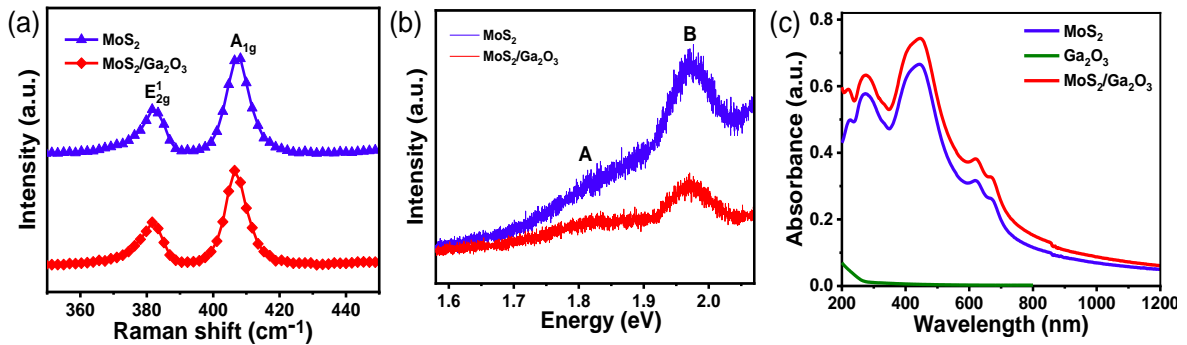


Figure 4.12 (a) Raman spectra (b) PL spectra (c) Absorbance spectra of pristine MoS₂, bare Ga₂O₃ and MoS₂/Ga₂O₃ on quartz substrate.

According to the optical absorbance measurements, MoS₂ has the ability to absorb radiation in the broad visible-NIR region as shown in Figure 4.12 (c). The absorbance spectra of MoS₂ consist of A and B exciton peaks at 620 nm and 670 nm, respectively. In addition, a shoulder peak was observed at ~445 nm, which is associated with the van Hove singularity [53]. The

Ga₂O₃, on the other hand, can only absorb UV-C light, and hardly absorbs any radiation in the visible range due to its wideband gap. Nevertheless, MoS₂/Ga₂O₃ heterojunction demonstrates improved absorption in the entire UV to NIR spectrum owing to synergistic effect of MoS₂ and Ga₂O₃ and strong interlayer coupling between them. This strong interlayer coupling leads to more efficient transport of photo-generated carriers across the junction, resulting in a continuous energy distribution and reducing potential energy barriers [54]. This, in turn, enhances the overall absorption of the heterojunction. Therefore, compared to pristine MoS₂ and Ga₂O₃, the MoS₂/Ga₂O₃ heterojunction exhibits significantly broadened optical absorbance.

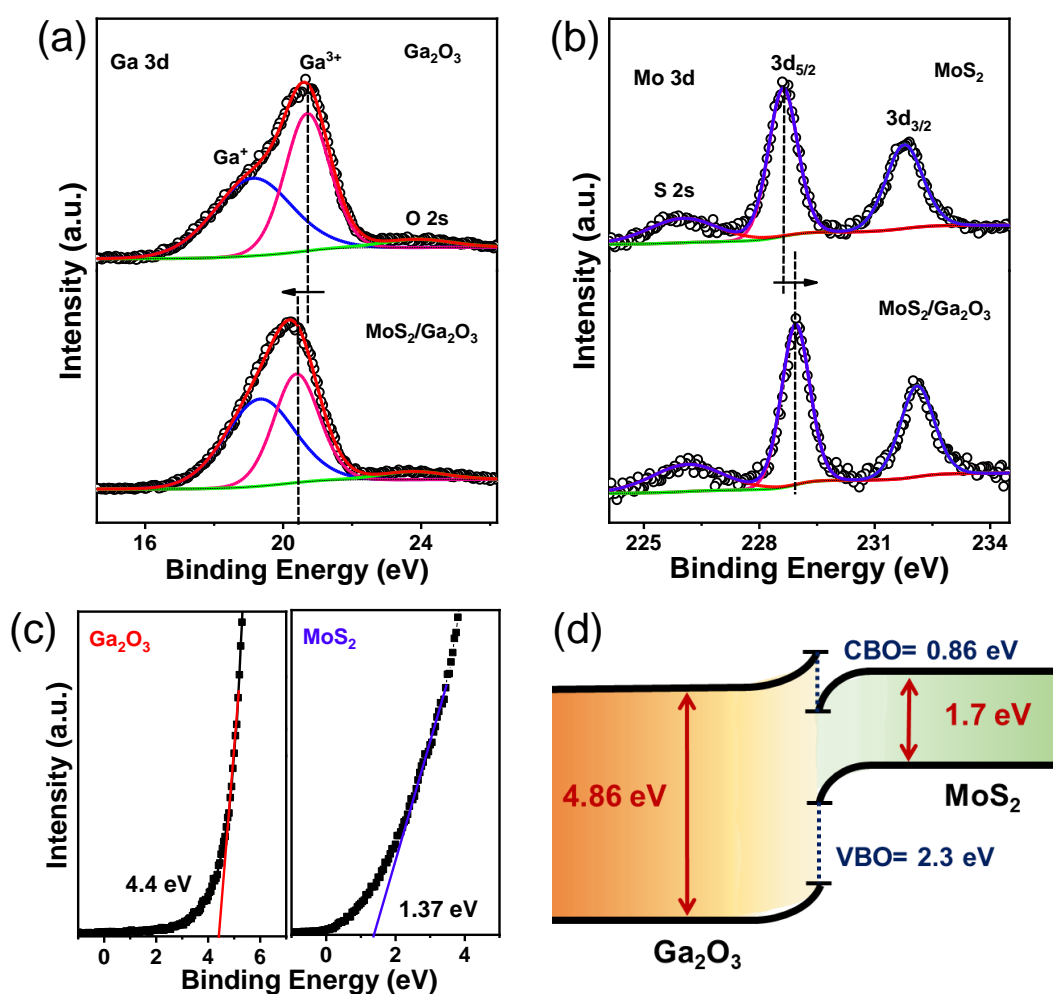


Figure 4.13 Binding energy measurements (XPS-UPS) and band-alignment of MoS₂/Ga₂O₃ heterojunction. (a), (b) High-resolution core-level XPS spectra of Ga 2p and Mo 3d for Ga₂O₃, MoS₂ and MoS₂/Ga₂O₃ interface. (c) Valence band spectra of pristine MoS₂ and Ga₂O₃. (d) Energy band-diagram of MoS₂/Ga₂O₃ heterostructure, exhibiting type-I alignment.

The charge dynamic and carrier extraction at the interface of any heterojunction is a critical attribute which needs to be investigated thoroughly in order to regulate and understand the device performance. In this regard, first and foremost, band-alignment was investigated using XPS and UPS technique. To study the change in chemical ambient as one goes down from Ga₂O₃ to MoS₂, XPS depth profile was performed where the data was recorded after etching the surface with 1 KeV Ar⁺ ion in each step. Since the top Ga₂O₃ film is ~ 5 nm, and the XPS being a surface-sensitive technique can give information about a depth of <10 nm, hence the XPS was recorded at a 1.3 nm etch rate to precisely probe the MoS₂/Ga₂O₃ interface.

Figures 4.13 (a) and (b) display the XPS spectra of the Ga 3d core levels for both pristine Ga₂O₃ and the MoS₂/Ga₂O₃ heterojunction and Mo 3d core levels for pristine MoS₂ and MoS₂/Ga₂O₃ heterojunction. The Ga 3d core level is deconvoluted into two peaks at 20.7 eV and 19.12 eV, which corresponds to the binding energy of Ga³⁺ (stoichiometric Ga₂O₃) and Ga⁺ (sub-stoichiometric GaO), respectively [45]. Additionally, a small peak or "dune" is also observed at 23.9 eV, which is associated with O 2s. The core level of Mo 3d is split into two peaks, Mo 3d_{5/2} and Mo 3d_{3/2} located at 228.62 eV and 231.8 eV, respectively corresponding to the Mo⁺⁴ oxidation state. These binding energy positions of Ga 3d and Mo 3d core levels align well with previously reported values for Ga₂O₃ and MoS₂ [45, 55]. A shift in the binding energy of the Ga 3d and Mo 3d core level was recognized at the MoS₂/Ga₂O₃ heterojunction, which is a result of charge transfer at the interface. The higher binding energy shift in Mo 3d core-level spectra indicates slight negatively charged in MoS₂, while the lower binding energy shift in Ga 3d core-level spectra suggests slight positively charged in Ga₂O₃ after forming heterostructure [24]. This shift in core-level spectra directly indicates the presence of interlayer coupling between MoS₂ and Ga₂O₃.

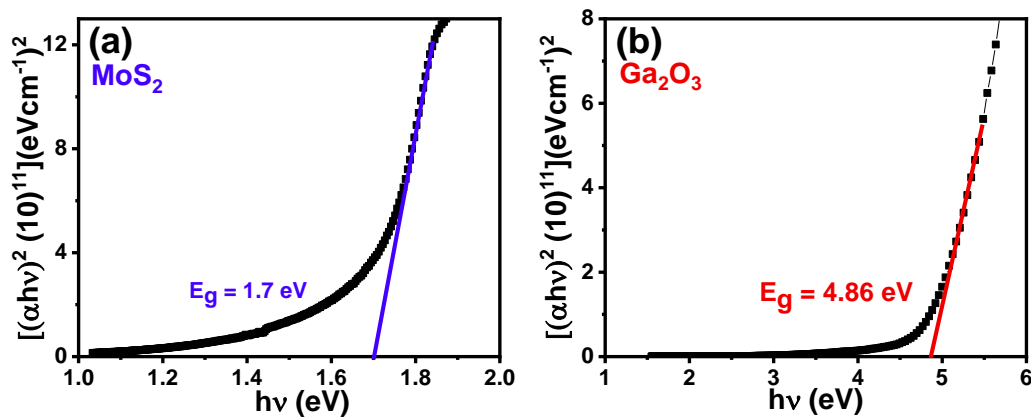


Figure 4.14 Bandgap of (a) MoS₂ and (b) Ga₂O₃ obtained from Tauc plot

The position of VBM was determined by extrapolating a linear fit of the leading edge of the valence band spectra relative to the Fermi level. The VBM of Ga₂O₃ and MoS₂ were evaluated to 4.4 eV and 1.37 eV, respectively, as shown in Figure 4.13 (c). The VBO at the MoS₂/Ga₂O₃ interface was extracted by Kraut's rule [25]:

$$VBO = (E_{Mo\ 3d}^{MoS_2} - E_{VBM}^{MoS_2}) - (E_{Ga\ 3d}^{Ga_2O_3} - E_{VBM}^{Ga_2O_3}) + \Delta E_{CL}(i) \quad (4.13)$$

Where, $\Delta E_{CL}(i) = (E_{Ga\ 3d}^{MoS_2/Ga_2O_3} - E_{Mo\ 3d}^{MoS_2/Ga_2O_3})$ is the binding energy difference between Mo 3d and Ga 3d core-levels measured at the MoS₂/Ga₂O₃ heterointerface. The term $(E_{Mo\ 3d}^{MoS_2} - E_{VBM}^{MoS_2})$ and $(E_{Ga\ 3d}^{Ga_2O_3} - E_{VBM}^{Ga_2O_3})$ represent valence band edges with reference to core-levels of MoS₂ and Ga₂O₃, respectively. The evaluated VBO at the heterojunction is 2.3 ± 0.1 eV. The positive value of VBO signifies VBM of MoS₂ is lies above the VBM of Ga₂O₃.

The CBO is determined using VBO and bandgap values of MoS₂ and Ga₂O₃ by the following equation:

$$CBO = E_g^{MoS_2} - E_g^{Ga_2O_3} + VBO \quad (4.14)$$

where $E_g^{MoS_2}$ and $E_g^{Ga_2O_3}$ represents the bandgap of MoS₂ and Ga₂O₃. The bandgap of MoS₂ (1.7 eV) and Ga₂O₃ (4.86 eV) were determined using Tauc plots, as shown in Figure 4.14. The measured CBO at the MoS₂/Ga₂O₃ heterointerface was found to be -0.86 ± 0.1 eV.

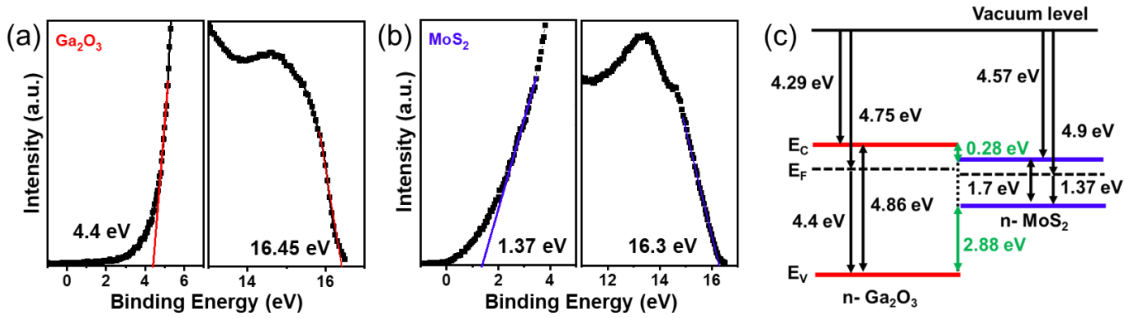


Figure 4.15 Ultraviolet photoelectron spectroscopy (UPS) spectra of (a) pristine MoS₂, (b) amorphous Ga₂O₃, and (c) Energy band-alignment by Anderson's affinity rule.

The work function and electron affinity of MoS₂ and Ga₂O₃ were determined by UPS spectra (Figures 4.15 (a) and (b)) using equations (4.7) and (4.8). The calculated values of work function and electron affinity are 4.9 eV and 4.57 eV for MoS₂, and 4.75 eV and 4.29 eV for Ga₂O₃, respectively. Using Anderson's electron affinity rule [56], the CBO and VBO at the MoS₂/Ga₂O₃ interface were estimated to be 0.28 eV and 2.88 eV, respectively (Figure 4.15), which also exhibit similar band-alignment as obtained from the Kraut's rule (Figure 4.13 (d)). These results confirm type-I band alignment formed at the MoS₂/Ga₂O₃ heterojunction.

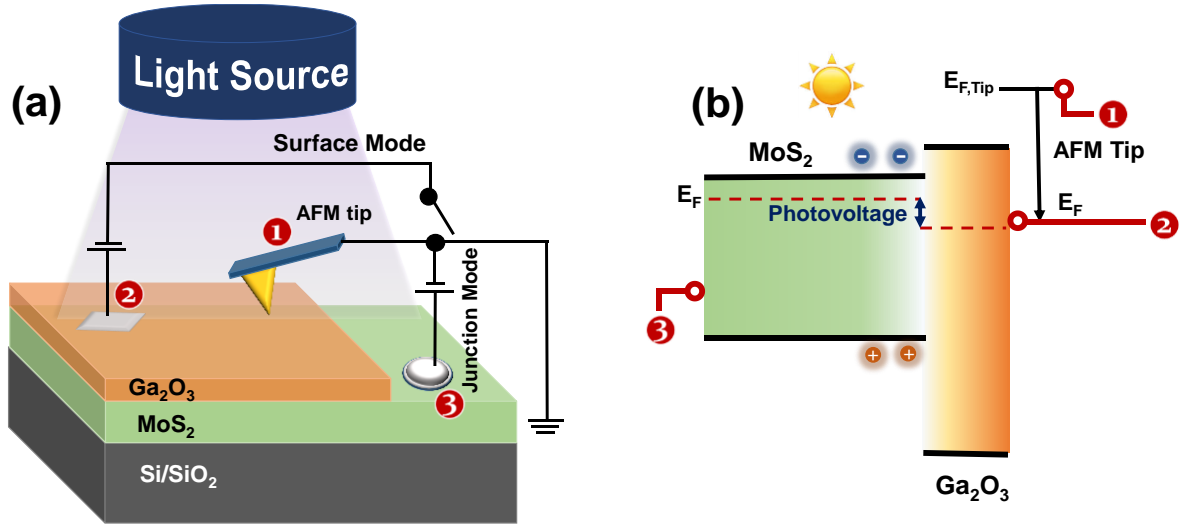


Figure 4.16 (a) Schematic illustration of surface and junction mode used for KPFM measurement. (b) Schematic representation of energy level-alignment between MoS₂ and Ga₂O₃ under illumination.

Taking a step further, KPFM measurements were carried out at MoS₂/Ga₂O₃ heterojunction in two different modes: Surface mode and junction mode to investigate the interface charge dynamics. A schematic representation of the KPFM setup for the sample measurements under surface and junction mode is shown in Figure 4.16 (a). In surface mode configuration, bias is applied between the KPFM tip and Ga₂O₃ while in junction mode configuration, bias is applied between the tip and bottom layer of MoS₂. Figure 4.16 (b) illustrates the energy level alignment of MoS₂ and Ga₂O₃ under white light illumination. Under illumination, photo-excited charge carriers are generated, which then get separated due to the built-in potential at the MoS₂/Ga₂O₃ heterojunction, creating a non-equilibrium state. In this state, the Fermi level gets split into two separate levels, known as quasi Fermi-levels [57]. The difference in energy between these two levels is known as the quasi-Fermi level splitting, quantified as photovoltage generated at the heterojunction as depicted in Figure 4.16 (b). The quasi-Fermi levels (or photovoltage) are crucial for evaluating the device performance precisely.

Initially, the local surface potential of bare MoS₂ was evaluated for reference. The surface morphology and surface potential map of bare MoS₂ are shown in Figure 4.17. The average surface potential of bare MoS₂ under dark and light conditions does not show any difference because the work function of MoS₂ is relatively constant and does not change significantly in the presence of light. The distribution of the average surface potential of heterojunction in two different modes surface and junction is evaluated in dark conditions as illustrated in Figure 4.18. In surface mode, the average surface potential value is found to be 426 mV while in junction mode, the surface potential value is 526 mV. In surface mode, surface potential

corresponds to the contact potential difference (CPD) between the tip and Ga₂O₃. Thus, any variation in surface potential is related to the work function of the top layer of Ga₂O₃. Since the top Ga₂O₃ film is only ~ 5 nm thin in nature, the estimated surface potential on the Ga₂O₃ surface may be influenced by the charge transfer between MoS₂ and Ga₂O₃. In junction mode, surface potential comes from the CPD between the tip and Ga₂O₃ along with the junction voltage present at MoS₂/Ga₂O₃ heterointerface. Thus, the built-in potential of the MoS₂/Ga₂O₃ interface is determined by subtracting the surface potential values in two modes, which comes to 100 mV. This built-in potential in the heterojunction facilitates the separation of charge carriers at the interface.

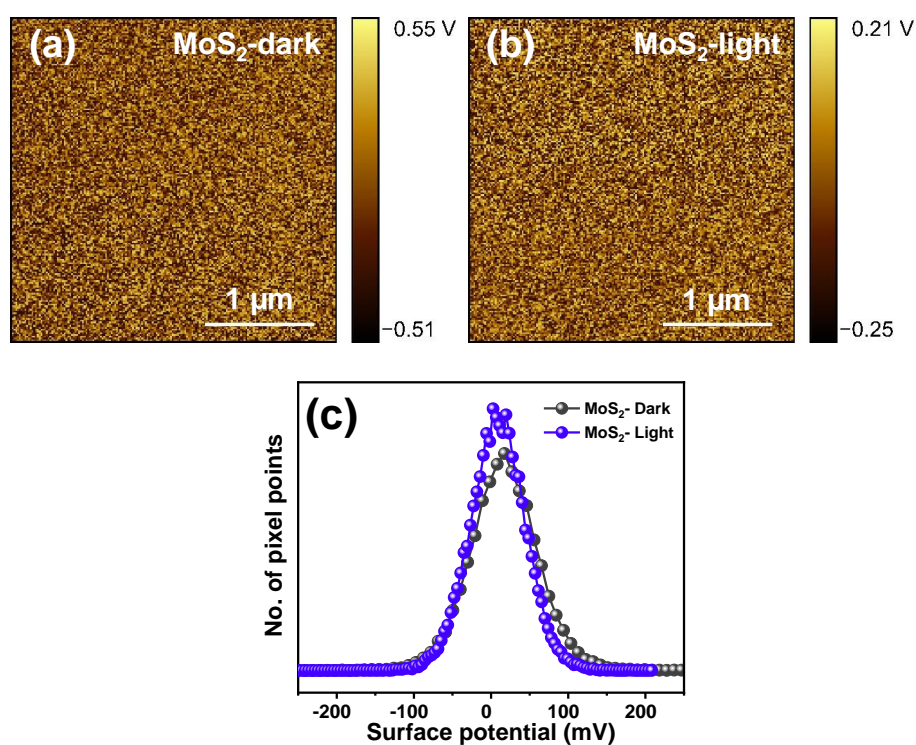


Figure 4.17 (a) and (b) Surface potential images of pristine MoS₂ in dark and light, (c) Distribution of the surface potential of MoS₂ under dark and white light conditions

Figures 4.19 (a)-(c) represent the topography and surface potential images of the MoS₂/Ga₂O₃ heterojunction in two different modes under illumination. In surface mode under illumination, the average surface potential of heterojunction is 410 mV, which is slightly less than the surface potential value observed under dark conditions (426 mV). Generally, the change in surface potential in Ga₂O₃ in the surface mode is not expected because the work function of Ga₂O₃ is constant. Furthermore, Ga₂O₃ is not sensitive to white light. Therefore, a negative shift observed in surface potential in light conditions with respect to dark is attributed to the charge transfer from Ga₂O₃ to MoS₂. In junction mode, heterojunction shows an average surface

potential value of 550 mV. In junction mode, a positive shift is observed in surface potential values in light with reference to dark conditions. Ga₂O₃ is quite thin and showed optical transparency for white light, underlying MoS₂ can strongly absorb the white light due to its narrow bandgap and generate electron-hole pairs. The photo-excited electrons of MoS₂ drift towards Ga₂O₃, hence the excess charge carriers in Ga₂O₃ under illumination, shifts the Fermi-level upward. Thus, the difference in surface potential values in two modes under illumination represents the photovoltage generated at the MoS₂/Ga₂O₃ interface. When exposed to light, this built-in potential allows for efficient separation of photo-generated electron-hole pairs at the interface, resulting in the generation of a photovoltage.

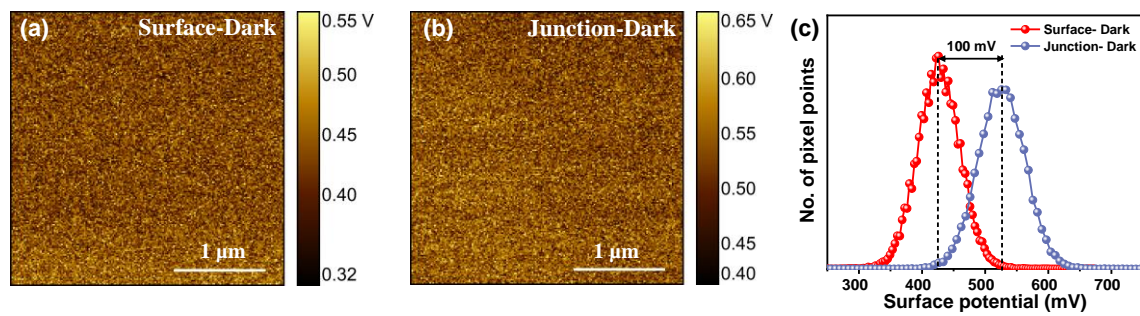


Figure 4.18 Surface potential images of MoS₂/Ga₂O₃ heterojunction in (a) Surface mode and (b) Junction mode under dark (c) Distribution of the surface potential of MoS₂ /Ga₂O₃ in two different modes under dark conditions.

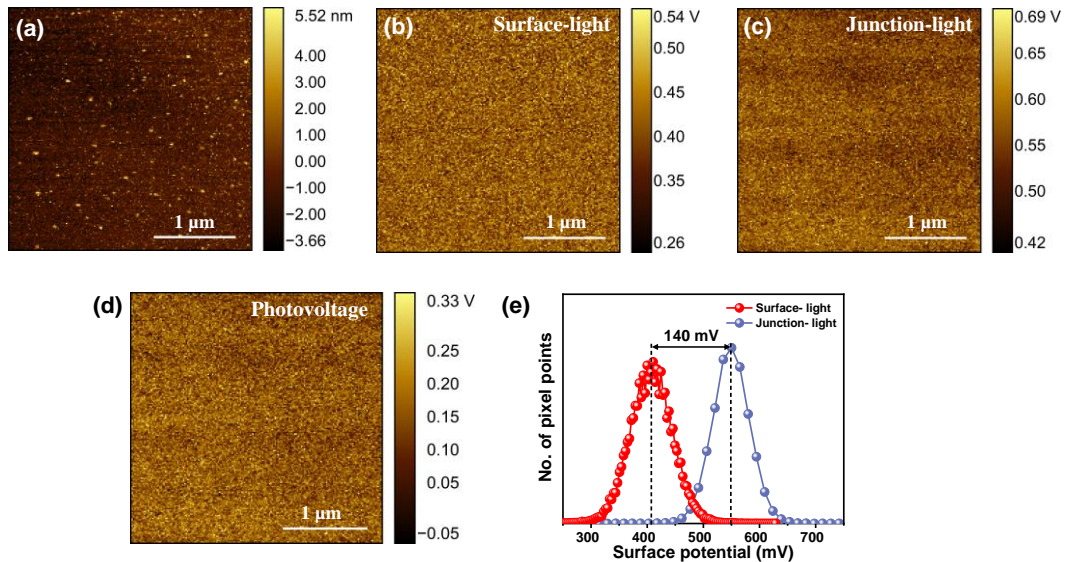


Figure 4.19 (a) Surface topography of MoS₂/Ga₂O₃ (Ga₂O₃ film on top of MoS₂), (b) and (c) are surface potential images of MoS₂/Ga₂O₃ heterojunction in surface and junction mode under white light illumination, (d) Photovoltage map, (e) Surface potential profiles for MoS₂ /Ga₂O₃ sample in two different modes under illumination.

Finally, we fabricated MoS₂/Ga₂O₃ heterojunction to test its photodetection capabilities and found that the device showed broadband photoresponse. A similar reference device of pristine MoS₂ was also fabricated to compare the photoresponse behaviour of heterostructure. Figures 4.20 (a) and (b) demonstrate the spectral photoresponse for pristine MoS₂ and MoS₂/Ga₂O₃ heterojunction over a broad spectrum range from UV-C to NIR (254-1200 nm). The insets of Figures 4.20 (a) and (b) present a schematic of the cross-sectional view of the fabricated photodetectors. The pristine MoS₂ consists of symmetric Au contacts that exhibit nearly (pseudo) Ohmic behavior. To fabricate heterojunction devices, we selected Au and In as the Ohmic contact electrodes for MoS₂ and Ga₂O₃, respectively, resulting in diode-like characteristics due to junction formation. The photoresponse of pristine MoS₂ showed only a slight increase in current upon exposure to light (visible-NIR) as compared to its dark current while, MoS₂/Ga₂O₃ heterojunction exhibited a substantial increment in photocurrent in broad spectrum regime (UV-C to NIR), depicted in Figure 4.20 (c). The enhanced broadband photoresponse of MoS₂/Ga₂O₃ heterostructure arises due to increased absorption and strong built-in potential at the interface. The increased absorption in the heterojunction, due to the formation of a high-quality heterointerface through interlayer interaction, generates a greater number of photo-excited charge carriers as compared to pristine MoS₂.

The built-in electric field across the MoS₂/Ga₂O₃ heterointerface facilitates the rapid separation of charge carriers, which subsequently contribute to the photocurrent. In contrast, the poor photoresponse of pristine MoS₂ is attributed to its high carrier recombination, and the absence of a built-in electric field. This behavior was further scrutinized by temporal photoresponse of pristine MoS₂ and MoS₂/Ga₂O₃ heterojunction under different (Visible, UV-A and UV-C) light illumination. Time-dependent photocurrent plots (Figures 4.20 (e)-(f)) clearly depict that pristine MoS₂ only responds to visible (600 nm) light with a slight increment in photocurrent from $\sim 0.34 \mu\text{A}$ to $0.37 \mu\text{A}$ ($\Delta I = 0.03 \mu\text{A}$) and showed negligible or no response under UV-A (365 nm) and UV-C (254 nm) radiation. However, under identical visible illumination, MoS₂/Ga₂O₃ heterojunction generates a large photocurrent from $\sim 5 \mu\text{A}$ to $12 \mu\text{A}$ ($\Delta I = 7 \mu\text{A}$), two orders of magnitude greater than the pristine MoS₂. Moreover, MoS₂/Ga₂O₃ heterostructure exhibits enhanced photocurrent in UV-A and UV-C illumination. Hence, MoS₂/Ga₂O₃ heterojunction manifests its potential in broadband light detection. Further, photodetector performance was evaluated by calculating its figures of merit i.e., responsivity (R), external quantum efficiency (EQE), and specific detectivity (D^*). The estimated values of responsivity as a function of wavelength for pristine MoS₂ and MoS₂/Ga₂O₃ heterostructure

are displayed in Figure 4.20 (g). Heterostructure exhibits high responsivity, more than the pristine MoS₂. It is observed that both photodetectors exhibit maximum photoresponse in the NIR region corresponding to the MoS₂ bandgap. MoS₂/Ga₂O₃ consists of high responsivity of 171 A/W⁻¹ under 900 nm illumination, as opposed to 0.55 A/W⁻¹ for pristine MoS₂. Additionally, the heterostructure exhibits significant responsivity even in UV-A (1.91 A/W⁻¹) and UV-C (1.88 A/W⁻¹) regions. EQE for the heterostructure as well as for pristine MoS₂ is evaluated under a broad spectrum regime as demonstrated in Figure 4.20 (h). The calculated EQE for the MoS₂/Ga₂O₃ heterostructure and for pristine MoS₂ is 2.4 × 10⁴ % and 76.5 % under 900 nm illumination. The heterostructure has 315 times higher EQE than the pristine MoS₂. An EQE greater than 100 % is evident of the fact that a higher number of electrons are extracted from a single incident photon, similar to typical photomultiplication photodetectors [36, 37]. This high EQE implies the highly sensitive nature of MoS₂/Ga₂O₃ heterostructure even for the small optical signal.

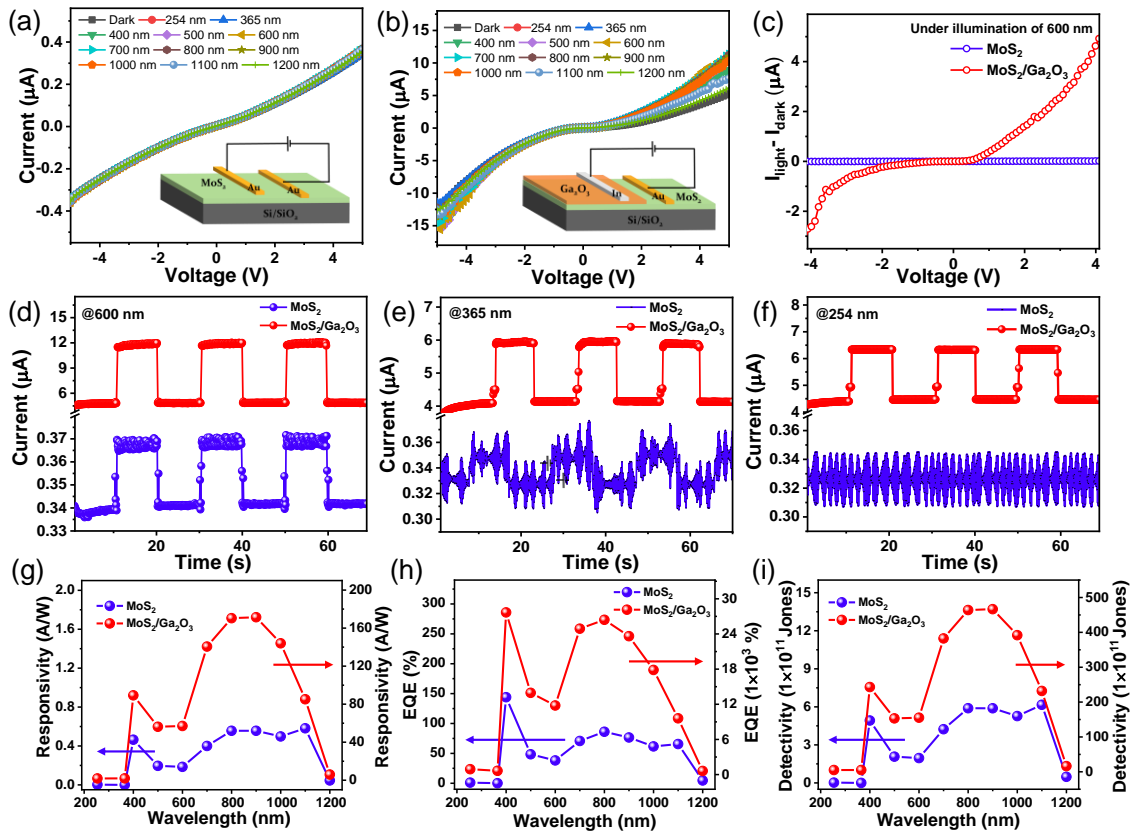


Figure 4.20 (a,b) I-V Characteristics of MoS₂ and MoS₂/Ga₂O₃ heterojunction under dark and light condition. (c) Comparative photocurrent of MoS₂ and heterojunction under incident light of 600 nm. (d-f) Temporal response of MoS₂ and MoS₂/Ga₂O₃ heterojunction devices under incident radiation of 600 nm, 365 nm and 254 nm, respectively. Comparative response plot between pristine MoS₂ and MoS₂/Ga₂O₃ heterojunction for (g) Responsivity, (h) EQE, and (i) Detectivity at 5V biasing as a function of wavelength.

Another figure-of-merit, specific detectivity is also evaluated for pristine MoS₂ and MoS₂/Ga₂O₃ heterostructure with respect to wavelength as illustrated in Figure 4.20 (i). The estimated detectivity for the heterostructure is of the order of $\approx 10^{13}$ Jones, which is much higher than the pristine MoS₂ photodetector ($\approx 10^{11}$ Jones). The high value of detectivity is observed under 900 nm illumination, indicating a higher ability to detect weak optical signals in the NIR region. For the UV-A and UV-C region, the detectivity is found to be 5.2×10^{11} Jones and 5.1×10^{11} Jones, respectively, which is comparable to the reported UV photodetectors.[59] The primary focus of the previous research on MoS₂/Ga₂O₃ heterostructures has been limited to the UV-C (solar blind) region.[45, 46] Other 2D/3D heterostructures have also been limited to either the UV-A/UV-C or Visible/NIR spectrum regions [50, 60, 61]. Therefore, the investigation of MoS₂/Ga₂O₃ heterostructure across a broader range of wavelengths is a crucial step in advancing optoelectronic technology by providing a deeper understanding of the material's properties and potential applications in this field. To better understand the photoresponse characteristics of MoS₂/Ga₂O₃ heterostructure in the broad spectrum, we measured the transient photocurrent (Figure 4.21). The bias voltage was kept constant at 1V during the measurement of the transient photo-response. The incident light radiation was periodically switched on/off in intervals of 10 seconds. Under various wavelength illuminations, consistent and repeatable photocurrent was observed without degeneration or persistent photoconductivity. However, it should be noted that the maximum photocurrent and responsivity occur at different wavelengths due to variations in incident light power density.

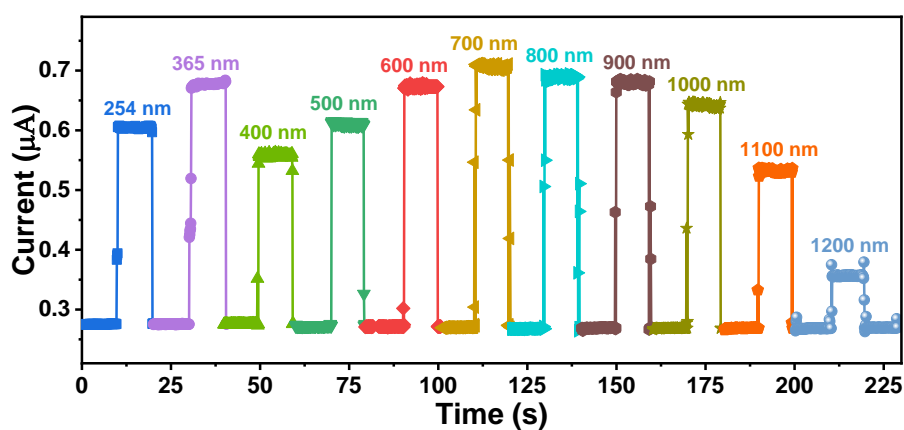


Figure 4.21 Transient photoresponse of MoS₂/Ga₂O₃ heterojunction from deep UV to NIR at low bias (1V).

The photodetector response speed (rise/fall time) is a crucial factor, particularly for applications in optical communication and imaging. In this study, the response speed of the MoS₂/Ga₂O₃

heterojunction photodetector was evaluated by utilizing an optical chopper to generate pulsed light as shown in Figure 4.22 (a). The photovoltage variation was then recorded using an oscilloscope to determine the response speed. Figures 4.22 (b) and (c) demonstrate that the MoS₂/Ga₂O₃ heterojunction exhibits a rapid response and outstanding long-term stability for both UV-C (254 nm) and visible light (650 nm). The rise time (T_r) and fall time (T_f) of the photodetector were measured by the interval for the response rise from 10% to 90% and the response decay from 90% to 10% of its peak value. The response time recorded for the visible range is in microseconds. The enlarged view of the rise and fall edges of photoresponse under 650 laser illumination (Figure 4.22 (d)) exhibits a fast response of 97/114 μ s. For the UV-C range, the response speed is 3 ms/2 ms, which is limited by broad and unfocussed source in the form of a pen-ray UV lamp. A comparison of the photodetector performance of MoS₂/Ga₂O₃ with previously reported MoS₂ based 2D/3D heterojunction photodetector is presented in Table 4.4 which corroborates its superior performance.

Table 4.4 Comparison of MoS₂/Ga₂O₃ photodetector performance with reported literature

S.No	Device Structure	Detection range	Responsivity (AW ⁻¹)	Detectivity (Jones)	Response time (T_r/T_f) (μ s)	Ref
1.	MoS ₂ /ZnO	300-800	1.35 @ 529 nm	4×10^{12}	-	[62]
2.	MoS ₂ /NiO	310-660 nm	370 @ 660 nm	2.6×10^{14}	3×10^5 / 1.6×10^6	[63]
3.	MoS ₂ /CuO	400-1200	10 @ 900 nm	1.8×10^{14}	84×10^3 / 85×10^3	[64]
4.	MoS ₂ /ZnO	300-1100	4.56 @ 400 nm	-	80×10^3 / 80×10^3	[65]
5.	MoS ₂ /TiO ₂	400-800 nm	1,099 @ White light	1.7×10^{13}	-	[50]
6.	MoS ₂ /GaN	365 nm	3×10^3 @ 365 nm	$\sim 10^{11}$	$\sim 1.8 \times 10^5$ / 1.4×10^6	[61]
7.	MoS ₂ /GaN	280-850 nm	1.8×10^4 @ 365 nm	7.46×10^{12}	10.5×10^4 / 84×10^3	[66]
8.	MoS ₂ / β -Ga ₂ O ₃	245 nm	0.43 @ 245 nm	-	-	[46]
9.	MoS ₂ / a-Ga ₂ O ₃	254 nm	33.9 @ 254 nm	-	90×10^3	[45]
10.	MoS ₂ / a-Ga ₂ O ₃	254-1200 nm	171 @ 900 nm	4.7×10^{13}	97/114	This work

*a = amorphous

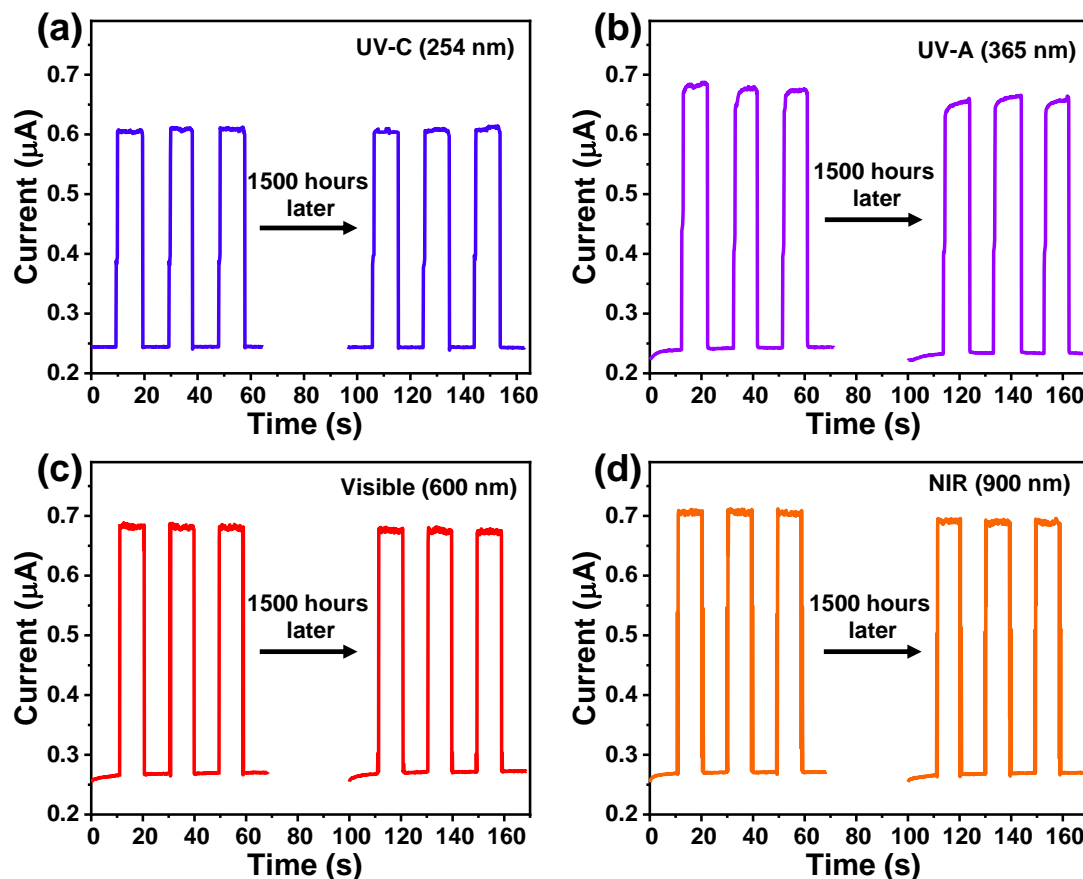


Figure 4.22 Transient photoresponse of MoS₂/Ga₂O₃ heterostructure in broad spectrum range from UV-C to NIR light irradiation at 1V bias over time in ambient conditions. The fabricated device shows negligible performance degradation after leaving in the ambient for 1500 hours.

In addition, the stability of the MoS₂/Ga₂O₃ photodetector was further examined by exposing it to an ambient condition for an extended period of time without any protective encapsulation. The device displayed exceptional durability and no significant changes were observed upon re-measurement in a broad spectrum regime after 1500 hours as shown in Figure 4.22. The stability of the device is directly linked to the exceptional air stability of MoS₂. Additionally, the MoS₂ film is coated with a thin layer of amorphous Ga₂O₃, which further protects the MoS₂ surface. Recently, a thin amorphous Ga₂O₃ glass was used to passivate monolayer WS₂ to preserve its exciton properties in ambient conditions [67]. Moreover, a-Ga₂O₃ passivated the graphene to preserve carrier mobility [68]. Thus, these findings demonstrate that the MoS₂/Ga₂O₃ heterojunction photodetector can maintain high performance under ambient conditions for an extended period of time, making it a suitable candidate for commercial photodetector.

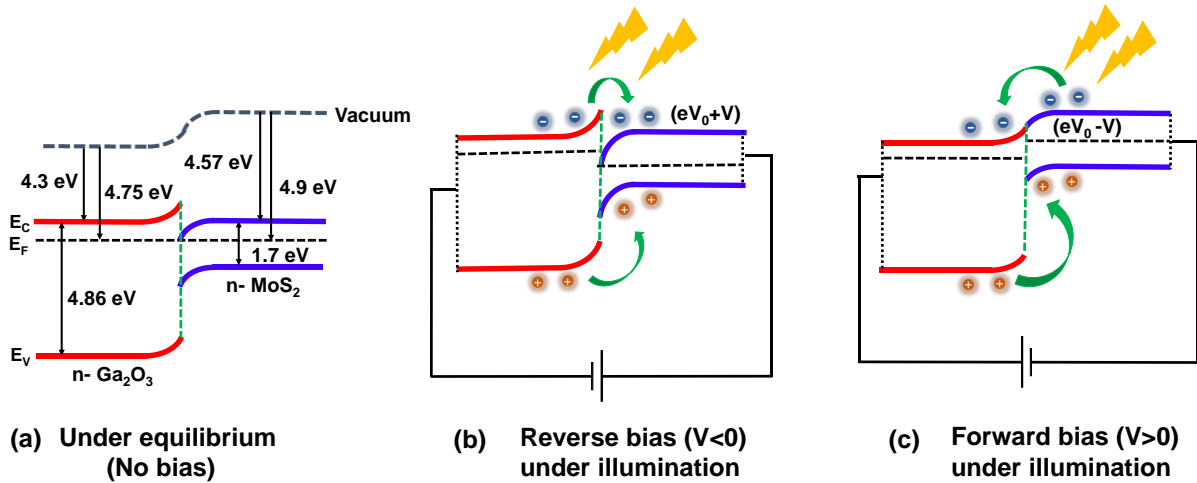


Figure 4.23 Energy band diagram of MoS₂/Ga₂O₃ heterojunction. (a) At equilibrium ($V=0$) under dark, (b) and (c) Reverse bias ($V<0$) and forward bias ($V>0$) conditions under illumination.

The energy level band diagrams are often utilized to study the photoresponse mechanism and carrier transport in heterojunctions. The band diagram of MoS₂/Ga₂O₃ heterointerface under an equilibrium condition and with reverse and forward bias under illumination is illustrated in Figures 4.23 (a)-(c). The MoS₂/Ga₂O₃ n-n heterojunction forms type I band alignment under zero bias conditions in dark, experimentally calculated with XPS (Kraut's rule) and UPS (Anderson's electron affinity rule) spectroscopy. Here, band diagram is based on the parameters obtained from UPS analysis i.e., work function and electron affinity. Usually, carrier densities of MoS₂ and Ga₂O₃ are reported to be of the order of 10^{13} - 10^{15} cm⁻² and 10^{17} cm⁻³, respectively [69, 70]. Under equilibrium, band bending occurs at the interface due to the difference in their Fermi-level positions and carrier densities. The electrons diffuse from Ga₂O₃ to MoS₂ and their Fermi levels become aligned, resulting in an electron depletion region in Ga₂O₃ and an electron accumulation region in MoS₂. The electron depletion and accumulation regions form a neutral depletion width, creating a built-in potential barrier (eV_0) for carrier transport. When the heterojunction is reverse biased ($V<0$) with respect to MoS₂ (i.e., positive terminal is connected to MoS₂ and negative terminal of the source is connected with Ga₂O₃), the barrier height at the interface increases ($eV_0 + V$) due to greater injection of electrons from Ga₂O₃ to MoS₂. This also causes holes to migrate from Ga₂O₃ to MoS₂, increasing the chances of carrier recombination. Now, the conduction is allowed only for the electrons while the holes keep accumulating in the valley of MoS₂, thereby restricting carrier transport and, hence lowering the photocurrent. In contrast, when the heterojunction is forward-biased ($V>0$) with respect to MoS₂, the barrier height decreases ($eV_0 - V$) due to injection of electrons from MoS₂ to Ga₂O₃. This causes a type II alignment to form at the interface (at $V>eV_0$), facilitating the

transfer of electrons from MoS₂ to Ga₂O₃ and holes from Ga₂O₃ to MoS₂. Under illumination, MoS₂ and Ga₂O₃ absorb the incident light and produce electron-hole pairs, which are effectively separated by the built-in electric field, resulting in an enhanced photocurrent. Thus, MoS₂/Ga₂O₃ heterostructure exhibits broad spectral response from deep UV to NIR, facilitated by the absorption of visible-NIR radiation by MoS₂ and UV light by Ga₂O₃. The robust built-in potential at the interface enables ultrafast response time, making the MoS₂/Ga₂O₃ heterostructure highly attractive for use in advanced optoelectronic applications.

4.2.2.3 Conclusions

In summary, a high quality MoS₂/Ga₂O₃ heterojunction was successfully fabricated using efficient and scalable sputtering technique. The MoS₂/Ga₂O₃ heterostructure was characterized using photoelectron spectroscopy and KPFM to probe the interfacial carrier dynamics and determine the band-alignment. The 2D/3D heterojunction of MoS₂/Ga₂O₃ showed broadband photoresponse from deep UV to NIR region. The fabricated MoS₂/Ga₂O₃ photodetector exhibited a ~315-fold enhancement in responsivity and EQE compared to pristine MoS₂ photodetector, with a highest responsivity and EQE of 171 AW⁻¹ and 2.4×10^4 % respectively, under 900 nm illumination at 5 V bias. The device also showed high sensitivity with a peak detectivity of 4.6×10^{13} Jones and ultrafast response speed of 97 μ s/114 μ s. Furthermore, the device is highly stable and shows negligible degradation in the device performance after leaving in ambient condition for more than a month. The enhanced performance is attributed to the favourable band alignment which improves carrier collection efficiency by eliminating the possibility of electron-hole recombination under forward bias. Our findings show that MoS₂/Ga₂O₃ heterostructures exhibit exceptional broadband photoresponse. These results open the door for designing highly efficient broadband photodetectors using advanced 2D/3D heterostructures.

4.2.3 Plasmonic Pt NPs decorated MoS₂ (Pt@MoS₂)

Localized surface plasmon resonance (LSPR) of metal nanostructures integrated with semiconductor has been extensively used to improve the device performance [71-73]. These nanoparticles (NPs) enormously increase light absorption through enhanced near electric field effects or via plasmon-induced hot carrier charge transfer from metal to semiconductor, which has been employed to extend the performance of MoS₂ beyond its bandgap and fundamental limit [74]. By tailoring the size and shape of plasmon metal NPs spectral selective photoresponse has been altered [75]. More recently, a huge photocurrent enhancement in layered MoS₂ is realized through “gap mode LSPR” where incident light gets squeezed into

Ag shell isolated NPs -Au film gap and a strong electromagnetic field emerging between the gap interacts with MoS₂ [76]. So far, only selected metal nanostructures such as Ag or Au NPs, nanoshells, nanorods etc. have been widely explored to enhance photocurrent in MoS₂, while other metals such as Pt or Pd have lacked attention. However, these plasmon metal NPs strongly absorb light and show strong inter-band activity over a broad spectral range. Moreover, Pt NPs advantageously offer low screening value ($\epsilon_{\infty} \approx 1$) and variable contribution of electrons (1 to 5 electrons per atom) as compared to Au ($\epsilon_{\infty} \approx 9$ and 1 electron per atom,) and Ag ($\epsilon_{\infty} \approx 4$ and 1 electron per atom) [77, 78]. This generates robustly boosted local field, which enhances the performance of photodetectors.

4.2.3.1 Experimental Section

4.2.3.1.1 Material synthesis

The large area VA-MoS₂ flakes were grown over p-Si/SiO₂ substrate using a modified tube-in-tube CVD technique, as discussed in section 4.2.1.1. The integration of Pt NPs over VA-MoS₂ (Pt@MoS₂) was done using a facile and efficient method of sputtering. This method of synthesizing Pt NPs is highly reproducible on a large scale. In this case, Pt NPs sputtered for 10s on pre-deposited MoS₂ flakes using Auto fine coater (JFC 16, JEOL) under an applied current of 30 mA.

4.2.3.2 Material characterizations

The surface morphology of samples was investigated using FESEM (FEI Nano SEM 450) with an integrated Energy Dispersive X-ray spectrometer (EDAX Ametek Octane Elect plus). Raman and PL were performed by LabRAM HR 800- HORIBA spectrometer using 532 nm excitation wavelength at room temperature. For the absorbance measurement, samples were synthesized on the quartz substrates. The absorbance spectra were taken using Perkin Elmer (Lambda 950, UV-Vis-NIR spectrophotometer) within the wavelength range of 400 nm – 1100 nm.

4.2.3.3 Device fabrication and photodetector measurements

The interdigitated Au electrodes (thickness ~150 nm) were patterned on VA-MoS₂ by thermal evaporation via shadow mask. Then, photodetector measurements were carried out on Au/VA-MoS₂/Au M-S-M device (photoactive area = 0.125 cm²). Afterward, Pt NPs were directly sputtered on the previously tested sample, and Au metal contacts were shadowed during Pt deposition. The corresponding device is named Au/Pt@MoS₂/Au M-S-M device. Photodetector measurements were performed using the Bentham PVE 300 system, consisting of a monochromator (TMC 300), 75 W xenon, and 100 W quartz halogen lamps and connected

to Keithley 6430 sourcemeter. The spectral photoresponse of these devices had been recorded in the wavelength range 400 nm -1100 nm. All the device measurements were carried out under normal atmospheric conditions in an optically closed chamber.

4.2.3.2 Results and discussion

The device schematic of Pt sensitized MoS₂ photodetector (Au/Pt@MoS₂/Au M-S-M device) is illustrated in Figure 4.24 (a). The surface morphology of VA-MoS₂ decorated with Pt NPs was analyzed using FESEM at different magnifications (Figures 4.24 (b) and (c)). FESEM images clearly show highly dense, uniform and evenly distributed Pt NPs deposited on VA-MoS₂ flakes. Some of these NPs might even be trapped under the vertically oriented flakes. The histogram shows the distribution of Pt NPs as obtained using ImageJ software, inset of Figure 1c. The NPs size varies in a narrow range between 3 nm and 35 nm with an average particle size of ~10 nm. These tiny (< 10 nm) Pt NPs are beneficial to improve the photosensitivity of semiconductor devices [79]. A few of these small NPs might have possibly agglomerated, producing larger-sized NPs. The calculated density of the Pt NPs is $\sim 2.3 \times 10^{11}$ counts per cm². EDX elemental mapping was also carried out for the selected area (Figure 4.24 (d)) to confirm the presence of constituent materials (Mo, S, and Pt), as depicted in Figure 4.24 (e)-(h). The uniform distribution of Pt NPs in EDX mapping confirms the presence of Pt NPs on each flake.

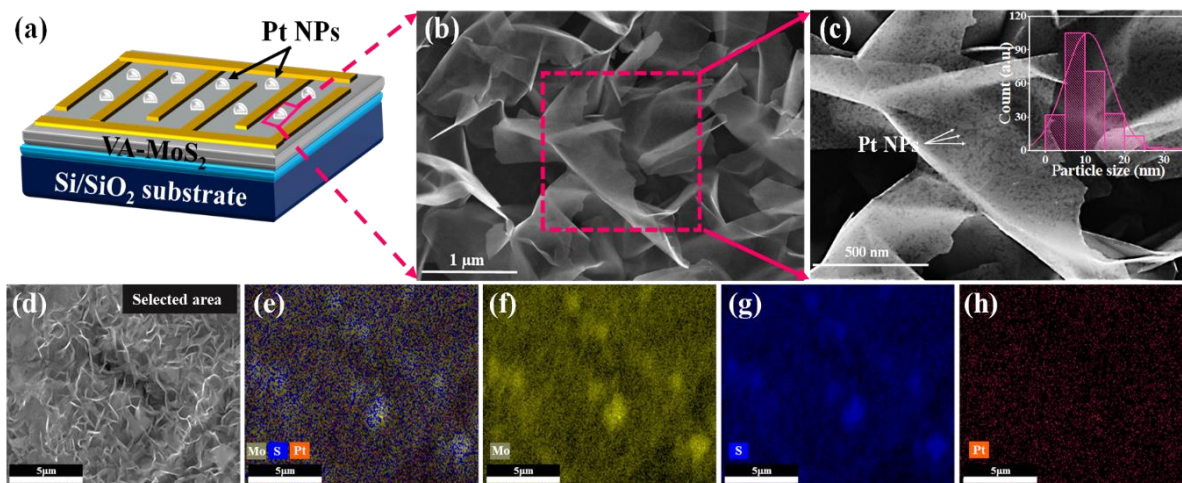


Figure 4.24 (a) Schematic of Au/Pt@MoS₂/Au M-S-M photodetector. (b) FESEM image of Pt@MoS₂. (c) Magnified FESEM image of (b), inset shows particle size histogram. (d) Area selected for elemental mapping. Elemental mapping of (e) Cumulative, (f) Molybdenum, (g) Sulfur, (h) Platinum.

Raman spectra were obtained for both VA-MoS₂ and Pt@MoS₂ samples using a 532 nm excitation source, as displayed in Figure 4.25 (a). Raman spectrum of the VA-MoS₂ sample

shows two prominent peaks corresponding to E_{2g}^1 (in-plane vibration) and A_{1g} (out of plane vibration) located at 383.28 cm⁻¹ and 408.07 cm⁻¹, respectively [47]. The difference between these two Raman modes is identified to be 24.79, which suggests the presence of a few layers of MoS₂ [48]. In addition to this, intensity ratio ($\frac{E_{2g}^1}{A_{1g}}$) value is 0.46 that confirms the formation of vertical flakes [80]. After the integration of Pt, both the Raman modes (E_{2g}^1 and A_{1g}) are observed at same positions, which indicates the absence of any stress or strain built-up in flakes due to the Pt NPs [81]. The metallic NPs drastically increased the background scattering count ascribed to the plasmon-induced enhancement in average electric field intensity in MoS₂. Thus, the intensity exhibits nearly 3.5- and 4-times enhancement of E_{2g}^1 and A_{1g} modes, respectively, suggesting strong plasmonic coupling effect. The augmentation in Raman scattering can be directly correlated with electromagnetic field intensity induced from LSPR of Pt NPs, which increases the spontaneous emission rate in the Pt@MoS₂ sample compared to VA-MoS₂ [82].

Further, to gain insight into the effect of Pt NPs on the optical properties of MoS₂, PL spectroscopy has been performed (Figure 4.25 (b)). The PL spectrum of the VA-MoS₂ sample shows two emission peaks centered at 1.81 eV and 1.94 eV, which corresponds to A and B excitons, respectively. The A exciton emission peak is attributed to the direct transition gap at the same K-values of the Brillion zone. In contrast, the B exciton peak appears due to splitting in the valence band resulting from interlayer coupling and spin-orbit coupling [51]. Notably, the Pt@MoS₂ hybrid does not show any emission peak, suggesting a strong PL quenching. The observed PL quenching in Pt@MoS₂ indicates the strong charge-transfer interaction between MoS₂ and Pt [52]. The absence of PL was also observed previously due to phase transition of MoS₂ from 2H (semiconducting) to 1T (metallic) in Li-intercalated study of MoS₂ [83]. However, in our case, after deposition of Pt on MoS₂, no structural phase change has occurred, as confirmed from the missing characteristic peaks of other structural phases of MoS₂ in the Raman spectrum. Therefore, the reduction in PL intensity in the Pt@MoS₂ sample arises due to the strong plasmonic coupling effect and annihilation of excitons by highly dense Pt NPs [84].

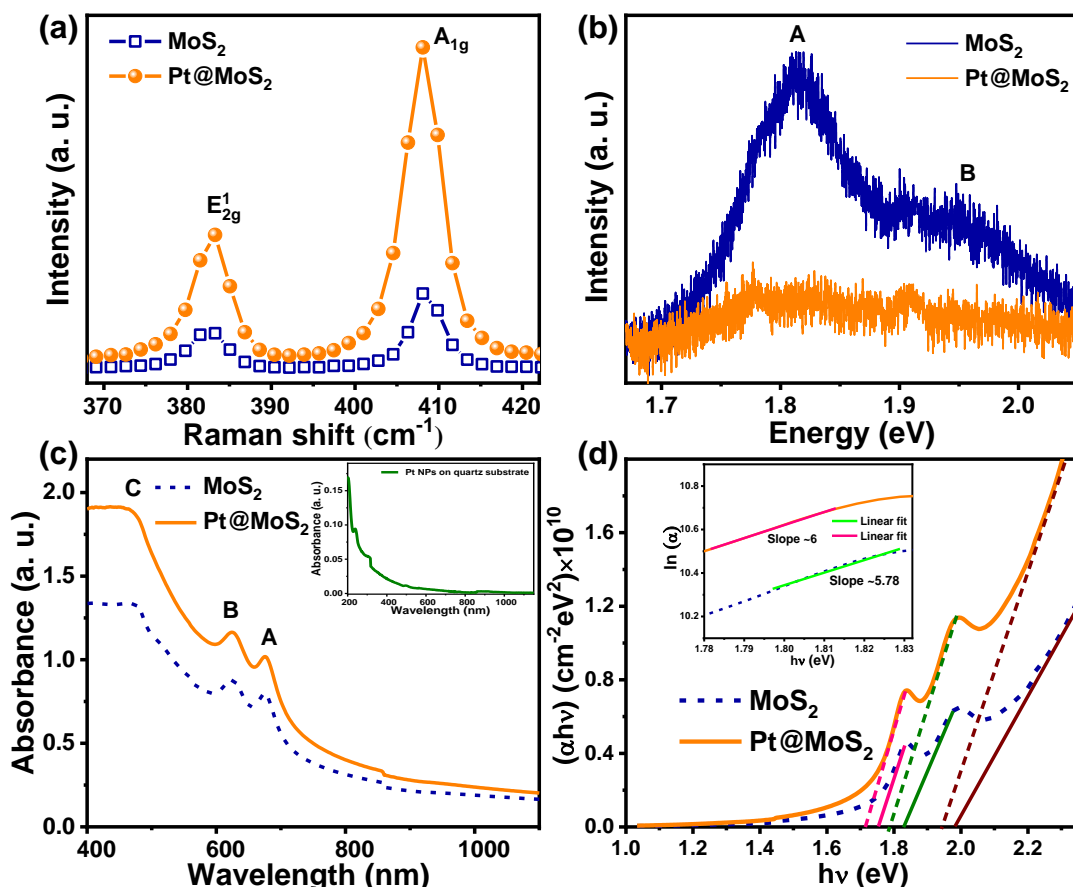


Figure 4.25 (a) Raman spectra, (b) Photoluminescence spectra, (c) Optical absorbance spectra of MoS₂ and Pt@MoS₂ samples, inset consist of absorbance of Pt NPs on quartz. (d) Tauc plot and Urbach energy calculation (inset) for both samples.

The absorbance spectra of synthesized VA-MoS₂ and Pt decorated MoS₂ are presented in Figure 4.25 (c). VA-MoS₂ exhibits broad (visible-NIR) absorption feature with two prominent peaks known as A and B excitons, respectively, which agrees with the literature [85]. In addition, absorbance spectra consists of broad absorption (shoulder peak-C excitons) by excitons associated with van Hove singularity [53]. Highly dense and low dimensional Pt NPs considerably absorb the incident radiation in the UV and visible region and absorbance decreases with increasing wavelength, as shown in inset of Figure 4.25 (c). The intense broad spectrum of Pt@MoS₂ is, therefore, ascribed to the combined effects of the MoS₂ characteristics, absorption due to Pt NPs, and strong plasmonic coupling of Pt NPs with MoS₂. Further, the direct bandgap of the samples was calculated using Tauc plots (the $(\alpha h\nu)^2$ vs. $h\nu$ plots) as shown in Figure 4.25 (d) [86].

Here, α is the absorption coefficient, and $h\nu$ is the incident photon energy. The bandgap of the samples is obtained by extrapolating the linear portion to the X-axis (energy). The main band transition corresponding to ~1.75 eV for the VA-MoS₂ sample, shows a slight red shift (1.71

eV) after incorporating Pt NPs. Also, the observed peaks at 1.83 eV and 1.97 eV for the VA-MoS₂ sample corresponds to A and B excitonic transitions display red shift for the Pt@MoS₂ to 1.79 eV and 1.94 eV, ascribed to charge transfer as corroborated by PL quenching [87]. Such observations conclude that the plasmonic effect increases the light absorption even if the highly dense Pt NPs later captured the generated excitons. This process leads to the further polarization of the Pt NPs and results in higher magnitude dipole oscillations. Thus, oscillating surface plasmons help in further generation of e-h pairs within the Pt@MoS₂ system. Moreover, the exponential shape of the absorption edge is observed according to the Urbach rule [88] following equation no. (4.15)

$$\alpha(\nu) = \alpha_0 \exp \left[\frac{(h\nu - E_0)}{E_U} \right] \quad (4.15)$$

Where α_0 and E_0 are characteristic parameters of the material. The constant E_0 is an estimation of the optical gap of the material according to Urbach theory and α_0 is directly proportional to the electron transition probability to the higher energy optical levels [89]. E_U is the Urbach energy as calculated from the reciprocal of the slopes of $\ln \alpha$ vs. $h\nu$ curves (Figure 4.26 (d)(inset)). Urbach energy is a primary variable, which contains all the information of band-tails. It is a measure of the width of the optical band tail, which arises within the bandgap due to the localized trap states [90]. E_U value of ~0.17 eV for the VA-MoS₂ signifying the presence of a few optically active defect states, which intrinsically exist within the material due to the synthesis process [91]. Two kinds of disorder form the tails in materials: structural and thermal (phonon induced). E_U further decreases to ~0.16 eV for Pt NPs decorated sample. This signifies the overall lessening of the trap states even after hot electron generation [92].

The wavelength-dependent current-voltage (I-V) photodetection characteristics of Au/MoS₂/Au and Au/Pt@MoS₂/Au structured M-S-M devices are depicted in Figures 4.26 (a) and (b). The behavior demonstrates that VA-MoS₂ responds to a broad spectral (visible to NIR) photoresponse. Moreover, dark current decreases after sensitizing the MoS₂ with Pt NPs, and the photocurrent significantly enhances. The M-S-M structure consists of interdigitated electrodes (Figure 4.24 (a)), which results in diode-like I-V curves, suggesting the formation of back-to-back Schottky junctions between Au and MoS₂. Therefore, on the application of an external bias, one of the junctions will be forward-biased, and the other will be simultaneously reverse-biased. This reverse barrier current helps in lowering the dark current. To further analyze the reduction in the dark current, the semi-logarithmic I-V curves are plotted (Figure

4.26 (c)). Considering forward bias and applying the thermionic emission (TE) model [93], the current across the junction is described by equation no. (4.16).

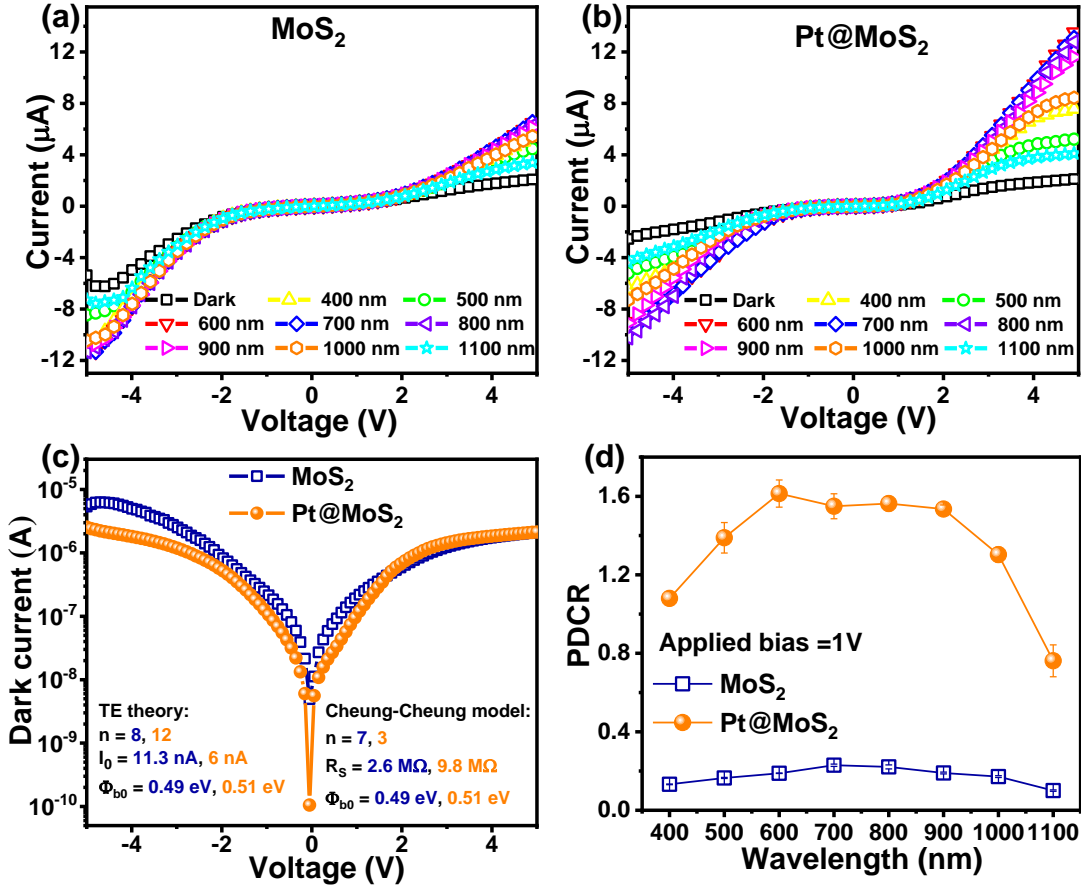


Figure 4.26 The I-V characteristics under dark and illumination of (a) MoS₂ and (b) Pt@MoS₂. (c) The dark I-V characteristics (semi-logarithmic) of pristine MoS₂ and Pt@MoS₂ is presented for comparison, Pt@MoS₂ exhibits less dark current. (d) Photo-to-dark current ratio (PDCR) of MoS₂ and Pt@MoS₂, Pt@MoS₂ device shows superior photoresponse as compared to pristine MoS₂.

$$I = I_0 \exp\left(\frac{q(V - IR_s)}{nkT}\right) \left[1 - \exp\left(-\frac{q(V - IR_s)}{kT}\right)\right] \quad (4.16)$$

where I_0 indicates the reverse saturation current, represented by equation no. (4.17).

$$I_0 = AA^*T^2 \exp\left(-\frac{q\Phi_{b0}}{kT}\right) \quad (4.17)$$

where A is the electrode contact area for one of the Schottky back-to-back junctions, A^* is the effective Richardson constant ($\sim 8 \times 10^{-6} \text{ A cm}^{-2} \text{ K}^{-2}$ for MoS₂) [94]. The symbols q , k , T , n , Φ_{b0} , and R_s denote the electronic charge, Boltzmann constant, the absolute temperature (in K), ideality factor, zero-bias barrier height, and series resistance of the device, respectively. According to the TE theory, n and Φ_{b0} are represented by equation (4.18) and (4.19).

$$n = \frac{q}{kT} \left[\frac{\partial V}{\partial (\ln I)} \right] \quad (4.18)$$

$$\Phi_{b0} = \frac{kT}{q} \ln \left(\frac{AA^*T^2}{I_0} \right) \quad (4.19)$$

The values of n , I_0 , and Φ_{b0} as extracted from the linear fit of the semi-logarithmic I-V curves are ~ 8 (and 12), ~ 11.3 nA (and 6 nA), and ~ 0.49 eV (and 0.51 eV) for Au/MoS₂ (and Au/Pt@MoS₂) junctions. The slight increase in barrier height and decrease in saturation current indicates that the metal-semiconductor (M-S) junction is affected by the Pt NPs. The Pt NPs possibly attract the conduction electrons due to their large electronegativity (2.28) and, therefore, a reduction in I_0 is observed. This, in turn, leads to an increase in barrier height as Pt NPs have to release the captured electrons to the conduction band. However, the ideality factor calculated from TE theory is high and shows further increment for the Au/Pt@MoS₂ junction. The high “ n ” values are primarily attributed to the Schottky behavior of the M-S junction, where the tunneling of carriers may happen due to a variety of reasons [95]. The tunneling process may result from the interface roughness, structural imperfections of TMDs, and irregularity in the TMD’s width [96]. Obviously, there are variations in the M-S interface roughness due to the irregularity in the MoS₂ flakes’ height (as shown in the FESEM images). However, the larger ideality factor for Au/Pt@MoS₂ junction (from TE theory) is possibly occurring as the diode series resistance (R_s) contributions are not considered. Therefore, we have extracted the R_s , n , and Φ_{b0} values using the Cheung-Cheung model [97] for a better explanation. According to the Cheung-Cheung model, forward I-V characteristics are expressed using equation (4.20), (4.21), and (4.22).

$$\frac{dV}{d(\ln I)} = IR_s + \frac{nkT}{q} \quad (4.20)$$

$$H(I) = V - \frac{nkT}{q} \ln \left(\frac{I}{AA^*T^2} \right) \quad (4.21)$$

$$H(I) = IR_s + n\Phi_{b0} \quad (4.22)$$

The initial R_s value is obtained from the slope of the linear fit of the $\frac{dV}{d(\ln I)}$ vs. I plot, and n is obtained from the intercept. These values of “ n ” are then used to calculate $H(I)$, and then Φ_{b0} is obtained from the intercept of the $H(I)$ vs. I curve. The R_s value is again obtained from the slope of these curves. The obtained values of n , average R_s , and Φ_{b0} are ~ 7 (and 3), ~ 2.6 M Ω (and 9.8 M Ω), and ~ 0.49 eV (and 0.51 eV) for Au/MoS₂ (and Au/Pt@MoS₂) junctions. Therefore, there is a substantial increase in diode series resistance with the incorporation of plasmonic Pt NPs, which in turn reduces the ideality factor. However, the ideality factor is still

high due to the high interfacial surface inhomogeneity [98]. The decreased I_0 and increased R_s also suggest the reduction in band-tail-related localized trap states in the presence of Pt NPs, which was also essentially concluded from the Urbach energy calculations.

On the other hand, photocurrent to the dark current ratio ($PDCR = I_{photo}/I_{dark}$, where $I_{photo} = I_{light} - I_{dark}$) is used to determine the performance of the devices under illuminating signal. It is calculated for both devices at an applied bias of 1 V from Figures 4.26 (a) and (b). The more significant value of PDCR in the Au/Pt@MoS₂/Au device reveals its sensitive nature. The Pt@MoS₂ device has an 8-fold increment in PDCR than VA-MoS₂ based device (even at a low bias of 1 V), corroborating the further enhanced broadband photoresponse of VA-MoS₂ by Pt NPs (Figure 4.26 (d)). The superior broadband photoresponse of the Pt@MoS₂ is ascribed to the efficient light absorption and production of strong electric field intensity at the Pt@MoS₂ interface and near the MoS₂ surface. The details of the photodetection mechanism are discussed later.

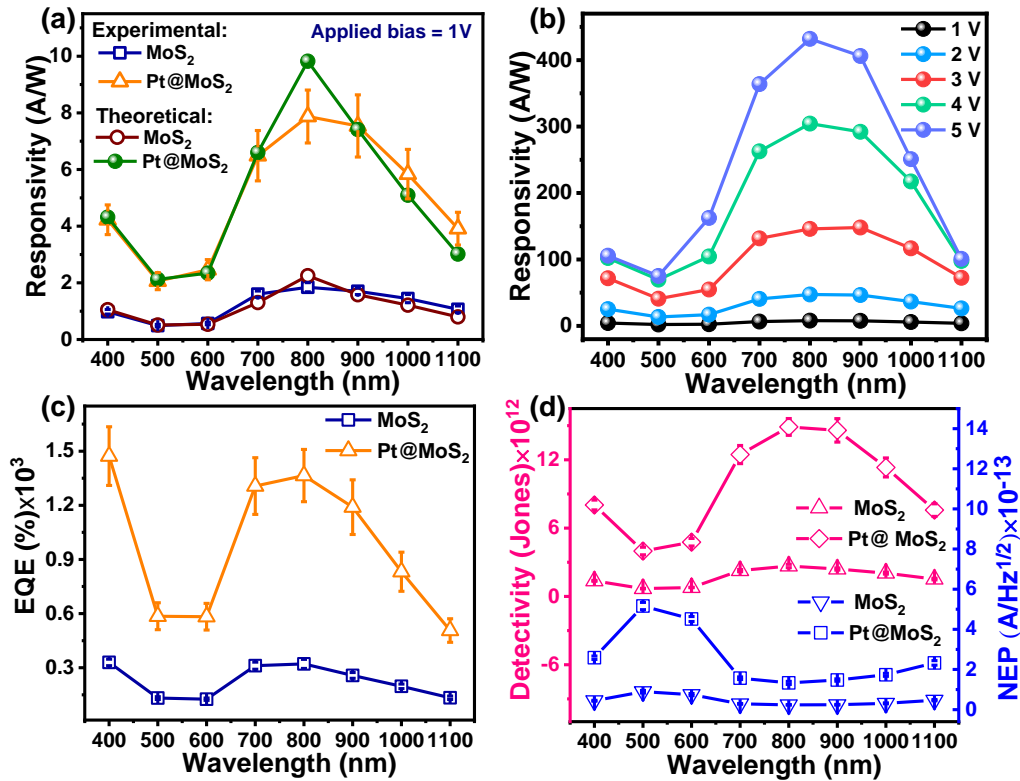


Figure 4.27 (a) Experimental and theoretical calculated responsivity of MoS₂ and Pt@MoS₂ photodetector at 1V. (b) Responsivity as a function of wavelength for different bias voltage. (c) External quantum efficiency. (d) Detectivity and NEP of the fabricated photodetector of MoS₂ and Pt@MoS₂ photodetector in broad visible-NIR regime at an applied bias of 1 V.

Different figures-of-merit of a photodetector can be evaluated to investigate photodetection phenomena further. The vital figures-of-merit are responsivity (R), external quantum efficiency (EQE), specific detectivity (D*), noise equivalent power (NEP), and signal to noise ratio (SNR). The evaluated responsivity at 1 V as a function of wavelength within 400 nm - 1100 nm is displayed in Figure 4a. The responsivity values at 1 V are 1.84 AW⁻¹ and 7.87 AW⁻¹ under 800 nm illumination for VA-MoS₂ and Pt@MoS₂ devices, respectively. Therefore, it is clear that Pt NPs enormously enhance the responsivity of the MoS₂ device in the broadband spectral range. To understand the underlying device physics, we have theoretically simulated the photodetector's responsivity, estimated photoconductive gain (G), transit time (τ_{tr}) and mobility (μ). It is done by correlating the responsivity with the materials' practically obtained absorption coefficient (α). The external quantum efficiency (ratio of the number of electron-hole pairs collected in producing I_{photo} and the number of incident photons) of a photodetector is expressed by equation no. (4.23) [92, 99].

$$\eta_{ext} = \frac{I_{photo}/q}{P_{inc}/h\nu} = \frac{I_{photo}}{P_{inc}} \cdot \frac{h\nu}{q} \quad (4.23)$$

It is closely correlated with the α of the material and the active length (t') of the absorbing region (see equation no. (4.24)).

$$\eta_{ext} = \eta_i \{1 - \exp(-\alpha t')\} \quad (4.24)$$

where η_i is the internal quantum efficiency (i. e., the ratio of the number of e-h pairs created and the number of photons absorbed). If all the incident photons are absorbed, then the η_i of a photodetector is related to the photogeneration rate (g_{ph}) the volume of the active region (V_A) according to equation no. (4.25).

$$\eta_i = \frac{g_{ph}}{R_{absorbed}} = \frac{g_{ph} V_A}{P_{inc}/h\nu} \quad (4.25)$$

The photocurrent is given by equation no. (4.26), when there is a photoconductive gain and if all the carriers are swept out before recombination.

$$I_{photo} = q g_{ph} V_A G = q \eta_i \left(\frac{P_{inc}}{h\nu} \right) G \quad (4.26)$$

Then, the responsivity is represented by equation no. (4.27).

$$R = \frac{\eta_{ext} q}{h\nu} = \eta_i \{1 - \exp(-\alpha t')\} \frac{q}{h\nu} = \frac{I_{photo}}{P_{inc} G} \{1 - \exp(-\alpha t')\} \quad (4.27)$$

For plasmonic photodetector, the responsivity is presented by equation no. (4.28) [100].

$$R = \gamma_c \{1 - \exp(-\alpha t')\} \frac{q\eta_i}{h\nu} = \gamma_c \frac{I_{photo}}{P_{inc}G} \{1 - \exp(-\alpha t')\} \quad (4.28)$$

Where γ_c is the coupling efficiency of the photonic mode into surface plasmon polariton (SPP) mode. Assuming coupling efficiency (γ_c) to be 90% for the plasmonic photodetector, the experimental responsivity can be simulated. Γ_G can be treated as a fitting parameter. It is seen from the practical curves that the responsivity at first increases and then starts decreasing after 800 nm (Figure 4.27 (a)). Therefore, to simulate experimental responsivity curves precisely, the whole spectrum is subdivided into two spectral regions (400 nm - 700 nm) and (800 nm - 1100 nm). Also, equation no. (4.27) and (4.28) are modified using two separated fitting parameters for two regions. A_1 and B_1 are used for VA-MoS₂ based photodetector, whereas A_2 and B_2 are used for plasmonic photodetector. The ideal equations do not include any contributions from the distribution of states between the M-S contacts. These states act as the enhancement factors related to photogeneration from the vertical structures of MoS₂. Therefore, the modified equations for the wavelength range 400 nm - 700 nm can be written as equation (4.29) and (4.30) for Au/MoS₂/Au and Au/Pt@MoS₂/Au devices, respectively.

$$R = A_1 \frac{I_{photo}}{P_{inc}G} \{1 - \exp(-\alpha t')\} \quad (4.29)$$

$$R = \gamma_c A_2 \frac{I_{photo}}{P_{inc}G} \{1 - \exp(-\alpha t')\} \quad (4.30)$$

Similarly, the modified equations Au/MoS₂/Au and Au/Pt@MoS₂/Au devices in the wavelength range 800 nm - 1100 nm can be written as:

$$R = B_1 \frac{I_{photo}}{P_{inc}G} \{1 - \exp(-\alpha t')\} \quad (4.31)$$

$$R = \gamma_c B_2 \frac{I_{photo}}{P_{inc}G} \{1 - \exp(-\alpha t')\} \quad (4.32)$$

Considering $A_1 = 1$, $B_1 = 2.1$, $A_2 = 23$ and $B_2 = 46$, exact theoretical fitting curves are obtained as shown in Figure 4a. It is observed that the values of these constants are high for the plasmonic device, probably because of the enhanced plasmonic absorption process (resulting from increased extinction cross-section and high density of smaller sized Pt NPs) into the device structure. This, in turn, increases the photogeneration rate. Now, considering equation (4.29) to (4.32), the experimental curves are fitted, and the obtained gain (G) values are 0.11 and 2.5 for Au/MoS₂/Au and Au/Pt@MoS₂/Au devices, respectively. Therefore, there is a gain mechanism involved, which is attributed due to the plasmonic effect. Under illumination, electron-hole pairs are created, which are expected to drift toward the opposite electrodes under

the applied bias. The holes are then trapped at the Pt@MoS₂ interface, whereas electrons circulate through the external circuit until the recombination with holes takes place. It can be interpreted as that irradiation of one photon can generate multiple carriers, which contributes to the total current in the circuit. As a consequence, a photoconductive gain for the plasmonic device is obtained [101]. Additionally, τ_{tr} and μ are estimated using equation no. (4.8) defined in section 4.2.1.2, represented as following:

$$G = \frac{\tau}{\tau_{tr}} = \frac{\tau \mu V}{L^2}$$

where τ represents the carrier lifetime, L = channel length, and V = applied voltage. The lifetime of the electron is considered as 50 ps for the MoS₂ [102]. Taking average channel length as 500 nm and the applied $V = 1$ V, τ_{tr} and μ values are obtained. τ_{tr} decreases from 450 ps (MoS₂ device) to 20 ps (plasmonic device). It can be seen that G is directly proportional to photogenerated carrier lifetime and inversely proportional to carrier transit time. The high value of G is attributed to the decreased carrier transit time, which directly contributes to the higher EQE of the device. Apparently, increased EQE value in Pt@MoS₂ ascribed to the efficient light absorbance and increased number of free carriers (due to hot electron injection from Pt to MoS₂) than MoS₂. Further, defect states generated by Pt NPs cannot be ignored, which also play a significant role in enhancing device efficiency. Also, the calculated μ values increase from ~ 5.56 cm²/V-s (MoS₂ device) to ~ 125 cm²/V-s (plasmonic device), which, in turn, improves the response time (rise and fall time) of the device. Figure 4.27 (b) shows that responsivity further increases with applied bias voltage and attains its maximum value of 432 AW⁻¹ at 5 V due to reduction in the transit time. Additionally, EQE also got enhanced in a broad wavelength range with increasing voltage ($6.7 \times 10^4\%$ at 5 V) due to the increased responsivity. The EQE improved nearly one order of magnitude to $1.4 \times 10^3\%$ even at a low bias of 1 V for the Pt@MoS₂ device compared to the VA-MoS₂ device ($3.2 \times 10^2\%$), as shown in Figure 4.27 (c). The large EQE (greater than 100%) over a wide spectral range implies photoconductive gain in the plasmonic hybrid system.

Moreover, NEP is represented by equation (4.33), which is the necessary illumination power to obtain signal-to-noise ratio (SNR) of unity (at a bandwidth, $B = 1$ Hz). SNR signifies a ratio between signal and noise power (calculated using equation no. (4.34)).

$$NEP = \frac{\sqrt{S}\sqrt{B}}{D} \quad (4.33)$$

$$SNR = \frac{I_{photo}^2}{(2qI_{dark}B + 2qI_{photo}B)} \quad (4.34)$$

The wavelength-dependent detectivity and NEP values of fabricated photodetectors (MoS₂ and Pt@MoS₂) are shown in Figure 4.27 (d). NEP is calculated to be $1.33 \times 10^{-13} \text{ W Hz}^{-1/2}$ ($2.4 \times 10^{-14} \text{ W Hz}^{-1/2}$) for Au/MoS₂/Au (Au/Pt@MoS₂/Au). The calculated detectivity value of the Pt@MoS₂ hybrid device is 1.48×10^{13} Jones at 800 nm irradiation for 1 V and 1.85×10^{14} at 5V, which is much greater than the reported large area TMDs or standard Si photodetector. The computed SNRs of the photodetectors are ~94 dB and ~105 dB for Au/MoS₂/Au and Au/Pt@MoS₂/Au, respectively, which signifies a low noise level for the plasmonic device (calculation details are given in supplementary information). Figure 4.28 illustrates the detectivity versus responsivity graph of the reported [72, 82, 103-107] plasmonic sensitized MoS₂ based photodetector with fabricated Pt NPs sensitized VA-MoS₂ photodetector. The results demonstrate the better performance of Pt@MoS₂ broadband photodetector compared to reported plasmonic MoS₂ based photodetectors.

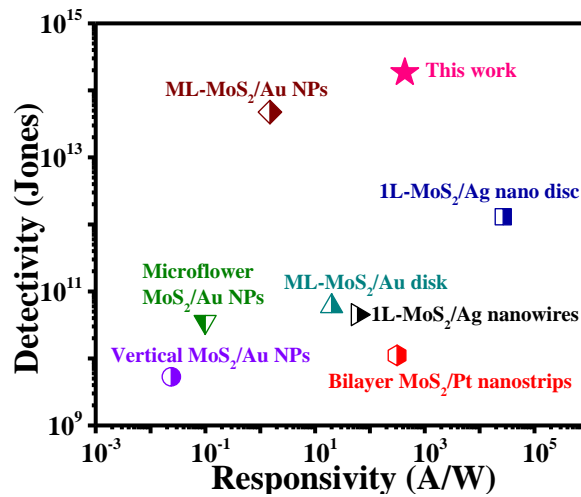


Figure 4.28 Detectivity versus responsivity plot for plasmon enhanced MoS₂ based photodetector.

The temporal response of the device assesses the reproducibility under on and off illumination conditions. Figure 4.29 (a) displays transient photoresponse of Pt@MoS₂ hybrid under broad illumination (400 nm - 1100 nm). A sharp increment of current is achieved when light is incident on the device and rapidly decays to its initial value (dark current) after turning off the light. From Figure 4.29 (a), it follows that photocurrent is maximum in the visible region (corresponding to a rectangular input light pulses of 600 nm). However, maximum photocurrent (600 nm) and responsivity (800 nm) occur at different wavelengths due to the change in power density of the incident light. The periodic switching with the light on/off for

MoS₂ and Pt@MoS₂ hybrid further confirms the lesser dark current in the plasmonic system with efficient photocurrent increment (Figure 4.29 (b)). The response time of the photodetector is one of the critical parameters that determine the signal detection limit. Rise time (T_r) (Fall time (T_f)) is the time interval in which current rises (falls) from 0.1 I_{\max} (0.9 I_{\max}) to 0.9 I_{\max} (0.1 I_{\max}) under illumination (dark condition), where I_{\max} is the maximum photocurrent. The calculated T_r (T_f) of MoS₂ and Pt@MoS₂ photodetectors are ~91 ms (157 ms) and ~87 ms (84 ms), respectively, as displayed in Figures 4.29 (c) and (d). A significant change in Pt@MoS₂' rise time is observed, which implies a reduction in carrier diffusion time. Most carriers drifted to the corresponding electrodes due to their increased mobility and decreased carrier transit time (as calculated from the theoretical model).

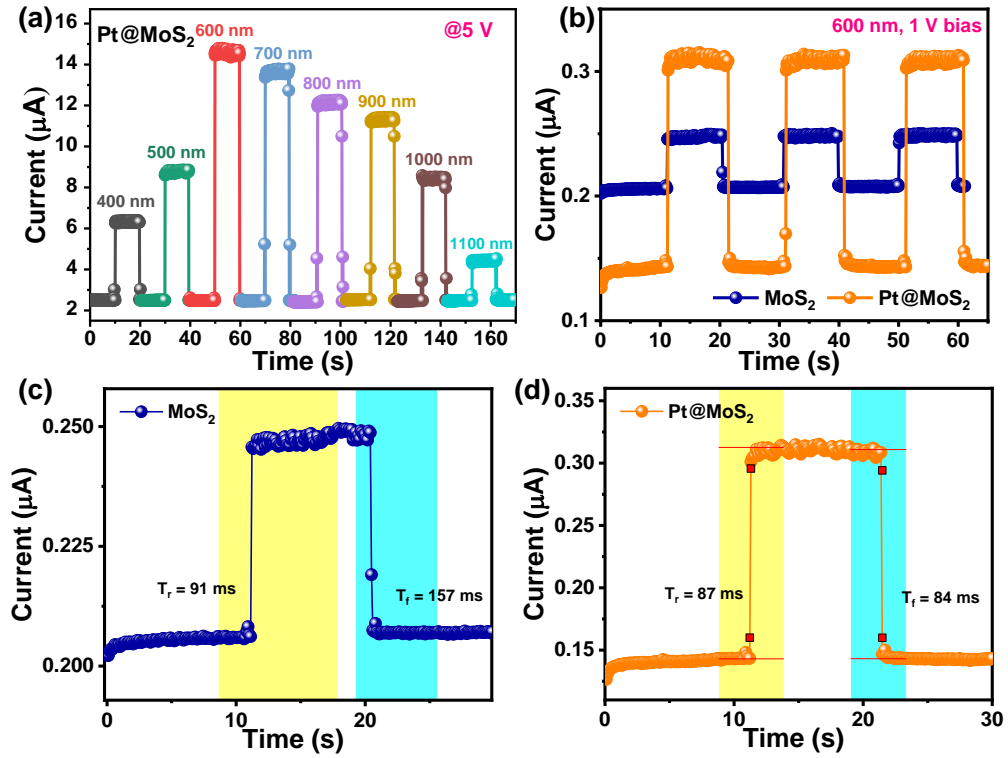


Figure 4.29 (a) Transient photoresponse of Au/Pt@MoS₂/Au for broad spectral range (400 nm - 1100 nm) at 5 V. (b) Temporal response of Au/MoS₂/Au and Au/Pt@MoS₂/Au device under 600 nm illumination at 1 V. (c) and (d) Corresponding response time (rise and fall time) of MoS₂ and Pt@MoS₂ photodetector, respectively.

To enhance the reliability of the Pt@MoS₂ device performance, other devices with the same geometry were also fabricated. The detailed distribution of different parameters (I_{photo} , R and D) are listed in Table 4.5. The data reveal that the fabricated devices exhibit Responsivity in the range of 410-445 mV with an average of 431.75 A/W. Moreover, the photoresponse of the fabricated Pt@MoS₂ photodetector is highly reproducible and shows no significant change even after 30 days from the first measurement as shown in Figure 4.30. A comparison of

various parameters with other reported plasmonic MoS₂ photodetectors is also shown in Table 4.6, which proves superiority of the fabricated photodetector.

Table 4.5 Device performance of different Pt @MoS₂ devices under illumination of 800 nm at 5 V bias

Pt decorated MoS ₂ (Pt@MoS ₂)						
Cell Number	Photocurrent I_{photo} (A)	Average I_{photo}	Responsivity R (A/W)	Average R	Detectivity D (Jones)	Average D
1	1.08×10^{-5}		432		1.84×10^{14}	
2	1.32×10^{-5}	$1.22 \pm 0.2 \times 10^{-5}$	445	431.75 ± 15	1.90×10^{14}	$1.66 \pm 0.2 \times 10^{14}$
3	1.48×10^{-5}		440		1.40×10^{14}	
4	1.02×10^{-5}		410		1.50×10^{14}	

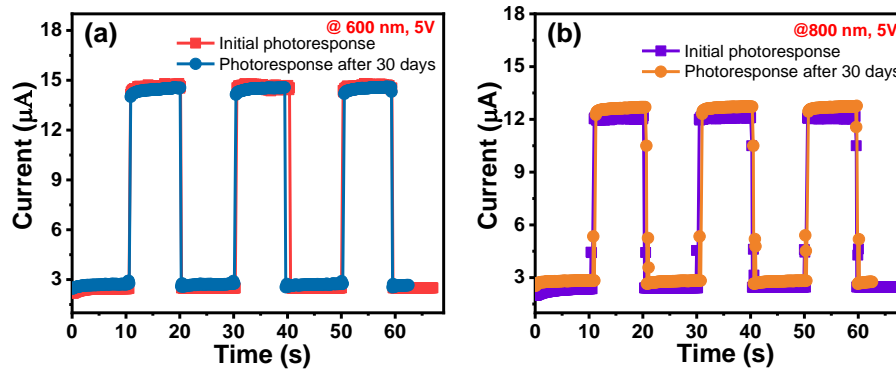


Figure 4.30 Transient photoresponse of Pt@MoS₂ in visible (600 nm) and NIR (800 nm) illumination measured at 5 V, showing initially measured response and response after 30 days of the same sample stored at normal ambient conditions. The data reveals high repeatability of the photoresponse with time.

The photodetection mechanisms of the devices can be well understood by the energy band diagram. First, the Fermi-level of MoS₂ and Au align and reaches equilibrium with a small Schottky barrier (~ 0.49 eV) at the Au-MoS₂ interface. Ideally, under illumination, VA-MoS₂ efficiently absorbs the light (energy $>$ bandgap) and generates e-h pairs. These photo-excited e-h pairs are separated by the applied source-drain bias voltage, which drifts in the opposite direction to the external circuit to generate photocurrent. However, localized trap states, charged impurities, or surface absorbates may capture photo-excited holes and electrons. The presence of more exposed edges in VA-MoS₂ results in a high surface-to-volume ratio and high Urbach energy. Therefore, the broad spectral response can be ascribed to the excitation of charge carriers in the defect's states located within the bandgap, which absorbs the radiation below the bandgap.

Table 4.6 Comparative performance of plasmon enabled MoS₂ photodetector. FL = few layer

Active Material	Synthesis Technique	Modified Method	Detection range	Responsivity (AW ⁻¹)	Detectivity (Jones)	Response time	Ref.
1L MoS ₂	CVD	Au nano shell	Visible (600 nm -750 nm)	0.9×10^{-3}	-	6 ms	[108]
2L MoS ₂	Mechanical Exfoliation	Asymmetric Au antenna array	Visible (532 nm)	1.1×10^5	-	~ 500 s	[74]
			NIR (1150 nm-1170 nm)	5.2	-	~500 s	
Au@MoS ₂ core-shell composite	CVD	Si-supported	White light (360 nm–660 nm)	22.3	-	< 20 ms	[109]
1L MoS ₂	CVD	Ag shell isolated NPs -Au film gap	Visible (532 nm)	287.5	-	19 ms/15 ms	[76]
1L MoS ₂	Gold-mediated exfoliation	Ag nanodisk array	Visible (440 nm-620 nm)	2.7×10^4	1.3×10^{12}	70 ms/ 410 ms	[107]
2L MoS ₂	Mechanical Exfoliation	Pt nanostrip	UV-Visible-NIR (325 nm, 532 nm, 980 nm)	312.5	1.1×10^{10}	-	[104]
FL Vertical MoS ₂	CVD	Au NPs	Visible (532 nm)	2.4×10^{-2}	5.3×10^9	0.1 s	[105]
FL Vertical MoS ₂	CVD	Pt NPs	Visible-NIR (400 nm-1100 nm)	7.87 (@1V) 432 (@5V)	1.48×10^{13} 1.85×10^{14}	87 ms/ 84 ms	This work

The responsivity of the Pt sensitized MoS₂ photodetector is significantly higher with an increment of 427% compared to VA-MoS₂, which is attributed to the plasmonic effect of Pt-NPs. The schematic of the plasmonic enhanced MoS₂ device is shown in Figure 4.31 (a). When light is incident on the Pt metal NPs, free conduction electrons of Pt NPs oscillate collectively with the resonance frequency of plasmon Pt NPs cloud, so-called LSPR phenomena occurs by the localized electric field of the Pt NPs in the vicinity of the MoS₂. The collective oscillation of electrons cloud dephases rapidly, predominantly releases the “plasmon energy” in three ways: (i) far-field scattering of light (radiative), (ii) near field enhancement of electromagnetic field intensity (non-radiative), and (iii) hot electron generation [110].

The light scattered by one NP could be trapped by another Pt NP, which results in a strong coupling effect. In addition to this, highly exposed edges with large surface areas of VA- MoS₂ can trap the Pt-NPs in between the vertical flakes and efficiently increase the contact cross-section at the Pt-MoS₂ junction. Therefore, it improves the overall absorption of MoS₂ in a

broad spectral range by trapping the light. The considerably enhanced absorption leads to increased generation of photo-excited e-h pairs. Those e-h pairs do not recombine radiatively (as proved by PL analysis) and subsequently improve the photocurrent of the Au/Pt@MoS₂/Au photodetector. Under resonance conditions, the incident light is confined into the small gap that augments the interfacial M-S and near field which resonantly excites the free electrons in the d-bands of Pt NPs, which is very close to the Fermi-level [104, 111] as illustrated in the band diagram (Figure 4.31 (b)). After that, excited plasmon dephases non-radiatively by Landau damping, and energy redistribution produces hot carrier electrons. When a strong coupling between MoS₂ and Pt occurs, plasmon-induced energetic “hot electrons” and excited d-band electrons are transferred to the conduction band of MoS₂ by crossing the Schottky barrier height while leaving the holes behind in Pt. Since metal contacts are taken from MoS₂, photo-excited charge carriers are separated by collecting them at the different ends of the metal electrodes. The plasmon enhanced near field and built-in electric field at the Pt-MoS₂ junction assist the effective separation of charge carriers. Therefore, in our case, at the Pt-MoS₂ interface, Pt (MoS₂) acts as an electron donor (acceptor). The excess of conduction band electrons in MoS₂ due to charge transfer significantly suppresses photogenerated charge carriers' recombination, which is beneficial for photodetectors.

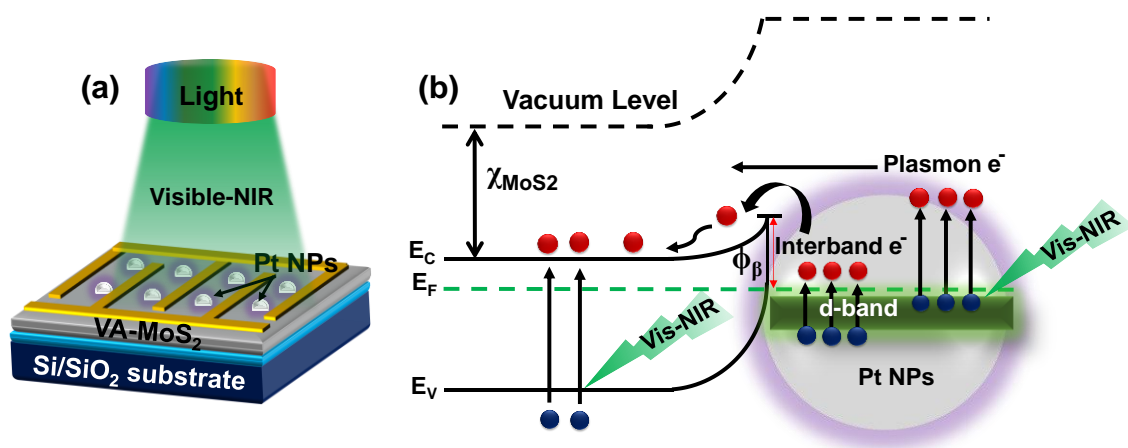


Figure 4.31 Device schematics and photodetection mechanisms. (a) Schematic illustration of plasmonic Pt NPs induced MoS₂ device under illumination. (b) Photoconduction mechanism at Pt-MoS₂ junction, hot electron of Pt transfers into the conduction band of MoS₂

Only those hot electrons, which have enough vertical momentum can cross the Schottky barrier from the Pt-MoS₂ interface proficiently, limiting the quantum efficiency. Quantum yield (QY) of hot electron injection into the semiconductor can be expressed by Fowler's equation [112]:

$$QY(\nu) = (h\nu - \phi_B)^2 / 4E_F h\nu \quad (4.35)$$

where $h\nu$ is the excitation energy, ϕ_B is Schottky barrier height at Pt-MoS₂ interface, E_F represents the Fermi-level energy at Pt. Therefore, the excitation energy of incident light and Schottky barrier height are the limiting factors that determine the hot electron transport. Lowering the barrier height at the Pt-MoS₂ interface allows more hot electrons into MoS₂, increasing the carrier collection rates, resulting in an increased photo-conversion efficiency in plasmon-induced hot carriers based nano-hybrid devices.

4.2.3.3 Conclusions

To summarize, we have designed Pt NPs decorated vertical oriented MoS₂ flakes for photodetector application. The large area VA-MoS₂ has been successfully synthesized employing the CVD method. Then, Pt-NPs are directly sputtered on MoS₂ sample to form Pt@MoS₂ hybrid system. Spectroscopic results reveal enhanced broad optical absorption with four-fold Raman intensity in Pt@MoS₂ as compared to VA-MoS₂ due to the LSPR effect. The significant PL quenching in Pt@MoS₂ manifests efficient charge transfer. The incorporation of Pt NPs further improves the junction quality of the device and reduces dark current, primarily due to the increase in series resistance. PDCR of VA-MoS₂ device dramatically increased on the integration of Pt NPs in the broad spectral range. The high values of responsivity, detectivity, and EQE (432 AW⁻¹, 1.85×10^{14} Jones, 6.7×10^4 %) are obtained in Pt@MoS₂, and can be attributed to the plasmon-induced enhanced field and trapping of light by Pt NPs. A theoretical model is employed to simulate the responsivity curve in the broad spectral regime, which reasonably agrees with experimentally calculated values. This helps to understand underlying device physics in terms of increased gain and mobility and decreased transit time. Further, the built-in electric field at the Pt-MoS₂ interface facilitates the carrier separation, resulting in an increased photoresponse with a fast response time (87 ms /84 ms). The present work promotes the use of Pt NPs in TMDs for their potential use in many practical applications such as light-harvesting, photo-electrochemical water splitting, and hydrogen evolution reactions, where augmented localized fields are required.

References

1. Ding, N., et al., *A novel approach for designing efficient broadband photodetectors expanding from deep ultraviolet to near infrared*. Light: Science & Applications, 2022. **11**(1): p. 91.
2. Maity, S., K. Sarkar, and P. Kumar, *A progressive journey into 2D-chalcogenide/carbide/nitride-based broadband photodetectors: recent developments and future perspectives*. Journal of Materials Chemistry C, 2021. **9**(41): p. 14532-14572.
3. Zumuukhorol, M., et al., *Broadband photodetector based on MoS₂/Ge heterojunction for optoelectronic applications*. Vacuum, 2023. **209**: p. 111746.
4. Fujita, T., et al., *Chemically exfoliated ReS₂ nanosheets*. Nanoscale, 2014. **6**(21): p. 12458-12462.
5. Zhang, Q., et al., *Extremely Weak van der Waals Coupling in Vertical ReS₂ Nanowalls for High-Current-Density Lithium-Ion Batteries*. Adv Mater, 2016. **28**(13): p. 2616-23.
6. Rahman, M., K. Davey, and S.Z. Qiao, *Advent of 2D Rhenium Disulfide (ReS₂): Fundamentals to Applications*. Advanced Functional Materials, 2017. **27**(10): p. 1606129.
7. Tongay, S., et al., *Monolayer behaviour in bulk ReS₂ due to electronic and vibrational decoupling*. Nature communications, 2014. **5**(1): p. 1-6.
8. Liu, E., et al., *High responsivity phototransistors based on few-layer ReS₂ for weak signal detection*. Advanced Functional Materials, 2016. **26**(12): p. 1938-1944.
9. He, M., et al., *Growth of vertical MoS₂ nanosheets on carbon materials by chemical vapor deposition: influence of substrates*. Materials Research Express, 2019. **6**(11): p. 1150c1.
10. Agrawal, A.V., K. Kaur, and M. Kumar, *Interfacial study of vertically aligned n-type MoS₂ flakes heterojunction with p-type Cu-Zn-Sn-S for self-powered, fast and high performance broadband photodetector*. Applied Surface Science, 2020. **514**: p. 145901.
11. Agrawal, A.V., et al., *Controlled Growth of MoS₂ Flakes from in-Plane to Edge-Enriched 3D Network and Their Surface-Energy Studies*. ACS Applied Nano Materials, 2018. **1**(5): p. 2356-2367.
12. Agrawal, A.V., et al., *Photoactivated Mixed In-Plane and Edge-Enriched p-Type MoS₂ Flake-Based NO₂ Sensor Working at Room Temperature*. ACS Sens, 2018. **3**(5): p. 998-1004.
13. Kumar, R., et al., *Highly selective and reversible NO₂ gas sensor using vertically aligned MoS₂ flake networks*. Nanotechnology, 2018. **29**(46): p. 464001.
14. Chakraborty, B., et al., *Symmetry-dependent phonon renormalization in monolayer MoS₂ transistor*. Physical Review B, 2012. **85**(16): p. 161403.
15. Mitra, S., et al., *Tailoring phonon modes of few-layered MoS₂ by in-plane electric field*. npj 2D Materials Applications 2020. **4**(1): p. 1-7.
16. McCreary, K.M., et al., *The effect of preparation conditions on Raman and photoluminescence of monolayer WS₂*. Scientific reports, 2016. **6**: p. 35154.
17. Mak, K.F., et al., *Atomically thin MoS₂(2): a new direct-gap semiconductor*. Phys Rev Lett, 2010. **105**(13): p. 136805.
18. Tran, M.D., et al., *Role of Hole Trap Sites in MoS₂ for Inconsistency in Optical and Electrical Phenomena*. ACS Appl Mater Interfaces, 2018. **10**(12): p. 10580-10586.
19. Mak, K.F., et al., *Tightly bound trions in monolayer MoS₂*. Nature materials, 2013. **12**(3): p. 207-211.

20. Mouri, S., Y. Miyauchi, and K. Matsuda, *Tunable Photoluminescence of Monolayer MoS₂ via Chemical Doping*. Nano Letters, 2013. **13**(12): p. 5944-5948.
21. Bellus, M.Z., et al., *Type-I van der Waals heterostructure formed by MoS₂ and ReS₂ monolayers*. Nanoscale Horizons, 2017. **2**(1): p. 31-36.
22. Kondekar, N.P., et al., *In situ XPS investigation of transformations at crystallographically oriented MoS₂ interfaces*. ACS applied materials, 2017. **9**(37): p. 32394-32404.
23. Hafeez, M., et al., *Large-area bilayer ReS₂ film/multilayer ReS₂ flakes synthesized by chemical vapor deposition for high performance photodetectors*. Advanced Functional Materials, 2016. **26**(25): p. 4551-4560.
24. Chiu, M.H., et al., *Band Alignment of 2D Transition Metal Dichalcogenide Heterojunctions*. Advanced Functional Materials, 2017. **27**(19): p. 1603756.
25. Kraut, E.A., et al., *Precise Determination of the Valence-Band Edge in X-Ray Photoemission Spectra - Application to Measurement of Semiconductor Interface Potentials*. Physical Review Letters, 1980. **44**(24): p. 1620-1623.
26. Zhang, K., et al., *Interlayer Transition and Infrared Photodetection in Atomically Thin Type-II MoTe₂/MoS₂ van der Waals Heterostructures*. ACS Nano, 2016. **10**(3): p. 3852-8.
27. Tang, Y., et al., *Distinctive Interfacial Charge Behavior and Versatile Photoresponse Performance in Isotropic/Anisotropic WS₂/ReS₂ Heterojunctions*. ACS Appl Mater Interfaces, 2020. **12**(47): p. 53475-53483.
28. Varghese, A., et al., *Near-Direct Bandgap WSe₂/ReS₂ Type-II pn Heterojunction for Enhanced Ultrafast Photodetection and High-Performance Photovoltaics*. Nano Lett, 2020. **20**(3): p. 1707-1717.
29. Zhai, X., et al., *Enhanced Optoelectronic Performance of CVD-Grown Metal-Semiconductor NiTe₂/MoS₂ Heterostructures*. ACS Appl Mater Interfaces, 2020. **12**(21): p. 24093-24101.
30. Chen, X., et al., *In-plane mosaic potential growth of large-area 2D layered semiconductors MoS₂-MoSe₂ lateral heterostructures and photodetector application*. ACS applied materials and interfaces, 2017. **9**(2): p. 1684-1691.
31. Ahn, J., et al., *Self-Powered Visible-Invisible Multiband Detection and Imaging Achieved Using High-Performance 2D MoTe₂/MoS₂ Semivertical Heterojunction Photodiodes*. ACS Applied Materials Interfaces 2020. **12**(9): p. 10858-10866.
32. Sun, M., et al., *Novel Transfer Behaviors in 2D MoS₂/WSe₂ Heterotransistor and Its Applications in Visible-Near Infrared Photodetection*. Advanced Electronic Materials, 2017. **3**(4): p. 1600502.
33. Ye, L., et al., *Near-Infrared Photodetector Based on MoS₂/Black Phosphorus Heterojunction*. Acs Photonics, 2016. **3**(4): p. 692-699.
34. Zhao, M., et al., *Interlayer coupling in anisotropic/isotropic van der Waals heterostructures of ReS₂ and MoS₂ monolayers*. Nano Research, 2016. **9**(12): p. 3772-3780.
35. Wang, X., et al., *Enhanced rectification, transport property and photocurrent generation of multilayer ReSe₂/MoS₂ p-n heterojunctions*. Nano Research, 2016. **9**(2): p. 507-516.
36. Liu, M., et al., *Ultra-Narrow-Band NIR Photomultiplication Organic Photodetectors Based on Charge Injection Narrowing*. The Journal of Physical Chemistry Letters, 2021. **12**(11): p. 2937-2943.

37. Yang, K., et al., *Smart Strategy: Transparent Hole-Transporting Polymer as a Regulator to Optimize Photomultiplication-type Polymer Photodetectors*. ACS Applied Materials Interfaces 2021. **13**(18): p. 21565-21572.
38. Zhao, Z., et al., *Highly sensitive all-polymer photodetectors with ultraviolet-visible to near-infrared photo-detection and their application as an optical switch*. Journal of Materials Chemistry C 2021. **9**(16): p. 5349-5355.
39. Xin, Y., et al., *Polarization-Sensitive Self-Powered Type-II GeSe/MoS₂ van der Waals Heterojunction Photodetector*. ACS Appl Mater Interfaces, 2020. **12**(13): p. 15406-15413.
40. Pezeshki, A., et al., *Electric and photovoltaic behavior of a few-layer α -MoTe₂/MoS₂ dichalcogenide heterojunction*. Advanced Materials, 2016. **28**(16): p. 3216-3222.
41. Lee, C.-H., et al., *Atomically thin p-n junctions with van der Waals heterointerfaces*. Nature nanotechnology, 2014. **9**(9): p. 676.
42. Wu, W.H., et al., *Self-powered photovoltaic photodetector established on lateral monolayer MoS₂-WS₂ heterostructures*. Nano Energy, 2018. **51**: p. 45-53.
43. Kaur, D. and M. Kumar, *A Strategic Review on Gallium Oxide Based Deep-Ultraviolet Photodetectors: Recent Progress and Future Prospects*. Advanced Optical Materials, 2021. **9**(9): p. 2002160.
44. Qin, Y., et al., *Amorphous Gallium Oxide-Based Gate-Tunable High-Performance Thin Film Phototransistor for Solar-Blind Imaging*. Advanced Electronic Materials, 2019. **5**(7): p. 1900389.
45. Yang, Y., et al., *Low Deposition Temperature Amorphous ALD-Ga₂O₃ Thin Films and Decoration with MoS₂ Multilayers toward Flexible Solar-Blind Photodetectors*. ACS Applied Materials & Interfaces, 2021. **13**(35): p. 41802-41809.
46. Zhuo, R., et al., *A self-powered solar-blind photodetector based on a MoS₂/ β -Ga₂O₃ heterojunction*. Journal of Materials Chemistry C, 2018. **6**(41): p. 10982-10986.
47. Li, H., et al., *From Bulk to Monolayer MoS₂: Evolution of Raman Scattering*. Advanced Functional Materials, 2012. **22**(7): p. 1385-1390.
48. Lee, C., et al., *Anomalous Lattice Vibrations of Single- and Few-Layer MoS₂*. ACS Nano, 2010. **4**(5): p. 2695-2700.
49. Wadhwa, R., et al., *Platinum nanoparticle sensitized plasmonic-enhanced broad spectral photodetection in large area vertical-aligned MoS₂ flakes*. Nanotechnology, 2022. **33**(25): p. 255702.
50. Liu, B., et al., *Enhanced photoresponse of TiO₂/MoS₂ heterostructure phototransistors by the coupling of interface charge transfer and photogating*. Nano Research, 2021. **14**(4): p. 982-991.
51. Splendiani, A., et al., *Emerging Photoluminescence in Monolayer MoS₂*. Nano Letters, 2010. **10**(4): p. 1271-1275.
52. Bhanu, U., et al., *Photoluminescence quenching in gold - MoS₂ hybrid nanoflakes*. Scientific Reports, 2014. **4**(1): p. 5575.
53. Klots, A.R., et al., *Probing excitonic states in suspended two-dimensional semiconductors by photocurrent spectroscopy*. Scientific Reports, 2014. **4**(1): p. 6608.
54. Xu, G., et al., *Binary-ternary transition metal chalcogenides interlayer coupling in van der Waals type-II heterostructure for visible-infrared photodetector with efficient suppression dark currents*. Nano Research, 2022. **15**(3): p. 2689-2696.
55. Wadhwa, R., et al., *Investigation of charge transport and band alignment of MoS₂-ReS₂ heterointerface for high performance and self-driven broadband photodetection*. Applied Surface Science, 2021. **569**: p. 150949.

56. Anderson, R.L., *Germanium-Gallium Arsenide Heterojunctions [Letter to the Editor]*. IBM Journal of Research and Development, 1960. **4**(3): p. 283-287.
57. Nisika, et al., *Engineering Cu₂ZnSnS₄ grain boundaries for enhanced photovoltage generation at the Cu₂ZnSnS₄/TiO₂ heterojunction: A nanoscale investigation using Kelvin probe force microscopy*. Journal of Applied Physics, 2021. **130**(19): p. 195301.
58. Arora, K., et al., *Ultrahigh Performance of Self-Powered β -Ga₂O₃ Thin Film Solar-Blind Photodetector Grown on Cost-Effective Si Substrate Using High-Temperature Seed Layer*. ACS Photonics, 2018. **5**(6): p. 2391-2401.
59. Kumar, A., M.A. Khan, and M. Kumar, *Recent advances in UV photodetectors based on 2D materials: a review*. Journal of Physics D: Applied Physics, 2022. **55**(13): p. 133002.
60. Wang, L., et al., *MoS₂/Si Heterojunction with Vertically Standing Layered Structure for Ultrafast, High-Detectivity, Self-Driven Visible–Near Infrared Photodetectors*. Advanced Functional Materials, 2015. **25**(19): p. 2910-2919.
61. Goel, N., et al., *Wafer-scale synthesis of a uniform film of few-layer MoS₂ on GaN for 2D heterojunction ultraviolet photodetector*. Journal of Physics D: Applied Physics, 2018. **51**(37): p. 374003.
62. Srivastava, A., et al., *Fabrication of MoS₂/ZnO Hybrid Nanostructures for Enhancing Photodetection*. IEEE Photonics Technology Letters, 2020. **32**(24): p. 1527-1530.
63. Chen, X., et al., *Fabry-Perot interference and piezo-phototronic effect enhanced flexible MoS₂ photodetector*. Nano Research, 2022. **15**(5): p. 4395-4402.
64. Lal Kumawat, K., et al., *A MoS₂/CuO-based hybrid p–n junction for high-performance self-powered photodetection*. Journal of Materials Chemistry C, 2022. **10**(38): p. 14159-14168.
65. Kumawat, K.L., et al., *Electrically Modulated Wavelength-Selective Photodetection Enabled by MoS₂/ZnO Heterostructure*. Physical Review Applied, 2022. **17**(6): p. 064036.
66. Jain, S.K., et al., *2D/3D Hybrid of MoS₂/GaN for a High-Performance Broadband Photodetector*. ACS Applied Electronic Materials, 2021. **3**(5): p. 2407-2414.
67. Wurdack, M., et al., *Ultrathin Ga₂O₃ Glass: A Large-Scale Passivation and Protection Material for Monolayer WS₂*. Advanced Materials, 2021. **33**(3): p. 2005732.
68. Gebert, M., et al., *Passivating Graphene and Suppressing Interfacial Phonon Scattering with Mechanically Transferred Large-Area Ga₂O₃*. Nano Letters, 2023. **23**(1): p. 363-370.
69. Heinemann, M.D., et al., *Oxygen deficiency and Sn doping of amorphous Ga₂O₃*. Applied Physics Letters, 2016. **108**(2): p. 022107.
70. Siao, M.D., et al., *Two-dimensional electronic transport and surface electron accumulation in MoS₂*. Nature Communications, 2018. **9**(1): p. 1442.
71. Miao, J., et al., *Surface Plasmon-Enhanced Photodetection in Few Layer MoS₂ Phototransistors with Au Nanostructure Arrays*. Small, 2015. **11**(20): p. 2392-2398.
72. Bang, S., et al., *Augmented Quantum Yield of a 2D Monolayer Photodetector by Surface Plasmon Coupling*. Nano Letters, 2018. **18**(4): p. 2316-2323.
73. Wang, H., et al., *Plasmonically enabled two-dimensional material-based optoelectronic devices*. Nanoscale, 2020. **12**(15): p. 8095-8108.
74. Wang, W., et al., *Hot Electron-Based Near-Infrared Photodetection Using Bilayer MoS₂*. Nano Letters, 2015. **15**(11): p. 7440-7444.
75. Sun, B., et al., *Tailoring of Silver Nanocubes with Optimized Localized Surface Plasmon in a Gap Mode for a Flexible MoS₂ Photodetector*. Advanced Functional Materials, 2019. **29**(26): p. 1900541.

76. Wu, Z.-Q., et al., *Gap-Mode Surface-Plasmon-Enhanced Photoluminescence and Photoresponse of MoS₂*. *Advanced Materials*, 2018. **30**(27): p. 1706527.
77. Knight, M.W., et al., *Aluminum Plasmonic Nanoantennas*. *Nano Letters*, 2012. **12**(11): p. 6000-6004.
78. Hunter, W.R., D.W. Angel, and G. Hass, *Optical properties of evaporated platinum films in the vacuum ultraviolet from 220 Å to 150 Å*. *Journal of the Optical Society of America*, 1979. **69**(12): p. 1695-1699.
79. Zhang, N., et al., *Near-field dielectric scattering promotes optical absorption by platinum nanoparticles*. *Nature Photonics*, 2016. **10**(7): p. 473-482.
80. Li, S., et al., *Edge-Enriched 2D MoS₂ Thin Films Grown by Chemical Vapor Deposition for Enhanced Catalytic Performance*. *ACS Catalysis*, 2017. **7**(1): p. 877-886.
81. Kukucska, G. and J. Koltai, *Theoretical Investigation of Strain and Doping on the Raman Spectra of Monolayer MoS₂*. *physica status solidi (b)*, 2017. **254**(11): p. 1700184.
82. Mukherjee, S., et al., *Plasmon Triggered, Enhanced Light–Matter Interactions in Au–MoS₂ Coupled System with Superior Photosensitivity*. *The Journal of Physical Chemistry C*, 2021. **125**(20): p. 11023-11034.
83. Xiong, F., et al., *Li Intercalation in MoS₂: In Situ Observation of Its Dynamics and Tuning Optical and Electrical Properties*. *Nano Letters*, 2015. **15**(10): p. 6777-6784.
84. Mukherjee, B., et al., *Exciton Emission Intensity Modulation of Monolayer MoS₂ via Au Plasmon Coupling*. *Scientific Reports*, 2017. **7**(1): p. 41175.
85. Castellanos-Gomez, A., et al., *Spatially resolved optical absorption spectroscopy of single- and few-layer MoS₂ by hyperspectral imaging*. *Nanotechnology*, 2016. **27**(11): p. 115705.
86. Wu, Z., et al., *Boosted photo-electro-catalytic hydrogen evolution over the MoS₂/MoO₂ Schottky heterojunction by accelerating photo-generated charge kinetics*. *Journal of Alloys and Compounds*, 2020. **832**: p. 154970.
87. Kumar, V., N. Nisika, and M. Kumar, *Modified Absorption and Emission Properties Leading to Intriguing Applications in Plasmonic–Excitonic Nanostructures*. *Advanced Optical Materials*, 2021. **9**(2): p. 2001150.
88. Ikhmayies, S.J. and R.N. Ahmad-Bitar, *A study of the optical bandgap energy and Urbach tail of spray-deposited CdS:In thin films*. *Journal of Materials Research and Technology*, 2013. **2**(3): p. 221-227.
89. Choudhury, A., et al., *Vapour transport grown photosensitive GeO₂ thin film*. *Materials Research Bulletin*, 2021. **142**: p. 111397.
90. Bonalde, I., et al., *Urbach tail, disorder, and localized modes in ternary semiconductors*. *Physical Review B*, 2004. **69**(19): p. 195201.
91. Zhou, W., et al., *Intrinsic Structural Defects in Monolayer Molybdenum Disulfide*. *Nano Letters*, 2013. **13**(6): p. 2615-2622.
92. Mondal, S., et al., *An experimental and theoretical understanding of a UV photodetector based on Ag nanoparticles decorated Er-doped TiO₂ thin film*. *Ceramics International*, 2021. **47**(10, Part B): p. 14879-14891.
93. Mondal, S., et al., *Detailed experimental and theoretical analysis of the high-temperature current conduction properties of Er-doped TiO₂ thin film based diodes*. *Materials Science in Semiconductor Processing*, 2021. **130**: p. 105834.
94. Di Bartolomeo, A., et al., *Asymmetric Schottky Contacts in Bilayer MoS₂ Field Effect Transistors*. *Advanced Functional Materials*, 2018. **28**(28): p. 1800657.
95. Milnes, A.G., *Heterojunctions and metal semiconductor junctions*. 2012: Elsevier.

96. Rai, A., et al., *Progress in Contact, Doping and Mobility Engineering of MoS₂: An Atomically Thin 2D Semiconductor*. Crystals, 2018. **8**(8).
97. Cheung, S.K. and N.W. Cheung, *Extraction of Schottky diode parameters from forward current-voltage characteristics*. Applied Physics Letters, 1986. **49**(2): p. 85-87.
98. Ghosh, A., et al., *GLAD synthesised erbium doped In₂O₃ nano-columns for UV detection*. Journal of Materials Science: Materials in Electronics, 2019. **30**(13): p. 12739-12752.
99. Bhattacharya, P., *Semiconductor optoelectronic devices*. 1997, Prentice Hall PTR.
100. Gosciniak, J., et al., *Plasmonic Schottky photodetector with metal stripe embedded into semiconductor and with a CMOS-compatible titanium nitride*. Scientific Reports, 2019. **9**(1): p. 6048.
101. Buscema, M., et al., *Photocurrent generation with two-dimensional van der Waals semiconductors*. Chemical Society Reviews, 2015. **44**(11): p. 3691-3718.
102. Wang, H., C. Zhang, and F. Rana, *Surface Recombination Limited Lifetimes of Photoexcited Carriers in Few-Layer Transition Metal Dichalcogenide MoS₂*. Nano Letters, 2015. **15**(12): p. 8204-8210.
103. Selamneni, V., et al., *MoS₂/Paper Decorated with Metal Nanoparticles (Au, Pt, and Pd) Based Plasmonic-Enhanced Broadband (Visible-NIR) Flexible Photodetectors*. Advanced Materials Interfaces, 2021. **8**(6): p. 2001988.
104. Kumar, R., et al., *Pt-Nanostrip-Enabled Plasmonically Enhanced Broad Spectral Photodetection in Bilayer MoS₂*. Advanced Optical Materials, 2017. **5**(9): p. 1700009.
105. Rahmati, B., et al., *Plasmonic improvement photoresponse of vertical-MoS₂ nanostructure photodetector by Au nanoparticles*. Applied Surface Science, 2019. **490**: p. 165-171.
106. Lee, S., et al., *Enhanced Photoresponsivity of Multilayer MoS₂ Phototransistor Using Localized Au Schottky Junction Formed by Spherical-Lens Photolithography*. Advanced Materials Interfaces, 2019. **6**(8): p. 1900053.
107. Lan, H.-Y., et al., *Gate-Tunable Plasmon-Enhanced Photodetection in a Monolayer MoS₂ Phototransistor with Ultrahigh Photoresponsivity*. Nano Letters, 2021. **21**(7): p. 3083-3091.
108. Sobhani, A., et al., *Enhancing the photocurrent and photoluminescence of single crystal monolayer MoS₂ with resonant plasmonic nanoshells*. Applied Physics Letters, 2014. **104**(3): p. 031112.
109. Li, Y., et al., *Superior Plasmonic Photodetectors Based on Au@MoS₂ Core-Shell Heterostructures*. ACS Nano, 2017. **11**(10): p. 10321-10329.
110. Tang, H., et al., *Plasmonic hot electrons for sensing, photodetection, and solar energy applications: A perspective*. The Journal of Chemical Physics, 2020. **152**(22): p. 220901.
111. Bornacelli, J., et al., *Nanoscale influence on photoluminescence and third order nonlinear susceptibility exhibited by ion-implanted Pt nanoparticles in silica*. Methods and Applications in Fluorescence, 2017. **5**(2): p. 025001.
112. Wu, K., et al., *Efficient hot-electron transfer by a plasmon-induced interfacial charge-transfer transition*. Science, 2015. **349**(6248): p. 632-635

Chapter 5: 2D MoS₂ heterostructures for hydrogen sensing

In this chapter, we present a novel approach for achieving selective hydrogen sensing at room temperature using vertically aligned MoS₂ functionalized with Pt nanoparticles (Pt@MoS₂). We provide a comprehensive investigation of the sensing performance of the Pt@MoS₂ sensor and discuss the underlying sensing mechanism. Additionally, we explore the effect of operating temperature on the sensor's performance. To gain further insights into the selective response of the Pt@MoS₂ sensor, we employ density functional theory (DFT) calculations to correlate gas adsorbate interactions with the sensing surface. Our results demonstrate that the Pt NPs sensitized MoS₂ sensor exhibits exceptional sensitivity, rapid response, and complete recovery. Our study suggests that Pt nanoparticles sensitized MoS₂ is a promising candidate for low power and room temperature hydrogen sensing applications, particularly for hydrogen vehicles and related technologies. Our findings contribute significantly to the advancement of hydrogen sensing technology by offering enhanced sensitivity and selectivity.

5.1 Requirement of highly sensitive room temperature hydrogen sensor

The rapid depletion of fossil fuel sources has drawn attention towards search for the next generation green fuel. Alternative fuels for instance biofuels, biodiesel and hydrogen (H₂) are trending among researchers to fulfill this demand. With the advancement in hydrogen production and storage, such as fuel cells, it has become one of the best alternatives for fossil fuels owing to its highest calorific value and zero carbon emission during combustion [1, 2]. But one of the biggest perils of hydrogen fuel is the self-combustion of H₂ even at lower concentration (above 4%) in the atmosphere [3]. This leads to an increased risk of explosions and danger to mankind. Moreover, the hydrogen flame is completely invisible to the naked eye, thereby enhancing the hazard involved in an unfortunate scenario. Therefore, considering safety issues, it becomes imperative to have an early and accurate detection of H₂ gas with high selectivity as well as sensitivity. To mitigate these adverse effects, various sensors detecting H₂ have been developed. Most of these are based on metal oxides (such as SnO₂, TiO₂, ZnO, WO₃, etc.) because of their high sensitivity [4-6]. However, this sensitivity is achieved only at higher working temperatures (> 200 °C) raising safety concerns since H₂ becomes more flammable at elevated temperatures. To increase the sensitivity of these sensors to H₂ gas at room temperature, noble metal catalysts such as Pt / Pd have been proposed due to enhanced absorption and dissociation [7-10]. For example, Alenezy et al. have demonstrated that decoration of thin Pd film over TiO₂ substantially enhances the sensitivity of H₂ gas at room

temperature [11]. Dhall et al. utilized Pt nanoparticles (NPs) to fabricated multi-wall carbon nanotube based hybrid (F-MWCNT/TiO₂/Pt) for H₂ sensing application at room temperature, and achieved 3.9 % sensitivity at low concentration of 0.05% [12]. Despite significant advancement in the sensitivity of conventional metal oxide based sensors, the selectivity issue of H₂ at low temperature is still unresolved.

Alternatively, 2D materials such as MoS₂, have also been proposed as potential candidates for gas sensing device applications due to their high surface to volume ratio, high carrier mobility and fast charge transport [13-17]. The reported literature suggests that bare MoS₂ sensors are insensitive to H₂ exposure [18, 19] whereas, heterostructures with MoS₂ or their nanocomposites exhibit high response and hence are being explored for H₂ sensing [20, 21]. Although they show good response, still, heterostructure based gas sensors often suffer from slow response/incomplete recovery at room temperature. In most of the reported work, in-plane MoS₂ has been utilized for gas sensing applications, but because of low active sites, they become less adsorbent to some gases while being unresponsive to others. In contrast, vertically aligned MoS₂ (VA-MoS₂) having a high aspect ratio, has more reactive edge sites and can have significantly enhanced gas adsorption [18, 22]. Cho et al. reported that VA-MoS₂ has five fold enhanced sensitivity as compared to in-plane MoS₂ to NO₂ gas, attributed to higher adsorption energy at the edge sites of the MoS₂ [23]. Kumar et al. also validated the enhanced adsorption of gas molecules in VA-MoS₂ with improved selectivity at room temperature for NO₂ gas [18]. However, the high adsorption energy of hydrogen and other gases at different active sites on MoS₂ flakes makes it difficult to desorb them and therefore, designing room temperature and hydrogen selective sensors becomes tough.

5.2 Experimental section

5.2.1 Synthesis of MoS₂ and Pt NPs decorated MoS₂ (Pt@MoS₂)

The large area VA-MoS₂ flakes on p-Si/SiO₂ substrate are synthesized via modified tube in tube atmospheric pressure chemical vapor deposition (APCVD) technique. Prior to deposition, substrates were cleaned in acetone for 20 minutes via ultra-sonication followed by nitrogen jet drying. Precursors of a high quality (Sigma Aldrich, 99.99%) MoO₃ and S powder were used to grow VA-MoS₂. The MoO₃ (0.057 g) and S (0.45 g) powder were placed in two individual zirconia boat and substrate was placed on top of MoO₃ boat in face down condition. Both the boats kept inside a small one-end closed quartz tube with the separation of ~ 18 cm. Afterwards, this small quartz tube was placed inside a bigger quartz tube furnace supplied with the CVD with three separate heating zones. The temperature of MoO₃ and S zone were raised to 800 °C

and 350 °C, respectively with 17.5 °C /min rate. The growth time of VA- MoS₂ flakes was 30 min under Ar gas flow rate of 175 sccm, which was kept constant throughout the deposition. Finally, the furnace was allowed to cool down naturally. The integration of Pt NPs over VA-MoS₂ (Pt@MoS₂) was directly performed through sputtering of Pt NPs on pre-deposited MoS₂ flakes using Auto fine coater (JFC 16, JEOL) under an applied current of 30 mA. Figure 5.1 shows the structural composition and synthesis process of Pt@MoS₂. The size of Pt NPs can be controlled by the sputtering time. Here, deposition times of Pt NPs were 5s and 10s with an average particle size of 4 ± 2 nm and 10 ± 5 nm, respectively, as depicted in Figure 5.2.

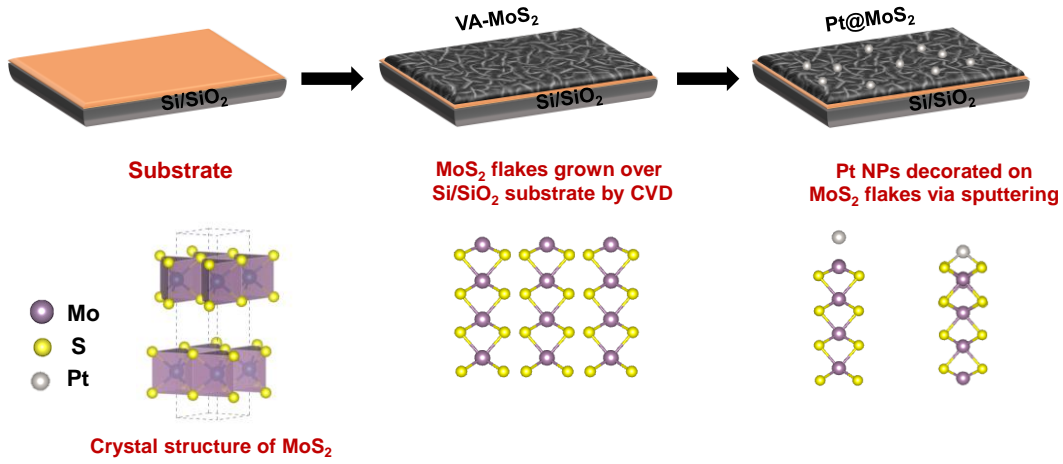


Figure 5.1 Structural composition and synthesis process of Pt@MoS₂.

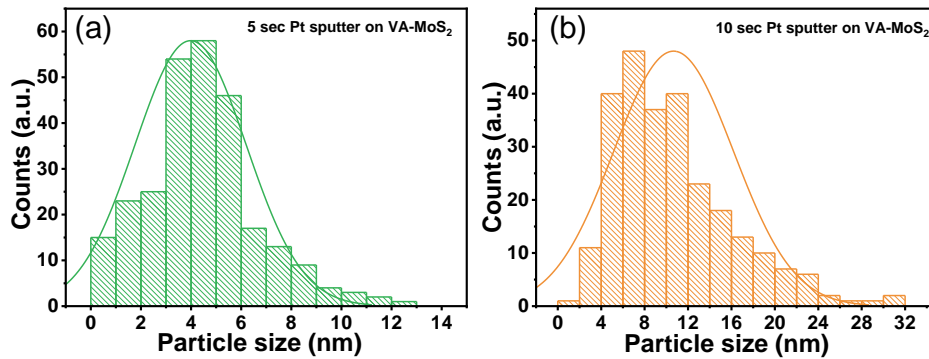


Figure 5.2 The particle size distribution of Pt nanoparticles sputtered for (a) 5s and (b) 10s. The bar graph shows that particles have an average size of $4 \text{ nm} \pm 2 \text{ nm}$ for 5s Pt sample and $10 \text{ nm} \pm 5 \text{ nm}$ for 10s Pt sample.

5.2.2 Characterizations

The surface topography of the VA-MoS₂ flakes were characterized by FESEM (NOVA NANOSEM). The Raman and PL measurements were recorded at room temperature with an excitation source of 532 nm using Horiba LabRAM HR Evolution. XPS measurements were carried out by Nexa (Thermofisher Scientific) using monochromatic Al K α ($h\nu = 1486.68 \text{ eV}$) and UPS measurements were performed using He (I) discharge lamp ($h\nu = 21.2 \text{ eV}$).

5.2.3 Device fabrication and gas sensing measurements

For device fabrication, an interdigitated metal contacts of Au/Cr (300/20 nm) were deposited on VA-MoS₂ flakes using shadow mask by thermal evaporator. In order to decrease the contact resistance, the device was annealed at 150 °C for 40 min in presence of Ar gas. The sensing performance of the device was evaluated for various H₂ gas concentration at different temperature (RT to 150 °C). An external heating filament was used to increase the temperature of the sensor. The sensor selectivity was investigated against NO₂, NH₃, H₂S, SO₂ and CO₂ gases. A Keithley 4200 was used to measure the change in relative resistance of the device at 2 V in a gaseous environment.

5.3 Results and Discussions

5.3.1 Structural, optical, and chemical properties

The surface topography of the VA-MoS₂ flakes and Pt NPs were investigated using field emission scanning electron microscopy (FESEM). Figure 5.3 (a) displays the FESEM image of highly uniform inter-connected VA-MoS₂ flakes, with Pt NPs on top. The as-grown VA-MoS₂ flakes have high surface-to-volume ratio with larger number of exposed active sites. The Pt NPs are evenly distributed over the MoS₂ flakes, which can be seen in the inset of Figure 5.3 (a).

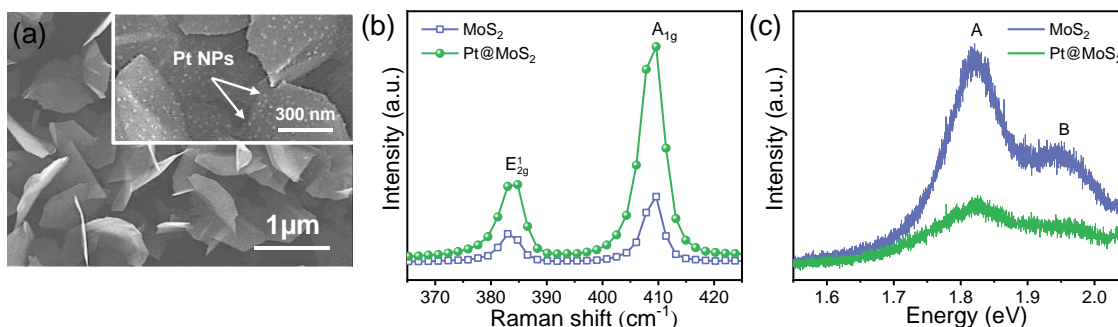


Figure 5.3 (a) FESEM image of Pt NPs decorated vertically aligned MoS₂ flakes, inset shows high magnification image. (b) Raman and (c) PL spectrum of MoS₂ (open-blue) and Pt@MoS₂ (solid-green).

The Raman spectra of MoS₂ and Pt@MoS₂ is illustrated in Figure 5.3 (b). The Raman spectra of MoS₂ exhibits two prominent peaks at 383 cm⁻¹ and 409.6 cm⁻¹ corresponding to in-plane (E_{2g}^1) and out of plane (A_{1g}) vibrational modes, respectively [24]. The Raman shift difference between E_{2g}^1 and A_{1g} vibrational mode is 26.6 cm⁻¹, which suggests the presence of few-layers of MoS₂. Additionally, the intensity ratio of $\frac{E_{2g}^1}{A_{1g}}$ is 0.43, which further affirms the formation of VA- MoS₂ flakes [23, 25]. After incorporation of Pt NPs, there is no significant change

observed in the position of E_{2g}^1 and A_{1g} vibrational modes, indicating no stress or strain is experienced by underlying MoS₂ flakes due to the Pt NPs [26]. Nonetheless, intensity of both the Raman vibrational modes of MoS₂ is drastically enhanced. The surface enhanced Raman scattering (SERS) in MoS₂ is ascribed to the augmented electromagnetic field intensity induced from localized surface plasmon resonance of Pt NPs [27, 28].

The PL spectra of VA-MoS₂ exhibits two characteristic emission peaks at 1.82 eV and 1.94 eV corresponding to A and B excitons, respectively as shown in Figure 5.3 (c). The A exciton peak is associated with direct bandgap transition while B exciton peak arises due to interlayer interaction and spin-orbit coupling in valence band of MoS₂ [29]. The PL emission intensity of MoS₂ is enormously reduced by 72% after incorporation of Pt NPs, suggesting PL quenching attributed to the strong charge transfer between Pt NPs and MoS₂ [27]. Here, PL quenching in Pt@MoS₂ infers the doping by Pt NPs ascribed to the change in electronic structure of the hybrid system. The Fermi-levels of VA-MoS₂ and Pt are 4.83 eV and 5.6 eV [30]. The difference in Femi-levels of MoS₂ and Pt leads to bend-bending with an offset value of 0.76 eV. Upon excitation, electrons from the excited states of MoS₂ are transferred to Pt cause p-doping in MoS₂. Since, transferred electrons have not decayed back to the original ground state, it leads to PL quenching in the Pt@MoS₂ hybrid [31].

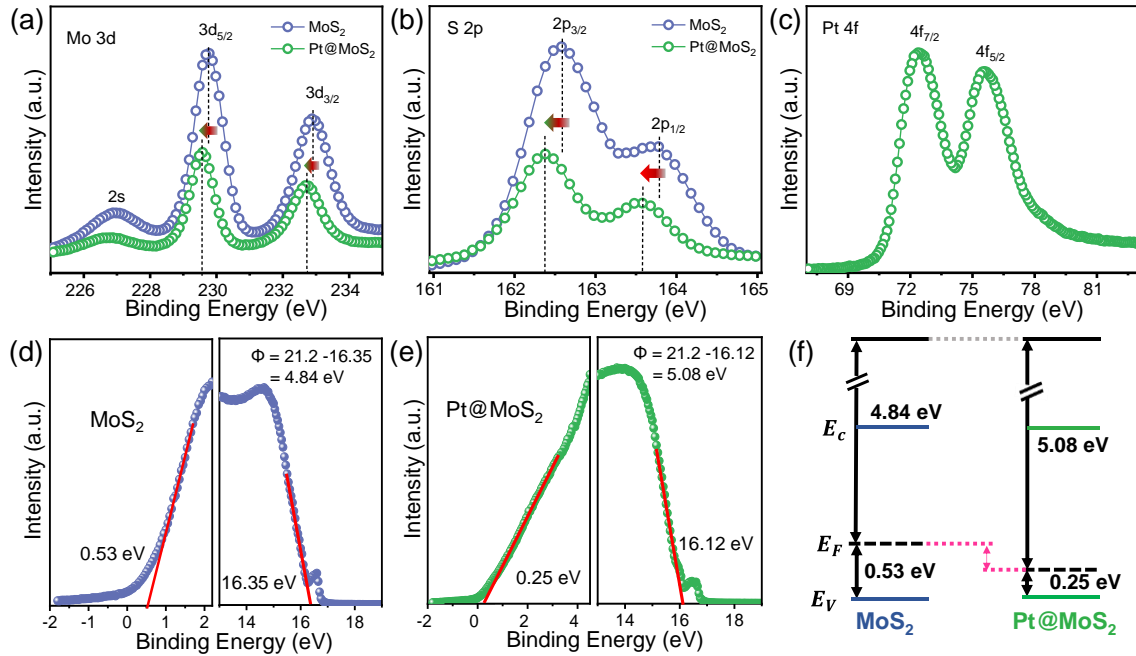


Figure 5.4 (a) Core level spectrum of Mo 3d (b) S 2p of MoS₂ and Pt@MoS₂, lower binding energy shift of Mo 3d and S 2p in Pt@MoS₂ indicate further p-doping in MoS₂ after incorporation of Pt NPs (c) Pt 4f spectrum of Pt@MoS₂ (d), (e) UPS spectrum of MoS₂ and Pt@MoS₂ respectively (f) Band alignment of pristine MoS₂ and Pt@MoS₂ determined from UPS data.

Further, XPS was performed to examine the elemental information about MoS₂ and Pt decorated MoS₂ sample. The high resolution XPS spectrum of Mo 3*d* and S 2*p* core level is shown in Figure 5.4 (a) and (b), respectively. The Pt 4*f* core-level peaks assigned to Pt 4*f*_{7/2} (72.38 eV) and Pt 4*f*_{5/2} (75.58 eV) confirm the presence of metallic Pt NPs in Pt@MoS₂ as demonstrated in Figure 5.4 (c). In case of pristine MoS₂, core level of Mo 3*d* splits into two peaks Mo 3*d*_{5/2} and Mo 3*d*_{3/2} corresponding to Mo⁺⁴ located at binding energy position 229.78 eV and 232.88 eV, respectively. The core level of S 2*p* splits into two doublet S 2*p*_{3/2} and S 2*p*_{1/2} centered at 162.58 eV and 163.78 eV, respectively, associated with divalent sulfide (S⁻²). These binding energy positions of Mo 3*d* and S 2*p* core level are consistent with the reported MoS₂ [32]. However, after integration of Pt NPs on MoS₂, a red shift of 0.2 eV is observed in both the core level of Mo 3*d* and S 2*p*. The observed red shift in Mo 3*d* and S 2*p* core level positions in Pt@MoS₂ re-inforces p-doping [33]. Figure 5.4 (d) and (e) represents the valence band region (left) and lower energy cut off in the binding energy curve (right) for the MoS₂ (blue) and Pt@MoS₂ (green) from the UPS data. The calculated valence band of the pristine MoS₂ is 0.53 eV with reference to Fermi-level, showing p-type nature of MoS₂ as Fermi-level lies close to valence band. The work functions of the samples are evaluated by subtracting the lower energy cut off from the energy of the used He (I) source. Therefore, calculated work-functions of MoS₂ and Pt@MoS₂ are 4.84 eV and 5.08 eV, respectively. Work function increases after incorporation of Pt NPs. Hence, Fermi-level shifts closer to the valence band (Figure 5.4 (f)), which again corresponds to p-doping in MoS₂. In addition to this, valence band minima position in the Pt@MoS₂ composite also reduces to 0.25 eV, consistent with the increased value of work function, further confirming the p-doping attributed to transferring of electrons from MoS₂ to Pt. Hence, XPS and UPS analysis are analogous and demonstrate the p- doping in MoS₂ after incorporation of Pt NPs.

5.3.2 Gas sensing performance

First, sensing behavior of pristine MoS₂ device was investigated towards NO₂ gas at various concentration from 50 ppm to 0.5 ppm at room temperature. Upon exposure of NO₂ gas, the resistance of the sensor decreases (Figure 5.5 (a)). The relative response of the sensor increases with increasing NO₂ concentration, depicted in Figure 5.5 (b). The gas sensing mechanism is directly based on the charge transfer between gas and MoS₂. Due to unpaired electron on Nitrogen atom, NO₂ acts as an electron acceptor gas and it extracts an electron from MoS₂. The decrease in resistance after NO₂ exposure, suggests the p-type characteristics of MoS₂. The change in resistance was also observed in the presence of H₂ gas, however its relative response

is less than that for NO₂ gas. The resistance profile of pristine MoS₂ and its corresponding response towards H₂ gas are displayed in Figure 5.5 (c) and (d), respectively. Further, sensing behavior of MoS₂ was investigated in the presence of different gaseous ambient. The selectivity curve confirms the sensitivity of the MoS₂ sensor response towards the NO₂ gas (Figure 5.5 (e)), which is well in agreement with the reported literature [19]. In contrast to MoS₂ sensor, Pt@MoS₂ sensor exhibits improved response towards H₂ gas and sensor's selectivity switched from NO₂ to H₂ gas. The improved sensing performance of Pt@MoS₂ towards H₂ gas is ascribed to the spillover effect and creation of additional adsorption sites on Pt NPs surface or Pt-MoS₂ interface.

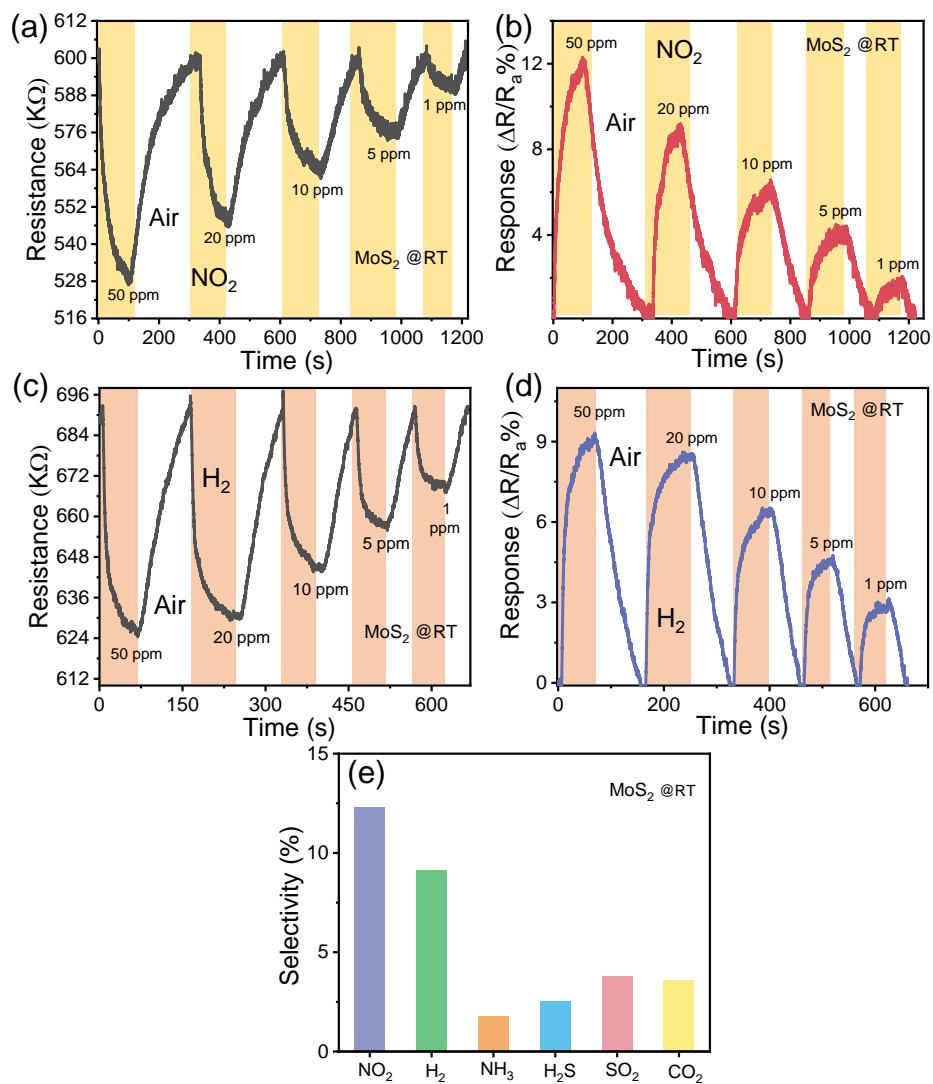


Figure 5.5 (a) Real time change in resistance of MoS₂ as function of NO₂ concentration at room temperature. (b) Corresponding response plot of MoS₂. (c) Resistance versus time profile of MoS₂ as a function under different H₂ concentration at room temperature. (d) Corresponding response plot of MoS₂. (e) Selectivity response against six different gases of MoS₂ sensor at room temperature.

The size of the Pt NPs also plays a crucial role in sensing performance. In the present study, we evaluated the sensing performance of Pt NPs decorated VA-MoS₂ with two different Pt thickness (sputter time 5 s and 10 s), named as Pt@MoS₂ (5) and Pt@MoS₂ (10), respectively. The particle size distribution of Pt nanoparticles demonstrated in Figure 5.2, which showed that the average size of Pt NPs are 4 nm for 5s and 10 nm for 10s sputter sample on VA-MoS₂. Both Pt@MoS₂ (5) and Pt@MoS₂ (10) shows the obvious enhanced sensing characteristic to H₂ gas (Figure 5.6 (a)). Further, we measured the response of these fabricated sensor for different concentration of H₂ (50 ppm, 20 ppm, 10 ppm and 1 ppm) as illustrated in Figure 5.6 (b). The small Pt NPs (corresponding to 5s Pt deposit) shows better response compared to the larger size Pt NPs. This is attributed to the fact that increased deposition time leads to increase in Pt film thickness, which subsequently increase the particle density as well as particle size. Thus, Pt NPs particles start agglomerating beyond a critical thickness of sputtered film, decreasing the number density of the particles and hence reducing the extent of Hydrogen (H) spillover onto the MoS₂ surface [27, 34]. The sensing results clearly depicts 5 s Pt deposited sample i.e. Pt@MoS₂ (5) is optimum to achieve the best sensing response. Hence, Pt@MoS₂ (5) was chosen for further measurements and is defined as Pt@MoS₂ henceforth.

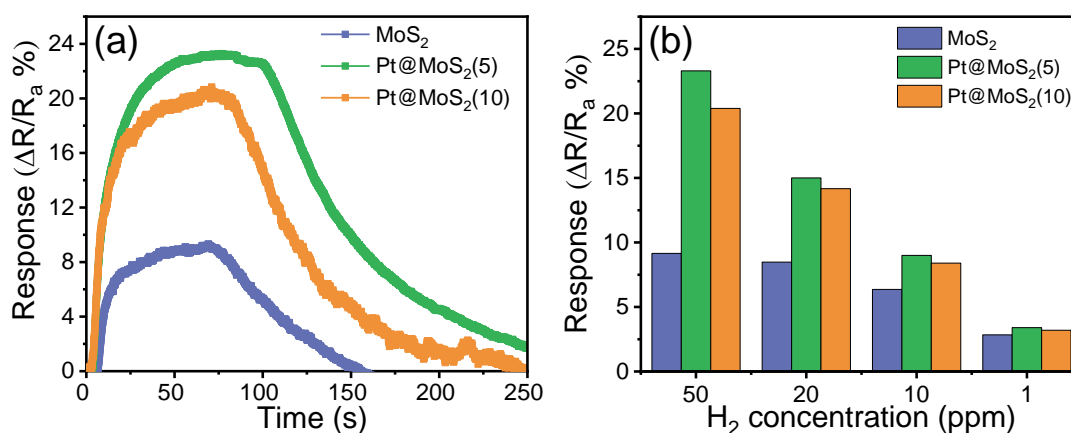


Figure 5.6 (a) Response versus time profile of MoS₂ and Pt@MoS₂ sensors for 50 ppm (H₂ gas); Here, 5 and 10 in Pt@MoS₂ represent the sputter time in seconds of Pt NPs deposited over pristine MoS₂ (b) Comparative response of the fabricated sensors (MoS₂ and Pt@MoS₂) as a function of H₂ concentration.

The schematic of Pt@MoS₂ sensor is shown in Figure 5.7 (a). The sensing performance of MoS₂ and Pt@MoS₂ were investigated for different concentration of H₂ gas at RT. Both the sensors MoS₂ and Pt@MoS₂ demonstrate same p-type conductivity as their resistance decreases upon H₂ exposure. The baseline resistance of MoS₂ was 692 K Ω while after incorporation of Pt NPs, baseline resistance of MoS₂ reduced to 200 K Ω . The decrease in baseline resistance of Pt@MoS₂ confirms further p-doping in MoS₂ after introducing Pt NPs,

corroborating XPS and UPS analysis. Upon H₂ exposure, Pt@MoS₂ exhibits considerable change in resistance with fast response and complete recovery at room temperature (Figure 5.7 (b)). Notably, Pt@MoS₂ is able to detect the H₂ gas below 1 ppm. The sensor's resistance decreases with increasing gas concentration. Here, sensing ability of the device were evaluated in term of relative response, response time and recovery time.

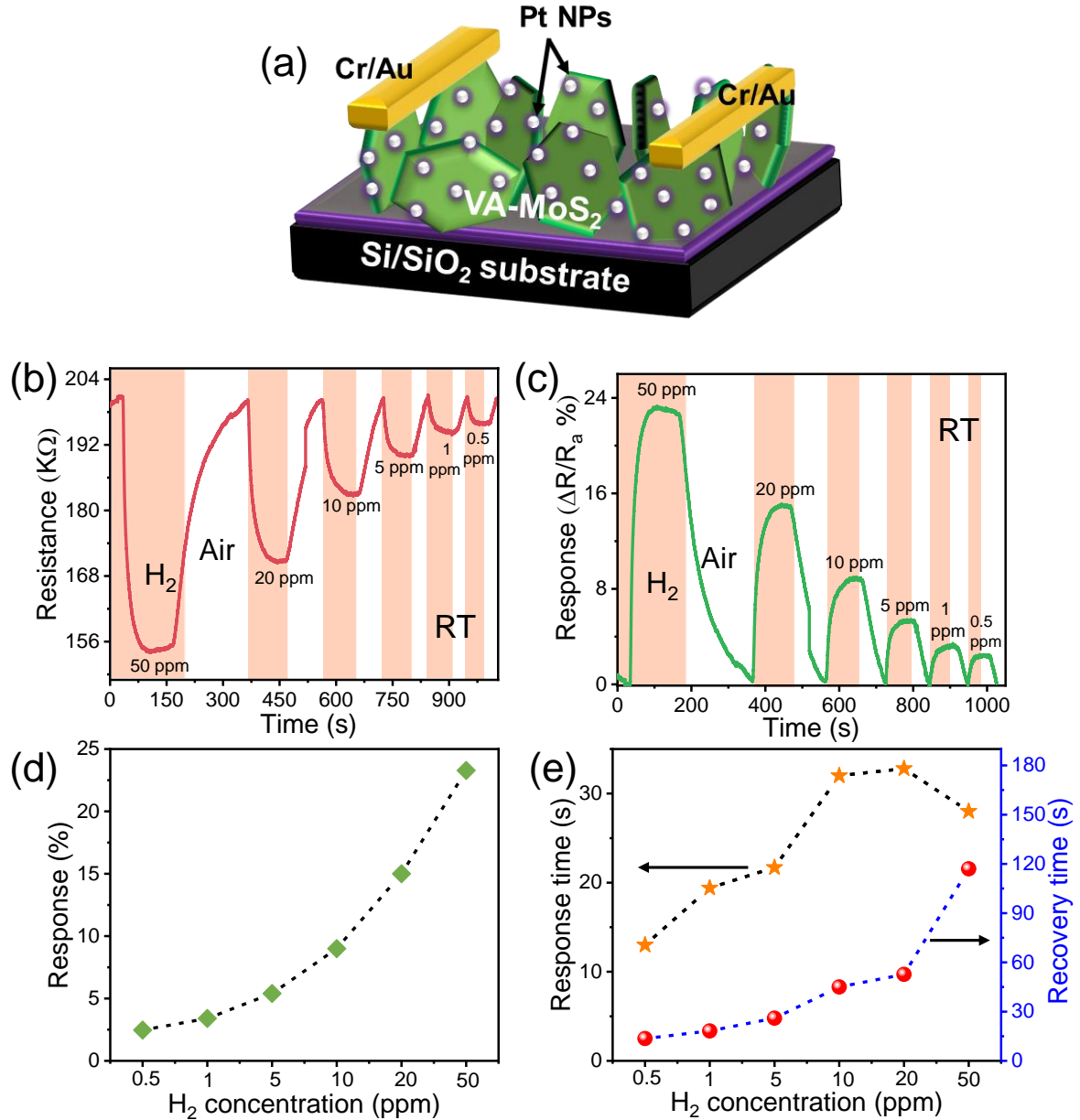


Figure 5.7 (a) Schematic of Pt NPs decorated VA-MoS₂ sensor. (b) Dynamic resistance change of Pt@MoS₂ sensor upon exposure to H₂ gas ranging from 50 to 0.5 ppm at room temperature (c) Corresponding response plot of Pt@MoS₂ sensor (d) Response of the fabricated Pt@MoS₂ sensor as a function of hydrogen concentration (e) Response and recovery time of the sensor for hydrogen concentration vary from 0.5 ppm to 50 ppm.

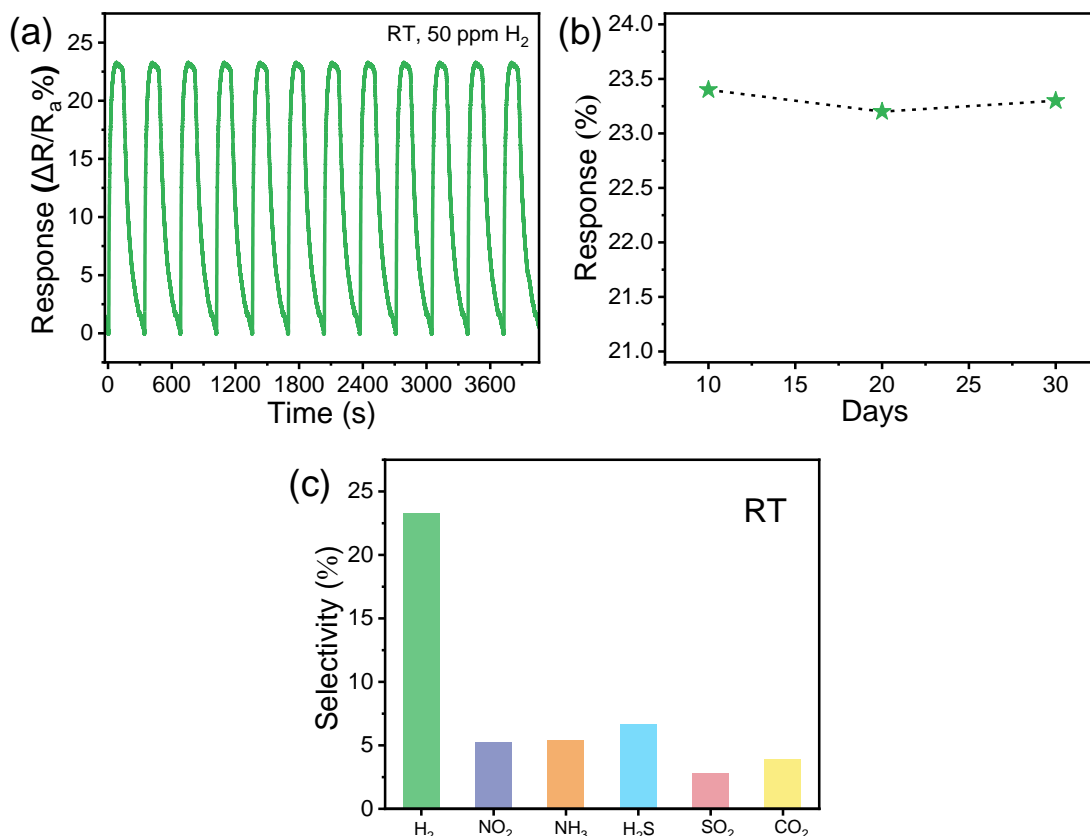


Figure 5.8 (a) Repeatability and (b) Stability of the fabricated Pt@MoS₂ gas sensor at room temperature when exposed to 50 ppm H₂, (c) Selectivity test histogram for Pt@MoS₂ against H₂, NO₂, NH₃, H₂S, SO₂, CO₂ gas at room temperature.

The relative response of the sensor is calculated by the formula $\Delta R/R_a \times 100\%$ where, $\Delta R = (R_a - R_g)$, R_a and R_g are the device resistance in the presence of air and gas, respectively. The relative response of the sensor at various H₂ concentrations is presented in Figure 5.7 (c). The Pt@MoS₂ showed the highest response of 23.2% for 50 ppm H₂ concentration compared with pristine MoS₂ (9 %). More importantly, Pt@MoS₂ exhibits reasonably good response of 2.5% even at very low concentration (0.5 ppm H₂). The significant response of Pt@MoS₂ sensor at 0.5 ppm H₂ gas suggests that Pt NPs can be utilized to develop highly sensitive low level detection (< 1 ppm) sensors. Figure 5.7 (d) shows response of the sensor increases with increasing gas concentration as more H₂ gas molecules interact with the surface of Pt and MoS₂. At RT, our fabricated Pt@MoS₂ device shows the lowest response/recovery time of 13 s/ 13s for 0.5 ppm of H₂ concentration. Response and recovery time of the sensor increases with increasing H₂ concentration and varies from 13 s to 32 s and 13 s to 117 s in the range of 0.5 ppm to 50 ppm, respectively, as presented in Figure 5.7 (e). Repeatability is a key prerequisite for evaluating the reliability of the sensor. The repeatability of the Pt@MoS₂ was investigated under 50 ppm H₂ at RT. The repetitive dynamic response with twelve consecutive cycles of the

Pt@MoS₂ is shown in Figure 5.8 (a). No significant change was observed in sensor response during the repeated exposure and removal of H₂ gas, which shows that the sensor retains its initial original response and has excellent repeatability. The stability of the Pt@MoS₂ sensor is also evaluated by measuring the sensor response at intervals of 10 days as illustrated in Figure 5.8 (b). It is clear from the response curve that the sensor's response toward H₂ was nearly constant for about a month corroborating that the fabricated sensor possesses substantial stability. The selectivity test of the Pt@MoS₂ was performed against six different gas exposure (Figure 5.8 (c)). The excellent selectivity towards H₂ gas is attributed to the strong adsorption of H₂ and weak adsorption of other gaseous molecules on the surface of the Pt@MoS₂ sensor at RT.

Further, we have analyzed the effect of operating temperature on the device performance. Figure 5.9 shows base resistance of the device decreases with temperature is attributed to desorption of oxygen from MoS₂ sites at higher temperature [19]. The calculated response of the Pt@MoS₂ at room temperature (RT), 50 °C, 100 °C and 150 °C is illustrated in Figure 5.10 (a). As sensing temperature of the device increases from RT to 100 °C, the response of the device increased from 23.2 % to 46 %. However, at 150 °C the device response starts declining (37%). Thus, the optimum temperature of the sensor is 100 °C.

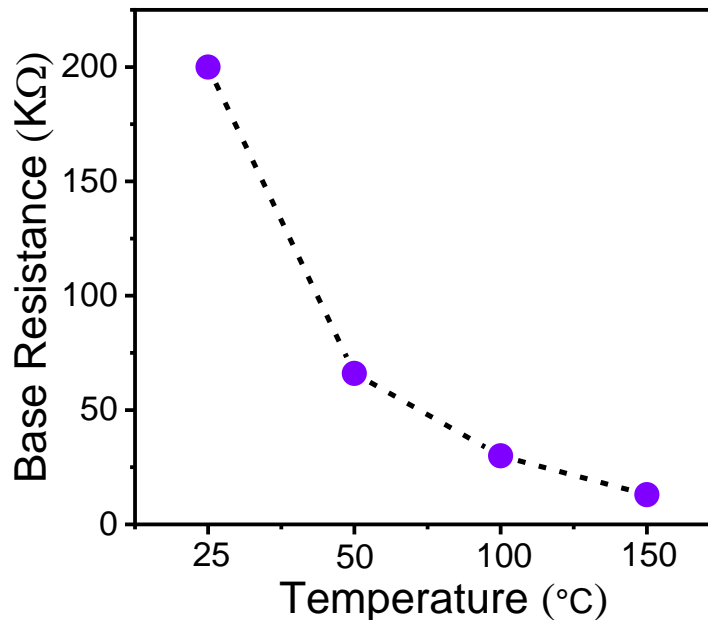


Figure 5.9 Base resistance of Pt@MoS₂ as a function of temperature.

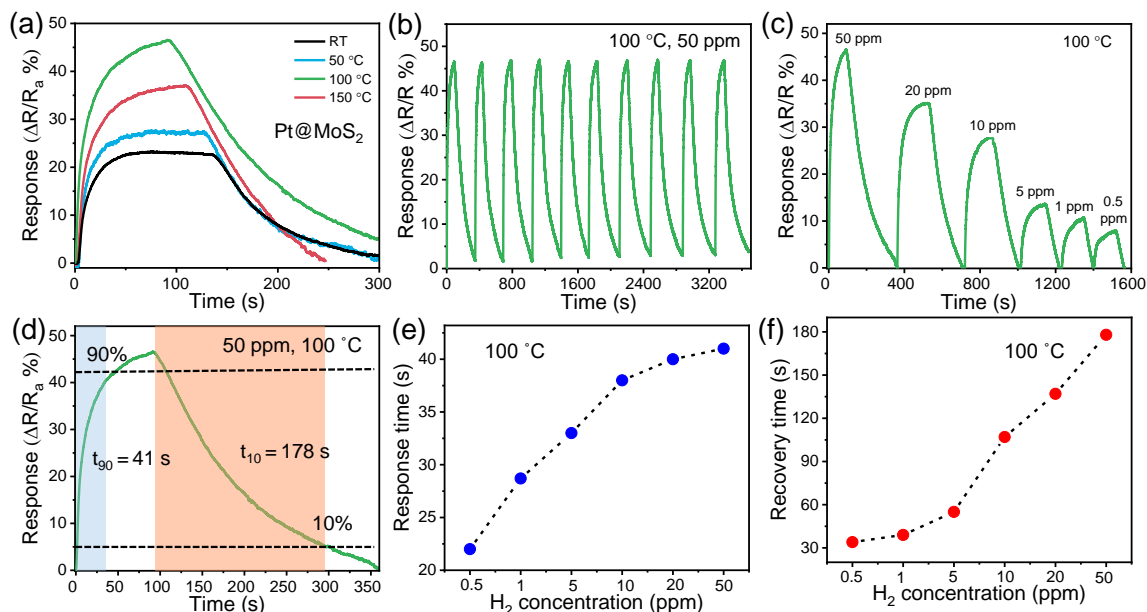


Figure 5.10 (a) Temperature dependent response curve of Pt@MoS₂ for H₂ sensing, at 100 °C sensor shows maximum response (b) Repetitive cycles of response variation of Pt@MoS₂ gas sensor at 100 °C towards 50 ppm H₂ concentration, (c) Response of the Pt@MoS₂ sensor towards 50 ppm to 0.5 ppm of H₂ at 100 °C (d) Response time plot of single cycle at 100 °C to calculate response and recovery time (e) Response and (f) Recovery speed of our fabricated Pt@MoS₂ sensor as a function of H₂ concentration at 100 °C.

Generally, it is believed that sensor's response is affected by multiple factors including, adsorption of oxygen species on the material surface, rate of adsorption and desorption of gas molecule, concentration of charge carriers etc. All these factors are function of temperature, which determines quantitatively the electrons involved in the surface reaction. Therefore, an optimum temperature (100 °C) here corresponds to maximum involvement of the active electrons in the surface reaction of the Pt NPs or interfaces with MoS₂. At the higher temperature (100-150 °C) for the fixed concentration of H₂ (50 ppm) the response time reaches nearly saturated ~ 41 s, whereas recovery speed is comparatively fast for 150 °C (102 s) than 100 °C (178 s). The faster recovery at higher temperature is attributed to fast desorption of H₂ gas on Pt catalysis at higher temperature (150 °C). The excellent sensing repeatability of Pt@MoS₂ for continuous ten consecutive exposure to H₂ gas (50 ppm) at 100 °C is demonstrated in Figure 5.10 (b). The time resolved response of Pt@MoS₂ in the concentration range 50 ppm to 0.5 ppm of H₂ is illustrated in Figure 5.10 (c). The sensor response increases monotonously with increasing concentration of exposed gas varying from 8 % to 46 %. Moreover, response and recovery time of the sensor were also calculated at this optimum temperature (100 °C) (Figure 5.10 (d)). The response time of the sensor varies from 22 s to 41 s, and reaches a saturation value at higher concentrations, indicating that the adsorption rate of

H₂ is almost constant for higher gaseous concentration (Figure 5.10 (e)). The recovery time of the fabricated device drastically reduces from 170 s to 34 s with reducing gas concentration. However, it reaches the saturation value at lower concentration, suggesting the desorption rate of H₂ is almost constant for low concentration range (Figure 5.10 (f)).

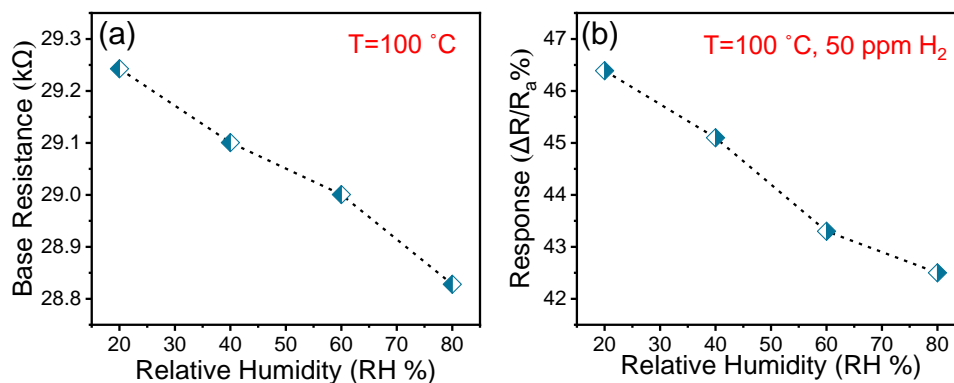


Figure 5.11 (a) Variation in baseline resistance with relative humidity from 20% to 80% for Pt@MoS₂ at 100 °C, (b) Corresponding response of Pt@MoS₂ at 50 ppm H₂ exposure under different relative humidity conditions.

For devices with any practical applications, it becomes imperative to study the effect of the ambient such as humidity which greatly affects the performance of 2D materials-based gas sensors.[35, 36] The effect of humidity on H₂ sensing for Pt@MoS₂ at 100 °C was investigated by changing the relative humidity from 20% to 80%. The humidity/ moisture content was created inside the sensing measurement chamber through water vapour and by adjusting the concentration of inlet water vapor relative humidity was controlled, which is detected by humidity sensor connected to the sensing chamber. Figure 5.11 (a) exhibits the baseline resistance of Pt@MoS₂ sensor under different relative humidity (20% to 80%) at 100 °C. The base resistance of the sensor decreases marginally with increasing relative humidity. Additionally, the sensor response towards hydrogen gas decreases with increasing humidity and showed a maximum of 4% decrement (Figure 5.11 (b)), implying an excellent performance even in a highly humid environment. Usually, the adsorption of water molecules on the sensor surface leads to resistance change and decreases the active sites for the adsorption of gas molecules. Under high humidity, large no. of water molecules are absorbed on the sensor surface and form a continuous layer resulting in reduced surface area and fewer active sites. At 100 °C, the chemisorbed-ions/ physisorbed-water molecules may get desorbed from the sensing surface and hence, may not significantly affect the sensor response. Thus, it can be concluded that the Pt@MoS₂ sensor has less effect of humidity and can be used for the development of smart and portable H₂ sensors. Moreover, the performance of Pt@MoS₂ sensor was compared

with previously reported 2D materials based H₂ sensor in Table 5.1. The sensing characteristics of our fabricated device reveals significantly good response with extreme low detection limit.

Table 5.1 Comparative response between the reported 2D materials based H₂ gas sensor and the present work

S. No	Device structure	Concentration (ppm)	Response (%)	Operating temperature	Limit of Detection (ppm)	Ref
1.	Edge enriched MoS ₂ flakes	10000	11	150 °C	N/A	[22]
2.	MoS ₂ Pyramids	10000	4	RT	N/A	[37]
3.	Porous MoS ₂ microstructure	700	27.5	120 °C	20	[38]
4.	Hollow MoS ₂ -Pt NPs	40000	12	RT	500	[39]
5.	Monolayer MoS ₂ -Pd nanocluster	140	17	RT + UV	20	[40]
6.	VA MoS ₂ -Pd NPs	500	33	RT	10	[41]
7.	RGO / MoS ₂ NPs	200	15.6	60 °C	200	[21]
8.	MoS ₂ /Si	40000	220.7	RT	5000	[20]
9.	Pd-MoS ₂ nanocomposite	10000	35.3	RT	50	[42]
10.	MoS ₂ - multi component alloy (Ag-Au-Cu-Pd-Pt) NPs	1000	32	80 °C	500	[43]
11.	Pd-graphene composite	50000	15.9	RT	100	[44]
12.	Graphene-Pd NPs	1000	33	RT	50	[45]
13.	Graphene –Pd/Ag nanocomposite	5000	16.2	RT	100	[46]
14.	Pt NPs decorated BP	6000	15	RT	500	[47]
15.	Pt NPs decorated VA-MoS ₂ flakes	50	23	RT	0.5	Present work
16.	Pt NPs decorated VA-MoS ₂ flakes	50	42.5	100 °C	0.5	Present work

5.3.3 Proposed sensing mechanism

In the normal ambient condition oxygen molecules are present and may get adsorbed on the surface of MoS₂ during synthesis or post synthesis. These adsorbed oxygen extract electron from the valence band of p- type MoS₂ and a hole accumulation layer (HAL) is developed near the surface, resulting in high resistance [48]. Pt NPs promotes catalytic oxidation and large no. of electrons are extracted from MoS₂ surface resulting in HAL extension, causing a resistance decline. Figure 5.12 represents the schematic of the sensing mechanism of Pt NPs sensitized VA-MoS₂ for H₂ sensing. The improved H₂ sensing performance of Pt@MoS₂ is attributed to spillover effect and creation of additional adsorption sites on Pt NPs surface or Pt-MoS₂

interface. In Pt@MoS₂, exposed H₂ gas molecules first get adsorbed on the catalytic Pt surface and dissociate into H atoms, which migrate to the MoS₂ surface via spillover effect. Thus, it offers surface reaction between H-atom and MoS₂ and supports the diffusion of H-atom into MoS₂ [49]. The resistance of the sensor decreases upon H₂ exposure, which implies H₂ withdraws electrons from the MoS₂. The possible H₂ adsorption reactions on the Pt@MoS₂ surface are as follows:

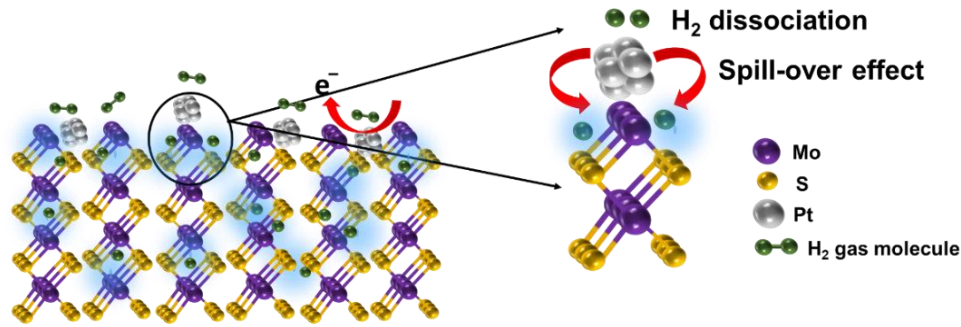
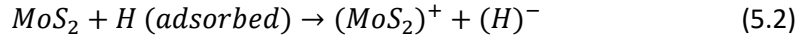
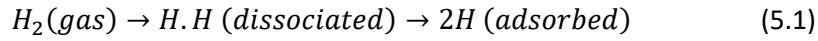


Figure 5.12 Proposed sensing mechanism of Pt@MoS₂ by Hydrogen spillover effect.

However, in case of pristine MoS₂, H₂ gas molecules get directly adsorbed on the active sites (Mo or S-site) of the MoS₂ and then dissociate into H atom via Mo-H and S-H [50]. Afterwards, diffusion of H-atom allowed at Mo edge to form H-S group. Moreover, dissociation of adsorbed H₂ on Pt (Pt-H) is very likely to occur due to nearly flat activation energy of H on Pt that allows diffusion of H-atom into the MoS₂ [51, 52]. Therefore, sensing performance in Pt@MoS₂ is ascribed by Pt NPs induced Hydrogen (H) spillover effect.

Density functional theory (DFT) calculations are conducted to provide a deeper insight into the sensing behavior of the fabricated sensors in terms of the adsorbent/gas interaction properties. The adsorption energies of gas molecules (H₂ and NO₂) are computed for MoS₂ and Pt@MoS₂ considering two different configurations, represented as T_M and T_S sites (described in Appendix II). Within Pt@MoS₂, a single Pt atom is placed at the top of Mo-layer of the Mo-edged vertical MoS₂ (T_M site) and at the top of S-layer of the S-edged MoS₂ (T_S site). Low positive formation energy (+0.70 eV for T_M site and -0.48 eV for T_S site) of Pt@MoS₂ indicates physisorption of Pt NPs on the top of the pristine MoS₂ surface, irrespective of Mo- or S-termination. Within Pt@MoS₂ bond distance between Pt-Mo and Pt-S are 2.29 Å and 2.46 Å, respectively. The adsorption energies, bond lengths, and electronic charge transfer for H₂ and NO₂ adsorbed

pristine MoS₂ (with Mo and S termination) and Pt@MoS₂ (T_M and T_S site) are provided in Table 5.2.

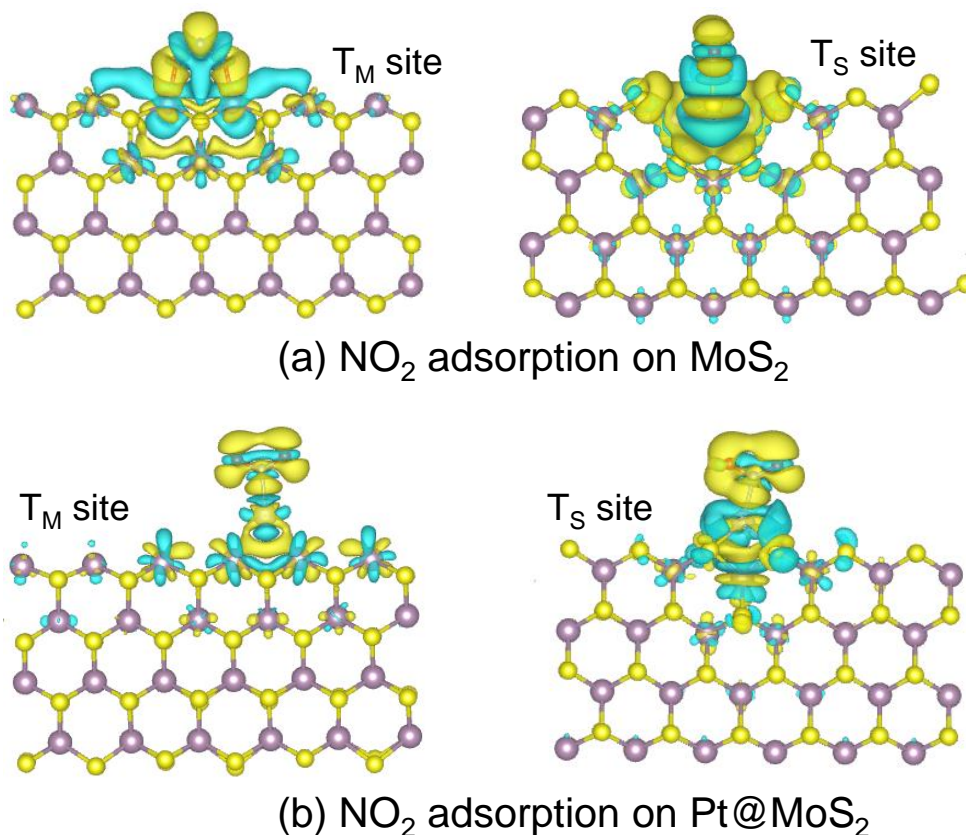


Figure 5.13 Charge density difference (CDD) plots of (a) NO₂ adsorbed on MoS₂ at the Mo-edge (T_M site) and S-edge (T_S site) (b) NO₂ adsorbed on Pt@MoS₂ at T_M and T_S site. Considering isosurface value of 0.001 e/Å³ and 0.0005 e/Å³ corresponds to T_M and T_S site, respectively. The yellow and cyan regions indicate the increase and decrease in the charge density values after gas adsorption.

As evident from the range of the adsorption energies, the NO₂ and H₂ gases are physisorbed on both MoS₂ and Pt@MoS₂ systems. Notably, irrespective of structural alignment, more negative NO₂ adsorption energy indicates higher NO₂ selectivity of pristine MoS₂ compared to Pt@MoS₂ system. This is further confirmed by the higher magnitude of charge transfer from MoS₂ to NO₂, compared to Pt@MoS₂ to NO₂. Moreover, the elongation of the N-O bond is more prominent within MoS₂/NO₂ (0.12 Å^{**}) compared to Pt@MoS₂/NO₂ (0.03 Å^{**}). For both the cases of VA-MoS₂ and Pt@MoS₂, NO₂ acts as electron acceptor as charge transfer occurs from system to gas molecules. On the other hand, H₂ adsorption is found to be stronger for Pt@MoS₂, signifying the high H₂ selectivity of Pt@MoS₂ compared to pristine MoS₂. The regions with the positive and negative charge density differences are represented in Figures 5.13 and 5.14 correspond to NO₂ and H₂ adsorption, respectively.

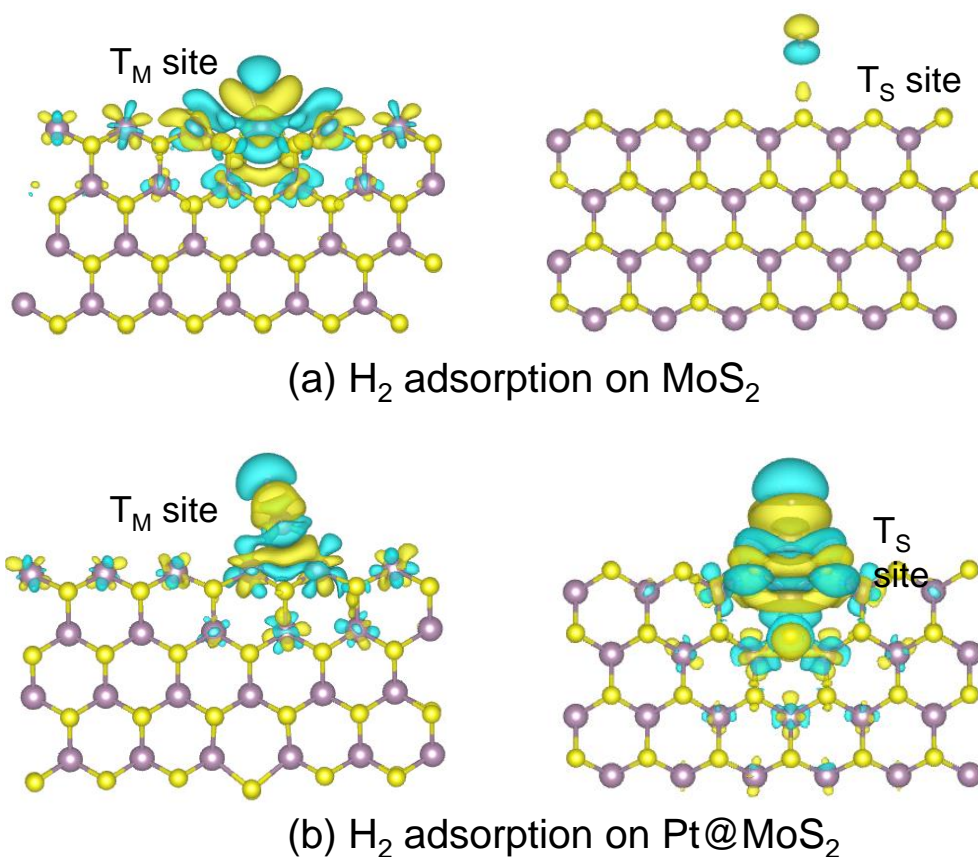


Figure 5.14 Charge density difference (CDD) plots of (a) H₂ adsorbed on MoS₂ at the Mo-edge (T_M site) and S-edge (T_S site) (b) H₂ adsorbed on Pt@MoS₂ at T_M and T_S site. Considering isosurface value of 0.0005 e/Å³ and 0.0001 e/Å³ corresponds to T_M and T_S site, respectively. The yellow and cyan regions indicate the increase and decrease in the charge density values after gas adsorption.

Interestingly, despite stronger adsorption, H-H bond elongation (0.07 Å^{**}) is found to be lower within Pt@MoS₂/H₂, compared to that within MoS₂/H₂ (0.20 Å^{**}). The smaller elongation of H-H bond in Pt@MoS₂ supports the dissociation of H₂ molecules via spill-over at Pt catalytic surface, which facilitate the migration of H atoms into MoS₂. Besides, charge transfer behaviour is found to be very interesting. In the case of Mo terminated-MoS₂, H₂ acts as an electron acceptor similar to NO₂ as the charge transfer occurs from MoS₂ to H₂ evident from positive charge transfer (+0.138e). Whereas, during H₂ adsorption, the total charge on the H₂ fragment within Pt@MoS₂/H₂ system (T_M site) reduces inferring H₂ as electron donor due to negative charge transfer (-0.028e). On the other hand, for both S-terminated MoS₂ and Pt@MoS₂, H₂ acts as electron acceptor gas. Although there is significant difference in the charge density distribution for S-terminated MoS₂ and Pt@MoS₂ (Figure 5.14, T_S site), the net charge transfer values are found to be very less (0.004e for MoS₂ and 0.003e Pt@MoS₂, respectively). Hence, the distinct response of sensors (MoS₂ for NO₂ selective and Pt@MoS₂

for H₂ selective sensing) is ascribed to the different gas adsorption depending upon the gas-adsorbate interaction or adsorption energy of gas molecules on the adsorbate system.

Table 5.2 Calculated gas adsorption energy, bond length and Bader charge difference (charge in the isolated state subtracted from the charge in the gas adsorbed state) of the gas adsorbed on MoS₂ and Pt@MoS₂.

System	Gas adsorption energy (eV)		Bond length (Å)		Bader charge differences (ΔQ)	
	T _M site	T _S site	T _M site	T _S site	T _M site	T _S site
MoS ₂ /NO ₂	-5.36	-2.42	Mo-O = 1.93 N-O = 1.33	S-N = 1.99 N-O = 1.22	+0.956e	+0.600e
Pt@MoS ₂ /NO ₂	-3.72	-1.44	Pt-N = 2.07 Mo-Pt = 2.55 N-O = 1.24	Pt-N = 2.10 S-Pt = 2.48 N-O = 1.23	+0.461e	+0.430e
MoS ₂ /H ₂	-1.87	-0.987	Mo-H = 1.84 H-H = 0.95	S-H = 4.18 H-H = 0.75	+0.138e	+0.004e
Pt@MoS ₂ /H ₂	-2.97	-1.01	Pt-H = 1.89 Mo-Pt = 2.61 H-H = 0.82	Pt-H = 1.73 S-Pt = 2.47 H-H = 0.92	-0.028e	+0.003e

5.4 conclusions

In conclusion, we have fabricated Pt NPs functionalized VA-MoS₂ sensor for enhanced sensing application. The large area flakes of VA-MoS₂ synthesized by CVD technique and Pt NPs directly sputtered over MoS₂ flakes to make Pt@MoS₂ composite. The PL quenching in Pt@MoS₂ suggests the efficient charge transfer between MoS₂ and Pt NPs. The XPS and UPS spectroscopy determined the band-alignment and p-doping effect after incorporation of Pt NPs. The Pt@MoS₂ sensor showed superior sensing response at RT (23% at 50 ppm H₂) and 100 °C (46% at 50 ppm H₂) is ascribed to Pt NPs induced H₂ spillover effect. Moreover, sensor can detect the H₂ over a wide concentration range (50- 0.5 ppm) in less than a minute. The sensor is highly selective to H₂ gas over other gas species (NO₂, NH₃, H₂S, CO₂ and SO₂). The high sensitivity and low detection ability (> 1 ppm) of the developed sensor at RT enable its usage many applications such as breath analyzer, process control and industrial leak.

References

1. Dutta, S., *A review on production, storage of hydrogen and its utilization as an energy resource*. Journal of Industrial and Engineering Chemistry, 2014. **20**(4): p. 1148-1156.
2. Singh, P.P., N. Nirmalkar, and T. Mondal, *Catalytic steam reforming of simulated bio-oil for green hydrogen production using highly active LaNi_xCo_{1-x}O₃ perovskite catalysts*. Sustainable Energy & Fuels, 2022. **6**(4): p. 1063-1074.
3. Cracknell, R.F., et al., *Safety Considerations in Retailing Hydrogen*. 2002, SAE International.
4. Lu, G., N. Miura, and N. Yamazoe, *High-temperature hydrogen sensor based on stabilized zirconia and a metal oxide electrode*. Sensors and Actuators B: Chemical, 1996. **35**(1): p. 130-135.
5. Shukla, S., et al., *Synthesis and characterization of sol-gel derived nanocrystalline tin oxide thin film as hydrogen sensor*. Sensors and Actuators B: Chemical, 2003. **96**(1): p. 343-353.
6. Zhou, Y., et al., *UV Illumination-Enhanced Molecular Ammonia Detection Based On a Ternary-Reduced Graphene Oxide-Titanium Dioxide-Au Composite Film at Room Temperature*. Analytical Chemistry, 2019. **91**(5): p. 3311-3318.
7. Wang, B., et al., *Palladium on paper as a low-cost and flexible material for fast hydrogen sensing*. Journal of Materials Science: Materials in Electronics, 2020. **31**(7): p. 5298-5304.
8. Hussain, G., et al., *Fast responding hydrogen gas sensors using platinum nanoparticle modified microchannels and ionic liquids*. Analytica Chimica Acta, 2019. **1072**: p. 35-45.
9. Luong, H.M., et al., *Sub-second and ppm-level optical sensing of hydrogen using templated control of nano-hydride geometry and composition*. Nature Communications, 2021. **12**(1): p. 2414.
10. Zhang, D., et al., *Room temperature hydrogen gas sensor based on palladium decorated tin oxide/molybdenum disulfide ternary hybrid via hydrothermal route*. Sensors and Actuators B: Chemical, 2017. **242**: p. 15-24.
11. Alenezy, E.K., et al., *Low-Temperature Hydrogen Sensor: Enhanced Performance Enabled through Photoactive Pd-Decorated TiO₂ Colloidal Crystals*. ACS Sensors, 2020. **5**(12): p. 3902-3914.
12. Dhall, S., K. Sood, and R. Nathawat, *Room temperature hydrogen gas sensors of functionalized carbon nanotubes based hybrid nanostructure: Role of Pt sputtered nanoparticles*. International Journal of Hydrogen Energy, 2017. **42**(12): p. 8392-8398.
13. Wadhwa, R., A.V. Agrawal, and M. Kumar, *A strategic review of recent progress, prospects and challenges of MoS₂-based photodetectors*. Journal of Physics D: Applied Physics, 2021. **55**(6): p. 063002.
14. Zhou, Y., et al., *UV light activated NO₂ gas sensing based on Au nanoparticles decorated few-layer MoS₂ thin film at room temperature*. Applied Physics Letters, 2018. **113**(8): p. 082103.
15. Late, D.J., et al., *Sensing Behavior of Atomically Thin-Layered MoS₂ Transistors*. ACS Nano, 2013. **7**(6): p. 4879-4891.
16. Zhang, D., et al., *Flexible self-powered high-performance ammonia sensor based on Au-decorated MoSe₂ nanoflowers driven by single layer MoS₂-flake piezoelectric nanogenerator*. Nano Energy, 2019. **65**: p. 103974.
17. Tang, M., et al., *Performance prediction of 2D vertically stacked MoS₂-WS₂ heterostructures base on first-principles theory and Pearson correlation coefficient*. Applied Surface Science, 2022. **596**: p. 153498.

18. Kumar, R., et al., *Highly selective and reversible NO₂ gas sensor using vertically aligned MoS₂ flake networks*. Nanotechnology, 2018. **29**(46): p. 464001.
19. Agrawal, A.V., et al., *Photoactivated Mixed In-Plane and Edge-Enriched p-Type MoS₂ Flake-Based NO₂ Sensor Working at Room Temperature*. ACS Sensors, 2018. **3**(5): p. 998-1004.
20. Liu, Y., et al., *Hydrogen gas sensing properties of MoS₂/Si heterojunction*. Sensors and Actuators B: Chemical, 2015. **211**: p. 537-543.
21. Venkatesan, A., et al., *Molybdenum disulfide nanoparticles decorated reduced graphene oxide: highly sensitive and selective hydrogen sensor*. Nanotechnology, 2017. **28**(36): p. 365501.
22. Agrawal, A.V., et al., *Fast detection and low power hydrogen sensor using edge-oriented vertically aligned 3-D network of MoS₂ flakes at room temperature*. Applied Physics Letters, 2017. **111**(9): p. 093102.
23. Cho, S.-Y., et al., *Highly Enhanced Gas Adsorption Properties in Vertically Aligned MoS₂ Layers*. ACS Nano, 2015. **9**(9): p. 9314-9321.
24. Kumar, D., et al., *Anisotropic electron–photon–phonon coupling in layered MoS₂*. Journal of Physics: Condensed Matter, 2020. **32**(41): p. 415702.
25. Agrawal, A.V., et al., *Controlled Growth of MoS₂ Flakes from in-Plane to Edge-Enriched 3D Network and Their Surface-Energy Studies*. ACS Applied Nano Materials, 2018. **1**(5): p. 2356-2367.
26. Mukherjee, S., et al., *Plasmon Triggered, Enhanced Light–Matter Interactions in Au–MoS₂ Coupled System with Superior Photosensitivity*. The Journal of Physical Chemistry C, 2021. **125**(20): p. 11023-11034.
27. Wadhwa, R., et al., *Platinum nanoparticle sensitized plasmonic-enhanced broad spectral photodetection in large area vertical-aligned MoS₂ flakes*. Nanotechnology, 2022. **33**(25): p. 255702.
28. Wang, Y., et al., *Ag decoration-enabled sensitization enhancement of black phosphorus nanosheets for trace NO₂ detection at room temperature*. Journal of Hazardous Materials, 2022. **435**: p. 129086.
29. Kumar, D., et al., *Coupled excitonic quasiparticle-electron–phonon and interlayer coupling in vertically and horizontally aligned MoS₂*. Journal of Materials Chemistry C, 2022. **10**(14): p. 5684-5692.
30. He, Z., et al., *Bidirectional tuning of phase transition properties in Pt:VO₂ nanocomposite thin films*. Nanoscale, 2020. **12**(34): p. 17886-17894.
31. Bhanu, U., et al., *Photoluminescence quenching in gold - MoS₂ hybrid nanoflakes*. Scientific Reports, 2014. **4**(1): p. 5575.
32. Amin, R., M.A. Hossain, and Y. Zakaria, *Interfacial Kinetics and Ionic Diffusivity of the Electrodeposited MoS₂ Film*. ACS Applied Materials & Interfaces, 2018. **10**(16): p. 13509-13518.
33. Nipane, A., et al., *Few-Layer MoS₂ p-Type Devices Enabled by Selective Doping Using Low Energy Phosphorus Implantation*. ACS Nano, 2016. **10**(2): p. 2128-2137.
34. Bhowmick, R., et al., *Hydrogen Spillover in Pt-Single-Walled Carbon Nanotube Composites: Formation of Stable C–H Bonds*. Journal of the American Chemical Society, 2011. **133**(14): p. 5580-5586.
35. Li, J., et al., *Improving Humidity Sensing of Black Phosphorus Nanosheets by Co-Doping Benzyl Viologen and Au Nanoparticles*. Journal of The Electrochemical Society, 2022. **169**(1): p. 017513.
36. Hashtroudi, H., et al., *Hydrogen gas sensing properties of microwave-assisted 2D Hybrid Pd/rGO: Effect of temperature, humidity and UV illumination*. International Journal of Hydrogen Energy, 2021. **46**(10): p. 7653-7665.

37. Agrawal, A.V., et al., *Enhanced adsorption sites in monolayer MoS₂ pyramid structures for highly sensitive and fast hydrogen sensor*. International Journal of Hydrogen Energy, 2020. **45**(15): p. 9268-9277.
38. Zhang, Y., W. Zeng, and Y. Li, *The hydrothermal synthesis of 3D hierarchical porous MoS₂ microspheres assembled by nanosheets with excellent gas sensing properties*. Journal of Alloys and Compounds, 2018. **749**: p. 355-362.
39. Park, C.H., et al., *Hydrogen Sensors Based on MoS₂ Hollow Architectures Assembled by Pickering Emulsion*. ACS Nano, 2020. **14**(8): p. 9652-9661.
40. Mai, H.D., et al., *Pd Nanocluster/Monolayer MoS₂ Heterojunctions for Light-Induced Room-Temperature Hydrogen Sensing*. ACS Applied Materials & Interfaces, 2021. **13**(12): p. 14644-14652.
41. Jaiswal, J., et al., *Fabrication of highly responsive room temperature H₂ sensor based on vertically aligned edge-oriented MoS₂ nanostructured thin film functionalized by Pd nanoparticles*. Sensors and Actuators B: Chemical, 2020. **325**: p. 128800.
42. Baek, D.-H. and J. Kim, *MoS₂ gas sensor functionalized by Pd for the detection of hydrogen*. Sensors and Actuators B: Chemical, 2017. **250**: p. 686-691.
43. Urs, K.M.B., et al., *Multi-component (Ag–Au–Cu–Pd–Pt) alloy nanoparticle-decorated p-type 2D-molybdenum disulfide (MoS₂) for enhanced hydrogen sensing*. Nanoscale, 2020. **12**(22): p. 11830-11841.
44. Martínez-Orozco, R.D., R. Antaño-López, and V. Rodríguez-González, *Hydrogen-gas sensors based on graphene functionalized palladium nanoparticles: impedance response as a valuable sensor*. New Journal of Chemistry, 2015. **39**(10): p. 8044-8054.
45. Chung, M.G., et al., *Flexible hydrogen sensors using graphene with palladium nanoparticle decoration*. Sensors and Actuators B: Chemical, 2012. **169**: p. 387-392.
46. Sharma, B. and J.-S. Kim, *Graphene decorated Pd-Ag nanoparticles for H₂ sensing*. International Journal of Hydrogen Energy, 2018. **43**(24): p. 11397-11402.
47. Lee, G., et al., *Platinum-functionalized black phosphorus hydrogen sensors*. Applied Physics Letters, 2017. **110**(24): p. 242103.
48. Choi, S.-W., et al., *Remarkable Improvement of Gas-Sensing Abilities in p-type Oxide Nanowires by Local Modification of the Hole-Accumulation Layer*. ACS Applied Materials & Interfaces, 2015. **7**(1): p. 647-652.
49. Karim, W., et al., *Catalyst support effects on hydrogen spillover*. Nature, 2017. **541**(7635): p. 68-71.
50. Sun, M., A.E. Nelson, and J. Adjaye, *Adsorption and dissociation of H₂ and H₂S on MoS₂ and NiMoS catalysts*. Catalysis Today, 2005. **105**(1): p. 36-43.
51. Lucci, F.R., et al., *H₂ Activation and Spillover on Catalytically Relevant Pt–Cu Single Atom Alloys*. The Journal of Physical Chemistry C, 2015. **119**(43): p. 24351-24357.
52. Papoian, G., J.K. Nørskov, and R. Hoffmann, *A Comparative Theoretical Study of the Hydrogen, Methyl, and Ethyl Chemisorption on the Pt(111) Surface*. Journal of the American Chemical Society, 2000. **122**(17): p. 4129-4144.

Chapter 6: Summary and Scope for Future Studies

This chapter provides a summary of the challenges that have been addressed during this thesis work. The achievement of goals set by the motivation described in Chapter 1 is discussed in depth. We have addressed different challenges associated with 2D layered MoS₂ growth and traced their development in photodetector and gas-sensing applications with enhanced device performance. The scalable sputtering and chemical vapor deposition (CVD) technique is adopted to synthesize large-area, highly uniform in-plane to vertically aligned flakes of MoS₂ on various substrates by proper optimization of the growth parameters. Various photodetectors based on MoS₂ heterostructures have been fabricated during this work that governs improved performances as compared to pristine MoS₂ photodetector. Moreover, we successfully address the long-standing issue of room temperature selective hydrogen sensing by fabricating Pt NPs decorated MoS₂ gas sensor.

6.1 Summary

6.1.1 Large area growth of MoS₂ from in-plane to vertically oriented flakes

- The controlled growth of large area MoS₂ is a prerequisite for the advancement in 2D technology.
- We have demonstrated wafer-scale growth of MoS₂ from in-plane to vertically oriented MoS₂ flakes using an industrial-compatible sputtering technique by proper optimization of growth parameters such as growth pressure and deposition time.
- We have performed morphological, structural, optical, and spectroscopic analyses using FESEM, AFM, XRD, Raman, UV-Vis, and XPS to characterize the MoS₂ films.
- The experimental finding reveals that MoS₂ growth is strongly dependent upon the growth pressure.
- A mechanism has been proposed to understand the growth kinetics from 2D in-plane to 3D vertical standing growth of MoS₂.
- The synthesized vertically aligned MoS₂ flakes are highly uniform, which is corroborated by wafer-scale spectroscopic analysis using Raman spectroscopy.
- The large area growth of vertically aligned MoS₂ flakes is highly reproducible and able to achieve even on various substrates (Si, quartz, sapphire, carbon fiber) suggesting substrate-independent growth.

- The optoelectronic behavior of synthesized vertically aligned MoS₂ is investigated by fabricating its metal-semiconductor-metal photodetector.
- The fabricated MoS₂ photodetector showed good photoresponse and fast optical switching under the light on and off conditions.

6.1.2 2D MoS₂ heterostructures for broadband photodetection

The low optical absorbance in 2D layered MoS₂ and the absence of a high-quality junction limits its photodetection ability. Hence, in order to improve the performance of the MoS₂ photodetector, we have fabricated and studied the various heterostructures of MoS₂ discussed as follows:

6.1.2.1 MoS₂/ReS₂ heterostructure

- In this work, we have studied charge transport and band alignment at the MoS₂-ReS₂ heterointerface and as a proof of concept, we have fabricated the photodetector of heterojunction.
- The large area highly uniform interconnected vertically oriented MoS₂ flakes deposited on Si/SiO₂ substrate using CVD technique and ReS₂ NSs directly drop-casted over MoS₂ to form MoS₂-ReS₂ heterostructure.
- Raman and PL spectroscopy is performed to investigate interlayer coupling and charge transport mechanism between MoS₂ and ReS₂.
- Photoelectron spectroscopy (XPS and UPS) is utilized to evaluate the band alignment, which reveals that type II alignment is formed between MoS₂ and ReS₂ interface.
- Further, we have fabricated the heterojunction photodetector and compared the device performance with a pristine MoS₂ photodetector under broad spectral illumination.
- The photodetector results reveal that the concentration of ReS₂ plays a critical role and showed the best photoresponse for 50 μ l ReS₂ based heterojunction i.e MoS₂-ReS₂ 50, which is further corroborated by SEM and UV-Visible spectroscopy.
- The MoS₂-ReS₂ photodetector shows enhance photoresponse with a high responsivity of 46 A/W at a low bias of 1V bias, which is approximately 16 times that of a pristine MoS₂ photodetector.
- The MoS₂-ReS₂ photodetector also exhibits a fast response speed with a rise/fall time of 20/19 ms, which is attributed to the spatial separation of charge carriers across the interface.

- Moreover, the MoS₂-ReS₂ heterostructure photodetector exhibits a self-driven response under broad illumination from 400-1100 nm with high responsivity and detectivity values of 1.28 A/W and 1.34×10^{13} Jones, respectively.

6.1.2.2 MoS₂/Ga₂O₃ heterostructure

- In this work, we have fabricated a scalable 2D/3D heterostructure of MoS₂/a-Ga₂O₃ using sputtering technique and studied its band alignment and charge carrier dynamics for broadband photodetection.
- Band alignment calculation from XPS and UPS shows type I alignment exists between MoS₂ and Ga₂O₃.
- Further, KPFM measurements were carried out at MoS₂/Ga₂O₃ heterojunction in two different modes: Surface mode and junction mode to investigate the interface charge dynamics.
- We have fabricated MoS₂/Ga₂O₃ heterojunction to test its photodetection capabilities and found that the device showed broadband photoresponse from deep UV to NIR.
- The fabricated MoS₂/Ga₂O₃ photodetector exhibited a ~315-fold enhancement in responsivity compared to pristine MoS₂ photodetector, with a highest responsivity of 171 A/W, under 900 nm illumination at 5 V bias.
- The MoS₂/Ga₂O₃ photodetector also showed high sensitivity with a peak detectivity of 4.6×10^{13} Jones and ultrafast response speed of 97 μ s/114 μ s.
- Moreover, the heterostructure device is highly stable and shows negligible degradation in the device performance after leaving in ambient conditions for more than a month.

6.1.2.2 Platinum nanoparticles decorated MoS₂ heterostructure

- In this work, vertically aligned MoS₂ flakes grown by CVD technique and Pt NPs directly sputtered over MoS₂ to form a plasmon-enabled Pt@MoS₂ photodetector.
- After incorporation of Pt NPs, the surface-enhanced Raman scattering (SERS) in MoS₂ is ascribed to the augmented electromagnetic field intensity induced by localized surface plasmon resonance of Pt NPs
- The integration of Pt NPs on vertically aligned MoS₂ flakes suppresses the dark current due to electron transmission inhibition by forming a Schottky junction at the Pt-MoS₂ interface.
- Pt@MoS₂ offers enhanced absorbance owing to absorption and scattering by Pt NPs and near-field enhancement. The plasmon-induced Pt@MoS₂ photodetector shows

broadband photoresponse from 400 to 1100 nm wavelength regime with a four-fold enhancement in photocurrent and an eight-fold increment in the photo-to-dark current ratio.

- The fabricated Pt@MoS₂ photodetector showed an enhanced responsivity of 432 A/W and specific detectivity of 1.85×10^{14} Jones at moderate bias (5V).
- The plasmon-enhanced near field and built-in electric field at the Pt-MoS₂ interface facilitate the carrier separation, resulting in an increased photoresponse with a fast response time of 87 ms /84 ms.
- Furthermore, a theoretical approach is adopted to calculate wavelength-dependent responsivity by correlating the quantum efficiency of the photodetector and the absorption coefficient, which matches well with experimental results.

6.13 2D MoS₂ heterostructures for hydrogen sensing

- The increasing demand of hydrogen as an alternative clean fuel emboldened the parallel development of extremely sensitive room-temperature H₂ sensors for safety purposes.
- In this direction, we have fabricated Pt NPs decorated vertically aligned MoS₂ selective H₂ sensor working at room temperature.
- The size of Pt NPs plays a crucial role in sensing performance.
- The sensing performance of the fabricated Pt@MoS₂ sensor is systematically investigated, and the possible sensing mechanism is discussed.
- The sensor exhibits a high sensitivity value of 23%, excellent reproducibility, fast response, and complete recovery at room temperature.
- The influence of operating temperature on the sensing performance is also investigated and achieves a maximum sensitivity value of 46% at 100 °C.
- The sensor can detect a wide range of H₂ concentrations with the lowest detection limit of 0.5 ppm.
- The sensor shows high reproducibility and stability over an extended period of time.
- The sensor is highly selective to H₂ gas over other gas species (NO₂, NH₃, H₂S, CO₂, and SO₂).
- We have also performed density functional theory calculations to validate our experimental results, which further demonstrate higher adsorption of H₂ for Pt@MoS₂ leading to improved and selective H₂ response.

6.2 Scope for future studies

The present thesis work has made significant contributions to the field by establishing new and promising results. However, there are still exciting opportunities to explore new challenges and advance the research further.

- Adoption of transfer techniques to form heterojunctions on large area MoS₂. This approach can significantly enhance the performance and functionality of MoS₂-based devices by enabling the integration of different materials with MoS₂.
- The fabrication of flexible and wearable devices has become an increasingly important area of research due to their potential applications in a variety of fields such as healthcare and consumer electronics. The development of such devices requires novel fabrication techniques and the use of flexible materials. This can lead to the creation of more versatile and practical devices that can be integrated into everyday life.
- The development of photodetector and gas sensor devices that can operate under extreme conditions can have a significant impact in various industries. For instance, high-temperature photodetectors can be used in high-temperature industrial processes, while gas sensors that can operate under high humidity conditions can be used in industries such as agriculture and environmental monitoring. The ability to create such devices can lead to the development of more reliable and robust sensing systems.

Appendix I

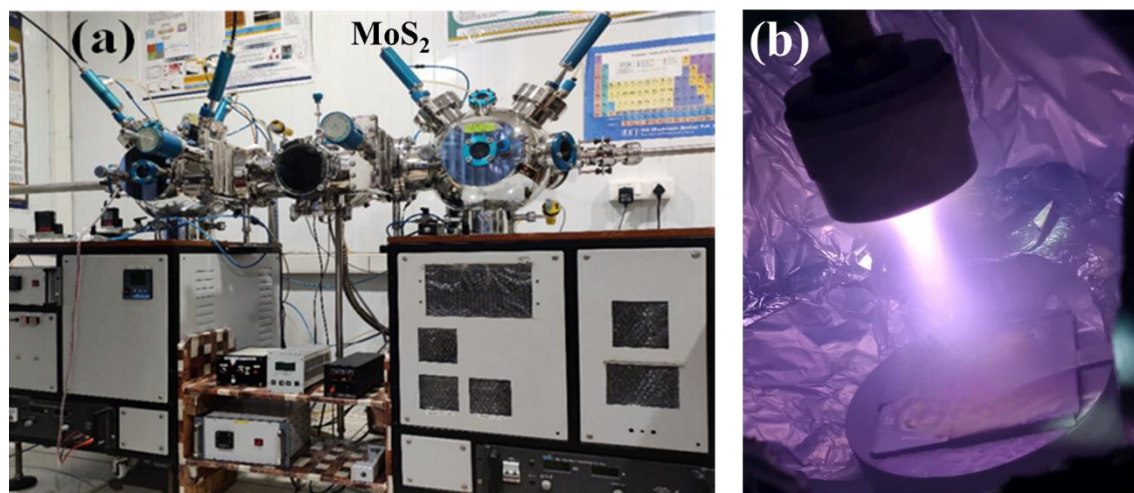


Figure AI.1 (a) Sputtering system used for MoS₂ deposition. (b) Real time image of MoS₂ plasma formation.



Figure AI.2 Atmospheric pressure chemical vapor deposition (APCVD) used to deposit MoS₂ flakes.

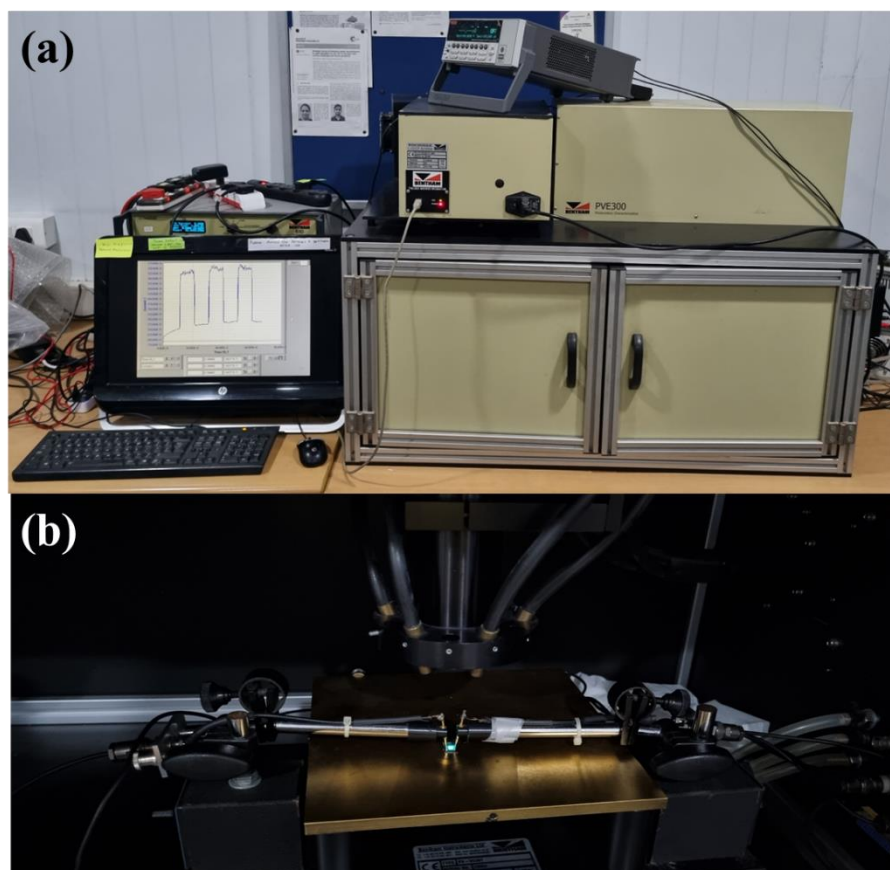


Figure AI.3 (a) Experimental setup used to measure photoresponse of fabricated MoS₂-based photodetectors. (b) Photodetector device under testing.



Figure AI.4 Gas sensing setup used to characterize MoS₂-based gas sensors.

Appendix II

Computational details of density functional theory

Plane-wave pseudopotential (PW-PP) based DFT calculations were carried out using Quantum Espresso package to provide an explicit description of the gas sensing properties of pristine and Pt-decorated VA-MoS₂ flakes. The VA-MoS₂ flakes were modelled considering $4 \times 6 \times 1$ supercell of MoS₂ monolayer consisting of 24 Mo and 48 S atoms. Vacuum regions of 15 Å was provided to both the X and Z directions to consider the vertical alignment and avoid inter-layer interactions. GGA-PBE functional was employed with ultrasoft pseudopotential (USPP) considering 680 eV as the plane-wave cut-off energy and $1 \times 2 \times 1$ k-grid points in the Brillouin zone. The convergence threshold of energy and force were set to 1.36×10^{-5} eV and 0.025 eV/Å, respectively. We have analysed both Mo-terminated (neglecting S-saturation) and S-terminated MoS₂, where Pt attached to Mo- and S-terminated MoS₂ are denoted as T_M site and T_S site, respectively. For the gas-adsorbed systems, NO₂ and H₂ molecules are placed at the top of Mo (T_M site) and S (T_S site) for MoS₂ and Pt sites for Pt@MoS₂, respectively. The formation energy (ΔE_f) of Pt@MoS₂ is calculated as $\Delta E_f = E_{Pt@MoS_2} - (E_{MoS_2} + E_{Pt})$, where $E_{Pt@MoS_2}$ and E_{MoS_2} are the energies of Pt decorated VA-MoS₂ and pristine VA-MoS₂ flakes. E_{Pt} is the energy of a single Pt atom calculated as the energy of the bulk Pt unit cell divided by the number of Pt atoms within the unit cell. The gas adsorption energies (ΔE_{ads}) are calculated as $\Delta E_{ads} = E_{X/gas} - (E_X + E_{gas})$, where $E_{X/gas}$, E_X , and E_{gas} are the energies of gas molecule-added X (X= MoS₂ or Pt@MoS₂), isolated MoS₂ or Pt@MoS₂, and isolated gas molecules, respectively. The adsorbent/gas interactions are demonstrated in terms of the charge density difference (CDD) plots and Bader charge analysis carried out using Bader code.

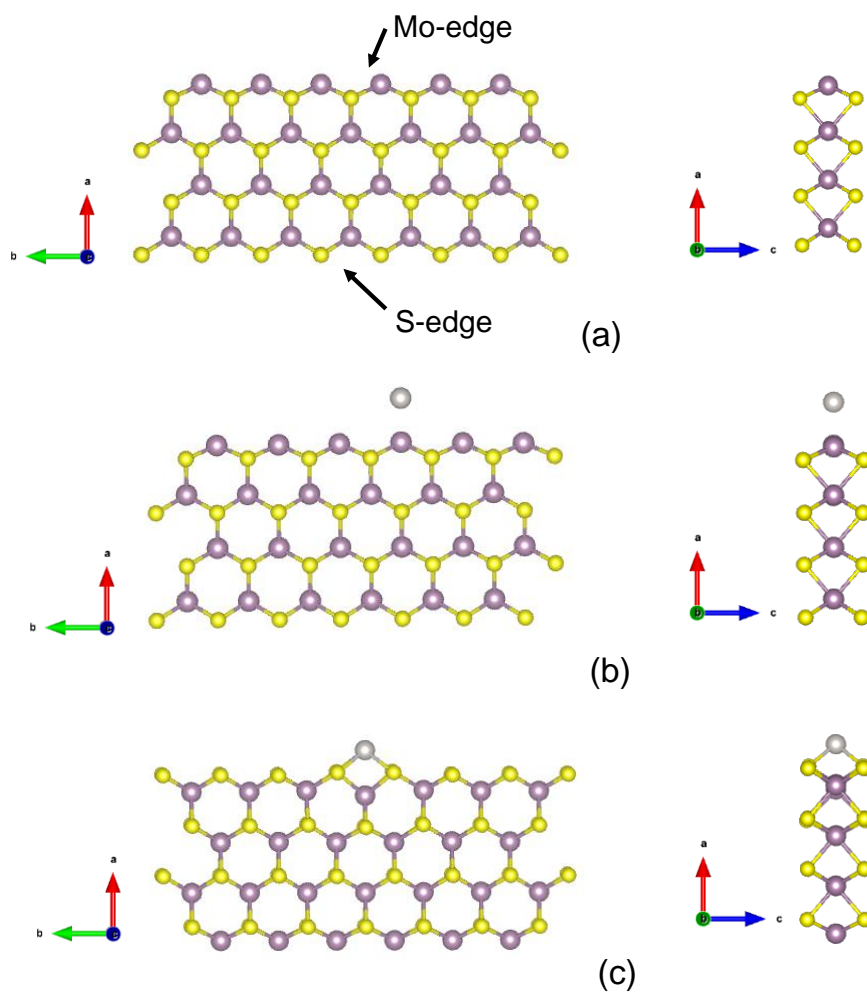


Figure AII.1 Optimized structures of (a) Pristine MoS₂, (b) Pt@MoS₂ (Pt added to Mo-edge-T_M site), and (c) Pt@MoS₂ (Pt added to S-edge - T_S site)

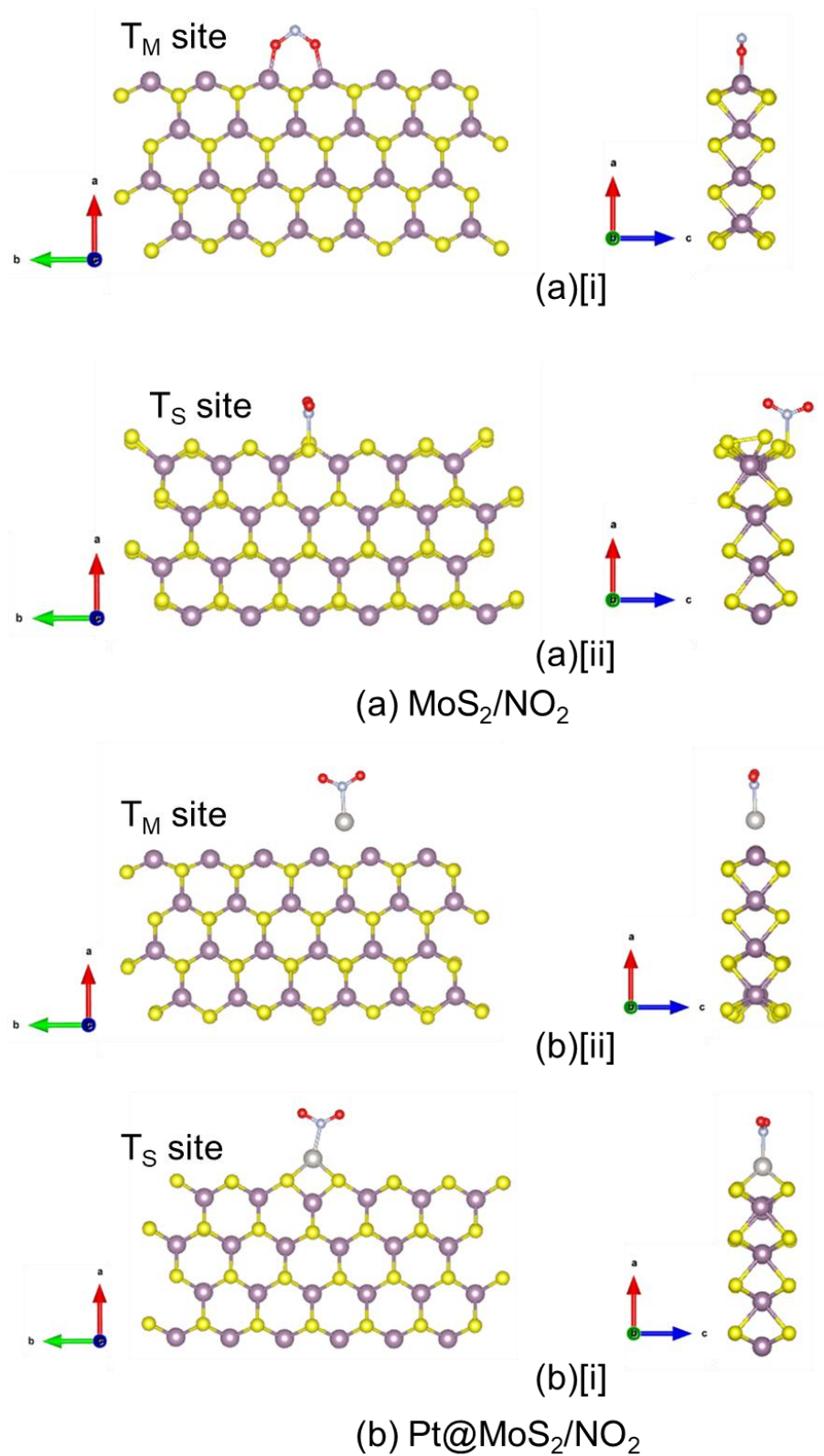


Figure AII.2 Optimized structures of (a) MoS_2/NO_2 [i] NO_2 adsorbed at the Mo-edge, [ii] NO_2 adsorbed at the S-edge and (b) $\text{Pt@MoS}_2/\text{NO}_2$ [i] NO_2 adsorbed on Pt@MoS_2 (T_M site), [ii] NO_2 adsorbed on Pt@MoS_2 (T_S site).

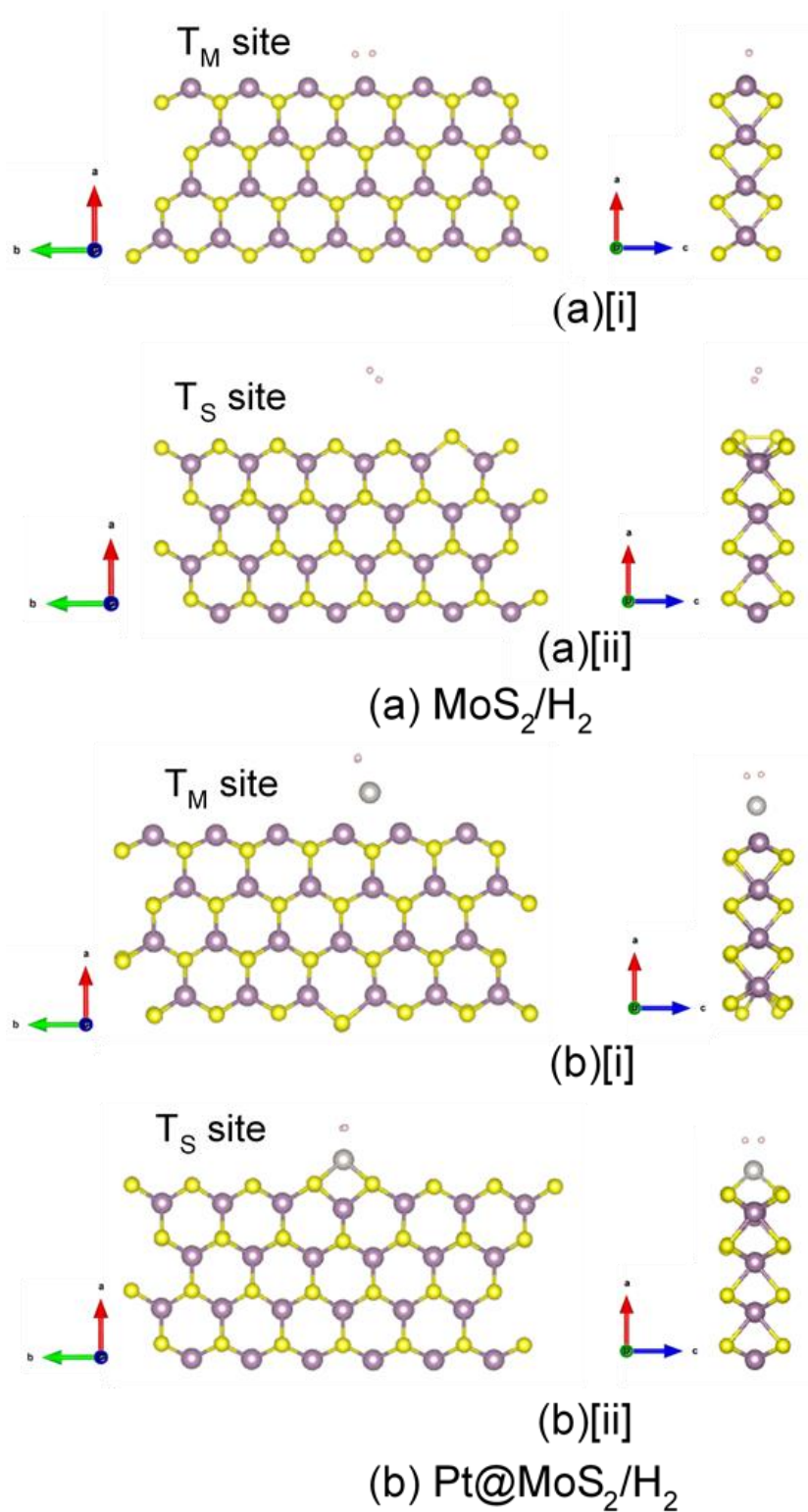


Figure AII.3 Optimized structures of (a) MoS_2/H_2 [i] H_2 adsorbed at the Mo-edge, [ii] H_2 adsorbed at the S-edge on MoS_2 and (b) $\text{Pt@MoS}_2/\text{H}_2$ [i] H_2 adsorbed on Pt@MoS_2 (T_M site), [ii] H_2 adsorbed on Pt@MoS_2 (T_S site).

List of Publications

1. **Riya Wadhwa**, A.V. Agrawal, Dushyant Kushavah, Aamir Mushtaq, S.K. Pal and Mukesh Kumar, Investigation of charge transport and band alignment of MoS₂-ReS₂ heterointerface for high performance and self-driven broadband photodetection, **Applied Surface Science** 569, (2021), 150949
2. **Riya Wadhwa**, A.V. Agrawal and Mukesh Kumar, A strategic review of recent progress, prospects and challenges of MoS₂-based photodetectors, **Journal of Physics D: Applied Physics** 55, (2021), 063002
3. **Riya Wadhwa**, Anupam Ghosh, Deepu Kumar, Pradeep Kumar, and Mukesh Kumar, Platinum nanoparticle sensitized plasmonic-enhanced broad spectral photodetection in large area vertical-aligned MoS₂ flakes, **Nanotechnology** 33, (2022), 255702
4. **Riya Wadhwa**, Sanjeev Thapa, Sonia Deswal, Pradeep Kumar, Mukesh Kumar, Wafer-scale controlled growth of MoS₂ by magnetron sputtering: from in-plane to inter-connected vertically-aligned flakes, **Journal of Physics: Condensed Matter** 35, (2023), 124002
5. **Riya Wadhwa**, Ashok Kumar, Ranjini Sarkar, Prajna Parimita Mohanty, Deepu Kumar, Sonia Deswal, Pradeep Kumar, Rajeev Ahuja, Sudip Chakraborty, Mahesh Kumar, Mukesh Kumar, Pt Nanoparticles on Vertically Aligned Large-Area MoS₂ Flakes for Selective H₂ Sensing at Room Temperature, **ACS Applied Nano Materials** 6, 4, (2023), 2527–2537
6. **Riya Wadhwa**, Damanpreet Kaur, Yuchen Zhang, Akhil Alexander, Deepu Kumar, Pradeep Kumar, Manoj Namboothiry, Quinn Qiao, Mukesh Kumar, Ultrafast and High-Performance UV-C to NIR Broadband Photodetector based on MoS₂/a-Ga₂O₃ heterostructures and impact of Band-alignment and Charge Carrier Dynamics, **Applied Surface Science** 632, (2023), 157597
7. Kulwinder Kaur, **Riya Wadhwa**, Anupam Ghosh, Nisika, Deepu Kumar, Pardeep Kumar and Mukesh Kumar, Residual strain engineering in seed layer assisted Kesterite Cu₂ZnSnS₄ absorber layer, **Materials Today Communications** 33, (2022), 104414
8. Gaurav Bassi, **Riya Wadhwa**, Sonia Deswal, Pradeep Kumar, Mukesh Kumar, Controlled and tunable growth of ambient stable 2D PtS₂ thin film and its high-performance broadband photodetector, **Journal of Alloys and Compounds** 955, (2023), 170233
9. Damanpreet Kaur, **Riya Wadhwa**, Nisika, Yuchen Zhang, Poojan Kaswekar; Quinn Qiao, Anju Sharma, Mark Poliks, Mukesh Kumar, Interfacial-mixing and band engineering induced by annealing of CdS and a-Ga₂O₃ n-n type thin film heterojunction and its impact on carrier dynamics for high-performance solar-blind photodetection, **ACS Applied Electronic Materials** 2023
10. Anupam Ghosh, **Riya Wadhwa**, Shivani, Sonia Deswal, Pradeep Kumar and Mukesh Kumar, Staggered band alignment of n-Er₂O₃/p-Si heterostructure for the fabrication of a high-performance broadband photodetector, **Journal of Physics D: Applied Physics (Communicated)**

Conferences/Workshops Attended

1. **Riya Wadhwa** and Mukesh Kumar, Poster presentation, High performance broadband self-powered MoS₂/ ReS₂ photodetector, International Symposium on Semiconductor Materials and Devices (ISSMD-2020), October 31-November 2, 2020, NIT Jalandhar.
2. **Riya Wadhwa** and Mukesh Kumar, Poster presentation, Highly sensitive, MoS₂/ReS₂ heterostructure with self-driven broadband photodetection, 5th International Conference on Emerging Electronics (IEEE-ICEE 2020), November 26-28, 2020, IIT Delhi.
3. **Riya Wadhwa** and Mukesh Kumar, Oral presentation, Energy level alignment and charge transport investigation at MoS₂-ReS₂ interface for broadband photodetector, Oral presentation, International Conference on Condensed Matter & Device Physics (ICCMDP)-2021, September 9-11, 2021, PDEU Gandhinagar.
4. **Riya Wadhwa** and Mukesh Kumar, Poster presentation, Band-alignment investigation of MoS₂-ReS₂ heterointerface with highly sensitive, self-driven broadband photo-response, E-MRS 2021 Fall Meeting, September 20-23, 2021, Poland.
5. **Riya Wadhwa** and Mukesh Kumar, Poster presentation, High performance self-powered MoS₂/ReS₂ broadband photodetector, 2021 MRS Fall meeting & Exhibit, December 6-8, 2021, Boston Massachusetts.
6. **Riya Wadhwa** and Mukesh Kumar, Poster presentation, Plasmon enhanced Pt nanoparticles decorated vertical oriented few-layer MoS₂ broadband photodetector, Light-Matter Interactions in Low Dimensional and Topological Photonic Materials 2022, January 27-February 1, 2022, IISC Bangalore.
7. **Riya Wadhwa** and Mukesh Kumar, Poster presentation, High performance self-driven broadband photodetector based on type II MoS₂ -ReS₂ van der Waals heterostructure, IUMRS-ICA 2022, December 19-23, 2022, IIT Jodhpur.
8. **Riya Wadhwa** and Mukesh Kumar, Poster presentation, Pt nanoparticle decorated large area vertically aligned MoS₂ flakes for photodetector and H₂ sensing applications, Anusandhan 1.0, 2023, IIT Mandi
9. INUP Familiarisation workshop on “*Basic training program on Nano Science and Technology*”, 2019, IISC Bangalore
10. Online Short-term course on “*Nanotechnology for Electronic and Photonic Devices*”, 2020, PEC, Chandigarh

Curriculum Vitae

Riya Wadhwa

Research Scholar

Functional and renewable energy material laboratory (FREM lab)

Department of Physics

Indian Institute of Technology Ropar, Rupnagar, Punjab, 140001, India

Researchgate: <https://www.researchgate.net/profile/Riya-Wadhwa>

Google Scholar: [Google Scholar/IIT Ropar/Riya-Wadhwa](https://scholar.google.com/citations?user=2017phz0006&hl=en)

Email: 2017phz0006@iitrpr.ac.in & riyawadhwa424@gmail.com

Contact: +91-9808349238

Date of Birth: December 6, 1995

RESEARCH INTEREST

- 2D Materials and Heterostructures
- Synthesis and characterization of 2D materials and thin films
- Wide bandgap semiconductors
- Photodetector
- Solar cell
- Gas sensor

EDUCATION

Doctor of Philosophy | *Physics*

January 18 – Present

Dissertation: *Fabrication of Two-dimensional MoS₂-based Heterostructures for Photodetector and Gas-sensing Applications*

Indian Institute of Technology Ropar, India

Performance/CGPA: 9.5

Master of Science | *Physics (2015-2017)*

Chaudhary Charan Singh University, Meerut, India

Performance/Percentage: 83.05

Bachelor of Science | *Physics, Chemistry, Mathematics (2012-2015)*

Chaudhary Charan Singh University, Meerut, India

Performance/Percentage: 81.75

ACADEMIC ACHIEVEMENTS

- Among top 1% students to get highest marks in 12th Board Examination (U.P)
- INSPIRE Fellow under SHE (2012-2017)
- Secured 543 All India Rank in Joint Admission test for Masters (JAM) Physics 2015
- Qualified Joint CSIR - UGC NET Examination Physics DEC 2016
- Secured 109 All India Rank in Graduate Aptitude Test in Engineering (GATE) Physics 2017.
- Secured 382 All India Rank in Joint Entrance Screening Test (JEST) Physics 2017
- Recognized for an outstanding 3-Minute Thesis presentation, crowned as the winner at Anusandhan 1.0, 2023, IIT Mandi

RESEARCH EXPERIENCE AND TECHNICAL SKILLS

- Expertise in synthesis of 2D materials such as MoS₂, PtS₂ through CVD and sputtering
- Experience in thin film process development
- Other methods known: spin coating, dip coating, chemical bath deposition
- Expertise in device fabrication: photodetector, gas sensor
- Equipment handling experience: Keithley, Bentham PVE 300, High-performance photodetector measurement with optical chopper interface with an oscilloscope, NANOMAGNETICS INSTRUMENTS ezHEMS (Hall effect set up)
- Characterization tools known: Raman and PL spectroscopy, XRD, XPS and UPS, KPFM with hands-on experience in SEM, AFM, and UV-Vis-NIR spectroscopy
- Expertise in Data Analysis Software: MS Office, Origin, XPS Peak fit, Gwyddion, ImageJ

OTHER COMPETINCES

- Confident in taking independent initiatives for research activities
- An excellent team player- can work and co-ordinate within a group
- Willing to take new challenges
- Curiosity and ability to learn new skills
- Leadership skills: Guided two master's students for their master thesis projects

TEACHING EXPERIENCE

- Teaching Assistantship in Physics experimental laboratory for undergraduate students (B. Tech): January 2018-May 2018, January 2019-May 2019, and January 2020-March 2020.
- Teaching Assistant at Department of Physics, Indian Institute of Technology, Ropar: **Physics for Engineers**- August 2019-December 2019, **Statistical Mechanics**- September 2020- December 2020, **Physics for Engineers (Preparatory course)** - January 2021-May 2021.
- Teaching Assistant at Central Research Facility, Indian Institute of Technology, Ropar: For operating atomic force microscopy (AFM)- August 2019 -December 2019